

WIND LOADING ANALYSIS OF THE UNICREDIT HIGH-RISE BUILDING

FREDERICO CARVALHO ÁLVARES DE MELO FERREIRA

Dissertação submetida para satisfação parcial dos requisitos do grau de
MESTRE EM ENGENHARIA CIVIL — ESPECIALIZAÇÃO EM ESTRUTURAS

Orientador: Professor Doutor Filipe Manuel Rodrigues Leite
Magalhães

Coorientador: Professor Doutor Pietro Giuseppe Crespi

JULHO DE 2014

MESTRADO INTEGRADO EM ENGENHARIA CIVIL 2013/2014

DEPARTAMENTO DE ENGENHARIA CIVIL

Tel. +351-22-508 1901

Fax +351-22-508 1446

✉ miec@fe.up.pt

Editado por

FACULDADE DE ENGENHARIA DA UNIVERSIDADE DO PORTO

Rua Dr. Roberto Frias

4200-465 PORTO

Portugal

Tel. +351-22-508 1400

Fax +351-22-508 1440

✉ feup@fe.up.pt

🌐 <http://www.fe.up.pt>

Reproduções parciais deste documento serão autorizadas na condição que seja mencionado o Autor e feita referência a *Mestrado Integrado em Engenharia Civil - 2013/2014 - Departamento de Engenharia Civil, Faculdade de Engenharia da Universidade do Porto, Porto, Portugal, 2014.*

As opiniões e informações incluídas neste documento representam unicamente o ponto de vista do respetivo Autor, não podendo o Editor aceitar qualquer responsabilidade legal ou outra em relação a erros ou omissões que possam existir.

Este documento foi produzido a partir de versão eletrónica fornecida pelo respetivo Autor.

To my Family and Friends

To my Parents

ACKNOWLEDGEMENTS

This work was only possible thanks to the exhaustless support, patience and friendship of my family, friends and colleagues who made this hard final year a lot easier.

Special acknowledgments have to be made:

- To Professor Pietro Crespi, for the friendship, never ending patience, support and knowledge which were essential for the current work and have contributed to my evolution as a future engineer.
- To Professor Filipe Magalhães, who, although far, never failed to support me when I needed.
- To Professor Nicola Giordano, for the friendship, support and for the shared knowledge related to other civil engineering projects.
- To Professor João Paulo Miranda Guedes, who, through his network made it possible for me to develop my work in a different environment.
- To Célia Ferreira for the careful review of the text.
- To my friends António Castilho, Filipe Valente, Gonçalo Ferreira, Miguel Pereira and Rodrigo Freitas for their friendship and support during this long period. Thanks for all the laughs, fun and good moments during these last five years.
- To my friends Francisco Ribeiro, José Ribeiro José, Miguel Braz and Vitor Azoia for their support as well as for all the great moments which gave me the strength to work even harder.
- To my Parents, for everything. Without their incredible support and patience it would have never been possible for me to get to where I am today.

ABSTRACT

The work developed in this thesis has as main objective the analysis of the quasi-static and dynamic components of the wind loads acting on the Unicredit high-rise building located in Milan, Italy.

The characteristics of the atmospheric boundary layer, the wind profiles used in the different existing codes and the description of the mean and fluctuating components of the action of wind are presented in order to understand their influence in the wind loads.

As the current work is applied to a specific building, its characteristics, such as geometric dimensions of the structural elements, interstory heights and materials used in its construction are described.

Afterwards, the comparison between the values of the wind pressures obtained in the wind tunnel and through the Eurocode is done in order to understand if the use of the wind tunnel test brought any advantage for the specific case of the Unicredit high-rise building.

Once obtained the quasi-static component of the wind action through the wind tunnel test, the response of the structure to this load is evaluated by means of a numerical model.

Finally the method used to introduce the resonant component by means of equivalent static forces is described and the response of the structure to the total action of the wind is compared to the response due to the quasi-static component. Also, the serviceability of the structure is evaluated taking into account the displacements and accelerations induced by the wind loading on the structure.

KEYWORDS: High-Rise Building Wind Tunnel Test, Wind Quasi-Static Component, Wind Resonant Component, Design Codes, High Frequency Force Balance Test.

Index

ACKNOWLEDGEMENTS i

ABSTRACT iii

1. Introduction 1

 1.1. THE EVOLUTION OF WIND ENGINEERING 1

 1.2. MOTIVATION.....5

 1.3. ORGANIZATION OF THE THESIS 6

2. The Atmosphere.....9

 2.1. INTRODUCTION9

 2.2. ATMOSPHERIC PROCESSES, PROPRIETIES AND CHARACTERISTICS.....10

 2.2.1. ATMOSPHERIC THERMODYNAMICS.....10

 2.2.2. ATMOSPHERIC HYDRODYNAMICS.....12

 2.2.3. GLOBAL ATMOSPHERIC CIRCULATION16

 2.2.4. THERMAL GENERATED SECONDARY CIRCULATIONS18

 2.2.5. LOCAL WINDS.....19

 2.3. THE ATMOSPHERIC BOUNDARY LAYER20

 2.3.1. MEAN WIND VELOCITY.....21

 2.3.2. EXTREME WINDS28

 2.3.3. WIND TURBULENCE34

3. Case Study: The Unicredit High-Rise Building.....41

 3.1. INTRODUCTION41

 3.1.1. PORTA NUOVA41

 3.1.2. CITTÀ DELLA MODA.....42

 3.2. TOWER A: STRUCTURAL CHARACTERISTICS.....43

 3.2.1. FLOOR PLANS43

 3.2.2. ELEVATION AND INTERSTORY HEIGHT46

 3.2.3. COLUMNS.....48

 3.2.4. WALLS48

 3.2.5. SLABS.....49

 3.2.6. SPIRE50

3.2.7. FACADE.....	51
3.2.8. MATERIALS.....	51
3.3. STATIC LOADS	52
3.3.1. TOWER.....	52
3.3.2. SPIRE.....	54

4. Application of EN 1991-1-4 and Wind Tunnel Tests: The Unicredit High-Rise Building

4.1. INTRODUCTION	55
4.2. EUROCODE	56
4.2.1. GENERAL	56
4.2.2. WIND VELOCITY.....	56
4.2.3. WIND ACTIONS	62
4.2.4. PRESSURE COEFFICIENTS.....	63
4.2.5. FRICTION COEFFICIENTS	71
4.2.6. STRUCTURAL FACTOR.....	72
4.2.7. BASE FORCES AND MOMENTS	73
4.3. WIND TUNNEL TEST	76
4.3.1. WIND TUNNEL LAYOUTS.....	77
4.3.2. NATURAL WIND FLOW SIMULATION.....	78
4.3.3. MODELLING OF STRUCTURES FOR WIND EFFECTS.....	80
4.3.4. MEASUREMENTS OF LOCAL PRESSURES	81
4.3.5. THE CRIACIV WIND ENGINEERING LABORATORY	82
4.3.6. WIND TUNNEL TESTING OF TALL BUILDINGS.....	84

5. Numerical Model: The Unicredit High-Rise Building

5.1. INTRODUCTION.....	101
5.2. GENERAL.....	105
5.2.1. ABSOLUTE REFERENTIAL SYSTEM	105
5.2.2. CONSTRUCTION STAGE	108
5.2.3. LOAD COMBINATIONS.....	111
5.3. QUASI-STATIC ANALYSIS	115
5.3.1. EFFECT OF THE VERTICAL LOADS	115
5.3.2. WIND ACTION EFFECT.....	118

6. Dynamic Effects of Wind: Unicredit High-Rise Building

6.1. INTRODUCTION	131
6.2. RESONANT WIND LOADS	131
6.3. STATISTICAL COMBINATION OF DESIGN WIND LOADS	139
6.4. ACCELERATIONS FROM RESONANT WIND LOADS.....	141
6.5. DYNAMIC ANALYSIS.....	142
7. Conclusions	153
7.1. FINAL CONSIDERATIONS	153
7.2. FUTURE DEVELOPMENTS.....	155

INDEX OF FIGURES

Figure 1.1 – Round house	1
Figure 1.2 – Cologne cathedral	2
Figure 1.3 – Tay bridge collapse	3
Figure 1.4 – Alan Davenport’s wind loading chain	4
Figure 1.5 – Tacoma Narrow Bridge collapse (a) and Ferrybridge cooling towers collapse aftermath (b).....	2
Figure 2.1 – Ancient wind rose	9
Figure 2.2 – Heat transport along the atmosphere [6].....	10
Figure 2.3 – Atmospheric convection phenomenon [9]	11
Figure 2.4 – Movement of an air particle due to pressure gradient forces [6].....	13
Figure 2.5 – Direction of an air particle subjected to Coriolis and pressure gradient forces [6].....	13
Figure 2.6 – Equilibrium of forces and trajectory of an air particle of geostrophic wind [11].....	14
Figure 2.7 – Equilibrium of forces in Gradient wind with constant velocity in cyclonic and anticyclonic flows [11].....	15
Figure 2.8 – Wind in the atmospheric boundary layer [11].....	16
Figure 2.9 – Equilibrium of forces in the atmospheric boundary layer [11]	16
Figure 2.10 – Simplified model of atmospheric circulation [6].....	17
Figure 2.11 – Tricellular meridional circulation model [6].....	17
Figure 2.12 – Hurricane’s cross-section [11].....	18
Figure 2.13 – Foehn wind [6].....	19
Figure 2.14 – Cross-section of a Thunderstorm [11].....	20
Figure 2.15 – Wind’s mean and fluctuating components [11]	21
Figure 2.16 – Schematic representation of roughness length z_0 [11]	25
Figure 2.17 – Schematic representation of displaced wind profile [11].....	25
Figure 2.18 – Equilibrium and Internal boundary layer after a roughness change [11]	27
Figure 2.19 – Wind flow on a ridge with an upwind slope angle smaller than 17° [12]	27
Figure 2.20 – Wind flow on a ridge with an upwind slope angle larger than 17° [12].....	27
Figure 2.21 – Graphic representation of wind directionality of the case study of Tower A, for 10, 50 and 500 years of return period.....	30
Figure 2.22 – Generalized Extreme Value Distribution with $k=-0.2$, $k=0$ and $k=0.2$ [14].....	32
Figure 2.23 – Measurement of wind speed at three different heights in Denmark [11]	34

Figure 2.24 – Representation of c and m as a function of the roughness length [11]	37
Figure 2.25 – van der Hoven spectrum [12].....	38
Figure 2.26 – von Karman/Harris type spectrum [14]	40
Figure 3.1 – Panoramic view of Milan with Porta Nuova’s new high-rise buildings	41
Figure 3.2 – Architectural rendition of Pelli’s Fashion City.....	42
Figure 3.3 – General view of Tower A (a) and Spire close up (b).....	43
Figure 3.4 – First floor plan [24]	44
Figure 3.5 – Core dimensions [23]	44
Figure 3.6 – Third to fourteenth floor plan [24].....	45
Figure 3.7 – Third to fourteenth floor cores [23].....	45
Figure 3.8 – Fourteenth to thirty secondth floor plan [24]	46
Figure 3.9 – Fourteenth to thirty secondth floor cores [23]	46
Figure 4.1 – Terrain roughness illustration, a) Terrain category 0, b) Terrain category I, c) Terrain category II, d) Terrain category III, e) Terrain category IV [26]	58
Figure 4.2 – Schematic representation of angular sector and upstream distance recommended by EN 1991-1-4 [26]	59
Figure 4.3 – Schematic representation of the effect of orography on wind velocity [26]	59
Figure 4.4 – Categories of exposure as a function of the geographic position of the site [28]	61
Figure 4.5 – Schematic representation of positive and negative pressures according to EN 1991-1-4 [26]	63
Figure 4.6 – External pressure coeficiente c_{pe} [26].....	64
Figure 4.7 – Velocity pressure profile and reference height z_e [26]	64
Figure 4.8 – Vertical wall division [26].....	65
Figure 4.9 – Velocity pressure profiles for the X and Y wind directions.....	69
Figure 4.10 – a) Windward and Leeward pressures for the 50 year return period wind action on the X direction, b) Windward and Leeward pressures for the 50 year return period wind action on the Y direction	70
Figure 4.11 – Reference areas for the frictional component of wind [26]	71
Figure 4.12 – General shapes of structures covered by the detailed procedure [26]	73
Figure 4.13 – Wind tunnel test 1/350 scaled model [34].....	76
Figure 4.14 – Layout of an open circuit wind tunnel [14]	77
Figure 4.15 – The University of Western Ontario Boundary-Layer Wind Tunnel [29].....	
Figure 4.16 – Pressure measurement system [34]	82
Figure 4.17 – CRIACIV Boundary Layer Wind Tunnel [33].....	83

Figure 4.1 – Schematic representation of the connection between a pressure tap and a transducer [34].....	84
Figure 4.19 – Map of the pressure taps [34].....	85
Figure 4.20 – Wind tunnel reference system [34].....	86
Figure 4.21 – Sign convention the base resultant forces [34].....	88
Figure 4.22 – High frequency base balance schematic representation [29]	89
Figure 4.23 – Wind tunnel test 1/100 scaled spire model [33]	91
Figure 4.24 – Sign convention for the base resultant forces on the spire. [33].....	93
Figure 4.25 – Minimum and maximum side widths	94
Figure 4.26 – c_p map for Gumbel extreme $F_x=1542$ kN for $\alpha=90^\circ$	94
Figure 4.27 – c_p map for Gumbel extreme $M_y=166443$ kN.m for $\alpha=90^\circ$	95
Figure 4.28 – Windward 1 and 2 wind profile for F_x	97
Figure 4.29 – Leeward 1 and 2 wind profile for F_x	97
Figure 4.30 – Windward 1 and 2 wind profile for M_y	98
Figure 4.31 – Leeward 1 and 2 wind profile for M_y	98
Figure 5.1 – Foundation of the numerical model.....	101
Figure 5.2 – Floor -2 of the numerical model.....	102
Figure 5.3 – Ground Floor of the numerical model.....	102
Figure 5.4 – Floor 1 of the numerical model.....	103
Figure 5.5 – Floor 2 of the numerical model.....	103
Figure 5.6 – Floor 3 of the numerical model.....	104
Figure 5.7 – Floor 16 of the numerical model.....	104
Figure 5.8 – Spire of the numerical model.....	105
Figure 5.9 – Unicredit high-rise building numerical model	105
Figure 5.10 – Reference System of the numerical model	106
Figure 5.11 – Angle between the local and global referential systems	106
Figure 5.12 – Construction stage 6	110
Figure 5.13 – Construction stage 20	111
Figure 5.14 – Construction stage 46	111
Figure 5.15 – Groups of columns considered	115
Figure 5.16 – Shear force diagram on the low-rise core due to the SLU 1 combination	116
Figure 5.17 – Shear force diagram on the right core due to the SLU 1 combination.....	116
Figure 5.18 – Shear force diagram on the left core due to the SLU 1 combination	117
Figure 5.19 – Shear force diagram on the central core due to the SLU 1 combination	117

Figure 5.1 – Representation of the displacement of the roof due to the SLU 1 combination	118
Figure 5.21 – Shear force diagram on the low-rise core due to the SLU 4 – 10 combination	119
Figure 5.22 – Finite element with the maximum shear force on the base of the low-rise core.....	119
Figure 5.23 – Shear force diagram on the right core due to the SLU 4 – 75 combination	120
Figure 5.24 – Finite element with the maximum shear force on the base of the right core	120
Figure 5.25 – Shear force diagram on the left core due to the SLU 4 – 10 combination.....	121
Figure 5.26 – Finite element with the maximum shear force on the base of the left core	121
Figure 5.27– Shear force diagram on the central core due to the SLU 4 – 31 combination.....	122
Figure 5.28 – Finite element with the maximum shear force on the base of the central core	122
Figure 5.29 – Representation of the displacement of the roof due to the SLE 3 - 10 combination	126
Figure 5.30 – Map of the Roof and Floor 1 drift according to the different wind directions	127
Figure 5.31 – Map of the total building drift according to the different wind directions.....	129
Figure 6.1 – Top view of mode shape1	134
Figure 6.2 – Side view of mode shape 1.....	135
Figure 6.3 – Top view of mode shape 2.....	135
Figure 6.4 – Front view of mode shape 2.....	135
Figure 6.5 – Top view of mode shape 3.....	136
Figure 6.6 – Perspective view of mode shape 3	136
Figure 6.7 – Power Spectral Density function of the base moment M_x for 0° direction.....	137
Figure 6.8 – Power Spectral Density function of the base moment M_y for 0° direction.....	137
Figure 6.9 – Power Spectral Density function of the base moment M_z for 0° direction.....	138
Figure 6.10 – Decomposition of torsional accelerations into translational accelerations.....	141
Figure 6.11 – Representation of the interstory drift for different wind directions	147
Figure 6.12 – Representation of the total building drift for different wind directions	148
Figure 6.13 – Power Spectral Density function of the base moment M_z for 315° direction	152

INDEX OF TABLES

Table 2.1 – Storm types and respective appropriate time scales [12]	29
Table 3.1 – Floor type and interstory heights of Tower A.....	46
Table 3.2 – Column dimensions	48
Table 3.3 – Wall Thickness.....	49
Table 3.4 – Slab Thickness	50
Table 3.5 – Interstory and height of the spire	50
Table 3.6 – Spire horizontal dimensions	51
Table 3.7 – Characteristic strength of concrete.....	52
Table 3.8 – Static loads applied on the tower	53
Table 3.9 – Static loads applied on the spire	54
Table 4.1 – Terrain category defined by EN 1991-1-4 [26]	57
Table 4.2 – Zoning of the fundamental basic wind velocity [28].....	60
Table 4.3 – Categories of exposure of the site [28].....	60
Table 4.4 – Recommended values of $c_{pe,1}$ and $c_{pe,10}$ for vertical walls of rectangular plan buildings... 65	
Table 4.5 – $c_{pe,10}$ values for $\frac{h}{d} = 1.894$ obtained by linear interpolation.....	66
Table 4.6 – $c_{pe,10}$ values for $\frac{h}{d} = 7.78$	67
Table 4.7 – Wind pressure values obtained through EN 1991-1-4	70
Table 4.8 – Friction coefficients	71
Table 4.9 – X direction wind forces obtained through EN 1991-1-4.....	74
Table 4.10 – Y direction wind forces obtained through EN 1991-1-4.....	74
Table 4.11 – Base moment obtained from EN 1991-1-4 for an X direction wind action	75
Table 4.12 – Base moment obtained from EN 1991-1-4 for a Y direction wind action	75
Table 4.13 – Influence areas of the pressure taps	86
Table 4.14 – Maximum values of the base resultant forces obtained by means of C_p integration.....	87
Table 4.15 – Design resultant base forces acting on the base of the spire	92
Table 4.16 – Comparison between the base resultant forces obtained through the EN 1991-1-4 and through the wind tunnel test	93
Table 4.17 – F_x base resultant force wind profile values.....	96
Table 4.18 – M_y base resultant moment wind profile values.....	96
Table 5.1 – Base resultant forces (C_p Integration) on the global reference system	107

Table 5.2 – Base resultant forces of the spire in the global reference system	107
Table 5.3 – Construction stages.....	108
Table 5.4 – Combination factors through the DM05 Italian Code	112
Table 5.5 – Reduction factors through the DM05 Italian Code	112
Table 5.6 – Limit State coefficients	114
Table 5.7 – Axial force on the base of the columns due to the SLU 1 combination	115
Table 5.8 – Increase of the axial force on the base of the columns due to the action of wind	118
Table 5.9 – Increase of the shear force on a particular finite element due to wind action.....	122
Table 5.10 – Shear force at the base of each core due to the SLU 1 combination	123
Table 5.11 – Increase of the shear force at the base of each core due to wind action	124
Table 5.12 – Shear force at the base of each core for the critical directions	124
Table 5.13 – Influence of the action of wind on the cores and on the columns	125
Table 5.14 – Interstory drift at roof and floor 1 level.....	127
Table 5.15 – Total building drift	128
Table 6.1 – Participation coefficients of the masses.....	132
Table 6.2 – Natural frequencies and respective periods.....	132
Table 6.3 – Modal participation masses.....	133
Table 6.4 – Natural frequencies of the new and old numerical models	142
Table 6.5 – Resonant base moments for the old and new numerical models	142
Table 6.6 – Resonant base moments for a 0.15 Hz and 0.30 Hz frequency.....	143
Table 6.7 – Resonant base moment $M_{R,X}$ for different damping coefficients ξ	144
Table 6.8 – Resonant base moment $M_{R,Y}$ for different damping coefficients ξ	144
Table 6.9 – Resonant base moment $M_{R,Z}$ for different damping coefficients ξ	144
Table 6.10 – Resonant and Gumbel base moments.....	145
Table 6.11 – Axial force at the base of the columns due to wind action with the resonant component.....	146
Table 6.12 – Shear force at the base of the cores due to wind action with the resonant component .	146
Table 6.13 – Interstory drift due to wind action with the resonant component.....	146
Table 6.14 – Total building drift due to wind action with the resonant component	147
Table 6.15 – Peak acceleration limits	149
Table 6.16 – Roof \ddot{X} translational acceleration.....	149
Table 6.17 – Roof \ddot{Y} translational acceleration.....	150
Table 6.18 – Roof $\ddot{\vartheta}$ angular acceleration	150
Table 6.19 – Translational component of the angular acceleration	150

1

Introduction

1.1. THE EVOLUTION OF WIND ENGINEERING

The history of Wind Engineering can be divided into five periods [1], the “traditional” period, the “empirical” period, the “establishment” period, the period of growth and the modern period.

The “traditional” period is considered as the historic period up to 1750 hence covering a wide range of different social and intellectual contexts.

Regarding the Wind Engineering field, all around the world, the different styles of structures which were subjected mainly to wind loading evolved by experience and by the development of the various traditions. These distinctive styles of structures were then inevitably confined into specific locations, varying between the different cultures since these different styles were greatly influenced by religion and by the diverse existing rituals.

As an example of these influences, one can analyze the specific case of the Iron Age people who lived in the Atlantic seaboard of Europe and to whom can be assigned the development of a particular style of structure known as the round house, shown in figure 1.1, characterized by its circular ground plan and conical roof. The inhabitants of this specific region followed rituals that made an intensive use of solar and lunar observations which were the base to many of their daily and seasonal routines, making the circular ground plan a characteristic of great importance.



Figure 1.1 – Round house

Despite of all these rituals it's possible to conjecture that this particular style of structure was also developed in part due to its location, since the Atlantic seaboard of Europe is one of the windiest parts of Europe. The conical shape of the roof made it possible to reduce the loadings when compared to rectangular roof forms which were more common in Central and Eastern Europe.

Even with the strong presence of religious traditions it was possible to observe some developments related with Wind Engineering between the 12th and 13th centuries.

The desire to glorify God joined with the rivalry between different religions led to the construction of grander churches leading to the inevitable growth of the wind loading, which in turn led to the development of new roofing methods, making the roofs more wind resistant.

The leading innovation consisted on the construction of spires as shown in figure 1.2. In the beginning these were simply pyramids with four faces which later evolved to conical structures.



Figure 1.2 – Cologne cathedral

Near the end of this period the intellectual atmosphere in Europe suffered a significant transformation with the Renaissance. In the seventeenth and eighteenth centuries the world saw the birth of modern science with major contributors from Newton, Euler and Bernoulli.

The beginning of the “empirical” period of Wind Engineering coincides with another period of major importance to Mankind, the Industrial revolution. It was during this period that the world saw the construction of the first iron bridge, across the River Severn in the UK.

With the industrial development that led to an increase of the metallic construction and to the birth of the steam engine there was a growth and an improvement on the road systems, bridges and the development of the railway which in turn led to a great economic development in Europe.

Intellectually this was the period of the development of classical hydrodynamics mainly due to the work of Euler, Newton and Bernoulli and later through Navier's formulation of the fundamental equations of fluid flow. Scientific experimentation started to gain importance and in 1759 were carried out the first fluid mechanics model experiments.

It was in this context of industrial development that the wind loading acting on the transport systems began to be significant, in particular due to the construction of the first long span bridges that inevitably suffered adverse effects caused by the wind action leading to some famous collapses such as Brighton Chain pier in 1836 due to aeroelastic oscillations and the collapse of the Tay bridge in 1879, shown in figure 1.3.



Figura 1.3 – Tay bridge collapse

The “establishment” period of the Wind Engineering appears at the beginning of the twentieth century. The Industrial revolution had started influencing every aspect of society, mainly in the military field, hence many of the developments made in the twentieth century were a result of military interests such as the theoretical and experimental study of atmospheric dispersion which had as main objective the understanding of aspects related to chemical warfare.

Large scale technological warfare led to the development of large government laboratories that had a great influence on the development of Wind Engineering.

The growing possibility and capacity of mobility by common citizens and by the different social classes led to an increase in the demand for high-level education, leading to the establishment of more Universities, many of them contributing to the development of Wind Engineering.

The appearance of new technologies and materials led to an increasing number of challenging constructions such as the first high-rise buildings and suspension bridges of ever increasing span. In this context emerged the first full-scale measurements with the objective of finding the “dimensions” of wind gusts.

Intellectually this period saw the development of boundary layer aerodynamics with the main contribute being given by Prandtl and von Karman, which together with the emergence of statistical theory of turbulence demonstrated the deficiencies of classical hydrodynamics. It was also the period of birth of extreme value theory, a field of great importance to the Wind Engineering.

The “establishment” period saw the advent of the three tools that are for Baker [1] the main Wind Engineering tools.

The first was the development of the wind tunnel, mainly due to the aeronautic industry. Another important tool was the development of codes of practice that could be used as guides, making it possible to define environmental loads such as the wind. The last of the three tools was the beginning of full-scale measurements of wind on structures.

It was while comparing the results of wind tunnel tests and full-scale measurements that Wind Engineering saw most of its progress being made in this period, in particular due to the correction applied to the wind tunnel tests achieved through the attempt to simulate the atmospheric boundary layer after it was noticed that before this correction was applied, the results obtained in wind tunnel tests didn't match with the results from full-scale measurements. Most of the progress in Wind Engineering in this period, in particular the progress related with wind tunnel test was made possible mainly because of the contributions made by Scruton, Jensen e Cermak.

During the twenty years that lasted the growth period of Wind Engineering there were major changes in society all over the world leading to great developments also in Wind Engineering.

In the western world this was a period of prosperity and economic growth that was starting to rise with the dissipation of the effects of World War 2 (1939-1945) and a period of optimism regarding the potential benefits of technology towards to society.

High-rise structures and other large structures were a trend in the developed world. There was a great development of computer technology making it possible to progress with other scientific instruments related with data acquisition.

It was in this context that Wind Engineering saw its greatest development, leading to the definition of Wind Engineering as a scientific area of interest and to the first international conferences, in which the main subjects were strong wind climatology, wind effects on low and high-rise buildings, bridges, masts and towers, wind damage among others.

During this period it has to be emphasized the contribution of Alan Davenport which in 1961 developed the concept of the wind loading chain, shown in figure 1.4, which can be understood as an analytical tool through which can be introduced the different variables that constitute the wind loading such as the local wind climate, the local wind exposure, the aerodynamic characteristics of the building shape and the potential for load increases due to possible wind-induced resonant vibrations [2].



Figura1.4 – Alan Davenport's wind loading chain.

Davenport was also deeply involved in the construction of the World Trade Center in New York and developed the University of West Ontario's laboratory which became one of the most important laboratories for Wind Engineering.

It was during this period that was developed the boundary layer wind tunnel not only has a research tool but also as reliable and robust mean for the commercial design of structures. A considerable number of different codes were also developed and the first journals related to Wind Engineering started to appear in particular the Journal of Wind Engineering and Industrial Aerodynamics.

The modern period of Wind Engineering started in 1980 with the adoption of the Journal of Wind Engineering and Industrial Aerodynamics as the official journal of the International Association of Wind Engineering.

This was a period with some social changes. In the western countries privatizations began which on one hand led to the closure of many national laboratories and on the other hand to a decrease of public confidence in science and in technology leading to a reduction of development.

Although the closure of many laboratories and the reduction of progress affected Wind Engineering development, there were some significant breakthroughs, in particular on the instrumentation of wind tunnels and with the advancement of new devices related to full-scale measurements.

1.2. MOTIVATION

Going back some sixty years, until the decade of the fifties, one can conclude that the majority of the buildings were, when compared to recent structures, relatively massive [3].

This massive appearance of older structures was a consequence of a design that was made for larger dead loads which resulted from the use of constructive systems, in the case of bridges, that led to reinforced concrete decks that were much heavier and to the use of nonstructural elements made from heavy masonry and rock in the case of buildings. Additionally it was also a result from a design through which were calculated heavier structural elements that in turn were an outcome of larger cross-sections resulting from the use of materials with considerable lower quality and resistance from those that are currently in use.

These massive structures were often more rigid than expected due to the difficulty of calculating the stiffness of their nonstructural elements.

This characteristic of older structures resulted in the fact that the real importance of wind loading was not accounted for a long period of time, concealing aerodynamic problems that later came to be of great importance to more recent structures and limiting the analyses of wind loading to its static behavior.

The development of new materials and constructive methods led to a new generation of structures such as long span bridges and high-rise buildings which were characterized by a significant reduction of their weight and damping as well as an increase of their flexibility, making them more susceptible to wind action.

The design of structures regarding wind forces has been evolving since the thirties until now thanks to different factors.

To begin with, there was a transformation in the structural properties of mass, stiffness and damping, with the average densities of buildings and large span bridges decreasing by a factor of 2. For its turn, material strength has increased by a factor of two and three in the case of structural steel and concrete, respectively. This increase of material strength led to a decrease of the dimensions of structural elements and thus to a reduction of their stiffness. The use of welding and pre-stressing and the decrease on the use of heavy masonry elements resulted in a significant reduction of damping.

Another factor one can add was the bounding of different knowledge areas such as Meteorology and Aeronautic Engineering with the field of Wind Engineering. This bounding made it possible to engage in a deeper study of the atmospheric boundary layer and the comparison between the flutter on aircrafts and bridges.

Not least important was the stimulus provided by structural failures, some even leading to the collapse of the structure. Among them there are the famous collapses of the Tacoma Narrow Bridge and the Ferrybridge cooling towers, shown on figure 1.5, and the structural problems caused by the wind on the Golden Gate Bridge.

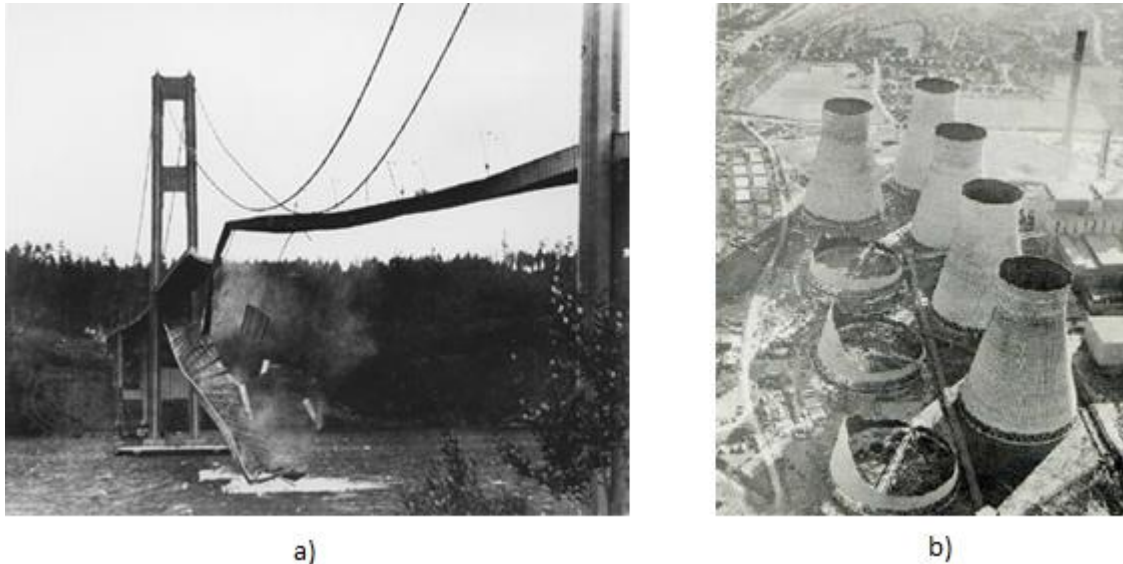


Figura 1.5 – Tacoma Narrow Bridge collapse (a) and Ferrybridge cooling towers collapse aftermath (b)

For the specific case of the Unicredit high-rise building (the case study of this work), the different problems that could have emerged due to aerodynamic instabilities were avoided thanks to the studies made in an earlier stage of the project which led to the current geometric shape of the building.

Once the good aerodynamic behavior of the tower was guaranteed, an analysis of the effect of wind action and the distribution of the forces developed by the wind loads on the different elements of the structure was needed. Furthermore, the evaluation of the functional behavior of the structure when submitted to the wind is of great importance since the comfort of its occupants depends upon the functional performance of the tower.

1.3. ORGANIZATION OF THE THESIS

The current work is divided into seven chapters.

Chapter 1 contains a brief historical introduction to Wind Engineering which exposes the key factors that allowed its evolution, and ultimately made it possible to construct increasingly higher with increased reliability. The different reasons that made the analysis of the wind action the relevant one to be considered and developed on the Unicredit high-rise building are exposed.

The first chapter ends with a description of the different chapters that constitute the current work.

The various mechanisms that generate the different types of winds, the characteristics of the atmospheric boundary layer and the different wind profiles in use are described in chapter two. In this chapter, the different extreme value distributions commonly used and the different descriptors of atmospheric turbulence will be described.

The description of the geometry of the case study structure and of its structural elements, the various materials used in the construction and the different considered loads can be obtained from chapter

three. This chapter also contains a brief description of the redevelopment project in which the Unicredit high-rise building is inserted.

The procedure used to obtain wind loads through the EN 1990 – 1 – 4 and the different aspects of wind tunnels and in particular the characteristics of the CRIACIV wind tunnel are described in Chapter four. The values of the base resultant forces obtained through C_p integration and through the High Frequency Force Balance (HFFB) test are also shown in this chapter along with a comparison between the wind pressure profiles obtained through the Eurocode and through the wind tunnel test.

In chapter five the numerical model used to extract different values which were relevant to both the static and resonant component of the response of the tower to the action of wind are described. The method used to change the base resultant forces from the reference system used in the wind tunnel test to the one used on the numerical model is described as well as the different combinations considered during the analysis. This Chapter ends with a static analysis of the response of the building to the mean and fluctuating components of the wind action.

The equivalent static forces of the resonant component of the response of the Unicredit high-rise building is obtained through the method described in Chapter six. The influence of this component to the overall response of the building is analyzed and the overall effect of the wind on the serviceability of the structure is evaluated.

The main conclusions obtained are discussed on chapter seven.

2

The Atmosphere

2.1. INTRODUCTION

Since the beginning of Mankind, wind has always been an important factor in our lives [4]. It inspired mythology, allowed us to expand the range of our transports and warfare and was also turned into a powerful source of energy.

Ancient Greeks believed that the wind was created by the Anemoi (Winds)[5], these were the wind Gods and each one of them was associated with different seasons and weather conditions and were assigned with their respective cardinal direction, shown in figure 2.1, from which their winds came.

The four main Gods or the four chief Anemoi corresponded to the four cardinal directions. Boreas was the bringer of cold winter air which made him the north wind. Notus, the south wind, was the bringer of the storms of late summer and autumn. Zephyrus, the west wind, was the bringer of spring and summer breezes. The last of the four Anemoi, Eurus, the east wind, was the only God which was not associated with any of the three Greek seasons.

The intercardinal directions Northeast, Northwest, Southeast and Southwest were also related to four other Gods, the Anemoi Thyellai (Tempest-Winds) which were respectively Kaikias, Skiron, Apeliotes and Lips.

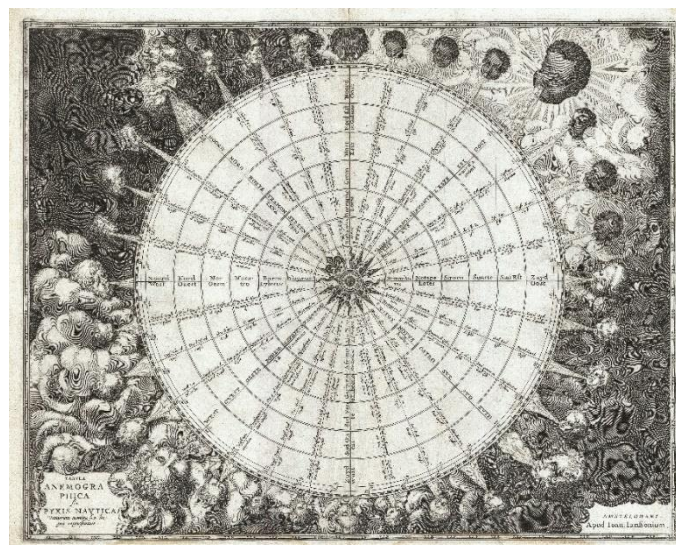


Figure 2.1 – Ancient wind rose

Today we know that the formation of wind arises mainly from variable solar heating of Earth's atmosphere both in time and space resulting from its rotation [3;6]. While the clouds reflect some of the radiation away the rest is trapped by greenhouse gases and absorbed by the earth. This radiation that heats the earth is then emitted in the form of terrestrial radiation which has a longer wave length than the initial radiation emitted by the Sun. Since the atmosphere is almost transparent to Sun radiation but the same can't be said for terrestrial radiation the latter is re-emitted to the ground, being this process repeated multiple times.

In this chapter the different proprieties and characteristics of atmospheric circulation, basic aspects of its functioning and the main atmospheric motions are presented.

2.2. ATMOSPHERIC PROCESSES, PROPRIETIES AND CHARACTERISTICS

2.2.1. ATMOSPHERIC THERMODYNAMICS

The temperature distribution in the atmosphere has a key role in the production of wind. The atmosphere's temperature can be influenced by different processes such as solar and terrestrial radiation, radiation in the atmosphere, compression and expansion of the air, molecular and eddy conduction and evaporation and condensation of the air.

As stated before, a part of the solar radiation is absorbed by the earth which in turn emits radiation that is absorbed by the layer immediately above the ground or above the surface of the ocean. This last layer will then reemit the radiation upward and downward. The first is then absorbed by a higher layer that will reradiate downward and upward, being this process repeated along the height of the atmosphere.

The action of the radiation in the atmosphere's temperature can be understood through the conceptual model represented in figure 2.2

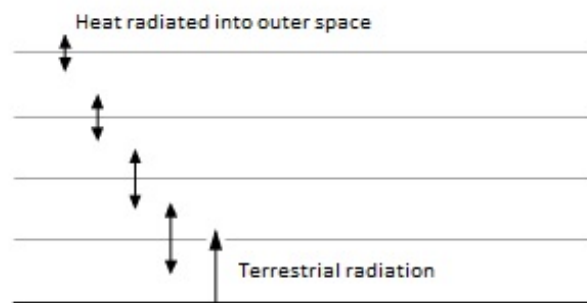


Figure 2.2 – Heat transport along the atmosphere [6]

As one can understand, atmospheric pressure is a consequence of the weight of the overlying air. A small mass that can be treated as a particle of dry air moving vertically experiences a change of pressure due to the change of the weight of that same overlying air to which corresponds a change of temperature. This change of temperature can then be determined by the equation of state of perfect gases and by the first law of thermodynamics [6;7;8;50].

$$pv = nRT \tag{2.1}$$

$$dq = c_v dT + pdv \tag{2.2}$$

where p is the absolute pressure, T the absolute temperature, v the specific volume and R a constant of proportionality called the gas constant which varies from gas to gas ($R = 287.06 \frac{J}{kg.K}$ for dry air), with n , the chemical amount of gas, given by,

$$n = MN \quad (2.3)$$

where M and N are respectively the molar mass and molar number. dq being the amount of heat transferred to the particle and c_v the specific heat at constant volume.

Considering that the vertical motion of a particle of air in the atmosphere is sufficiently rapid, the heat exchange of the particle with its surroundings may be considered insignificant leading to $dq = 0$ being these an adiabatic process. From these assumption is then possible to come up with a relation between the pressure of a perfect gas and its respective temperature known as the Poisson's or dry adiabatic equation,

$$\frac{T}{T_0} = \left(\frac{p}{p_0}\right)^{\frac{R}{c_p}} \quad (2.4)$$

where c_p is the specific heat at constant pressure and $R/c_p = 0.288$.

When a mass of air moves upward adiabatically (without heat transfers) it will expand in order to get a lower pressure resulting in a decrease of its own temperature.

Since the variation of pressure can be written as a function of height and the differences in temperature are small when compared to their absolute value (absolute temperature), Poisson's equation can thus be linearized,

$$T = T_0 - \gamma_a(Z - Z_0) \quad (2.5)$$

where T and T_0 are the temperatures at heights Z and Z_0 respectively, being T_0 and Z_0 the temperature and height correspondent to its initial position and γ_a is the adiabatic lapse rate that can be understood as the temperature drop of adiabatically ascending air which is approximately $1 \text{ }^\circ\text{C}/100 \text{ m}$ in the earth's atmosphere.

Since the height at which the element is located is the same as its surrounding ambient air and so is its pressure, one can conclude from the equation of state that to the temperature difference $T' - T$ at a same height Z corresponds a difference of density between the element of air and the ambient air, being T' and T the temperatures of the element of air mass and of the ambient air respectively.

Then if $T < T'$ or $\gamma > \gamma_a$ a buoyancy force is generated in such a way that it will act upwards moving the element further away from its original position, in this case the stratification of the atmosphere is

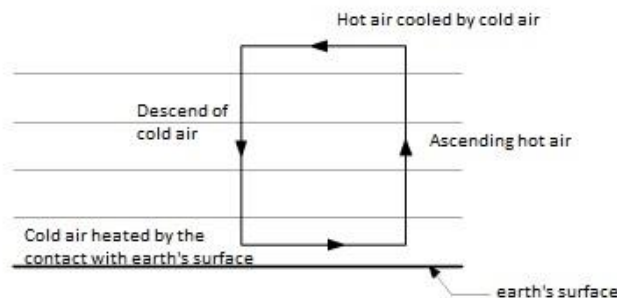


Figure 2.3 – Atmospheric convection phenomenon [9]

said to be unstable. In this particular case, the mass of air tends to continue its motion producing a convective phenomenon as the one represented in figure 2.3 [9].

If in turn $T > T'$ or $\gamma < \gamma_a$ then the buoyancy force will act downward making the particle tend to return to its original position and making the stratification of the atmosphere stable.

If the lapse prevailing in the atmosphere is adiabatic, then $T = T'$, $\gamma = \gamma_a$ and the stratification is said to be neutral.

The transfer of heat in a turbulent flow occurs mainly by eddy activity [10], thus eddy heat conduction involves the transfer of heat by means of the movement of air in which heat is stored [6]

Molecular conduction in turn is a diffusion process that effects a transfer of heat. This heat transfer is possible due to the motion of individual molecules and can be considered negligible to atmospheric processes when compared with eddy activity.

Dalton's law states that the pressure of moist air is equal to the sum of partial pressures of its components, the water vapor pressure and that of the dry air.

Then, if the water vapor pressure exceeds the pressure value known as saturation vapor pressure, which is known to increase rapidly with the increase of the moist air's temperature, condensation of the excess moisture will occur, leading to a release of heat of condensation (which is equal to the heat that is necessary to change the phase of the water from liquid to vapor in the beginning) that contributes to the expansion of an ascending particle which before saturation is done only by means of its internal energy. This leads to a temperature drop of the saturated adiabatically ascending particle that is slower than the temperature drop of dry or moist unsaturated air, thus permitting the convection of air to higher levels of the atmosphere.

2.2.2. ATMOSPHERIC HYDRODYNAMICS

Considering once again a particle of air of mass m , according to Newton's second law, its motion is determined by,

$$\sum F = m \cdot a \quad (2.6)$$

where a is the acceleration and $\sum F$ the sum of the forces acting on the particle.

Analyzing an infinitesimal volume of air with dimensions dx , dy and dz subjected only to mean pressures and no other forces acting on the lower and upper face which can be characterized by the values p and $p + \frac{dp}{dz} dz$ respectively, then the net vertical force acting on the volume will be given by $-\frac{dp}{dz} dx dy dz$, being $-\frac{dp}{dx}$ and $-\frac{dp}{dy}$ the net forces per unit of volume acting in the x and y horizontal directions respectively. The resultant of these forces is then called the horizontal pressure gradient ($-\frac{dp}{dn}$, where n is the normal to some contour of constant horizontal pressure) which is the driving force that initiates the horizontal motion of air.

The horizontal pressure gradient can then be transformed into a net force per unit mass $\frac{1}{\rho} \frac{dp}{dn}$ known as the pressure gradient force shown in figure 2.4.

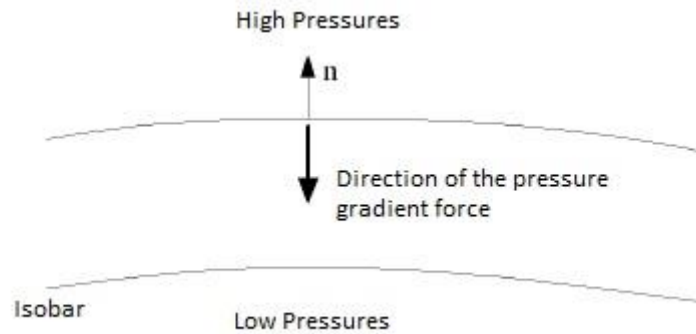


Figure 2.4 – Movement of an air particle due to pressure gradient forces [6]

It is then relatively easy to conclude that if a particle of air is subjected only to the action of pressure gradient forces it will move from regions of high pressure to regions of low pressure.

In the case of a particle which follows a straight line when defined with respect to an absolute referential and which is not subjected to any other external forces, to an observer on the rotating earth it will appear as if the particle is following a curved trajectory. This can be explained by an apparent force known as the Coriolis force characterized by the vector,

$$F_c = 2 \cdot m \cdot (v \times w) \quad (2.7)$$

where m is the mass of the particle, w is the angular velocity vector of the earth, and v is the velocity of the particle relative to a coordinate system rotating with the earth.

The Coriolis force magnitude acting per unit of mass on a particle moving with velocity v in a plane which is parallel to the surface of the earth will be given by,

$$F_c = m \cdot f \cdot v \quad (2.8)$$

being f the Coriolis parameter which is defined by $f = 2 \cdot w \cdot \sin \phi$, where ϕ is the latitude of the point considered.

The influence of the earth's surface decreases with height, thus considering a particle located at a sufficient height, in such a way that the effects of friction caused by the ground on wind become negligible, then, in unaccelerated flow, the horizontal motion of air is given by the balance among the pressure gradient, the Coriolis force and the centrifugal force.

If this same particle started a motion in the direction of the pressure gradient force, it would be deflected by the Coriolis force, making the particle to move along the resultant of these two forces, as shown in figure 2.5.

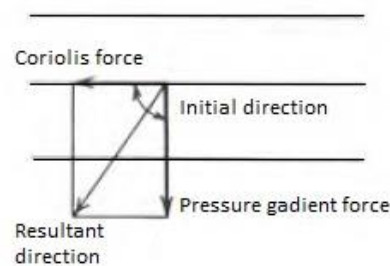


Figure 2.5 – Direction of an air particle subjected to Coriolis and pressure gradient forces [6]

If the particle was accelerated until it reached the balance point between the Coriolis force and the pressure gradient force the magnitude of the two would be the same but with opposite ways, making them perpendicular to the wind direction which in turn would be parallel to the isobars (lines that unite points with the same pressure), originating the geostrophic wind, as shown in figure 2.6 [11;49].

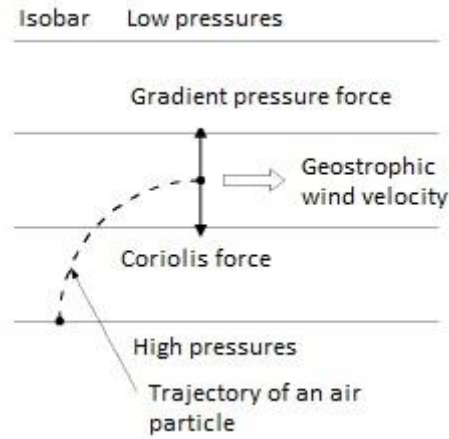


Figure 2.6 – Equilibrium of forces and trajectory of an air particle of geostrophic wind [11]

The geostrophic wind velocity is given by,

$$G = \frac{1}{\rho \cdot f} \frac{dp}{dn} \quad (2.9)$$

where $\frac{\partial p}{\partial n}$ is the pressure gradient, ρ is the air density and f is the Coriolis parameter.

When the centrifugal force is added to the problem the isobars turn into curves rather than straight lines, with the centrifugal force and pressure gradient forces acting in the direction normal to the isobars resulting in a wind (not geostrophic) motion that continues to be along the latter.

The wind will only be known as geostrophic until the moment that centrifugal forces can no longer be ignored. Since wind follows a curved path in the vicinity of a low-pressure center or a high-pressure center [11] and in turn centrifugal forces are related with the radius of a curved motion, if this radius is sufficiently large, than the effect of centrifugal forces can be ignored. On the contrary in the cases in which the radius is small, the centrifugal forces have to be taken into account originating the so called gradient wind.

The gradient wind's motion equations in relation to polar coordinates are,

$$f \cdot v_{gr} \pm \frac{v_{gr}^2}{r} = \frac{1}{\rho} \frac{dp}{dn} \quad (2.10)$$

where + and - correspond, respectively, to cyclonic winds (circulating around a center of low pressure) or anticyclonic winds (circulating around a center of high pressure) and r is the radius of curvature of air trajectory.

The gradient wind's velocity, v_{gr} , differs from the cyclonic winds where,

$$v_{gr} = -\frac{f \cdot r}{2} + \sqrt{\frac{r}{\rho} \frac{dp}{dn} + \left(\frac{f \cdot r}{2}\right)^2} \quad (2.11)$$

and the anticyclonic winds where,

$$v_{gr} = \frac{f \cdot r}{2} - \sqrt{\left(\frac{f \cdot r}{2}\right)^2 - \frac{r}{\rho} \frac{dp}{dn}} \quad (2.12)$$

being these equations valid only for the North Hemisphere. The cyclonic and anticyclonic winds are represented in figure 2.7.

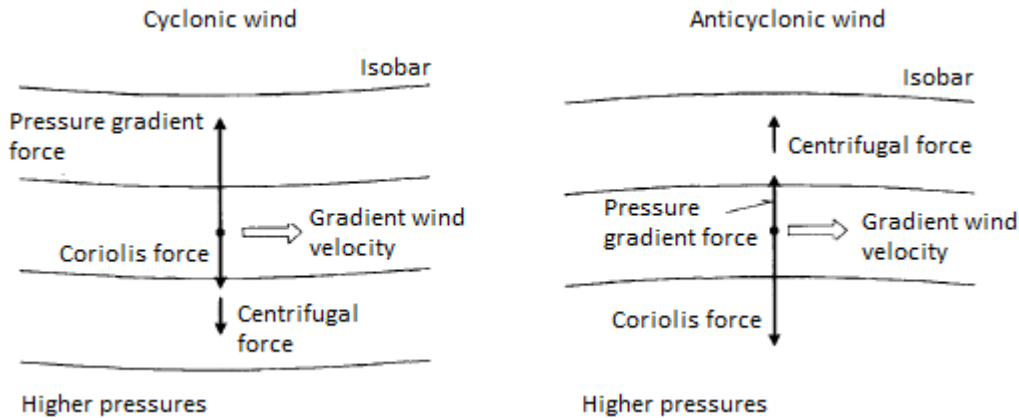


Figure 2.7 – Equilibrium of forces in Gradient wind with constant velocity in cyclonic and anticyclonic flows [11]

Analyzing the equations of gradient wind's velocity, one can conclude that in the case of anticyclonic wind its velocity will be limited to $v_{gr} = \frac{f \cdot r}{2}$ whereas in the most common case corresponding to cyclonic winds there is no limit to the value of v_{gr}

The velocity of geostrophic wind can also be expressed as a function of gradient wind's velocity

$$G = v_{gr} \left(1 + \frac{v_{gr}}{f \cdot r}\right) \quad (2.13)$$

leading to $v_{gr} < G$.

As stated before, when a particle is located at a sufficient height, one can neglect the effects of friction on the motion of air.

In meteorology, the surface that is used as reference when the effects of friction start to become negligible and thus the winds can be explained by the theory of gradient winds is known as the 850 mb surface which is located at a height of approximately 1 to 2 km reaching down to approximately 1 km above the surface in case of very low pressures. It is known from experience that in the case of strong winds, the maximum gust velocity near the ground is of the same order of magnitude as the wind velocity found at the 850 mb surface [11].

On the contrary, layers of air which are closer to the surface of the earth suffer a horizontal drag force which retards its flow, in Wind Engineering it is said that these sub-layers are included in the boundary layer of the atmosphere [6], which normally is 1 km thick, where the effects of friction cannot be ignored, being the atmosphere present above this boundary layer called free atmosphere.

Furthermore, the wind velocity variation resulting from friction is accompanied by a variation of its direction along the height of the atmospheric boundary layer, being this effect spread until it reaches the height of geostrophic or gradient wind [11;48].

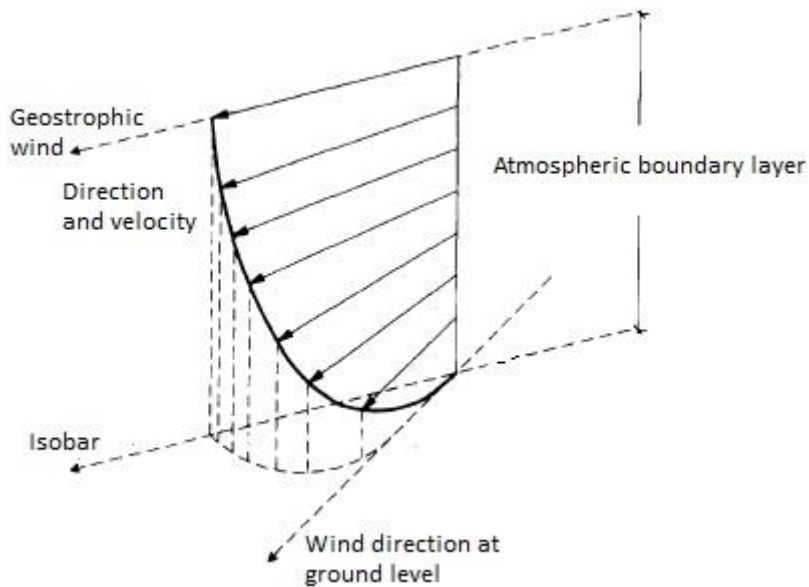


Figure 2.8 – Wind in the atmospheric boundary layer [11]

In the same way as in the previous cases of geostrophic or gradient wind, the equilibrium of forces in the boundary layer can also be represented schematically.

The figure 2.9 illustrates a state of equilibrium corresponding to a wind direction which crosses the isobars.

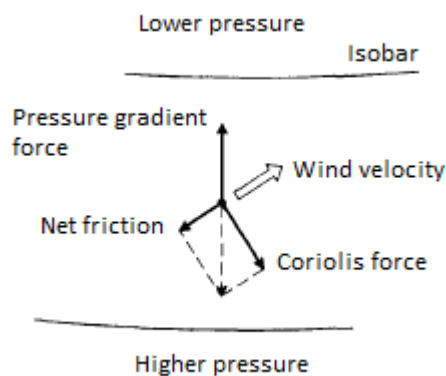


Figure 2.9 – Equilibrium of forces in the atmospheric boundary layer [11]

As one can see from figure 2.8, wind direction continues to change through the boundary layer while the wind velocity gradually decreases to zero when it hits earth’s surface level.

2.2.3. GLOBAL ATMOSPHERIC CIRCULATION

As seen before, wind is a result of pressure differences resulting from variable solar heating of earth's surface.

To understand the global atmospheric circulation we have to analyze first the distribution of energy on earth which results from radiation coming from the sun.

There is a surplus of energy close to the equatorial region and a deficiency near the poles. Thus at the Equator, earth's surface level air is heated, expanding and rising and leading to low pressure while at the poles earth's surface level air cools and contracts leading to a flow that creates a high pressure. This distribution of low and high pressures creates a flow between the two regions as shown in figure 2.10.

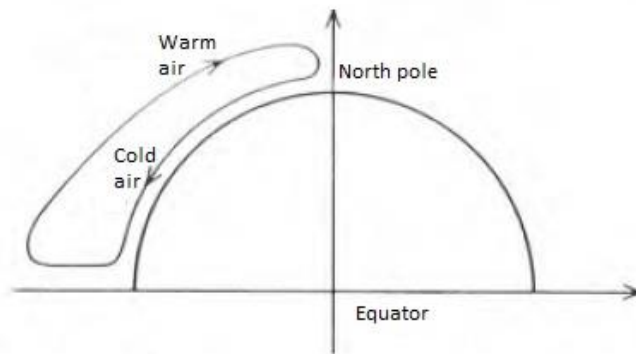


Figure 2.10 – Simplified model of atmospheric circulation [6]

The combined effects of earth's rotation and that of friction break this flow into three different circulation cells as shown in figure 2.11. This tricellular meridional circulation models gets then even more complicated when added the seasonal and geographical effects. The first lead to a variation in position as well as in intensity of the pressure belts, being caused by the annual march of the sun north and south of the equator. The second is caused by differences in physical proprieties and by the distribution of water and land along the globe.

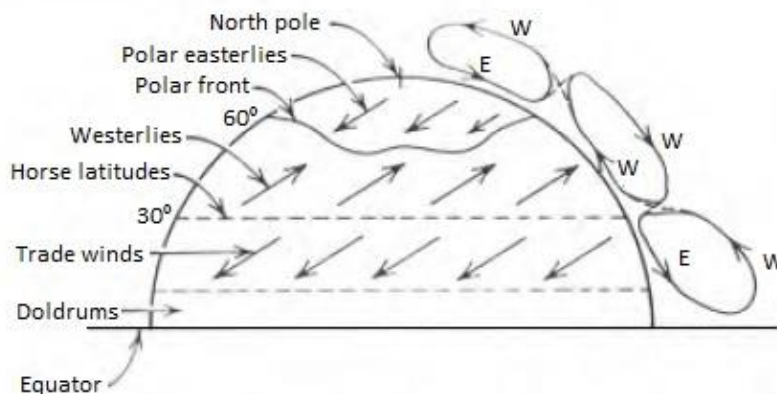


Figure 2.11 – Tricellular meridional circulation model [6]

In the equatorial region warm air flows upwards flowing away from the Equator when high altitudes are reached. The fictitious or apparent Coriolis force resulting from earth's rotation then diverts the flow eastwards originating a westerly wind at high altitudes and prevents it from going further north

originating a high pressure belt being the theoretical hypothesis of the three circulation cells model compatible with the existence of this permanent subtropical high pressure belt located close to 30-40° latitude also known as horse latitudes.

High pressure is responsible for the beginning of a flow towards Equator at ground level, which is bent westwards due to the Coriolis force, forming an easterly wind known as trade wind.

The subtropical high pressure region present at approximately 30° latitude mentioned above is originated by the inability of the flow away from the Equator at high altitude to penetrate further north due to the Coriolis force. In turn, in the layers near the earth's surface, flow is pushed towards the north by the subtropical high pressure zone becoming a westerly wind due to the Coriolis force which diverts it eastwards.

The high pressure present at the North Pole leads to an air flow to the south at low altitude which is diverted by the Coriolis force westwards originating the easterly polar wind.

When the warm westerly wind from the temperate zone and the easterly polar wind pass along each other at a 60° latitude they form the polar front. This surface is inclined north due to the temperature differences between the air masses, with the warm air flowing above the cold one and being its equilibrium very sensitive to changes in temperature, velocity and humidity of both, potentially leading to some instabilities [6,11].

2.2.4. THERMAL GENERATED SECONDARY CIRCULATIONS

Secondary circulations are of the thermally direct type if the centers of high or low pressure around which they develop are created when the lower levels of the atmosphere are heated or cooled.

Monsoons are seasonal winds that develop around thermally produced continental highs or lows in the winter and summer respectively. The latter occurs due to a slower heating of the sea comparing to the ground surface originating a colder air over the sea. As the ground gets hotter the air close to it raises causing a void leading to a flow of wind, at low altitudes, which is directed away from the sea and into the shore. In winter the opposite occurs.

The monsoons phenomenon is especially common in Asia due to its vast land mass.

Hurricanes or tropical cyclones are typically developed over tropical oceans where the water exceeds 26°C in temperature and are usually located at latitudes of between 5° and 20°, gathering their energy from the latent heat released by the condensation of water vapor.

In these regions, warm air is occasionally lifted to high altitudes by upwinds. If the right climatological conditions are gathered, the hot and humid air forms a cloud in which vapor condenses releasing latent heat, which can involve large amount of energy. The hurricane formed is then composed of five main regions as shown in figure 2.12. The first consists of a roughly circular, relatively dry core of light winds, known as the eye, around which the storm is centered. The second region consists of a vortex in which warm and moist air is convected at high altitudes, forming tall convective clouds. The condensation of water vapor resulting from the rise of moist air results in heavy rainfall and in the release of latent heat. The air then flows to a third outflow layer. While in the fourth region, the flow is vortexlike settling slowly into the boundary layer of the fifth region [6,11].

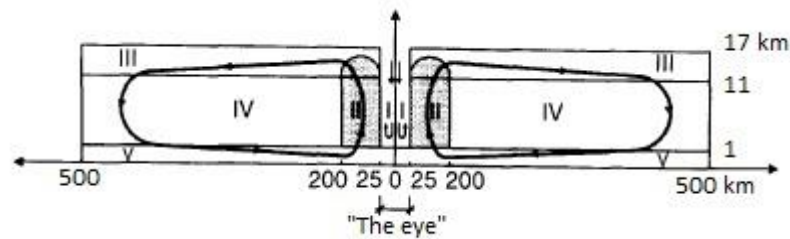


Figure 2.12 – Hurricane's cross-section [11]

Hurricanes are more common during the late summer and early autumn months. This is an extremely destructive phenomenon since its winds can reach up to 250km/h, its diameters are usually of the order of several hundred kilometers, and can last several days.

2.2.5. LOCAL WINDS

Small-scale local winds have little influence on the global atmosphere circulation. Nonetheless the intensity of these weather systems is sometimes considerable and even decisive for the design of buildings and other structures.

Strong, local storms sometimes form due to varying ground heights. Air flowing across a mountain ridge is forced by the mountain slope to rise. If the mass of air rises to sufficient great heights with an adiabatic cooling, this will lead to condensation and precipitation on the windward side. When the air passes the highest point, having lost most of its initial water-vapor content, it flows down again. This forced descend originates an adiabatic compression resulting in a dry descending air with high temperatures known as foehn wind (figure 2.13), common on the Rocky Mountains, a region in the United States.

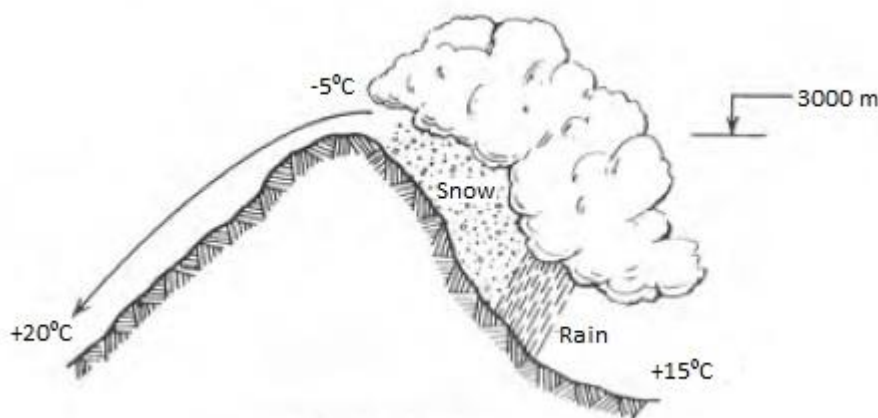


Figure 2.13 – Foehn wind [6]

Consider now the case of a mass of air which is forced to ascend due to an ice-covered region located at relatively high altitudes. This ice-covered region will cool the air in such a way that the adiabatic heating occurred during the descent may not be sufficient to change it to a foehn wind. Thus the cold air falls gravitationally into the warmer region on the leeside transforming its potential energy into kinetic one. This wind known as bora winds are more common in the northeast region of the Adriatic and are characterized by gusts of 150-200km/h separated by periods of calm.

Thunderstorms are phenomena that have a length scale of about 10 km, a lifetime of an one hour and that need the existence of tall convective clouds produced by the upward motion of warm, moist air as shown in figure 2.14. This upward motion may be due to thermal instability or by the presence of mountain slopes or of a front.

The condensation of rising, humid air releases energy and produces heavy precipitation which initiates the downward motion at the center. Part of the water condensed and turned into precipitation is evaporated in the underlying atmosphere that cools and sinks. The cold downdraft spreads over the ground and produces squally winds, corresponding to the mature stage of the thunderstorm that can last up to 30 minutes.

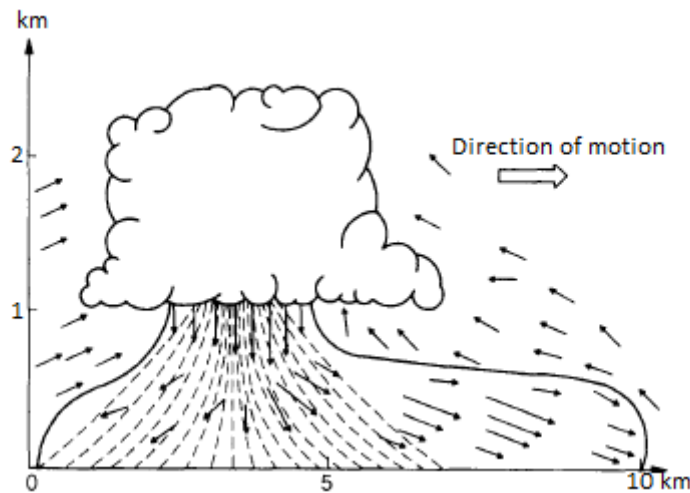


Figure 2.14 – Cross-section of a Thunderstorm [11]

Tornadoes develop within a severe thunderstorm and consist of a vortex of air about a vertical or inclining axis with a typical diameter of about 300 meters and moving with a velocity around 30-100 km/h in a path of approximately 15 km long and with maximum tangential speeds that have been estimated to reach 350 km/h, thus containing the most powerful of all winds. Just below the tornado occurs a sudden fall of barometric pressures which subject the external surfaces of buildings to a powerful suction. This kind of phenomenon is most frequent and violent in the United States, occurring with less frequency in Australia, Western Europe, Japan, India and Russia [6,11].

2.3. THE ATMOSPHERIC BOUNDARY LAYER

As described, the earth’s surface creates a horizontal drag force that acts on the moving air. This effect is then spread out throughout the height of the atmospheric boundary layer (which depends upon the wind intensity, roughness of terrain and angle of latitude) due to a turbulent mixing. Thus the wind conditions in the boundary layer are described as being mechanically generated, even though its formation is related with geostrophic wind velocity at high altitudes which in turn has a thermal origin.

Within the boundary layer, the wind speed increases with elevation until it reaches the gradient speed at the top of this layer. This variation of mean wind velocity is known as a wind profile.

The wind in the boundary layer may then be characterized by a wind profile for the mean wind velocity and by the additional turbulence or fluctuating component.

This means that considering a Cartesian coordinate system where the x-axis corresponds to the direction of the mean wind velocity, the y-axis is horizontal and the z-axis vertical and positive upwards, then the

wind velocity $U(t)$ is composed of a mean component $U(z)$ (that depends only on the height z above the ground) in the x -axis direction, and a fluctuating component (u,v,w) in three orthogonal directions (x,y,z) as shown in figure 2.15.

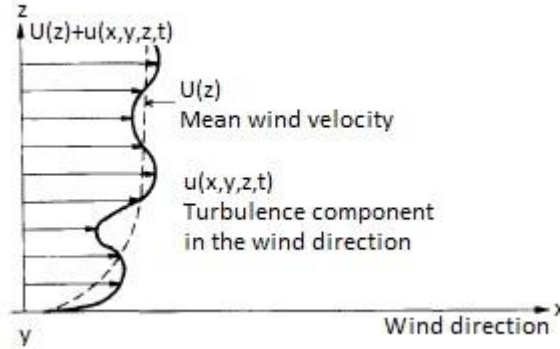


Figure 2.15 – Wind’s mean and fluctuating components [11]

The velocity at a given time t can then be represented as

$\bar{U}(z) + u(x, y, z, t)$ in the longitudinal direction

$v(x, y, z, t)$ in the lateral direction

$w(x, y, z, t)$ in the vertical direction

2.3.1. MEAN WIND VELOCITY

The mean component $\bar{U}(z)$ is defined as the average of the fluctuating velocity $U(t)$ over the average time T at a specific height z . This average time T of the mean wind speed varies within the different existing codes, being $T=10$ min in Japan’s code and in ISO4354 and 1 hour in the UK.

Atmospheric motion is known to be ruled by the fundamental equations of continuum mechanics which include the equation of continuity and the equation of balance of momenta which correspond to Newton’s second law.

2.3.1.1. Equations of Mean Motion

If the equations of continuity and of balance of momenta are averaged with respect to time then:

$$U \frac{dU}{dx} + V \frac{dU}{dy} + W \frac{dU}{dz} + \frac{1}{\rho} \frac{dp}{dx} - fV - \frac{1}{\rho} \frac{d\tau_u}{dz} = 0 \quad (2.14)$$

$$U \frac{dU}{dx} + V \frac{dU}{dy} + W \frac{dU}{dz} + \frac{1}{\rho} \frac{dp}{dy} + fV - \frac{1}{\rho} \frac{d\tau_v}{dz} = 0 \quad (2.15)$$

$$\frac{1}{\rho} \frac{dp}{dz} + g = 0 \quad (2.16)$$

$$U \frac{dU}{dx} + V \frac{dU}{dy} + W \frac{dU}{dz} = 0 \quad (2.17)$$

which are known as equations of mean motion and where U , V and W are the mean velocity components along the x , y and z axes and p , ρ , f and g are the mean pressure, the air density, the Coriolis parameter and the acceleration of gravity respectively. τ_u and τ_v are the shear stresses in the x and y axes respectively which oppose to the relative horizontal sliding between parallel layers of the fluid, in this case the air, and are fundamental to solve the equations of mean motion since it's necessary that phenomenological relations also known as closure relations be assumed defining these same stresses which can be represented by,

$$\tau_u = \rho K(x, y, z) \frac{dU}{dz} \quad (2.18)$$

$$\tau_v = \rho K(x, y, z) \frac{dV}{dz} \quad (2.19)$$

To the equations of mean motion then have to be added empirical relations that describe the specific response to external effects if the continuous medium considered, such as the Hooke's law in the case of a linearly elastic body.

2.3.1.2. Mean velocity profiles in horizontally homogeneous flow and the Ekman spiral

Considering now that a large storm is originated within a horizontal site of uniform roughness and over a sufficiently large fetch, then there will be a region where the flow is horizontally homogeneous. In the specific case of the atmospheric boundary layer, the horizontal pressure gradient counteracts boundary layer growth thus maintaining the horizontal homogeneity of the flow.

If equilibrium conditions are maintained, and considering equations (2.14) and (2.15) then the variation with height of mean velocity depending on mean motion shear stresses can be represented by,

$$V_g - V = \frac{1}{\rho f} \frac{d\tau_u}{dz} \quad (2.20)$$

$$U_g - U = -\frac{1}{\rho f} \frac{d\tau_v}{dz} \quad (2.21)$$

where V_g and U_g are the components of the geostrophic wind velocity G along the y and x -axes respectively.

If the eddy viscosity is assumed as being constant and the shear stresses τ_u and τ_v are represented by the equations (2.18) and (2.19), then the equations (2.20) and (2.21) originate the Ekman Spiral model which has the boundary conditions $U = V = 0$ for $z = 0$ and $U = U_g$, $V = V_g$ for $z = \infty$ represented in figure 2.8.

However, the assumption of a constant eddy viscosity with height, although mathematically convenient, is physically incorrect leading to discrepancies between the equations and the observations made.

Later an attempt to solve equations (2.20) and (2.21) was made by meteorologists considering a variation of eddy viscosity with height thus corresponding to a more physically correct approach.

More recently there has been developed a different type of approach to this problem based on similarity considerations analogous to the ones used in the two-dimensional boundary layer flow's theory.

This approach considers a division of the boundary layer into two different regions, a surface and an outer layer. In the first the shear τ_0 , known as the Reynolds stress, can be expressed as a function F of

the flow velocity at a distance z close to the ground, the roughness of the terrain which can be represented by a roughness length z_0 and the density ρ of the air.

$$\tau_0 = F(Ui + Vj, z, z_0, \rho) \quad (2.22)$$

where i and j are unit vectors in the x and y directions respectively.

Writing equation (2.22) in a nondimensional form, which describes the flow in the surface layer,

$$\frac{Ui + Vj}{u_*} = f_1\left(\frac{z}{z_0}\right) \quad (2.23)$$

where

$$u_* = \sqrt{\frac{\tau_0}{\rho}} \quad (2.24)$$

which is known as the shear velocity of the flow and f_1 is a function of the ratio z/z_0 .

For its turn, in the outer layer, the reduction of velocity $|(U_g i + V_g j) - (Ui + Vj)|$ at a height z depends similarly as for the surface layer upon the surface shear τ_0 but also upon the height to which the effect of the wall stress has diffused in the flow known as the boundary layer thickness δ , and upon the density ρ of the air.

This leads to the nondimensional expression,

$$\frac{Ui + Vj}{u_*} = \frac{U_g i + V_g j}{u_*} + f_2\left(\frac{z}{\delta}\right) \quad (2.25)$$

where f_2 is a function to be defined.

If a hypothesis in which a gradual change occurs from conditions near the surface to conditions in the outer layer is considered, then it may be assumed the existence of a region in which both equations (2.23) and (2.25) are valid.

It is well known that for the case of the analogous two-dimensional problem, the functions f_1 and f_2 must be logarithms. Thus the requirements of the problem will be satisfied if this two functions are defined as

$$f_1(\xi) = \left(\ln \xi^{\frac{1}{k}}\right) i \quad (2.26)$$

$$f_2(\xi) = \left(\ln \xi^{\frac{1}{k}}\right) i + \frac{B}{k} i \quad (2.27)$$

where B and k are constants.

Considering equations (2.23) and (2.25) and substituting f_1 and f_2 for their respective equations (2.26) and (2.27), then,

$$\frac{Ui + Vj}{u_*} = \frac{1}{k} \left[\ln\left(\frac{z}{\delta}\right) + \ln\left(\frac{\delta}{z_0}\right) \right] i \quad (2.28)$$

$$\frac{Ui + Vj}{u_*} = \frac{U_g i + V_g j}{u_*} + \frac{1}{k} \ln\left(\frac{z}{\delta}\right) i + \frac{B}{k} j \quad (2.29)$$

If the equations (2.28) and (2.29) above are equated in the overlapped region, then,

$$\frac{U_g}{u_*} = \frac{1}{k} \ln \left(\frac{\delta}{z_0} \right) \quad (2.30)$$

$$\frac{V_g}{u_*} = -\frac{B}{k} \quad (2.31)$$

and

$$G = \sqrt{B^2 + \ln^2 \left(\frac{\delta}{z_0} \right)} \frac{u_*}{k} \quad (2.32)$$

where the boundary layer thickness δ can be shown to be

$$\delta = c \frac{u_*}{f} \quad (2.33)$$

where c is a constant.

From experiments made on wind tunnels and in the atmosphere, the constant k , known as von Karman's constant is assumed to be $k \approx 0.4$, while the constant c is of the order of 0.25-0.3.

2.3.1.3. The Logarithmic Wind Profile

Since in the structural wind engineering field the main concern revolves around the effects of strong winds, then it can be considered that the flow is neutrally stratified. This is a result of a sufficient mixing of air which leads to a dominance of mechanical turbulence over that of heat convection. [6,11,12]

It has been demonstrated that for strong wind conditions the logarithmic law constitutes a good mathematical model to describe the wind speed profile in uniformly roughness conditions.

This law can be formulated based upon a dimensional analysis:

$$U(z) = \frac{u_*}{k} \ln \left(\frac{z}{z_0} \right) \quad (2.34)$$

where z is the height above the surface, z_0 is the roughness length, $U(z)$ is the mean speed and $k \approx 0.4$. The equation (2.34) is valid up to an height above ground defined by

$$z_l = b \frac{u_*}{f} \quad (2.35)$$

where b is a constant.

According to Dyrbye [6], the roughness length z_0 can be described as the size of a vortex formed as a result of friction between air and the ground surface, and corresponds to the height above ground at which the mean wind velocity is zero as figure 2.16 illustrates.

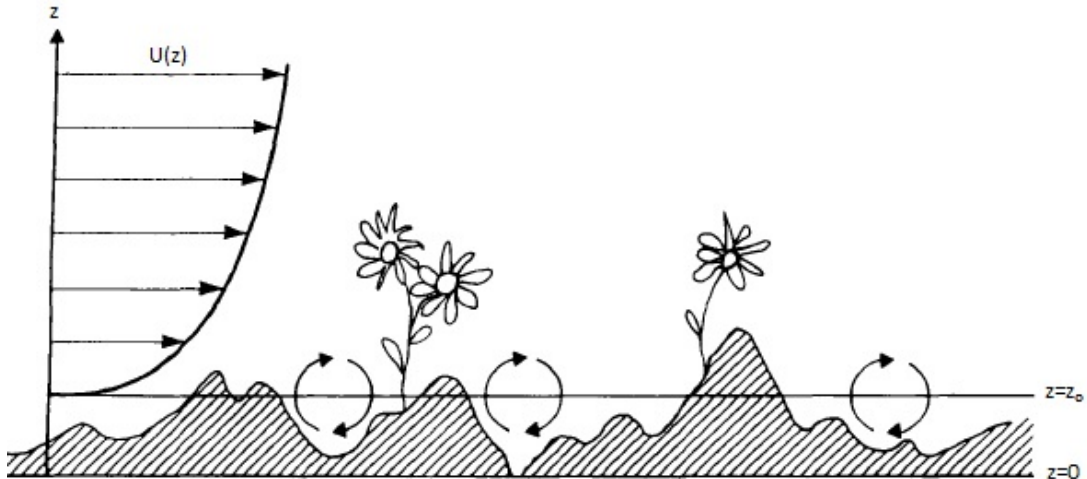


Figure 2.16 – Schematic representation of roughness length z_0 [11]

The roughness length has been estimated from measurements made all over the world leading to different terrain categories corresponding to different values of z_0 . Furthermore, the roughness length has also been theoretically estimated. Roughness elements, those which contribute to surface roughness, increase frictional forces leading to increase wind turbulence.

Businger [11] developed an empirical equation to account with the roughness length of roughness elements which are uniformly distributed over a terrain

$$z_0 = 0.5h \frac{A_r}{A_t} \tag{2.36}$$

where h is the roughness element height, A_r is the area of the element normal to the wind direction and A_t is the ground area per roughness element.

For the case in which the elements are very close to each other, corresponding to a situation where A_r and A_t are of the same order of magnitude, a new surface is formed by the top of these elements and the flow will be raised. These case then leads to a displacement d in the logarithmic profile represented in figure 2.17 and taken in account by the equation 2.37 below:

$$U(z) = \frac{u_*}{k} \ln \left(\frac{z - d}{z_0} \right) \tag{2.37}$$

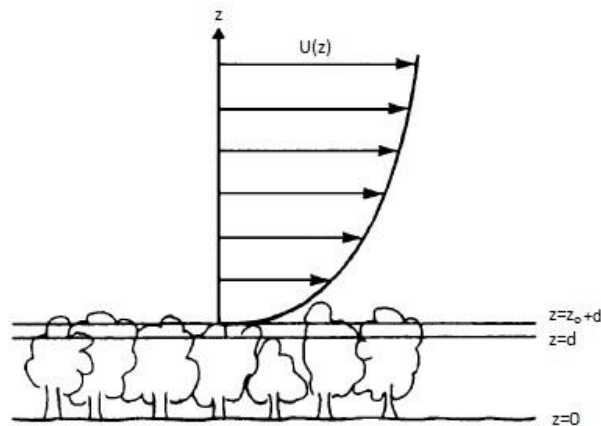


Figure 2.17 – Schematic representation of displaced wind profile [11]

2.3.1.4. The Corrected Logarithmic Wind Profile

Even though in the case of strong winds the velocity of the logarithmic law has been confirmed through different measurements and observations, a more precise expression was developed based on the mathematical model of Harris and Deaves. [11,12]

$$U(z) = \frac{u_*}{k} \left[\ln \left(\frac{z-d}{z_0} \right) + 5.75 \left(\frac{z-d}{Z_g} \right) - 1.875 \left(\frac{z-d}{Z_g} \right)^2 - \frac{4}{3} \left(\frac{z}{Z_g} \right)^3 + \frac{1}{4} \left(\frac{z}{Z_g} \right)^4 \right] \quad (2.38)$$

where Z_g is known as the gradient height and is defined as

$$Z_g = \frac{u_*}{6f} \quad (2.39)$$

where f is the Coriolis parameter.

In the same way as the non-corrected logarithmic profile, the corrected one fits experimental data accurately and has the advantage of covering surface roughness changes.

2.3.1.5. The Power Law Profile

The power law is an empirical law which was developed to fit the field data in order to describe the mean velocity profile in horizontally homogeneous terrain. This empirical law is extensively used due to its simplicity:

$$U(z) = U(z_{ref}) \left(\frac{z}{z_{ref}} \right)^\alpha \quad (2.40)$$

where α is an exponent which depends upon the roughness of terrain and z_{ref} is a reference height, usually 10m.

2.3.1.6. The Influence of Roughness Change and Topography in Inhomogeneous Terrain

In the previous cases the flow was considered as horizontally homogeneous, this being a consequence of the assumption that the surface roughness was uniform over an infinite plane. This assumption does not correspond to a realistic situation in which a site is limited in size, leading to a change of roughness as a mass of air passes through different sites. In the end this different roughnesses will have an effect on the flow which is not considered in the horizontally homogeneous flow.

Considering the simple case of a sudden roughness change along a line perpendicular to the direction of the mean flow between a terrain with roughness length z_{01} and another with roughness length z_{02} , then on the terrain before the roughness shift and above a height h_2 upwind of the discontinuity, the wind flow is horizontally homogeneous and the velocity is determined only by the roughness length z_{01} .

Below a height h_1 after the roughness shift, on the so called equilibrium layer, wind velocity depends only on the roughness length z_{02} . In the region between the heights h_1 and h_2 illustrated in figure 2.18, both roughnesses influence wind velocity, thus corresponding to a gradual transition region.

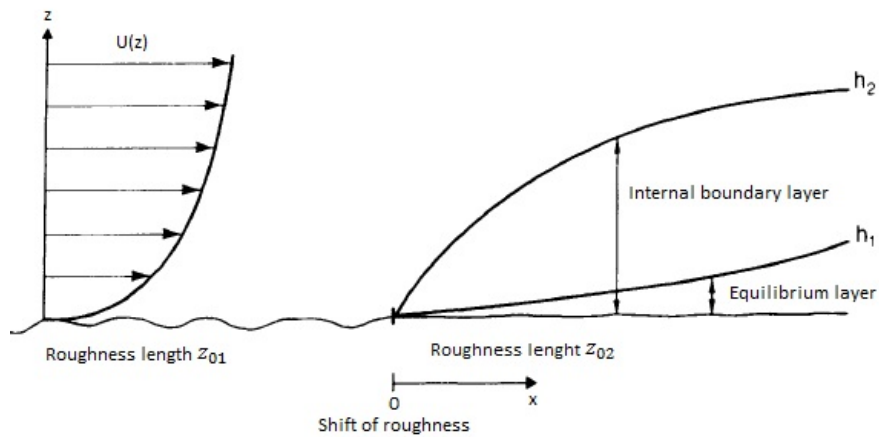


Figure 2.18 – Equilibrium and Internal boundary layer after a roughness change [11]

The height of the internal boundary layer in which the region between heights h_1 and h_2 is contained was formulated by William P. Elliott [11] and is given by:

$$h_2(x) = z_{02} \left[0.75 + 0.03 \ln \left(\frac{z_{01}}{z_{02}} \right) \right] \left(\frac{x}{z_{02}} \right)^{0.8} \tag{2.41}$$

where x is the distance measured from the discontinuity that characterizes the roughness shift. The height h_2 of the internal boundary layer will increase with x until the entire flow adjusts to the roughness length z_{02} [6], and will increase more rapidly after a shift to a rougher terrain than after a shift to a smoother terrain.

Topographical features such as escarpments, cliffs, ridges and hills can have an important effect on mean and gust wind speeds and are usually considered in wind engineering applications.

If the wind flow is obstructed by an escarpment or by the crests of hill for example, then the air is forced to go into a smaller area leading to a speed and wind pressure increase.

This effect can be shown through the example illustrated in figures 2.19 and 2.20.

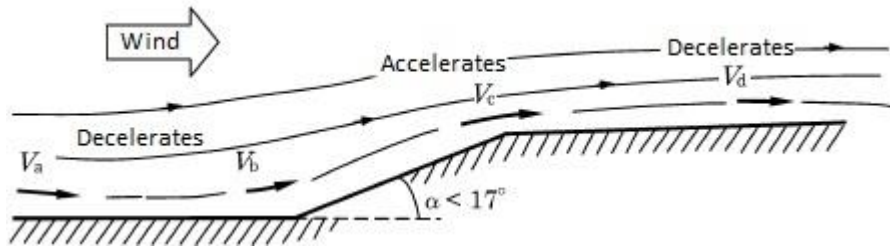


Figure 2.19 – Wind flow on a ridge with an upwind slope angle smaller than 17° [12]

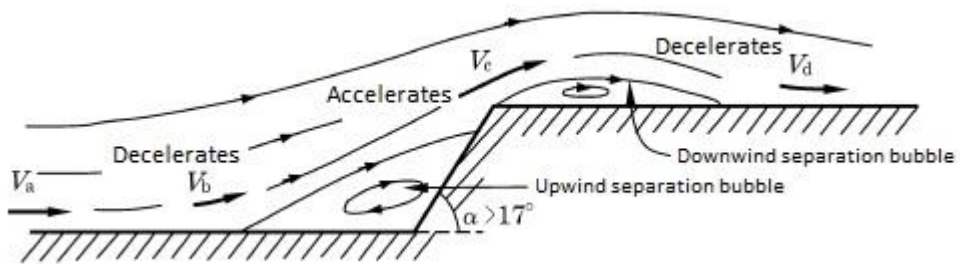


Figure 2.20 – Wind flow on a ridge with an upwind slope angle larger than 17° [12]

Consider the wind flow normal to the upstanding face of a ridge. When the flow reaches the upwind foot of the slope its speed decreases to its minimum value, accelerating to its maximum near the crest and decelerating again downwind of the crest. If the upwind slope angle is approximately larger than 17° the flow will separate from the slope face forming bubbles as represented in the figure 2.20.

2.3.2. EXTREME WINDS

Well-behaved climates, those in which it is not expected to occur extraordinary winds that are considerably stronger than the annual extremes, are characteristic of temperate regions of Europe.

In these type of climates the prediction of long-term wind extremes can be done through a statistic analysis of series of the largest annual wind speeds. This analysis then corresponds to a critical and uncertain part of the process made to determine the appropriate design wind speeds and its correspondent wind loads. An accurate estimation of these extreme wind speeds can avoid additional costs of “over-design” and diminish the risk of under-estimates, thus enabling a balance between the security of the structure and its final cost [13].

In 1928 Fisher and Tippett developed a theoretical work in which were established the limiting forms of the distribution of the largest value in a fixed sample and identified the three types of asymptotic distributions, the Type-I or Gumbel distribution, the Type-II or Fisher-Tippett distribution and the Type-III or reverse Weibull distribution [14].

Two years later the use of the symmetrical bell-shaped Gaussian distribution to represent extreme wind speed was purposed. However this approach was rejected since it failed to take into account the work developed earlier by Fisher and Tippett.

In 1954, Gumbel promoted the use of the Type-I distribution for the analysis of the extreme wind speeds.

A year later Jenkinson proved that the three asymptotic distributions could be represented by the Generalized Extreme Value Distribution. However the Type-I or Gumbel distribution continued to be the main distribution to be used for the extreme value analysis until the 1970's 1980's when a series of events originated wind speeds that exceeded considerably those determined by the Gumbel's analysis and gave way to a discussion about sampling errors inherent in the recorded data base and the necessity to separate data originated by different types of storms.

Once again, the work done by Davenport on the Wind Engineering field and in this particular case his contribution to the prediction of wind loads based on the use of probability and statistics has to be recognized.

2.3.2.1. Wind Speed Data

The quality of the data used on the analysis of extreme wind speed is a crucial factor for an accurate estimation of their respective wind loads. Thus this data, regarding a specific location, has to be reliable and has to constitute a micrometeorologically homogeneous set. A micrometeorologically homogeneous set is achieved if all the data is considered to have been obtained under identical or equivalent micrometeorological conditions such as averaging time, height above ground and roughness of surrounding terrain [6].

Wind speed data is measured by an anemometer. Pulses of voltage are generated by the anemometer as it spins in the wind and are posteriorly received by an analog device which counts the number of pulses over a certain time period [15].

The time period or time scale in which the analog device counts the number of pulses should be chosen as a function of the different storm types common in a specific region. Thus, the largest time scale is probably obtained for gravity winds that can last for several days in the Antarctic region, while the smallest time scale corresponds to thunderstorms since it leads to high wind speeds at a specific location for a few minutes [12].

Table 2.1 – Storm types and respective appropriate time scales [12]

Storm type	Time scale
Storms induced by strong frontal depressions	1h
Overshooting gust fronts in frontal depressions	30s / 1min
Tropical cyclones	10min / 15min
Thunderstorms	30s / 1min
Gravity winds	1h

The World Meteorological Organization (WMO) and other codes such as ISO 4354, ENV 1991-2-4 and AIJ use the 10 min-average to estimate the mean wind speed [14, 16]. This period of time is typically sufficiently long to incorporate most of the shorter period fluctuations, known as turbulence, in natural wind and is simultaneously sufficiently short to represent a period of near-constant background mean wind. Although a shorter period of time could be chosen for averaging the wind speed, this will typically produce more erratic values. Ten 1 min-averages taken during a 10 min-period, for example, will lead to values that lie both below and above the 10 min-average used by WMO and if a 1 min-random sample of the ten considered above is analyzed, its mean wind speed is likely to be higher and lower than the true mean wind speed. Thus one can conclude that the use of shorter periods to estimate the mean wind speed leads to a greater variance and hence to a less reliable analysis [17].

If, on the other hand, various averaging times have been used during the period of record, the data has to be adjusted to a common averaging time [6].

The height above ground is another important factor to consider in the wind data. If during the period of record the height at which an anemometer is installed changes, then its respective data must be adjusted to a common height.

The roughness of the surrounding terrain can also have a great influence on the wind data collected. This can be due to the relocation of the anemometer from a town to a neighboring airport station or even due to the growth of a city over the years as in the case of Hamburg. Thus the records have to be adjusted to a common terrain roughness. [6,12]

The prediction of extreme wind speeds is usually made considering the full set of extremes at a site. However, for certain studies, the partitioning of data may turn out to be an advantage not only due to the usefulness of knowing, for example, the direction of maximum wind speed but also because a simpler data set may lead to a more accurate prediction of extreme wind speed behavior.

On the contrary, a reduction of the amount of data due to its partitioning leads to an increase of the standard errors and may introduce unnecessary complexity.

According to Palutikof [13] the partitioning of data can be made by wind direction, season or meteorological mechanism.

2.3.2.2. Wind Directionality

The increase of knowledge in the field of aerodynamics of buildings revealed the variation of structural response not only as a function of wind speed but also as a function of its direction. Following this same line of thought, Moriarty and Templeton suggested that the consideration in the design stage of the building of wind directionality could lead to an optimization of the design and thus to a considerable cost minimization.

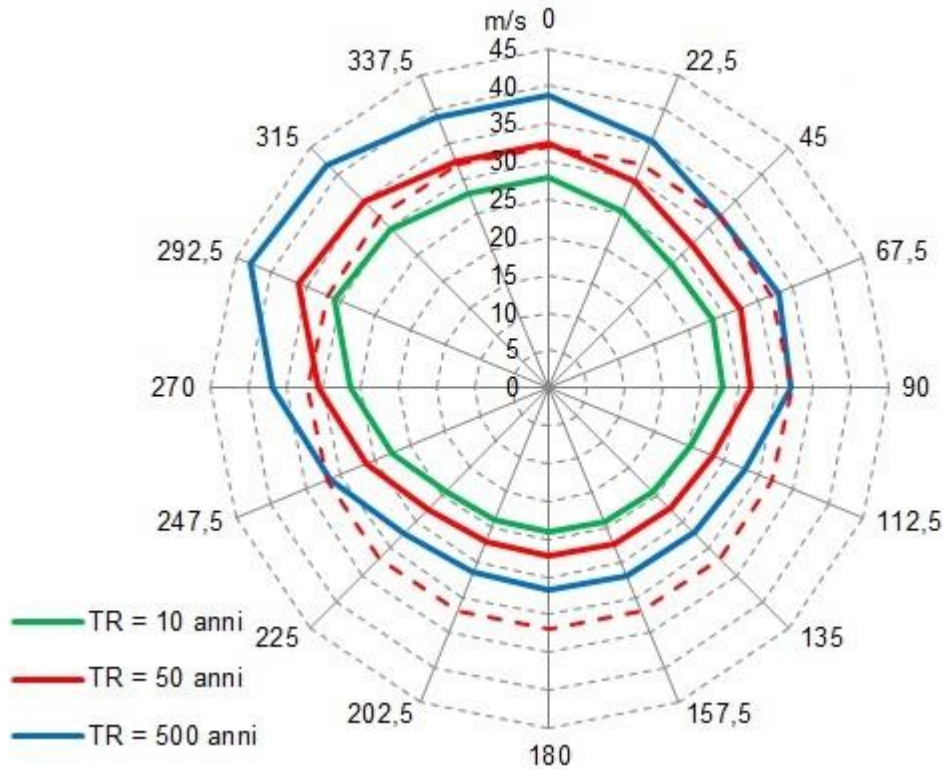


Figure 2.21 – Graphic representation of wind directionality of the case study of Tower A, for 10, 50 and 500 years of return period

The response of a structure to wind with a given speed can be directional independent or directional dependent depending on whether the structure itself is axi-symmetric or non axi-symmetric respectively. According to C.W. Liu [18], the directionality effects can be taken into account through different proposed methods.

The first method treats wind velocity as a stationary two-dimensional vector process with speed and directions where the response is expressed as a function of direction and the cumulative probability is determined by a Poisson distribution with a parameter known as mean crossing rate. Since this parameter is calculated from the wind spectra and from the joint probability density function of wind speed and direction, then the accuracy of the method depends greatly on the correct estimation of both wind spectra and the joint probability density function. This method is normally not recommended in structural design.

A second method consists on expressing the wind effect in terms of a directional dependent function of wind velocity. The first step is to determine the annual maximum wind speed in each directional sector in a particular year through which can then be found the annual maximum wind effect such as pressure or moment on the respective directional sectors. A time series of the largest annual wind effects can then

be constructed and a standard extreme value analysis is performed to determine the extreme wind effects for any return periods.

The last method is simple, general and may be applied to any type of structure. It consists on finding the extreme value distribution of wind speed in each directional sector and it is based on the assumption that there is no correlation between extreme wind speeds at two adjacent directional sectors and thus the cumulative probability distribution of the largest annual wind effect will be equal to the product of the cumulative probabilities of the equivalent wind speeds in each directional sector. As in reality the extreme wind speeds at two adjacent directional sectors are in fact correlated, the method tends to be conservative.

The wind directionality problem is further developed on [6,12,14,18]

2.3.2.3. Return Period

The return period or annual risk of exceedence can be defined as the period of time T in which the maximum wind speed is exceeded, on average, only once or as the inverse of the complementary cumulative distribution of the extremes

$$T(U) = \frac{1}{\text{Probability of exceedence of } U} = \frac{1}{1 - F_U(U)} \quad (2.41)$$

where $F_U(U)$ is the cumulative probability distribution function of the maximum wind speed, and if the annual is being considered, then the return period is measured in years.

Thus considering the definition of return period above, if the relative importance of a structure leads to the need of a probability of exceedence of the maximum wind speed that has to be less or equal to 2% in any one year, then the return period to be considered should be at least of 50 years [14].

The return period $T(U)$ should not be confused with the expected lifetime of a structure L . Once the difference between these two periods of time is clarified and assuming that all years are statistically independent of each other, then the risk or probability of exceedence of a wind speed over the lifetime of a structure $r_L(U)$ can be determined by

$$r_L(U) = 1 - \left[1 - \left(\frac{1}{T(U)} \right) \right]^L \quad (2.42)$$

2.3.2.4. Extreme Value Distributions

The theory of extreme value was first applied to the prediction of flood heights and later to other different geophysical variables such as wind speeds and earthquake accelerations and is based on the application of one or more of the three asymptotic extreme value distributions identified on the work by Fisher and Tippett in 1928. They showed that if a sample of n cases is chosen from a parent distribution and from each sample the maximum value is selected, then the distribution of the maxima approaches one of three limiting forms as the size of the samples increases.

These three families were later combined into a single distribution by Von Mises in 1936 (in French) and by Jenkinson in 1955 (in English). This distribution is known today as the generalized extreme value (GEV) distribution and has the cumulative distribution function

$$F_e(U) = \exp \left[-(1 - ky)^{\frac{1}{k}} \right] \quad (2.43)$$

where k is a shape parameter which determines the type of extreme value distribution.

y is a standardized or reduced variate which is given by

$$y = \frac{U - \beta}{\alpha} \tag{2.44}$$

where β is the mode of the extreme value distribution or location parameter and α is the dispersion or scale parameter.

If $k < 0$ the GEV distribution is known as the Fisher-Tippett Type II or Frechet distribution. When $k > 0$ GEV distribution becomes a Type III or reverse Weibull distribution. As k tends to 0 the cumulative distribution function of the GEV distribution represented by equation (2.43) becomes, in the limit,

$$F_e(U) = \exp[-\exp(-y)] \tag{2.45}$$

which corresponds to a Type I or Gumbel distribution.

Holmes [14] plotted the GEV distribution using different values of k ($k=0.2$; $k=0$ and $k = -0.2$) and Gumbel probability paper in such a way that the Gumbel distribution is represented as a straight line as shown in figure 2.22.

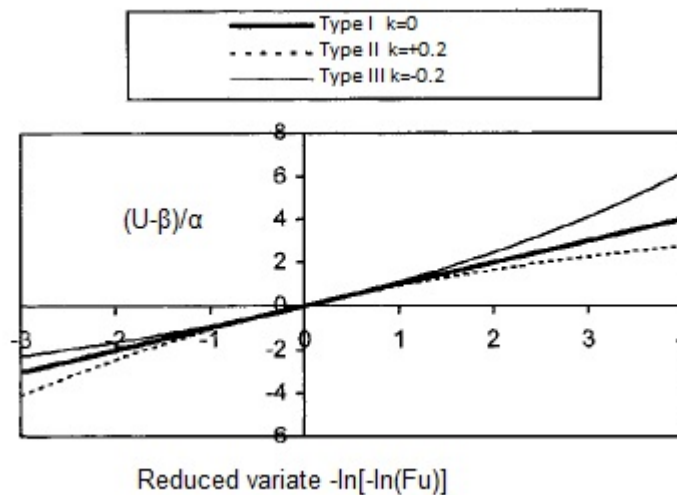


Figure 2.22 – Generalized Extreme Value Distribution with $k=-0.2$, $k=0$ and $k=0.2$ [14]

From the analysis of the plotted GEV distribution, one can conclude that the Type III or reverse Weibull distribution ($k>0$) has a finite upper tail, which can not be exceeded with probability of 1 and is thus appropriate for variables that are bounded on the high side. Since it is expected the existence of an upper limit for the wind speed produced by the atmosphere, it is widely accepted that the Weibull probability density function constitutes a good model for wind speed distributions.

The Type II distribution has a finite lower tail, while Type I distribution is unlimited on both sides. Thus both of these extreme value distributions predict unlimited values and are therefore suitable distributions for variables that are unbounded.

As seen before, the return period $T(U)$ is given by equation 2.41. Thus for the quantile with return period $T(U)$, the cumulative probability is given by

$$F(U) = 1 - \frac{1}{T(U)} \tag{2.46}$$

If equations (2.43) and (2.44) are combined and solved for U , then for the case of extreme wind estimation and for a return period T :

$$U_T = \beta + \frac{\alpha}{k} \left\{ 1 - \left[\ln \left(1 - \frac{1}{T} \right) \right]^k \right\}, k \neq 0 \quad (2.47)$$

$$U_T = \beta - \alpha \ln \left[- \ln \left(1 - \frac{1}{T} \right) \right], k=0 \quad (2.48)$$

As the form of the parent distribution determines the type of GEV distribution and the parent distribution of Type I extremes include the Weibull distribution, then the extremes of wind speeds are often modeled by the Type I.

In 1954 Gumbel developed a methodology for fitting recorded annual maxima to the Type I distribution that is easily applicable to practical, current situations.

As described, for the specific case of the Gumbel distribution ($k=0$), the cumulative distribution is represented by equation (2.45) and the quantile U_T with respect to the return period T is given by equation (2.48). If large values of return period are considered equation (2.48) this can be expressed as

$$U_T = \beta + \alpha \ln T \quad (2.49)$$

As one can notice, the calculation of U_T through the Gumbel distribution is simpler since there are only two parameters required: α and β .

The most common procedure for the determination of the values of β and α consists of a graphic process.

The first step of the calculation consists on the selection of the largest wind speed in each calendar year from the time series of observation. These values are then ranked in order of smallest (U_1) to largest (U_N), and to each value is calculated an empirical value $F(U_m)$ of the probability of non exceedence from each ranked position U_m , known as plotting positions. Many of the studies on wind extremes use:

$$F(U_m) = \frac{m}{N + 1} \quad (2.50)$$

although, for the special case of the Gumbel distribution an almost unbiased plotting is given by:

$$F(U_m) = \frac{m - 0.44}{N + 0.12} \quad (2.51)$$

where m is a ranked position among the N values selected from the tie series of observation.

For each annual maxima is then necessary to estimate a value of y_{Gumbel} , known as the Gumbel reduced variate, which corresponds to an estimate of the term $-\ln \left[- \ln \left(1 - \frac{1}{T} \right) \right]$ present in equation (2.48).

$$y_{Gumbel} = - \ln \{ - \ln [F(U_m)] \} \quad (2.52)$$

Once calculated the values of $F(U_m)$ and hence y_{Gumbel} for each value of U and plotting y_{Gumbel} against values of U instead of $F(U_m)$ against U a linearized graph of the cumulative distribution function with the axes reversed is obtained.

Solving the equation (2.44), of the standardized or reduced variate y , for U gives:

$$U = \alpha y + \beta \quad (2.53)$$

By fitting the straight line generated by the equation above to the plotted points mentioned, which may be done by eye or by using linear regression, the parameters α and β corresponding respectively to the

slope which gives the dispersion and to the intercept which will give an estimate of the mode, can thus be found.

2.3.3. WIND TURBULENCE

Natural wind is always turbulent, this meaning that the flow is chaotic, with wind speeds that vary randomly with time as represented in figure 2.23.

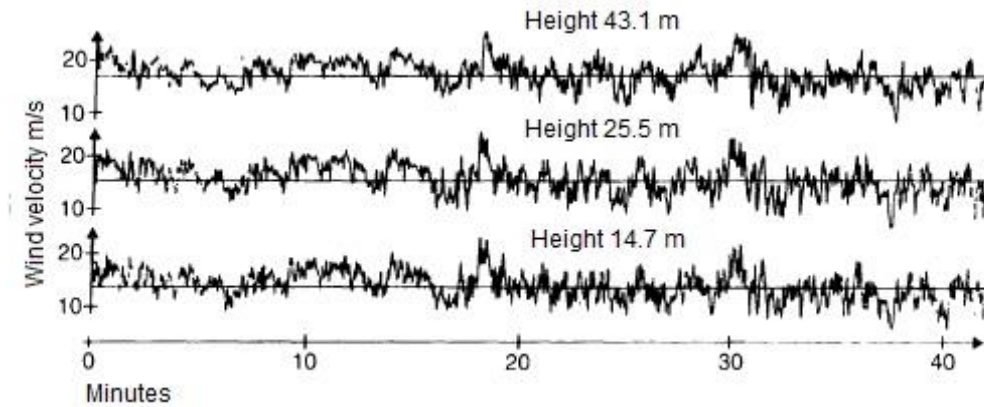


Figure 2.23 – Measurement of wind speed at three different heights in Denmark [11]

Since a turbulent wind flow varies in a complex, random way not only in time but also in space, its features (such as turbulence intensity and scale, gust and peak factor, power spectrum, spatial-/temporal-correlations and so on) must be described in a statistical manner, being treated mathematically as a stationary, stochastic process with a zero mean value.

The analysis of these features of wind turbulence are useful mainly because, for a structure, the turbulence in the air flow may have a great influence on its aerodynamic behavior and on its respective laboratory tests. Furthermore rigid structures and rigid members are subjected to time dependent loads which suffer from fluctuations due, in part, to wind turbulence. A flexible structure, in turn, may exhibit resonant amplification effects due to wind fluctuations.

If the steady or mean component of wind speed is subtracted to the total velocity component, the resulting deviation can be quantified. This deviation can be both positive and negative, hence the need to square it before averaging it. In order to give a quantity with the units of wind speed the square root has to be applied.

This process can be mathematically written as:

$$\sigma_u = \sqrt{\frac{1}{T} \int_0^T [U(t) - \bar{U}(z)]^2 dt} \quad (2.54)$$

and is known as standard deviation, where T is the averaging time which should be equal to the duration of the strong winds in a storm and is commonly assumed to belong to the interval between 10 minutes and 1 hour.

$U(t)$ is the total velocity component in the direction of the mean wind which is equal to $\bar{U}(z) + u(t)$, where, as seen before, $\bar{U}(z)$ is the mean wind speed at a height z and $u(t)$ is the longitudinal or the component of the turbulence in the mean wind direction.

The components of turbulence in the lateral horizontal direction $v(t)$ and in the vertical direction $w(t)$ can also be quantified by their respective standard deviations σ_v and σ_w .

2.3.3.1. Turbulence Intensity

The simplest descriptor of atmospheric turbulence is turbulence intensity.

Turbulence intensity is defined as the ratio of the standard deviation of velocity fluctuation to the mean speed both at a height z .

Thus the turbulence intensity for the different components of fluctuation are given by:

$$I_u(z) = \frac{\sigma_u(z)}{\bar{U}(z)} \quad (2.55)$$

$$I_v(z) = \frac{\sigma_v(z)}{\bar{U}(z)} \quad (2.56)$$

$$I_w(z) = \frac{\sigma_w(z)}{\bar{U}(z)} \quad (2.57)$$

According to Dyrbye [11], the three standard deviations are close to zero at geostrophic wind heights and thus so are their turbulence intensities, considering its definition. Furthermore experimental results obtained by Davenport (1967), Harris (1970) and Armit (1976) showed that the standard deviations regarding the three directions u , v and w usually decrease with height very slowly up to the heights of ordinary structures and can be considered almost constant up to approximately half the height of the internal boundary layer, as stated by Armit (1976).

For the specific case of a homogeneous terrain, and up to a height of 100-200m, the standard deviation of the three components are approximately:

$$\sigma_u = Au_* \quad (2.58)$$

$$\sigma_v = 0.75\sigma_u \quad (2.59)$$

$$\sigma_w = 0.5\sigma_u \quad (2.60)$$

where $A \approx 2.5$ if $z_0=0.05$ and $A \approx 1.8$ if $z_0=0.3$.

Considering equation (2.55) and the logarithmic law for the wind profile, in the case of a flat terrain the turbulence intensity is given by:

$$I_u(z) = \frac{1}{\ln \frac{z}{z_0}} \quad (2.61)$$

And thus, the turbulence intensity at some height z is simply related to the surface roughness z_0 .

2.3.3.2. Turbulence Scale

A turbulent flow can be thought of as a superposition of eddies (coherent patterns of velocity, vorticity and pressure) which are spread over a wide range of sizes.[19]

Turbulent eddies observed in the atmospheric boundary layer are spatially extensive structures, and, ideally, their analysis requires information from many points in space. However, the greater part of the data available is still derived from measurements in space as a function of time.

The space-time structure of eddies can be characterized by a cross-correlation function. This function describes the existing relation between a specific component of turbulence i ($i = u, v, w$) at a specific point $P_1(x, y, z)$ at a given time t , with the same component of turbulence i at a different specific point $P_2(x + \Delta x, y + \Delta y, z + \Delta z)$ at a time $t + \tau$.

$$R_i(P_1, P_2, \tau) = \frac{1}{T} \int_{t_0}^{t_0+T} i(P_1, t) i(P_2, t + \tau) d\tau \quad (2.62)$$

The respective correlation coefficient is given by

$$\rho_i(P_1, P_2, \tau) = \frac{R_i(P_1, P_2, \tau)}{\sigma_i(P_1)\sigma_i(P_2)} \quad (2.63)$$

The correlation coefficient varies between 0 and 1 whether the points are further or closer to each other in space or in time.

The autocorrelation coefficient of each turbulence component u, v and w as a function of time, corresponds to the application of the cross-correlation function to a single point P [9].

The autocorrelation coefficient $\rho_u^T(z, \tau)$ of the turbulence component u can thus be represented as:

$$\rho_u^T(z, \tau) = \frac{R_u(P, \tau)}{\sigma_u^2(z)} \quad (2.64)$$

For horizontally homogeneous flow, the autocorrelation function depends only on height z above ground and on time difference τ between measurements of the turbulence component.

The characteristic time of memory or characteristic period of fluctuation of u , designated as time scale $T(z)$ is given by:

$$T(z) = \int_0^{\infty} \rho_u^T(z, \tau) d\tau \quad (2.65)$$

Integral length scales are measures of the average size of the vortices in the wind.

Since that there are three dimensions of the eddies associated to each one of the three turbulence components, then altogether there are nine integral scales of length.

$$\begin{aligned} &L_u^x L_u^y L_u^z \\ &L_v^x L_v^y L_v^z \\ &L_w^x L_w^y L_w^z \end{aligned}$$

where L_u^x, L_u^y and L_u^z are the average longitudinal, transversal and vertical dimensions of the eddies associated with mean wind direction turbulence component u .

The cross correlation coefficient of the turbulence component u between two points separated longitudinally by a distance Δx and measured simultaneously is represented by $\rho_u(z, \Delta x)$, being the integral length scale represented mathematically by:

$$L_u^x = \int_0^{\infty} \rho_u(z, \Delta x) d\Delta x \quad (2.66)$$

If it is assumed that the flow disturbance moves with the velocity $U(z)$, hence corresponding to the convected “frozen turbulence” of Taylor’s hypothesis, which states that a statistical description of temporal turbulence variations could be based on a spatial wind velocity field characteristics, then

$\Delta x = U(z)\tau$ leading to $\rho_u(z, \Delta x) = \rho_u^T(z, \tau)$ and the longitudinal integral length scale is then given by:

$$L_u^x = U(z)T(z) \quad (2.67)$$

Usually full-scale measurements are used to estimate the turbulence scales. However, these estimates depend significantly upon the degree and length of stationary of the record being analyzed and can sometimes be influenced by the wind velocity itself. This dependence leads to an extensive scatter of the results, which usually vary widely from experiment to experiment.

In 1975, Counihan suggested an empirical expression for the longitudinal integral length scale which can be applied to the height range from 10 to 240 meters and is represented by:

$$L_u^x = Cz^m \quad (2.68)$$

where C and m depend on the roughness length z_0 and can be determined through figure 2.24.

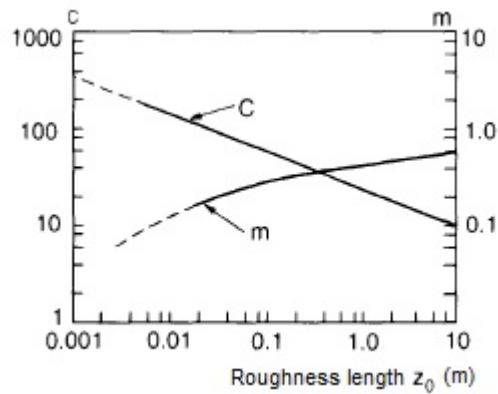


Figure 2.24 – Representation of c and m as a function of the roughness length [11]

According to Dyrbye [11] the integral length scales L_u^y and L_u^z can be expressed as a function of L_u^x :

$$L_u^y \approx 0.2L_u^x \quad (2.69)$$

$$L_u^z \approx 0.3L_u^x \quad (2.70)$$

2.3.3.3. Gust Factor and Peak Factor

Engineers have been greatly concerned with the characteristics of wind gustiness in relation to the dynamic loading produced on structures.

This concern is also present in many design codes and standards for wind loadings which use a peak gust wind speed for design purposes.

As stated before, natural wind is a random process. As the peak gust is itself a part of natural wind, then it can also be represented as a random variable.

If it is assumed that the longitudinal wind velocity has a Gaussian probability distribution (measurements have shown that the wind velocity components in the atmospheric boundary layer follow closely this probability distribution), then the average or expected peak gust \hat{U} is given approximately by:

$$\hat{U}(z) = \bar{U}(z) + g_u \sigma_u(z) \quad (2.71)$$

where g_u is a peak factor which usually is equal to about 3.5.

Since these gusts do not occur simultaneously at all heights, the profile of peak gust with height for a specific type of terrain corresponds to an envelope of the gust wind speed with height.

Long-term wind measurements are made with meteorological equipment that does not have a perfect response in order to measure peak gust wind speed. This makes the peak gust wind speed dependable on the response characteristics. Thus, usually, this speed is obtained by picking the highest 2-3 sec average within a period, since common instruments such as those of the pressure tube type and small cup anemometers have an equally short period of response [14].

The gust factor G is a theoretical conversion between an estimate of the mean wind speed and the expected highest gust wind speed of a given duration within a stated observation period and can be represented as the ratio of the maximum peak gust with a specific period (e.g. 10 min) to the mean wind speed.

$$G = \frac{\hat{U}(z)}{\bar{U}(z)} \quad (2.72)$$

Even though semi-empirical theories available are based on many sets of observations, gust factors continue to be extremely useful for making forecasts of the most likely gust wind speed that will accompany its respective mean wind speed forecasted within a specific period of observation and at a same height above ground.

However, due to the assumptions made for the theoretical estimation of gust factors, if the mean wind is not steady within the period of observation (stationarity), or if there are varying roughness conditions on a fetch or the direction of winds is changing during the observation period, then the observed gust is likely to deviate from the expected gust obtained from the statistical theory [17].

2.3.3.4. Power Spectrum

van der Hoven developed a spectrum in which there are distinct peaks separated by a gap as shown in figure 2.25. To the left of this gap and related to low frequencies and to the movement of a large scale weather system due to global conditions the so called macro-meteorological peak can be seen. The gap between the two peaks, known as the spectral gap, corresponds to a frequency range which contains almost no energy. The micro-meteorological peak, located on the right side of the spectral gap, is related to the turbulence caused, among others, by topographic effects, terrain roughness and obstacles around the site.

The dynamic wind forces used in building design are evaluated by the wind fluctuations in the micro-meteorological peak.

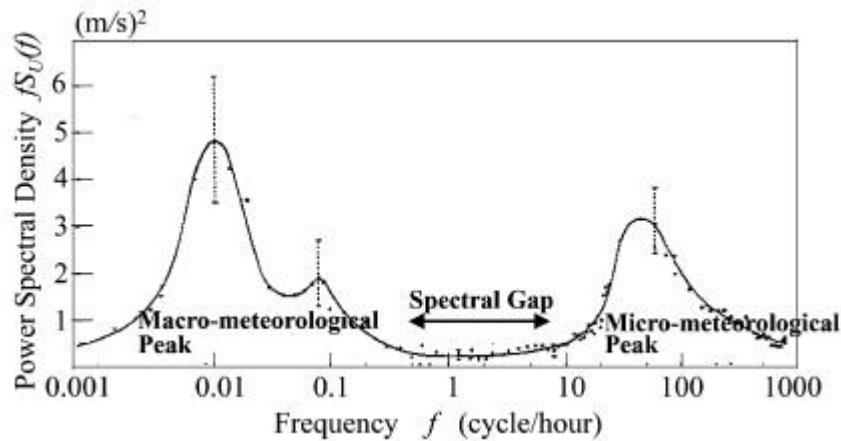


Figure 2.25 – van der Hoven spectrum [12]

As already mentioned, the turbulent velocity fluctuations may be considered to be caused by a superposition of eddies. Each one of these eddies can be characterized by a periodic motion of circular frequency $\omega = 2\pi n$ or by a wave number $k = 2\pi/\lambda$ where λ is the wavelength [6].

While these eddies interact both with each other and with the mean flow, it is from the latter that they derive their energy. The large energy-containing eddies, which contain most of the kinetic energy, arise through instabilities in the background flow and are themselves subjected to instabilities provoked by the interaction with other eddies. This interaction leads to a breakup of larger eddies into smaller ones. The repetition of this process in successively smaller scales (known as eddy cascade) originates sufficiently small eddies that are directly affected by viscosity which converts the kinetic energy of eddies into heat. [19]

A large size eddy results in a long period or low frequency fluctuation, while a small size eddy will correspond to a short period or high frequency fluctuation.

The distribution of turbulence energy with frequency is described by a power spectral density function which when nondimensionalized with the appropriate scaling parameters can be reduced to a set of universal curves that are functions only of z/L in the surface layer. On a practical level, it provides engineers with the equations they need for the design of structures concerning wind loads.

Considering only the micro-meteorological peak, the power spectrum consists of three parts: the production or energy-containing range, the inertial range and the dissipation range. The first corresponds to the low frequency end and is where the turbulence is generated in the form of large eddies due to instabilities of the mean wind. The part of the inertial range closer to the production range corresponds to the breakup of larger eddies and the transfer of its momentum to smaller ones. As stated before, it will occur a cascade-like effect which corresponds to successively smaller eddies and thus to successively higher frequencies. When eddies become so small that viscosity becomes predominant, kinetic energy starts to be converted into internal energy and the dissipation range is reached, corresponding to the high frequency end.

The spectrum is defined in such a way that the contribution to the variance, in the range of frequencies from n to $n + dn$, is given by $S_u(n) \cdot dn$, where $S_u(n)$ is the spectral density function for $u(t)$.

The power spectrum representing the micro-meteorological wind speed fluctuation can be defined through different mathematical forms.

The Fichtl and McVehll model gives a general mathematical expression in which the power spectrum is defined as

$$\frac{nS_u(n)}{\sigma_u^2} = \frac{4f^*}{(1 + \alpha f^{*\beta})^{\frac{5}{3\beta}}} \quad (2.73)$$

Where

$$f^* = \frac{nL_u^x}{\bar{U}} \quad (2.74)$$

$$\alpha = 1.5 \frac{4^\beta}{b^\beta} \quad (2.75)$$

$$b = \frac{1.5\beta\Gamma\left(\frac{5}{3\beta}\right)}{\Gamma\left(\frac{1}{\beta}\right)\Gamma\left(\frac{2}{3\beta}\right)} \quad (2.76)$$

and Γ is Gamma function.

When $\beta=1$, $\beta=5/3$ and $\beta=2$ the general expression corresponds respectively to the Kaimal, Panofsky and Karman type spectrum.

The latter which was adopted by many codes, is the most common and mathematically correct for the longitudinal velocity component and was adapted for wind engineering by Harris in 1968.

The Karman/Harris form is commonly used in the non-dimensional form

$$\frac{nS_u(n)}{\sigma_u^2} = \frac{4\left(\frac{nL_u^x}{\bar{U}}\right)}{\left(1 + 70.8\left(\frac{nL_u^x}{\bar{U}}\right)^2\right)^{\frac{5}{6}}} \quad (2.77)$$

Where L_u^x is a turbulence length scale, n is the frequency and \bar{U} the mean wind speed.

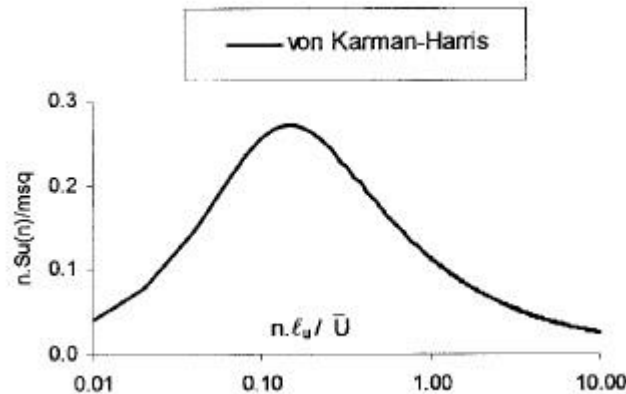


Figure 2.26 – von Karman/Harris type spectrum [14]

The spectrum represented above only contains one peak. The value of n/\bar{U} at which the peak occurs is determined by the value of L_u^x . Hence for higher values of the latter, higher values of \bar{U}/n at the peak or λ (wavelength) are obtained.

3

Case Study

The Unicredit High-Rise Building

3.1. INTRODUCTION

3.1.1. PORTA NUOVA

Porta Nuova is a 290 000 sqm area between Brera and Piazza della Repubblica, located 1.5 km from Milan's Duomo which includes the districts of Garibaldi, Varesine and Isola shown in figure 3.1.



Figure 3.1 – Panoramic view of Milan with Porta Nuova's new high-rise buildings

Its redevelopment constitutes Italy's most significant urban redevelopment project and intends to recreate a strategic center for Milan through the implantation of a 160 000 sqm pedestrians zone with a 5 km cycle path, a large park (Giardino di Porta Nuova) with 90 000 sqm, residential apartments, offices and retail spaces which, when completed, will constitute the Porta Nuova Business District.

Thanks to its location and connections, some renowned firms and banks such as Accentura, Axa, Mitsubishi Corporation, Telecom or Unicredit opted to move their headquarters to this new Business District, served by Centrale and Garibaldi railway stations, both served by high speed trains, 4 underground lines and other public transports in its close surroundings. These public transports can be used to reach the two busiest airports of Milan, the Linate and Malpensa airports situated, respectively, at a distance of 10 and 52 km.[20]

3.1.2. CITTÀ DELLA MODA

The Fashion City (Città della Moda) shown in figure 3.2, located within the Porta Nuova redevelopment project, was designed by Cesar Pelli, an Argentine American architect who designed the world renown and award-winning projects such as the Pacific Design Center in West Hollywood, the World Financial Center in New York or even the twin Petronas Towers in Kuala Lumpur. [21, 22]

Pelli's idea was to make of the Fashion City a new area which would be perfectly integrated in the existing surroundings, corresponding at the same time to a place where the different activities which move and characterize Italian and Milanese economy, such as design, fashion and culture, would come together.



Figure 3.2 – Architectural rendition of Pelli's Fashion City

This new city evolves around a Podium, a pedestrian square with 100 m in diameter situated 6 m above the surrounding terrain, between Corso Como and Garibaldi railway station, known as Piazza Gae Aulenti.

The connection of the Podium area with both the Garibaldi railway station and the Corso Como area was achieved by means of two different solutions. While the first meant a significant modification of the pre-existing road-system, the second, consisting of an aerial pedestrian passage, followed the plan started by the "Comune di Milano" to turn the Corso Como area into a more pedestrian friendly zone.

The Podium is surrounded by sustainable buildings which will be used as offices (50 485 sqm), residences (15 000 sqm) and will also contain spaces dedicated to fashion, creativity, communication and production (20 000 sqm) as well as a 300 bedroom hotel, restaurants and commercial areas (10 000 sqm). Beneath this Podium an 40 000 sqm parking lot will enable a relief of traffic from the surrounding neighborhoods.[23]

The three office towers, varying from 10 to 32 floors, present in the Podium area are made of steel and reinforced concrete with reflective glass facades and are the largest components of the Fashion City. However, and despite their size, each one of these buildings is certified with LEED (Leadership in Energy and Environmental Design) Gold. This green building certification that recognizes best-in-class building and practice was achieved due to advanced building systems, high efficiency lighting and daylight controls which allow a more natural process of heating and cooling of the buildings thus reducing the amount of energy spent.

3.2. TOWER A: STRUCTURAL CHARACTERISTICS

3.2.1. FLOOR PLANS

The Unicredit high-rise building shown in figure 3.3, also known as Tower A of Fashion City is a high-rise building characterized by a nonsymmetrical, curvilinear floor plan of constant radius with an inner part, with a longitudinal length of 52.6 m, connected to the Piazza Gae Aulenti and an outer part, with a longitudinal length of 73.9 m, facing the park and the Bosco Vertical residential area. The non-symmetry is a result of the presence of a circular shape with an approximated radius of about 11.5 m inserted on the inner part of the structure which raises to the roof floor on top of which is placed a spire. The floor plans are represented in figures 3.4 to 3.9.



Figure 3.3 – General view of Tower A (a) and Spire close up (b)

The slabs of the 18 m width building are prolonged about 12 m into the Piazza Gae Aulenti for the underground floors and for the 2 first floors above ground thus creating a larger reception area for the existing services and commercial areas.

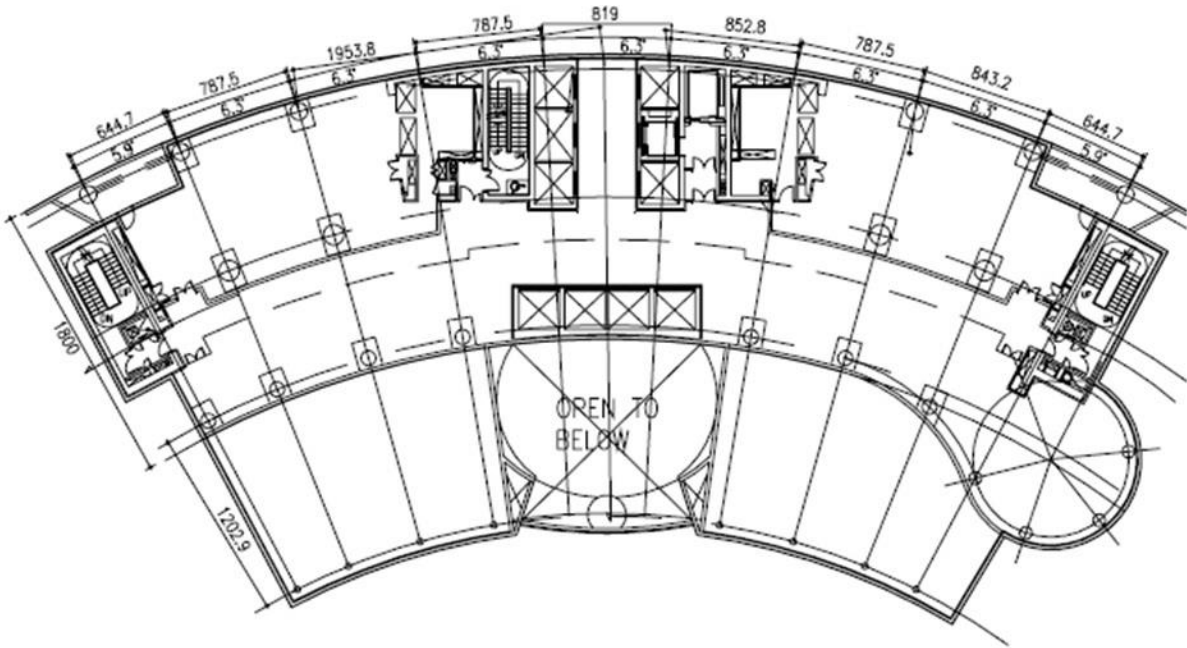


Figure 3.4 – First floor plan [24]

The building is made of different structural elements which can be joined into two different groups. The two reinforced concrete cores of the lateral extremities and the two central-outer cores which develop along the full height of the structure along with the central-inner core present only up to the height of the fourteenth floor are the structural elements responsible for the resistance of the building to horizontal actions. It's in these structural elements that the stairwells and elevator shafts are placed. It should be referred that the two central-outer cores are connected to each other by a reinforcement beam (concealed by the false ceiling) which gives them an increased rigidity.

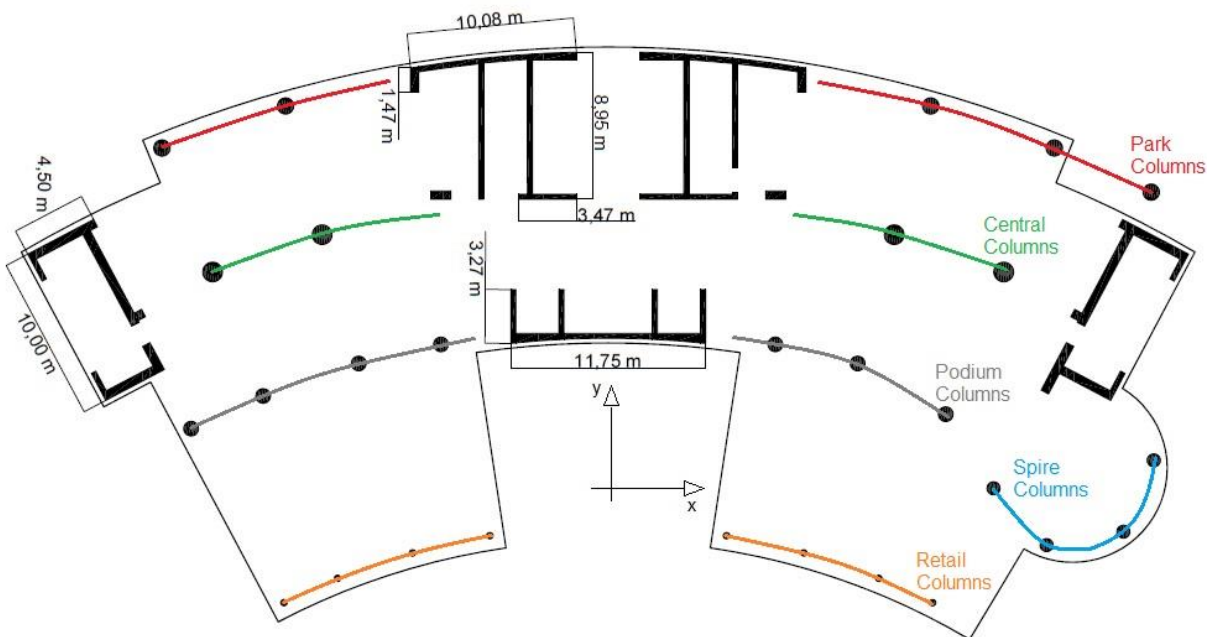


Figure 3.5 – Core dimensions [23]

The columns, in turn, are the structural elements which are mainly used to resist vertical loadings. As stated before, the slabs of the underground floors and those of the two first floors above ground occupy a larger area hence needing a larger number of columns. Thus, up to the second floor, the columns are divided into four different sets. The inner set, which will be called as the retail columns, sustains the slabs that give cover to the reception floors and is made up of eight columns. The outer set (park columns) has six columns while the central one only has four (central columns). Since the elevator shaft of the central-inner core only goes up to the height of the fourteenth floor, the number of columns of this set (Podium columns) will change at this floor from seven to nine which will continue all the way up to the last floor. Apart from the sets of columns mentioned before there exists another one corresponding to the four columns which support the slabs of the circular part of the structure (Spire Columns) as it can be seen in figure 3.5.

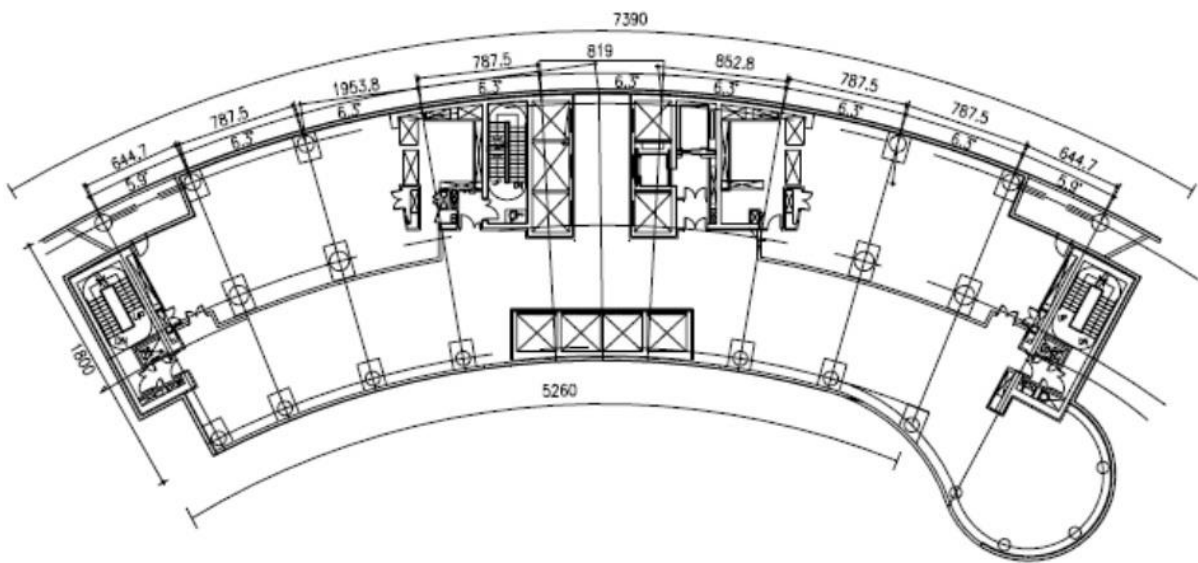


Figure 3.6 – Third to fourteenth floor plan [24]

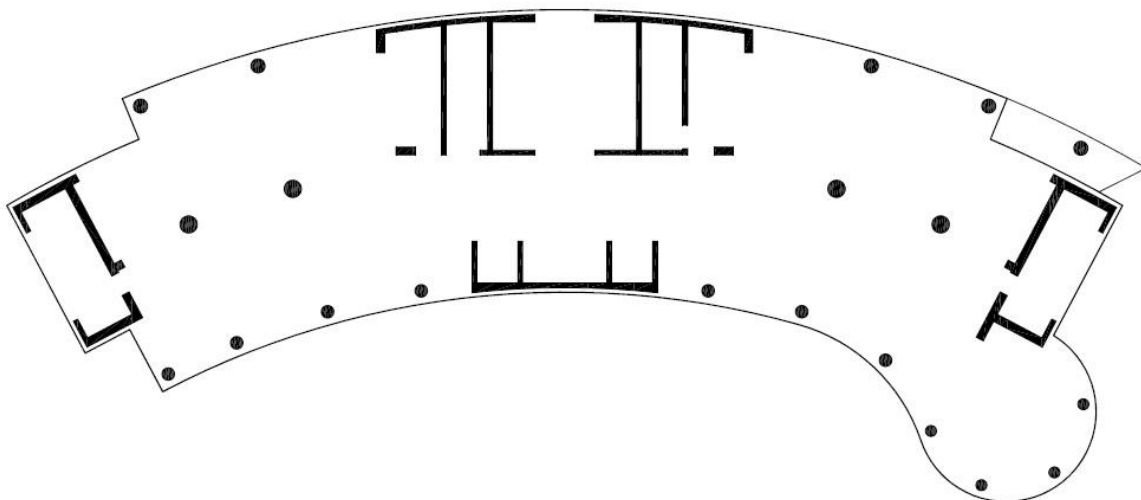


Figure 3.7 - Third to fourteenth floor cores [23]

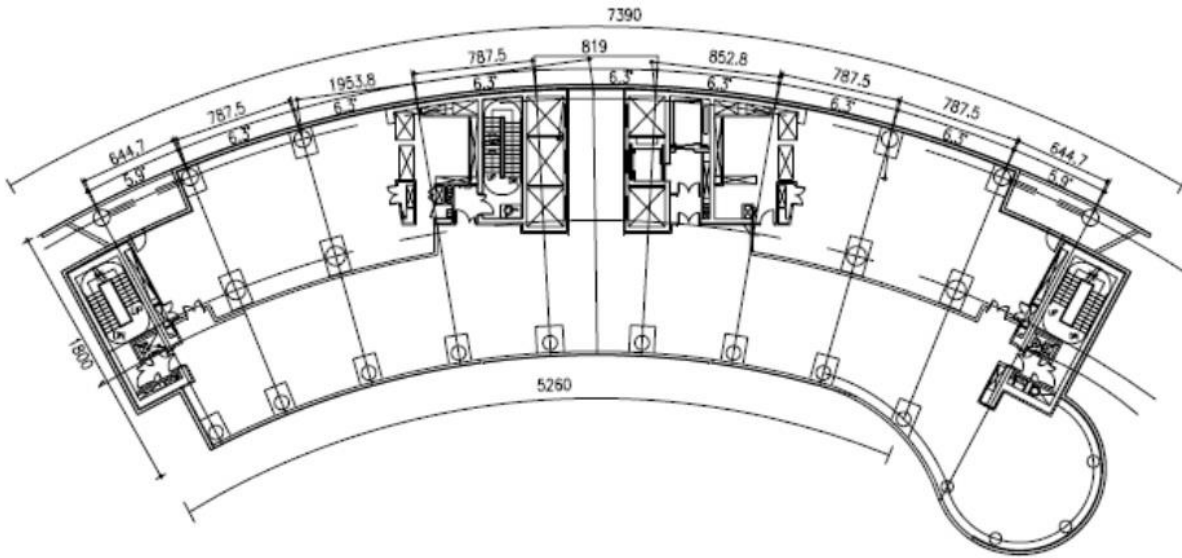


Figure 3.8 - Fourteenth to thirty secondth floor plan [24]

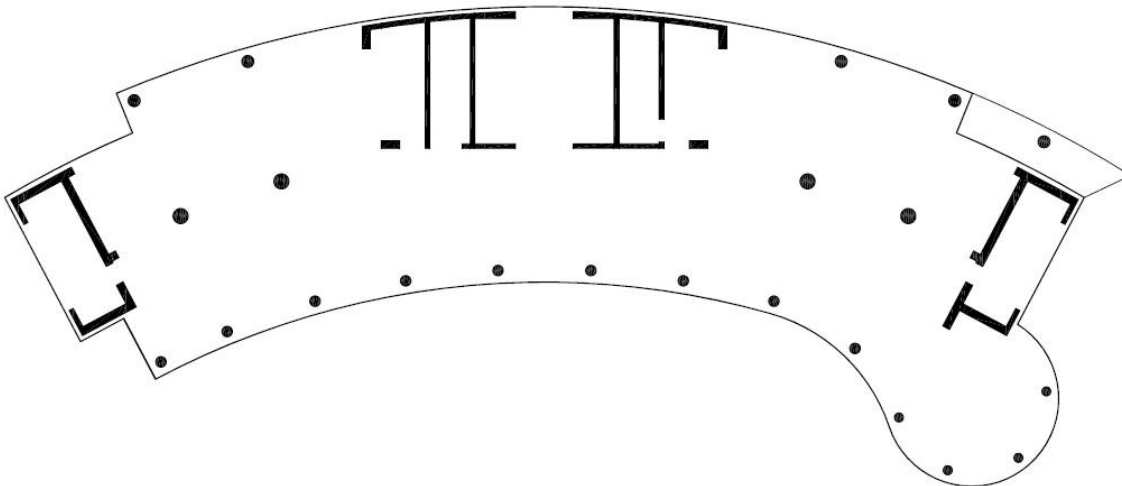


Figure 3.9 - Fourteenth to thirty second floor cores [23]

3.2.2. ELEVATION AND INTERSTORY HEIGHT

The structure of Tower A is composed of 32 floors above ground and 4 underground with respectively above and underground heights of 139.01 m and -11.55 m.

On table 3.1 the different interstory heights, the total height of each floor, the height of each floor in reference to the ground and the different floor types are presented.

Table 3.1 – Floor type and interstory heights of Tower A

Floor	Floor Type	Interstory height (m)	Total Height (m)	Height from ground (m)
Foundation	Elect./Archive	2.050	117.950	-11.550
-3	Garbage Room	3.100	120.00	-9.500

-2	Archive	3.330	123.100	-6.400
-1	Archive	3.070	126.430	-3.070
0	Retail/Piazza	6.000	129.500	0.000
1	Retail/Mechanical	5.900	135.500	6.000
2	General Interest	5.120	141.400	11.900
3	Office	4.075	146.520	17.020
4	Office	4.075	150.595	21.095
5	Office	4.075	154.670	25.170
6	Office	4.075	157.745	29.245
7	Office	4.075	162.820	33.320
8	Office	4.075	166.895	37.395
9	Office	4.075	170.970	41.470
10	Office	4.075	175.045	45.545
11	Office	4.075	179.120	49.620
12	General Interest	5.120	183.195	53.695
13	Office	4.075	188.315	58.815
14	Office	4.075	192.390	62.890
15	Office	4.075	196.465	66.965
16	Office	4.075	200.540	71.040
17	Office	4.075	204.615	75.115
18	Office	4.075	208.690	79.190
19	Office	4.075	212.765	83.265
20	Office	4.075	216.840	87.340
21	Office	4.075	220.915	91.415
22	Office	4.075	224.990	95.490
23	Office	4.075	229.065	99.565
24	Office	4.075	233.140	103.640
25	Office	4.075	237.215	107.715
26	Office	4.075	241.290	111.790
27	Office	4.075	245.365	115.865
28	Office	4.075	249.440	119.940
29	Office	4.075	253.515	124.0150

30	General Interest	5.620	257.590	128.090
31	Mechanical	5.300	263.210	133.710
Roof	Mechanical roof	-	268.510	139.010

3.2.3. COLUMNS

As stated before the columns can be divided into different groups accordingly to their inner or outer position. Besides the “retail columns”, “Podium columns”, “central columns” and “park columns”, an extra set of columns were added to characterize the dimension of the columns placed on the underground floors of the park side, the “underground external columns”. The set of columns placed on the circular shape of the building which raises to the roof and on top of which is placed the spire are known as the “spire columns”.

In the following table the different cross sections of the various sets of columns and their respective variations along the different floors are presented.

Table 3.2 – Column dimensions

Floor	Column dimensions as sides length or diameter (m)					
	Retail columns	Podium columns	Central columns	Park columns	Spire Columns	Underground external columns
Foundation to -3	0.60x0.60	1.30x1.30	1.60x1.60	1.30x1.30	1.10x1.10	0.60x0.60
-2 to -1	0.60x0.60	1.25x1.25	1.25x1.25	1.25x1.25	1.00x1.00	0.60x0.60
0 to 1	0.40x0.40 φ0.40	φ1.10	φ1.30	φ1.10	φ0.85	-
2 to 3	-	φ1.10	φ1.30	φ1.10	φ0.85	-
4 to 7	-	φ1.05	φ1.20	φ1.05	φ0.85	-
8 to 11	-	φ0.95	φ1.05	φ0.95	φ0.75	-
12 to 15	-	φ0.85	φ0.95	φ0.85	φ0.75	-
16 to 19	-	φ0.75	φ0.85	φ0.75	φ0.65	-
20 to 23	-	φ0.65	φ0.75	φ0.65	φ0.65	-
24 to 27	-	φ0.55	φ0.65	φ0.55	φ0.45	-
28 to 31	-	φ0.45	φ0.55	φ0.45	φ0.45	-

3.2.4. WALLS

The walls that compose the different cores possess different thicknesses that vary with the position of these walls. Thus the lateral left and right cores are constituted by internal and external walls while the

central outer and inner cores (or high-rise and low-rise) are divided into walls in the longitudinal x direction and in the transversal y direction of the building represented in figure 3.5. These two axis will later be related to the reference system of the numerical model.

A variation with height of some of these walls, specifically between the above and underground floors, is also noticeable.

In table 3.3, apart from the walls mentioned above, a description is made of the thicknesses of the foundation walls and the thickness of the walls of the service elevator connecting the underground floors and the first two above ground floors.

Table 3.3 – Wall Thickness

Floor	Thickness (m)								Found. walls	Service elevator
	Left core		Right core		High rise core		Low rise core			
	Internal walls	External walls	Internal walls	External walls	x walls	y walls	x walls	y walls		
Found. to -3	0.5	0.6	0.5	0.6	0.6 or 0.5	0.8 or 0.3	0.95 or 1.1	0.3 or 0.2	0.3 or 0.5	0.3
-2	0.5	0.6	0.5	0.6	0.6 or 0.5	0.8 or 0.3	0.95 or 1.2	0.3	0.3 or 0.5	0.3
-1	0.5	0.6	0.5	0.6	0.6 or 0.5	0.3	0.25 or 0.5	0.25 or 0.3	0.3 or 0.5	0.3
0 to 1	0.5	0.55 or 0.5 or 0.3	0.5	0.55 or 0.5 or 0.3	0.5	0.3	0.25 or 0.4	0.2 or 0.3	-	0.3
2 to 13	0.5	0.55 or 0.5 or 0.3	0.5	0.55 or 0.5 or 0.3	0.5	0.3	0.25 or 0.4	0.2 or 0.3	-	-
14	0.5	0.55 or 0.5 or 0.3	0.5	0.55 or 0.5 or 0.3	0.5	0.3	0.05	0.05	-	-
15 to 31	0.5	0.55 or 0.5 or 0.3	0.5	0.55 or 0.5 or 0.3	0.5	0.3	-	-	-	-

3.2.5. SLABS

Table 3.4, contains the various thicknesses of the slabs which compose the different floors. Every floor of the structure is composed at least by two different thicknesses, a result of the different thickness adopted for the circular part of the slab.

In the same way as in the case of the columns, and in order to differentiate the various slabs, different zones were considered. The current part of the floor plan, common to every floor, will contain the “normal slabs”. The slabs within the circular part of the building will be known as “circular slabs”. The “retail slabs” constitute the part of the floor that serves as the reception for services and commercial area in the first two floors. The slabs closer to the side of the park from the foundation mat to floor 0 are known as “park slabs”.

Finally, in order to prevent a shear failure of the slabs around the columns, different column drops were adopted.

Table 3.4 – Slab Thickness

Floor	Thickness (m)				
	Normal Slabs	Retail slabs	Park slabs	Circular slabs	Column drops
Foundation	2.20	2.20 or 0.85 or 0.80 or 0.50	0.85 or 1.40	2.20	-
-3 to -1	0.25	0.40	0.40	0.265	-
0	0.225	0.40	0.50	0.265	-
1 to 2	0.25	0.40	-	0.265	0.475
3 to 29	0.225	-	-	0.265	0.45
30 to roof	0.25	-	-	0.265	0.475

3.2.6. SPIRE

The spire connected to the penultimate floor of Tower A is a steel structure with a first story made in reinforced concrete. This steel structure has a height of 85.765 m and was placed at the top of Tower A with the help of a helicopter.

Tables 3.5 and 3.6 contain, respectively, the vertical and horizontal dimensions of this steel structure.

Table 3.5 – Interstory and height of the spire

Spire Floor	Building Floor	Interstory height (m)	Total height	Height from ground (m)	Height from the connection floor (m)
1	32	4.075	268,510	139.010	5.300
2	33	4.075	272,585	143.085	9.375
3	34	4.075	276,660	147.160	13.450

4	35	4.075	280,735	151.235	17.525
5	36	4.075	284,810	155.310	21.600
6	37	4.075	288,885	159.385	25.675
7	38	4.075	292,960	163.460	29.750
8	39	4.075	297,035	167.535	33.825
9	40	4.075	301,110	171.610	37.900
10	41	4.075	305,185	175.685	41.975
11	42	4.075	309,260	179.760	46.050
12	43	4.075	313,335	183.835	50.125
13	44	4.075	317,410	187.910	54.200
14	45	4.075	321,485	191.985	58.275
15	46	4.075	325,560	196.060	62.350
16	47	4.075	329,635	200.135	66.425
17	48	4.075	333,710	204.210	70.500
18	49	4.075	337,785	208.285	74.575
19	50	7.115	341,860	212.360	78.650
Top	-	-	348,975	219.475	85.765

Table 3.6 – Horizontal dimensions

Spire Floor	Building Floor	X direction (m)	Y direction (m)
1	32	9.930	9.459
2	33	7.581	7.581
3 to 5	34 to 36	7.285	7.285
6	37	7.285	5.121
7	38	7.285	4.802
8 to 9	39 to 40	4.802	5.070
10 to 13	41 to 44	2.754	2.754
14	45	2.501	2.096
15 to 16	46 to 47	1.360	1.360
17 to 19	48 to 50	-	-

3.2.7. FACADE

The facade of Tower A is materialized by a continuous double skin glass wall in which the inner glass skin is directly supported by the different floors while the outer one is fixed on the floor’s edge. The two glass skins are separated by a gap in which air flows, leading to a better control of heating and cooling conditions inside the building and hence to an energy saving.

3.2.8. MATERIALS

The structure of Tower A is construed in reinforced concrete with the mechanical characteristics of the concrete given by Part 1 of Eurocode 2 [25], which are shown in the table 3.7.

The spire in turn is construed in galvanized steel S355 J2 (ex Fe510 grade D) according to UNI EN 10025.

Table 3.7 – Proprieties of concrete

Elements	f_{ck} (MPa)	E (GPa)	ρ (kN/m ³)
Foundation	35	32	25
Slab	55	36	25
	45 from level 117.95 to level 129.50	34	
Walls	55 from level 129.50 to level 146.52	36	25
	45 from level 146.52 to level 268.51	34	
Columns	45 from level 117.95 to level 129.50	34	25
	75 from level 129.50 to level 268.51	39	

3.3. STATIC LOADS

3.3.1. TOWER

The static loads applied to the tower are its self-weight (SW), superimposed dead loads (DL), the facade weight, live loads on the floors (LL), live loads on the stairs and snow loads.

3.3.1.1. Self-Weight

The self-weight is calculated taking into account the volumic weight of the different materials that compose a structure and their respective dimensions. Since the tower part of the building is a reinforced concrete structure, the volumic weight of its elements is $\rho=25$ kN/m³. The self-weight of the slabs is applied on the structure as a pressure load (kN/m²).

3.3.1.2. Superimposed dead loads

The superimposed dead loads applied on the building are a result of the layers of different materials that compose the non-structural part of the floors. Thus, the “normal slabs”, “retail slabs” and “circular slabs” defined before and the “park slabs” belonging to the underground floors have to withstand a

superimposed dead load of 2 kN/m^2 , the same that was also considered for the dead loads applied on the stairs.

The “park slab” of floor 0 is located on the outside of the tower and is thereby accessible to everyone. The different non-structural materials that compose this slab leads to a superimposed dead load of 8 kN/m^2 .

3.3.1.3. Facade Weight

The facade applied on Tower A as a weight of 0.75 kN/m^2 which is applied on the boundary of the floors as a uniform distributed load with a value equal to $0.75Ih_i$, where Ih_i is the interstory height of floor i .

3.3.1.4. Live Loads

The floor live loads and the stairs live loads were adopted taking into account Part 1 of Eurocode 1 and the respective Italian National Annex. The values of the different live loads were adopted accordingly to the different uses of each floor.

3.3.1.5. Snow Loads

The snow loads were adopted taking into account Part 3 of Eurocode and considering the accumulation on the facade and on the roof of the tower.

The values of the different static loads applied to the tower are shown in table 3.8

Table 3.8 – Static loads applied on the tower

Floor	Use	SW (kN/m^2)	DL (kN/m^2)	LL (kN/m^2)	Facade (kN/m^2)	Snow (kN/m^2)
		$h_{\text{slab}}=2.20$				
		$h_{\text{slab}}=1.40$				
Foundation	Archive	$h_{\text{slab}}=0.85$	2	6	-	-
		$h_{\text{slab}}=0.80$				
		$h_{\text{slab}}=0.50$				
		$h_{\text{slab}}=0.40$				
-3	Garbage	$h_{\text{slab}}=0.265$	2	7.5	-	-
		$h_{\text{slab}}=0.25$				
		$h_{\text{slab}}=0.40$				
-2 to -1	Archive	$h_{\text{slab}}=0.265$	2	6	-	-
		$h_{\text{slab}}=0.25$				
		$h_{\text{slab}}=0.40$				
0	Retail	$h_{\text{slab}}=0.50$	2	4	0.75	-
	Piazza	$h_{\text{slab}}=0.40$	8	10		

		$h_{slab}=0.265$				
		$h_{slab}=0.25$				
1	Mechanical	$h_{slab}=0.40$	2	7.5	0.75	-
	Retail	$h_{slab}=0.265$	2	4		
		$h_{slab}=0.25$				
2	G. Interest	$h_{slab}=0.40$	2	5	0.75	2.724
	Retail	$h_{slab}=0.265$	2	4		
		$h_{slab}=0.25$				
3 to 11	Office	$h_{slab}=0.265$	2	3	0.75	-
		$h_{slab}=0.25$				
12	G. Interest	$h_{slab}=0.265$	2	5	0.75	-
		$h_{slab}=0.25$				
13 to 29	Office	$h_{slab}=0.265$	2	3	0.75	-
		$h_{slab}=0.25$				
30	G. Interest	$h_{slab}=0.265$	2	5	0.75	-
		$h_{slab}=0.25$				
31	Mechanical	$h_{slab}=0.265$	2	7.5	0.75	-
		$h_{slab}=0.25$				
Roof	Mechanical	$h_{slab}=0.265$	2	7.5	0.75	2.778
		$h_{slab}=0.25$				

3.3.2. SPIRE

Apart from the self-weight of the elements that compose the spire, the floor grill and the live loads are applied on all the horizontal elements as uniform loads. The facade weight, which is composed by both glass walls and metallic meshes, and the snow loads are applied on the horizontal external elements of each floor.

Table 3.9 shows the different loads applied to the spire.

Table 3.9 – Static loads applied on the spire

Load	Load value (kN/m ²)
Floor grill (Dead Load)	1.25
Facade metallic mesh (Dead Load)	0.23
Façade glass wall (Dead Load)	0.64
Live Load	1.00
Snow	0.10

4

Application of EN 1991-1-4 and Wind Tunnel Tests The Unicredit High-Rise Building

4.1. INTRODUCTION

Structural engineers can obtain wind load information from either different codes or standards, wind tunnel tests, proven and/or properly validated numerical methods and appropriate full-scale data. This chapter focuses on wind loads obtained through the first two methods mentioned above.

Wind loads obtained through codes or standards constitutes a relatively recent method which has achieved a wide acceptance, becoming so common that it is often the only source of information, regarding wind loading calculations, used by many practicing structural engineers. These codes are based on extensive research but constitute however simplified models of wind loading, leading to an analysis that can sometimes lacks in accuracy.

The growing necessity for world trade has been reducing the number of loading standards such as in the case of the different codes used in many European countries which were harmonized into a single code. The main codes currently in use are the, EN 1991-1-4 – Wind Actions [26], ASCE 07-05 – Minimum Design Loads for Buildings and Other Structures [27], the AIJ Recommendations for Loads on Buildings [28], the Australian Standard AS1170.2 – Structural Design Actions – Wind Actions [29] and the British Standard Loading for Buildings – Part 2 – Code of Practice for Wind Loads [30].

Due to the simplified models used in the codes and standards and to many limitations of their applicability in buildings and other structures with less common characteristics, shapes or dimensions that are not covered by the code's rules, the loads estimated can lead to situations in which the real load will sometimes be higher, thus leading to safety hazards, or lower, leading in this case to a non-optimized design and hence to an increased cost of the structure.

Although the most accurate measurements for determining wind loads will be those made on full-scale structures, the most appropriate is the one that uses model tests in a wind tunnel.

Wind tunnel tests are believed to be used since 1893 (Kernot) and are currently used not only for investigations that constitute the basis for the rules in different codes but also to determine the wind loads on structures that are not covered by them. In order to obtain a good estimation of the wind loads on a structure through wind tunnel testing, different requirements such as a good simulation of the natural wind flow and a good modeling of the structure through a dimensional analysis must be fulfilled. This and other aspects of wind tunnel testing are dealt with below [11, 14].

4.2. EUROCODE

The origin of Eurocodes goes back to 1975 when the Commission of the European Community developed a program in the field of construction in order to eliminate technical obstacles and to harmonize technical rules for the design of construction works. The first generation of Eurocodes appeared in the 1980's after a development program that took fifteen years.

Eurocodes provide common structural rules to be applied in the project of current structures and their respective components and consist of the full text of the Eurocode, which may include any annexes. The full text can be preceded by a National title page and National forward, and may be followed by a National annex which only contains information on the parameters which were left open for national choice and which are to be used for the design of buildings and civil engineering works to be developed in the country concerned [26, 31].

4.2.1. GENERAL

The main objective of EN 1991 1-4, Eurocode: Actions on Structures – General Actions – Part 1-4: Wind Actions, in its particular case, is to provide guidelines for the determination of natural wind actions for the structural design of buildings and other civil engineering works for the whole structure, parts of it or elements attached to the structures such as components, cladding units, safety and noise barriers.

Part 1-4 can be applied to buildings and civil engineering works with heights up to 200 m and bridges having no span greater than 200 m.

The modification of the effects of the wind due to other actions such as snow, traffic or ice as well as the changes to the structure during the stages of execution should be taken into account.

Wind actions obtained through EN 1991-1-4 are characteristic values determined from the basic values of wind velocity with an annual probability of exceedence of 0.02 corresponding to a 50 year return period and can be represented by a set of pressures or forces whose effects are equivalent to the extreme effects of the turbulent wind.

The response of the structure depends on its size, shape and dynamic characteristics. Part 1-4 covers dynamic response due to along-wind turbulence in resonance with the respective along-wind vibrations of a fundamental flexure mode shape but it does not give guidance to specific cases where more than the fundamental mode of vibration needs to be considered for the correct analysis of its dynamic behavior. The response should be calculated from the peak velocity pressure to the reference height in the undisturbed wind field, the force and pressure coefficients and the structural coefficient $c_s c_d$.

4.2.2. WIND VELOCITY

As seen on Chapter 2, wind velocity is composed by a mean and a fluctuating component.

The EN 1991-1-4 uses the basic wind velocity v_b to determine the mean wind velocity v_m and the turbulence intensity to represent the fluctuating component of the wind.

4.2.2.1. Mean Wind

The basic wind velocity corresponds to the fundamental basic wind velocity $v_{b,0}$ affected by the directional and seasonal factors c_{dir} and c_{season} respectively and can thus be calculated by

$$v_b = c_{dir} \cdot c_{season} \cdot v_{b,0} \quad (4.1)$$

$v_{b,0}$, known as the fundamental basic wind velocity, is the parameter that characterizes the geographical variation of strong winds in a standard position and is defined by the EN 1991-1-4 as “the characteristic 10 minute mean wind velocity, irrespective of wind direction and time of year, at 10 m above ground level in open country terrain with low vegetation such as grass and isolated obstacles with separations of at least 20 obstacle heights”. This terrain is known in Part 1-4 as a category II terrain. The values of $v_{b,0}$ are given in the respective National Annexes and the recommended value for c_{dir} and c_{season} is 1.

If a different return period (from that mentioned in 4.2.1) and thus a different probability p for an annual exceedence is considered the respective 10 minutes mean wind velocity can be obtained by multiplying the basic wind velocity, v_b , by the probability factor c_{prob} given below

$$c_{prob} = \left(\frac{1 - K \cdot \ln(-\ln(1 - p))}{1 - K \cdot \ln(-\ln(0.98))} \right)^n \quad (4.2)$$

where K is the shape parameter depending on the coefficient of variation of the extreme-value distribution and has a recommended value of 0.2. n is the exponent with a recommended value of 0.5.

The variation with height of the mean wind velocity $v_m(z)$ at a height z above the terrain is given on Eurocode by the following expression

$$v_m(z) = c_r(z) \cdot c_0(z) \cdot v_b \quad (4.3)$$

where $c_r(z)$ and $c_0(z)$ are the roughness and orography factors respectively, which translate the dependence of the variation with height of the mean wind velocity upon the terrain roughness and orography.

The roughness factor $c_r(z)$ takes into account the height above ground level and the ground roughness of the terrain upwind of the structure in the wind direction considered and is given by

$$c_r(z) = k_r \cdot \ln\left(\frac{z}{z_0}\right) \text{ for } z_{min} \leq z \leq z_{max} \quad (4.4)$$

$$c_r(z) = c_r(z_{min}) \text{ for } z \leq z_{min} \quad (4.5)$$

where z_0 is the roughness length, $k_r = 0.19 \left(\frac{z_0}{z_{0,II}}\right)^{0.07}$ is the terrain factor depending on the roughness length z_0 , $z_{0,II}$ is the roughness length for a category II terrain. z_{max} is to be taken as 200m, unless otherwise stated in the National Annex and z_{min} is given on table 4.1.

Analyzing equation 4.3 one can conclude that it is based on the logarithmic velocity profile mentioned in Chapter 2.

Table 4.1 – Terrain category defined by EN 1991-1-4 [26]

Terrain Category	z_0 (m)	z_{min} (m)
0 Sea or costal area exposed to the open sea	0.003	1
I Lakes or flat and horizontal area with negligible vegetation and without obstacles	0.01	1

II Area with low vegetation such as grass and isolated obstacles (trees, buildings) with separation of at least 20 obstacle heights	0.05	2
III Area with regular cover of vegetation or building or with isolated obstacles with separations of maximum 20 obstacles heights (such as villages, suburban terrain or permanent forest)	0.3	5
IV Area in which at least 15% of the surface is covered with buildings and their average height exceeds 15m	1.0	10

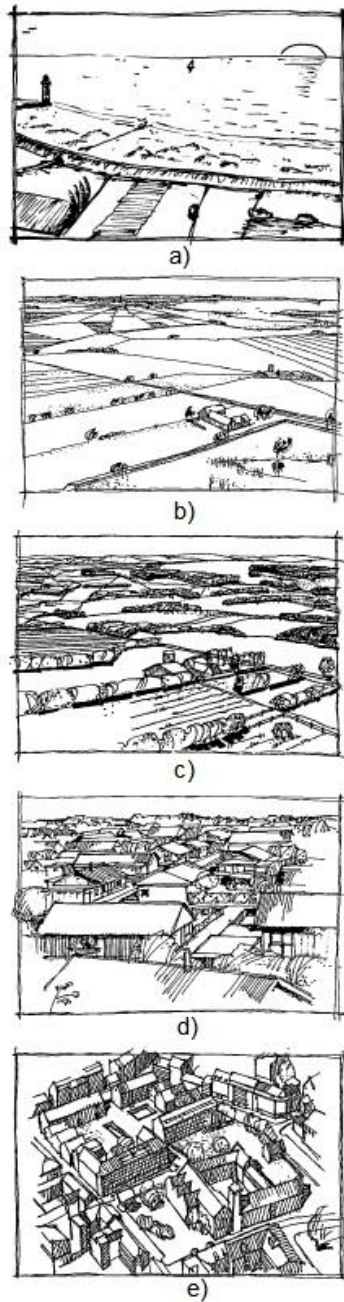


Figure 4.1 – Terrain roughness illustration, a) Terrain category 0, b) Terrain category I, c) Terrain category II, d) Terrain category III, e) Terrain category IV [26]

The effects of changes of roughness shown in Chapter 2 are also considered by the Eurocode. For a certain direction of wind, the terrain roughness to be considered depends on the ground roughness and on the upstream distance with uniform terrain roughness (given in Annex A.2) within a limited angular sector around the considered direction.

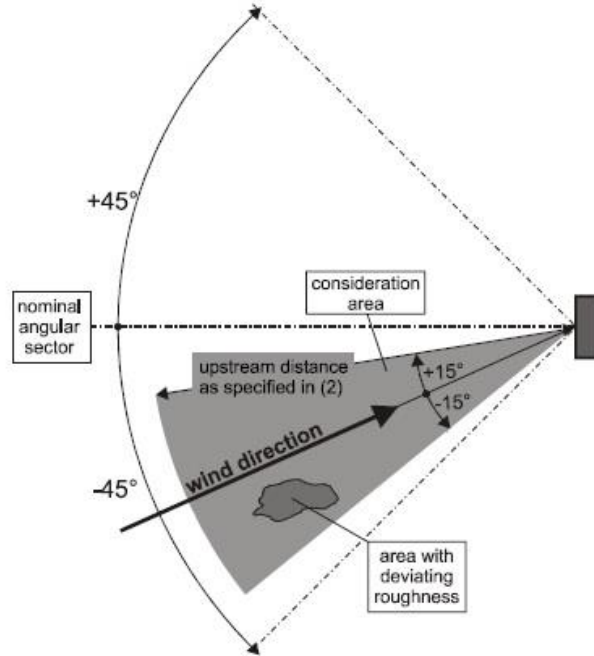


Figure 4.2 – Schematic representation of angular sector and upstream distance recommended by EN 1991-1-4 [26]

The Eurocode recommends that for a pressure or force coefficient defined for a nominal angular sector, the lowest roughness length within any 30° angular wind sector should be used. Furthermore, when there is the possibility to choose between two or more terrain categories within the “consideration area” shown on figure 4.2, the area with the lowest roughness should be used.

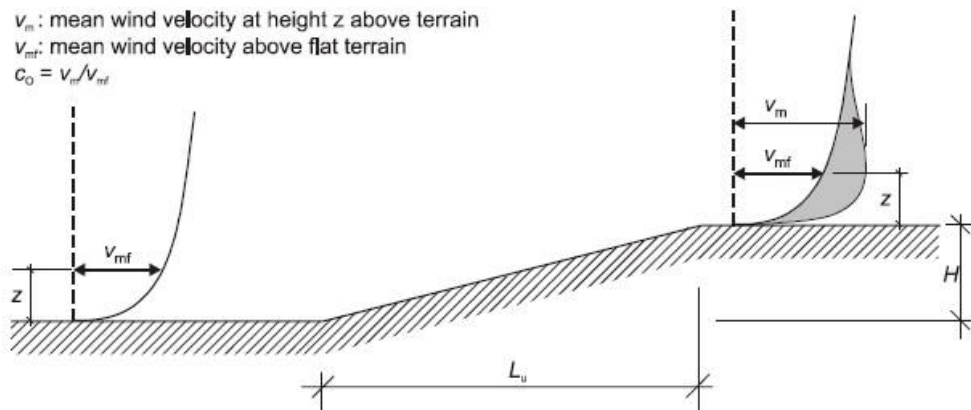


Figure 4.3 – Schematic representation of the effect of orography on wind velocity [26]

The effects of orography, schematically represented on figure 4.3, can be neglected if the increase of wind velocity due to hills, cliffs and other orographic elements is limited to 5% and if the average slope of the upwind terrain is less than 3°, the recommended value is 1. For the cases in which these conditions are not observed, the orography factor should be determined through the National Annex and Annex A.3 of EN 1991-1-4.

As seen before, a group of closely spaced obstacles makes the flow rise. This effect can be taken into account by considering the displacement height h_{dis} given in the National Annex.

Considering the recommendations made by the Eurocode regarding the different parameters which characterize the mean wind speed and the characteristics of Tower A exposed in Chapter 3 the following values are obtained.

For the specific case of Milan (Lombardia, Zone 1 from the Italian National Annex, tables 4.2 and 4.3 and figure 4.4), the fundamental basic wind velocity is $v_{b,0,Milan} = \bar{v}_{b,0} = 25m/s$ since $a_s \leq a_0$, where a_s is the height above sea level of the site.

Table 4.2 – Zoning of the fundamental basic wind velocity [32]

Zone	Description	$\bar{v}_{b,0}$	a_0
1	Valle d'Aosta, Piemonte, Lombardia, Trentino Alto Adige, Veneto, Friuli Venezia Giulia (except the province of Trieste)	25	1000
2	Emilia Romagna	25	750
3	Toscana, Marche, Umbria, Lazio, Abruzzo, Molise, Campania, Puglia, Basilicata, Calabria (except the province of Reggio Calabria)	27	500
4	Sicilia and the province of Reggio Calabria	28	500
5	Sardegna (region to the east of the theoretical line that connects Capo Teulada to l'isola della Meaddalena)	28	750
6	Sardegna (region to the west of the theoretical line that connects Capo Teulada to l'isola della Meaddalena)	28	500
7	Liguria	28	1000
8	Province of Trieste	30	1500
9	Islands (except Sicilia and Sardegna) and open sea	31	500

Following the recommendation of the National Annex, $c_{dir} = 1$ and $c_{season} = 1$ and thus

$$v_b = c_{dir} \cdot c_{season} \cdot v_{b,0} = 1 * 1 * 25 = 25m/s \quad (4.6)$$

Tower A is located in an urban center, corresponding to a category V terrain according to the Italian National Annex (table 4.3), where the corresponding values of z_0 and z_{min} are 0.7 m and 12 m respectively and thus

$$k_r = 0.19 \left(\frac{z_0}{z_{0,II}} \right)^{0.07} = 0.19 \left(\frac{0.7}{0.05} \right)^{0.07} = 0.23 \quad (4.7)$$

Table 4.3 – Categories of exposure of the site [32]

Category of exposure	k_r	z_0 (m)	z_{min} (m)
I	0.17	0.01	2
II	0.19	0.05	4
III	0.20	0.10	5
IV	0.22	0.30	8
V	0.23	0.70	12

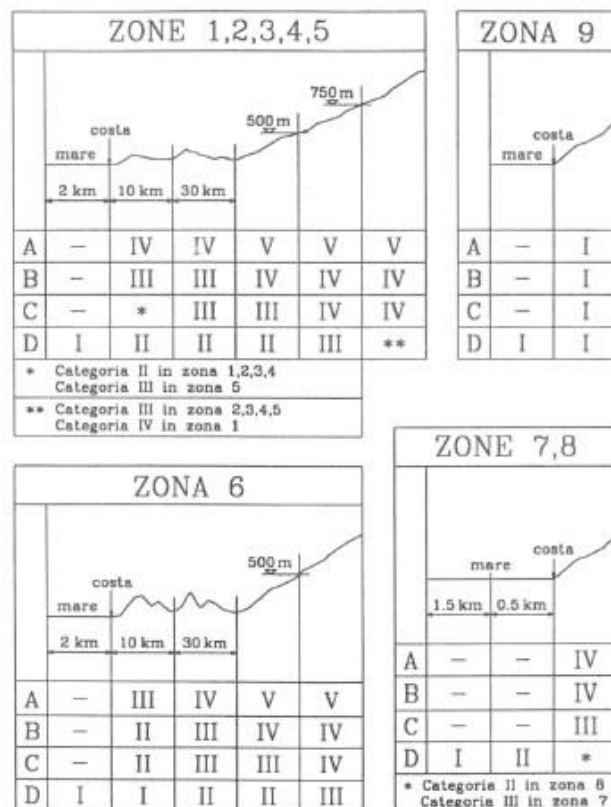


Figure 4.4 – Categories of exposure as a function of the geographic position of the site [32]

Adopting the recommended value for the orography factor $c_0(z) = 1$.

$$v_m(z) = c_r(z) \cdot c_0(z) \cdot v_b = 0.23 \ln\left(\frac{z}{1}\right) * 1 * 25 \quad (4.8)$$

For the analysis through the Eurocode and in order to compare the results between the latter and the wind tunnel test where a reference height of $z = 140 \text{ m}$ was considered, this same height will be considered for the current analysis. This approximation does not constitute a significant error since the height of the facade of the building is variable and thus in some points it is slightly higher than 140 and in others it is somewhat smaller.

$$c_r(z) = 0.23 \ln\left(\frac{140}{0.7}\right) = 1.21 \quad (4.9)$$

$$v_m(z) = 0.23 \ln\left(\frac{140}{0.7}\right) * 1 * 25 = 30.27 \text{ m/s} \quad (4.10)$$

4.2.2.2. Wind Turbulence

On Chapter 2 the turbulence intensity at some height z , $I_v(z)$ was defined as the ratio of the standard deviation of the turbulence to the mean wind velocity.

The recommended expressions given by the Eurocode to calculate $I_v(z)$ are

$$I_v(z) = \frac{\sigma_v}{v_m(z)} = \frac{k_l}{c_0(z) \cdot \ln\left(\frac{z}{z_0}\right)} \text{ for } z_{min} \leq z \leq z_{max} \quad (4.11)$$

$$I_v(z) = I_v(z_{min}) \text{ for } z < z_{min} \quad (4.12)$$

where σ_v is the standard deviation, k_l is the turbulence factor given in the National Annex, and $c_0(z)$ and z_0 are, respectively, the orography factor and the roughness length defined in 4.2.2.1.

For the specific case of Italy, the recommended value of k_l is 1 and thus for the height of Tower A

$$I_v(z) = \frac{k_l}{c_0(z) \cdot \ln\left(\frac{z}{z_0}\right)} = \frac{1}{1 * \ln\left(\frac{140}{0.7}\right)} = 0.1887 \quad (4.13)$$

4.2.2.3. Peak Velocity Pressure

The recommended expression to determine the peak velocity pressure $q_p(z)$ at a height z is given by

$$q_p(z) = [1 + 7 \cdot I_v(z)] \cdot \frac{1}{2} \cdot \rho \cdot v_m^2(z) = c_e(z) \cdot q_b \quad (4.14)$$

where ρ is the air density which depends on the altitude, temperature and barometric pressure and has a recommended value of 1.25 kg/m^3 . The value 7 is based on a peak factor of 3.5.

$c_e(z)$ is the exposure factor expressed by

$$c_e(z) = \frac{q_p(z)}{q_b} \quad (4.15)$$

q_b is the basic velocity pressure and can be calculated through

$$q_b = \frac{1}{2} \cdot \rho \cdot v_b^2 \quad (4.16)$$

Unlike older codes, EN 1991-1-4 does not provide gust velocities, which would need to be converted to dynamic pressures for equivalent static design of structure, but instead gives the gust dynamic pressure known in the Eurocode as the peak velocity pressure $q_p(z)$.

Considering the values obtained for $I_v(z)$ and $v_m(z)$ for z equal to the height of the building.

$$q_p(z) = [1 + 7 \cdot I_v(z)] \cdot \frac{1}{2} \cdot \rho \cdot v_m^2(z) = \left[1 + 7 \frac{1}{1 \cdot \ln\left(\frac{140}{0.7}\right)}\right] * \frac{1}{2} * 1.25 * 30.27^2 \quad (4.17)$$

$$q_p(z) = 1329.56 \text{ N/m}^2$$

4.2.3. WIND ACTIONS

For the determination of wind actions on structures and structural elements, both external and internal wind pressures should be taken into account. According to EN 1991-1-4, the resultant net pressure on a

wall, roof or element is the difference between the pressures on the opposite surfaces, taking into account their respective signals, where the pressure directed towards the surface is taken as positive, and suction, directed away from the surface is considered to be negative, as shown on figure 4.5.

The external wind pressure, w_e , can be determined by the expression

$$w_e = q_p(z_e) \cdot c_{pe} \quad (4.18)$$

where $q_p(z_e)$ is the peak velocity pressure, z_e is the reference height for the external pressure and c_{pe} is the pressure coefficient for the external pressure.

The internal wind pressure, w_i , is given by

$$w_i = q_p(z_i) \cdot c_{pi} \quad (4.19)$$

where $q_p(z_i)$ is the peak velocity pressure, z_i is the reference height for the internal pressure and c_{pi} is the pressure coefficient for the external pressure.

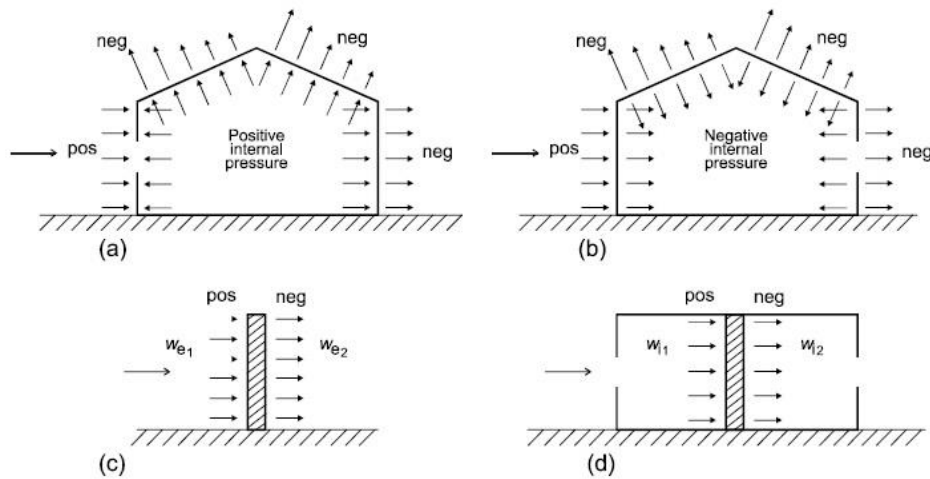


Figure 4.5 – Schematic representation of positive and negative pressures according to EN 1991-1-4 [26]

4.2.4. PRESSURE COEFFICIENTS

Different structures have different appropriate aerodynamic coefficients. For the specific case of buildings, the most appropriate is the pressure coefficient.

As seen before, external and internal wind pressures should be considered and thus so external pressure coefficients and internal pressure coefficients. Furthermore, EN 1991-1-4 divides the external pressure coefficients into local and overall coefficients which depend on the size of the loaded area A which corresponds to the area of the structure that produces the wind action in the section to be calculated.

Overall coefficients, $c_{pe,10}$ give the pressure coefficients for loaded areas of 10 m^2 or more, while local coefficients, $c_{pe,1}$ give the pressure coefficients for loaded areas up to 1 m^2 and thus are intended for the design of small elements.

For areas between 1 m^2 and 10 m^2 , the external pressure coefficient c_{pe} may be determined, according to Eurocode, by

$$c_{pe} = c_{pe,1} - (c_{pe,1} - c_{pe,10}) \log A \quad (4.20)$$

which can be schematically represented by

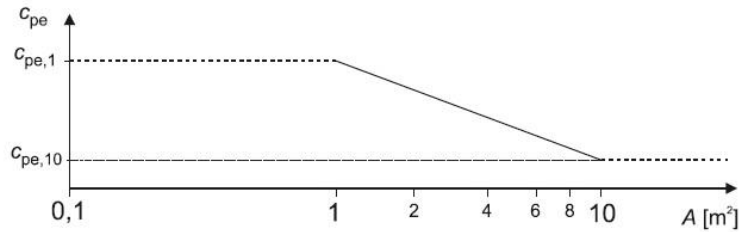


Figure 4.6 – External pressure coefficient c_{pe} [26]

4.2.4.1. Vertical walls of rectangular plan buildings

Depending on the aspect ratio $\frac{h}{b}$, a wall of a building can be divided into different parts, each one with a respective reference height, z_e , corresponding to different velocity pressures which will form the profile of velocity pressure acting on the wall.

If a building has a height h smaller than its side b , then the building should be considered as one part.

For a building with a height h greater than b , but smaller than $2b$ it may be considered to be divided into two parts where the lower one extends upwards from the ground up to height equal to b and the upper part extends from that same height b to the top of the building.

In the case of a building with a height h greater than $2b$ a division in multiple parts may be considered. This division consists of a lower part which extends from the ground up to a height equal to b , an upper part extending downwards from the top by a height equal to b . The resulting middle region may be divided into horizontal parts with a height h_{strip} . The different scenarios are shown in figure 4.7.

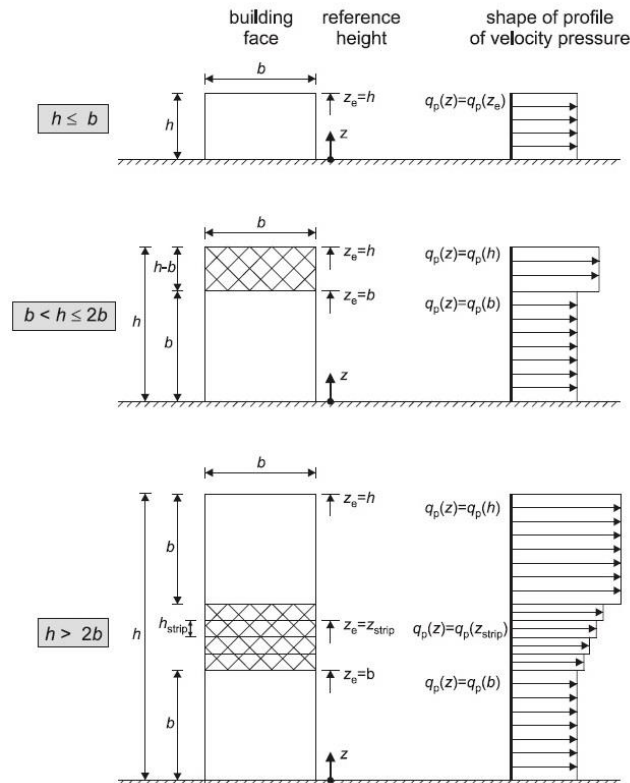


Figure 4.7 – Velocity pressure profile and reference height z_e [26]

Figure 4.8 shows the division of a building into its windward, leeward and side walls corresponding to zones D, E and A,B and C, where the last three correspond to the division of the side walls into smaller zones.

The recommended values of $c_{pe,1}$ and $c_{pe,10}$ are given in table 4.2, depending on the ratio h/d . If intermediate values of h/d are obtained, linear interpolation may be applied.

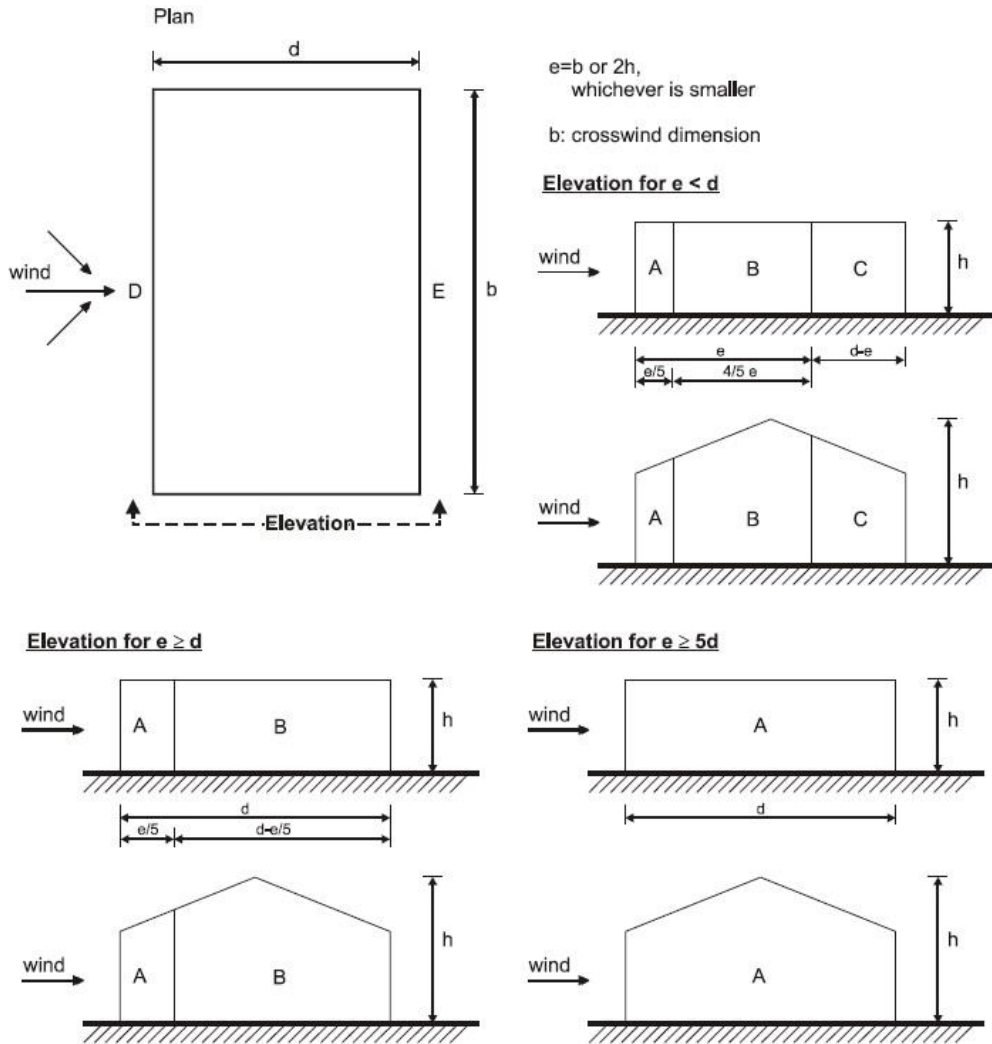


Figure 4.8 – Vertical wall division [26]

Table 4.2 – Recommended values of $c_{pe,1}$ and $c_{pe,10}$ for vertical walls of rectangular plan buildings

Zone	A		B		C		D		E	
h/d	$c_{pe,10}$	$c_{pe,1}$								
5	-1.2	-1.4	-0.8	-1.1	-0.5	+0.8	+1.0	-0.7		
1	-1.2	-1.4	-0.8	-1.1	-0.5	+0.8	+1.0	-0.5		
≤ 0.25	-1.2	-1.4	-0.8	-1.1	-0.5	+0.7	+1.0	-0.3		

In order to determine the wind loads on Tower A through EN 1991-1-4 the plan of the building will be considered as a rectangle with dimensions 18x73.9. Two main directions corresponding to the axes X and Y represented in figure 3.5 will be considered.

The only external coefficient that is of interest for the analysis is the overall coefficient $c_{pe,10}$ since there weren't obtained any areas smaller than 10 m².

Beginning by the analysis of direction Y , the first step is to identify the division of the building according to figure 4.8.

The corresponding dimensions for the wind action along the Y axis direction are $h=140$ m, $b=73.9$ m and $d=18$ m.

EN 1991-1-4 states that

$$e = \min\{b; 2h\} \tag{4.21}$$

$$e = \min\{73.9; 280\} = 73.9 \text{ m} \tag{4.22}$$

For $e \geq d$, the sidewall of the building is divided into two different zones A and B.

$\frac{h}{d} = 7.78 > 5$ and thus the overall pressure coefficients to be used are given in table 4.3

Table 4.3 - $c_{pe,10}$ values for $\frac{h}{d} = 7.78$

Zone	A	B	D	E
$c_{pe,10}$	-1.2	-0.8	+0.8	-0.7

Considering figure 4.7 the vertical walls will be divided into two parts since $b \leq h < 2b$.

The values that will constitute the profile of velocity pressure will correspond, according to the rules related in figure 4.7, to the velocity at the height of the building $z_{sup} = 140$ m and to an inferior height $z_{inf} = 73.9$ m.

The values for z_{sup} were calculated in equation (4.10), (4.13) and (4.17)

$$v_m(z_{sup}) = 30.27 \text{ m/s}$$

$$I_v(z_{sup}) = 0.1887$$

$$q_p(z_{sup}) = 1329.56 \text{ N/m}^2$$

The values corresponding to z_{inf} are

$$v_m(z_{inf}) = 0.19 \left(\frac{0.7}{0.05}\right)^{0.07} \ln\left(\frac{73.9}{0.7}\right) * 1 * 25 = 26.62 \text{ m/s} \tag{4.23}$$

$$I_v(z_{inf}) = \frac{1}{1 * \ln\left(\frac{73.9}{0.7}\right)} = 0.2146 \tag{4.24}$$

$$q_p(z_{inf}) = \left[1 + 7 \frac{1}{1. \ln\left(\frac{73.9}{0.7}\right)} \right] * \frac{1}{2} * 1.25 * 26.62^2 = 1108.48 \text{ N/m}^2 \quad (4.25)$$

Once the values for direction Y are obtained, the values for the direction X can be determined following the same procedure.

The dimensions to be considered for the wind action along the X axis direction are $h=140$ m, $b=18$ m and $d=73.9$ m leading to

$$e = \min\{b; 2h\}$$

$$e = \min\{18; 280\} = 18 \text{ m} \quad (4.26)$$

For $e < d$, the sidewall of the building is divided into three different zones A, B and C.

Since $\frac{h}{d} = 1.894$ it will be necessary to proceed to a linear interpolation of the values given in table 4.4 in order to obtain the overall pressure coefficients $c_{pe,10}$.

Table 4.4 - $c_{pe,10}$ values for $\frac{h}{d} = 1.894$ obtained by linear interpolation

Zone	A	B	C	D	E
h/d	$c_{pe,10}$	$c_{pe,10}$	$c_{pe,10}$	$c_{pe,10}$	$c_{pe,10}$
5	-1.2	-0.8	-0.5	+0.8	-0.7
1.894	-1.2	-0.8	-0.5	+0.8	-0.545
1	-1.2	-0.8	-0.5	+0.8	-0.5

Since $h > 2b$, where b is the value present in figure 4.7, the building will be divided into an upward and a downward part each with a height equal to $b=18$ and a middle part which in turn is divided in strips with height h_{strip} as stated before. The middle part has a height of $140 - 2 * 18 = 104$ m. Considering its division into 5 strips each one with a height $h_{strip} = 20.8$ m, the values of v_m , I_v and q_p for the different reference heights are given below

For $z_{sup} = 140$ m

$$v_m(z_{sup}) = 30.27 \text{ m/s}$$

$$I_v(z_{sup}) = 0.1887$$

$$q_p(z_{sup}) = 1329.56 \text{ N/m}^2$$

For $z_{inf} = 18$ m

$$v_m(z_{inf}) = 0.19 \left(\frac{0.7}{0.05}\right)^{0.07} \ln\left(\frac{18}{0.7}\right) * 1 * 25 = 18.55 \text{ m/s} \quad (4.27)$$

$$I_v(z_{inf}) = \frac{1}{1 * \ln\left(\frac{18}{0.7}\right)} = 0.308 \quad (4.28)$$

$$q_p(z_{inf}) = \left[1 + 7 \frac{1}{1. \ln\left(\frac{18}{0.7}\right)} \right] * \frac{1}{2} * 1.25 * 18.55^2 = 678.91 \text{ N/m}^2 \quad (4.29)$$

For $z_{strip1} = z_{inf} + h_{strip} = 18 + 20.8 = 38.8 \text{ m}$

$$v_m(z_{strip1}) = 0.19 \left(\frac{0.7}{0.05}\right)^{0.07} \ln\left(\frac{38.8}{0.7}\right) * 1 * 25 = 22.94 \text{ m/s} \quad (4.30)$$

$$I_v(z_{strip1}) = \frac{1}{1 * \ln\left(\frac{38.8}{0.7}\right)} = 0.2491 \quad (4.31)$$

$$q_p(z_{strip1}) = \left[1 + 7 \frac{1}{1. \ln\left(\frac{38.8}{0.7}\right)} \right] * \frac{1}{2} * 1.25 * 22.94^2 = 902.42 \text{ N/m}^2 \quad (4.32)$$

For $z_{strip2} = z_{strip1} + h_{strip} = 38.8 + 20.8 = 59.6 \text{ m}$

$$v_m(z_{strip2}) = 0.19 \left(\frac{0.7}{0.05}\right)^{0.07} \ln\left(\frac{59.6}{0.7}\right) * 1 * 25 = 25.39 \text{ m/s} \quad (4.33)$$

$$I_v(z_{strip2}) = \frac{1}{1 * \ln\left(\frac{59.6}{0.7}\right)} = 0.225 \quad (4.34)$$

$$q_p(z_{strip2}) = \left[1 + 7 \frac{1}{1. \ln\left(\frac{59.6}{0.7}\right)} \right] * \frac{1}{2} * 1.25 * 25.39^2 = 1037.82 \text{ N/m}^2 \quad (4.35)$$

For $z_{strip3} = z_{strip2} + h_{strip} = 59.6 + 20.8 = 80.4 \text{ m}$

$$v_m(z_{strip3}) = 0.19 \left(\frac{0.7}{0.05}\right)^{0.07} \ln\left(\frac{80.4}{0.7}\right) * 1 * 25 = 27.10 \text{ m/s} \quad (4.36)$$

$$I_v(z_{strip3}) = \frac{1}{1 * \ln\left(\frac{80.4}{0.7}\right)} = 0.2108 \quad (4.37)$$

$$q_p(z_{strip3}) = \left[1 + 7 \frac{1}{1. \ln\left(\frac{80.4}{0.7}\right)} \right] * \frac{1}{2} * 1.25 * 27.10^2 = 1136.7 \text{ N/m}^2 \quad (4.38)$$

For $z_{strip4} = z_{strip3} + h_{strip} = 80.4 + 20.8 = 101.2 \text{ m}$

$$v_m(z_{strip4}) = 0.19 \left(\frac{0.7}{0.05}\right)^{0.07} \ln\left(\frac{101.2}{0.7}\right) * 1 * 25 = 28.42 \text{ m/s} \quad (4.39)$$

$$I_v(z_{strip4}) = \frac{1}{1 * \ln\left(\frac{101.2}{0.7}\right)} = 0.201 \quad (4.40)$$

$$q_p(z_{strip4}) = \left[1 + 7 \frac{1}{1. \ln\left(\frac{101.2}{0.7}\right)} \right] * \frac{1}{2} * 1.25 * 28.42^2 = 1215.18 \text{ N/m}^2 \quad (4.41)$$

For $z_{strip5} = z_{strip4} + h_{strip} = 101.2 + 20.8 = 122 \text{ m}$

$$v_m(z_{strip5}) = 0.19 \left(\frac{0.7}{0.05}\right)^{0.07} \ln\left(\frac{122}{0.7}\right) * 1 * 25 = 29.49 \text{ m/s} \quad (4.42)$$

$$I_v(z_{strip5}) = \frac{1}{1 * \ln\left(\frac{101.2}{0.7}\right)} = 0.1938 \quad (4.43)$$

$$q_p(z_{strip5}) = \left[1 + 7 \frac{1}{1. \ln\left(\frac{101.2}{0.7}\right)} \right] * \frac{1}{2} * 1.25 * 29.49^2 = 1280.54 \text{ N/m}^2 \quad (4.44)$$

The two velocity pressure profiles obtained for each direction X and Y are represented in figure 4.9.

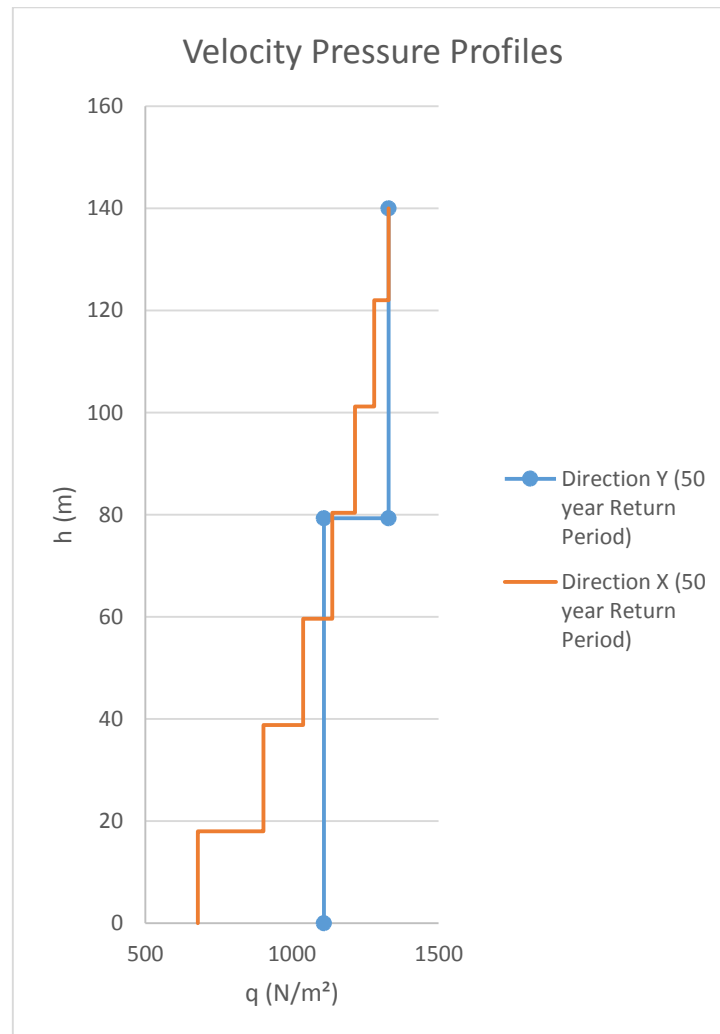


Figure 4.9 – Velocity pressure profiles for the X and Y wind directions

Considering equation (4.18) and the pressure coefficients given by tables 4.3 and 4.4, the respective absolute values of wind pressures for the windward and leeward sides for directions X and Y at the reference heights considered above are presented in table 4.5 and represented in figure 4.10 as wind pressure profiles.

Table 4.5 – Wind pressure values obtained through EN 1991-1-4

z_{ref}	Direction Y				Direction X			
	Windward		Leeward		Windward		Leeward	
	$c_{pe,10}$	$ w_e $	$c_{pe,10}$	$ w_e $	$c_{pe,10}$	$ w_e $	$c_{pe,10}$	$ w_e $
18	+0.8	886.784	-0.7	775.936	+0.8	543.128	-0.545	370.006
38.8	+0.8	886.784	-0.7	775.936	+0.8	721.937	-0.545	491.819
59.6	+0.8	886.784	-0.7	775.936	+0.8	830.265	-0.545	565.612
79.3	+0.8	886.784	-0.7	775.936	+0.8	909.360	-0.545	619.502
80.4	+0.8	1063.648	-0.7	930.692	+0.8	909.360	-0.545	619.502
101.2	+0.8	1063.648	-0.7	930.692	+0.8	972.144	-0.545	662.273
122	+0.8	1063.648	-0.7	930.692	+0.8	1024.432	-0.545	697.894
140	+0.8	1063.648	-0.7	930.692	+0.8	1063.648	-0.545	724.610



Figure 4.10 – a) Windward and Leeward pressures for the 50 year return period wind action on the X direction, b) Windward and Leeward pressures for the 50 year return period wind action on the Y direction

4.2.4.2. Internal Pressures

As seen before, the net pressure is the result of the difference between the pressures on the opposite sides of a wall, the external and internal pressures. The latter depends as stated in EN 1991-1-4 [26] “on the size and distribution of the openings in the building envelope”. Due to the advanced double skin façade installed in the building, in order to improve its energetic performance it is expected that the façade constitutes an impermeable barrier and since there are no openings in the building, these conditions lead to an internal wind pressure $w_i = 0$.

4.2.5. FRICTION COEFFICIENTS

According to EN 1991-1-4, the effects of wind friction on the surface will only have to be taken into account if the total area of all surfaces parallel or making a small angle with the wind direction, $A_{parallel}$ is over 4 times the total area of all external surfaces perpendicular to the wind $A_{perpendicular}$, both windward and leeward.

The friction forces are given by

$$F_{fr} = c_{fr} \cdot q_p(z_e) \cdot A_{fr} \tag{4.45}$$

where c_{fr} is the friction coefficient, A_{fr} is the area of external surface parallel to the wind represented in figure 4.11 and z_e is the reference height that should be taken equal to the structure height above ground.

For different surface materials. EN 1991-1-4 provides different friction coefficients.

Table 4.6 – Friction coefficients

Surface	Friction coefficient c_{fr}
Smooth (i.e. steel, smooth concrete)	0.01
Rough (i.e. rough concrete, tar-boards)	0.02
Very rough (i.e. ripples, ribs, folds)	0.04

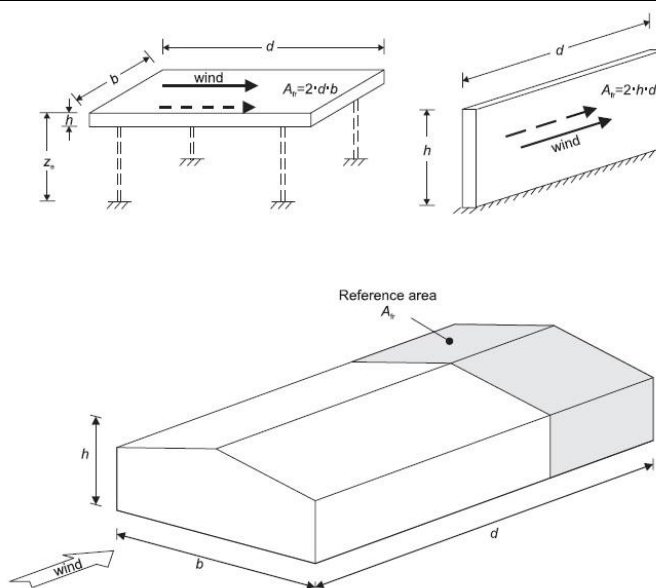


Figure 4.11 – Reference areas for the frictional component of wind [26]

According to EN 1991-1-4, friction forces should be applied on the area of the external surfaces parallel to the wind direction which is located beyond a distance, here identified as d_{fr} , from the upwind eaves or corners, equal to the minimum between $2b$ or $4h$.

For wind along the X direction

$$A_{parallel} = 2 * 73.9 * 140 + 73.9 * 18 = 22022.2 \text{ m}^2 \quad (4.46)$$

$$4 * A_{perpendicular} = 4 * (2 * 18 * 140) = 20160 \text{ m}^2 \quad (4.47)$$

For wind along the Y direction

$$A_{parallel} = 2 * 18 * 140 + 73.9 * 18 = 6370.2 \text{ m}^2 \quad (4.48)$$

$$4 * A_{perpendicular} = 4 * (2 * 73.9 * 140) = 82768 \text{ m}^2 \quad (4.49)$$

And thus the friction force should be considered only along the X direction.

$$d_{fr} = \min\{2b, 4h\} = \min\{2 * 18, 4 * 140\} = 36 \text{ m} \quad (4.50)$$

In order to take into account the effect of the friction forces on the base moment, this force will be divided into its component applied on the roof $F_{fr \text{ roof}}$ and into two parallel components applied at half the height on either side of the building $F_{fr \text{ wall}}$. Corresponding to the analogous area represented by a solid grey hatch in figure 4.10.

$$F_{fr \text{ roof}} = c_{fr} \cdot q_p(z_e) \cdot A_{fr \text{ roof}} = 0.01 * 1329.56 * (73.9 - 36) * 18 \quad (4.51)$$

$$F_{fr \text{ roof}} = 9.07 \text{ kN}$$

$$F_{fr \text{ wall}} = c_{fr} \cdot q_p(z_e) \cdot A_{fr \text{ wall}} = 0.01 * 1329.56 * (73.9 - 36) * 140 \quad (4.52)$$

$$F_{fr \text{ wall}} = 70.55 \text{ kN}$$

4.2.6. STRUCTURAL FACTOR

The structural factor is composed of a size factor c_s and a dynamic factor c_d that take into account, respectively, the non-simultaneous occurrence of peak wind pressures on a surface and is thereby a reduction factor ($c_s \leq 1$) and the effect of the vibrations of the structure due to turbulence which may lead to an increase of wind actions and is therefore an increase factor ($c_d \geq 1$).

EN 1991-1-4 presents a variety of cases in which a structure or part of it, with specific characteristics or dimensions, can be considered to have a structural factor $c_s, c_d = 1$. Among them are buildings with a height less than 15 m, façade and roof elements having a natural frequency greater than 5 Hz, framed buildings having structural walls and being less than 100 m high and with a height less than 4 times the in-wind depth and chimneys with circular cross-sections with a height less than 60 m and 6.5 times its diameter.

Tower A cannot be inserted into this specific group of structures and although the Eurocode gives a detailed procedure for the determination of the structural factor regarding structures that are not included in the group mentioned above, the application of this procedure is limited to structures corresponding to one of the shapes represented in figure 4.12, and to structures where only the along-wind vibration in the fundamental mode is significant.

The structural factor is given by

$$c_s \cdot c_d = \frac{1 + 2 \cdot k_p \cdot I_v(z_e) \cdot \sqrt{B^2 \cdot R^2}}{1 + 7 \cdot I_v(z_e)} \quad (4.53)$$

$$c_s = \frac{1 + 7 \cdot I_v(z_e) \cdot \sqrt{B^2}}{1 + 7 \cdot I_v(z_e)} \quad (4.54)$$

$$c_d = \frac{1 + 2 \cdot k_p \cdot I_v(z_e) \cdot \sqrt{B^2 + R^2}}{1 + 7 \cdot I_v(z_e) \cdot \sqrt{B^2}} \quad (4.55)$$

where z_e is the reference height presented in figure 4.12, k_p is the peak factor defined in the Eurocode as “the ratio of the maximum value of the fluctuating part of the response to its standard deviation”. I_v is the turbulence intensity, B is the background factor and R is the resonance response factor which allow, respectively, for the lack of full correlation on the structure surface and for turbulence in resonance with the vibration mode.

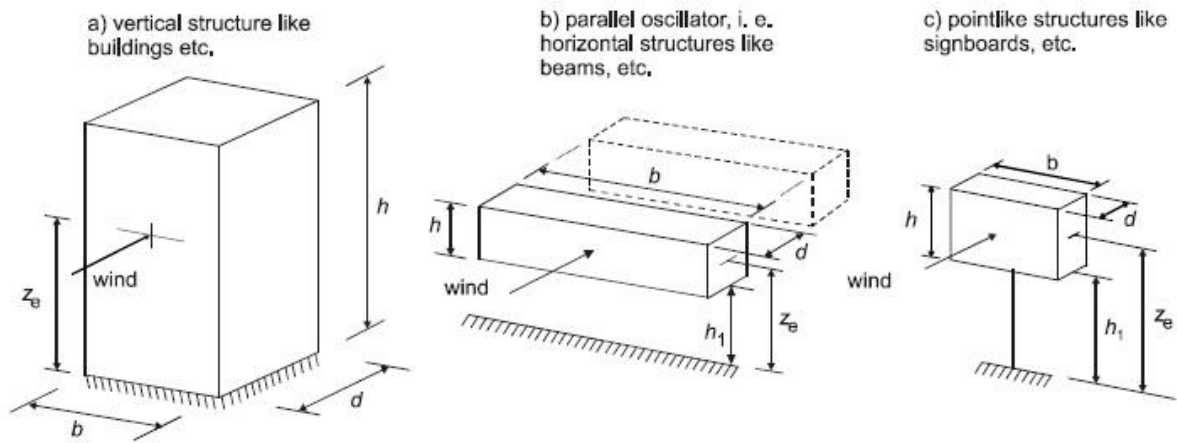


Figure 4.12 – General shapes of structures covered by the detailed procedure [26]

According to Annex B.2, it is on the safe side to use $B^2 = 1$ and thus $c_s = 1$.

In an earlier stage of the project, the building was designed in such a way that its shape and dynamic properties lead to a good behavior when confronted with the dynamic loads generated by the wind action that could potentially lead to aerodynamic instabilities. Thus the dynamic factor c_d can be considered as equal to 1.

Once calculated the structural factor $c_s \cdot c_d$, EN 1991-1-4 allows the determination of the wind force F_w acting on a structure through the vectorial summation of the forces $F_{w,e}$, $F_{w,i}$ and F_{fr} , where

$$F_{w,e} = c_s \cdot c_d \cdot \sum_{surfaces} w_e \cdot A_{ref} \quad (4.56)$$

$$F_{w,i} = \sum_{surfaces} w_i \cdot A_{ref} \quad (4.57)$$

$$F_{fr} = c_{fr} \cdot q_p(z_e) \cdot A_{fr} \quad (4.45)$$

4.2.7. BASE FORCES AND MOMENTS

Considering now the width of the building in the perpendicular direction to that of the wind in both the X and Y axis, respectively $b = 18\text{ m}$ and $b = 73.9\text{ m}$, and the division in height defined in 4.2.4.1 that originates the velocity and wind pressure profiles represented in figures 4.9 and 4.10, it is possible to determine the different reference areas in which the different wind pressures w_e are applied and hence the respective forces $F_{w,e}$.

Tables 4.7 and 4.8 presents the areas A_i in which the windward and leeward sides of the building were divided, the heights Δh of each considered segment as well as its width b .

The pressure coefficients and wind pressures obtained before and the respective forces $F_{w,e}$ are also shown.

Table 4.7 – Y direction wind forces obtained through EN 1991-1-4

A_i	Direction Y				$c_{pe,10}$		$ w_e \left(\frac{N}{m^2}\right)$		$F_{w,e,Y} (kN)$	
	z_{ref} (m)	Δh (m)	b (m)	A_{ref} (m^2)	Wind ward	Lee ward	Wind ward	Lee ward	Wind ward	Lee ward
$A_{2,Y}$	140	66.1	73.9	4884.8	0.8	-0.7	1063.65	930.692	5195.72	4546.24
$A_{1,Y}$	73.9	73.9	73.9	5461.2	0.8	-0.7	886.79	745.936	4842.94	4073.71

Table 4.8 – X direction wind forces obtained through EN 1991-1-4

A_i	Direction X				$c_{pe,10}$		$ w_e \left(\frac{N}{m^2}\right)$		$F_{w,e,X} (kN)$	
	z_{ref} (m)	Δh (m)	b (m)	A_{ref} (m^2)	Wind ward	Lee ward	Wind ward	Lee ward	Wind ward	Lee ward
$A_{7,X}$	140	18	18	324	0.8	-0.545	1063.65	930.69	344.62	301.54
$A_{6,X}$	122	20.8	18	374.4	0.8	-0.545	1024.43	896.38	383.39	335.61
$A_{5,X}$	101.2	20.8	18	374.4	0.8	-0.545	972.15	850.63	363.97	318.48
$A_{4,X}$	80.4	20.8	18	374.4	0.8	-0.545	909.36	795.69	340.46	297.91
$A_{3,X}$	59.6	20.8	18	374.4	0.8	-0.545	830.26	726.47	310.85	271.99
$A_{2,X}$	38.8	20.8	18	374.4	0.8	-0.545	721.94	631.69	270.29	236.51
$A_{1,X}$	18	18	18	324	0.8	-0.545	543.13	475.24	175.97	153.98

Once determined the forces $F_{w,e,X}$ and $F_{w,e,Y}$, it is possible to determine the base forces F_x and F_y and the base moments M_y and M_x . In order to calculate the base moments it is assumed that the force $F_{w,e}$ related to a specific pressure w_e is applied at half the height Δh of each area A_i since the pressure is constant in height within each segment considered.

Tables 4.9 and 4.10 show, apart from the forces $F_{w,e}$ already presented in tables 4.7 and 4.8, the moment arm z_M used to determine the base moments M_b introduced by the different forces $F_{w,e}$ as well as the increase of moment and of shear force.

Table 4.9 – Base moment obtained from EN 1991-1-4 for a Y direction wind action

A_i	$F_{w,e,Y} (kN)$		$F_{w,e,Y} (kN)$	$\sum F_{w,e,Y} (kN)$	$z_M (m)$	$M_{w,X} (kN.m)$	$\sum M_{w,X} (kN.m)$
	Wind ward	Lee ward					
$A_{2,Y}$	5195.72	4546.24	9741.96	9741.96	106.95	1041902.6	1041902.6
$A_{1,Y}$	4842.94	4073.71	8916.65	18658.6	36.95	329470	1371372.8

And thus the base shear value is $V_{b,Y} = 18658.6 \text{ kN}$ and the base moment $M_{b,X} = 1371372.8 \text{ kN.m}$

Table 4.10 – Base moment obtained from EN 1991-1-4 for an X direction wind action

A_i	$F_{w,e,X} (kN)$		$F_{w,e,X} (kN)$	$\sum F_{w,e,X} (kN)$	$z_M (m)$	$M_{w,Y} (kN.m)$	$\sum M_{w,Y} (kN.m)$
	Wind ward	Lee ward					
$A_{7,X}$	344.62	301.54	646.16	646.16	131	84647	84647
$A_{6,X}$	383.39	335.61	719	1365.16	111.6	80240.4	164887.4
$A_{5,X}$	363.97	318.48	682.45	2047.61	90.8	61966.5	226853.9
$A_{4,X}$	340.46	297.91	638.37	2685.98	70	44685.9	271539.8
$A_{3,X}$	310.85	271.99	582.84	3268.82	49.2	28675.7	300215.5
$A_{2,X}$	270.29	236.51	506.8	3775.62	28.4	14393.1	314608.6
$A_{1,X}$	175.97	153.98	329.95	4105.57	9	2969.6	317578.2

And thus the base shear value is $V_{b,Y} = 4105.57 \text{ kN}$ and the base moment $M_{b,X} = 317578.2 \text{ kN.m}$

Considering now the values obtained in equations (4.51) and (4.52) for the friction forces of the wind and the corresponding moment arms $z_M = 140 \text{ m}$ for the roof friction force $F_{fr \text{ roof}}$ and $z_M = 70 \text{ m}$ for the walls friction forces $F_{fr \text{ wall}}$, the corresponding contribution to the overall shear base force and base moment can be determined.

Since $F_{fr \text{ roof}} = 9.07 \text{ kN}$ and $F_{fr \text{ wall}} = 70.55 \text{ kN}$ then, the contribution of the friction force to the shear base force in the X direction is $F_{fr} = 150.17 \text{ kN}$ corresponding to $\frac{150.17}{4105.57+150.17} * 100 = 3.53\%$ of the overall shear base force.

The base moment resulting from the wind friction forces is $M_{fr} = 11146.8 \text{ kN.m}$ hence corresponding to $\frac{11146.8}{317578.2+11146.8} * 100 = 3.39\%$ of the overall base moment.

The values determined above were calculated on the basis of a 50 year return period as stated earlier. As seen before if a different return period is needed, equation (4.2) can be used to obtain the respective values of $v_m(z)$ by multiplying $v_{b,50}$ by c_{prob} or by multiplying $q_{p,50}(z)$ by c_{prob}^2 , where $v_{b,50}$ and $q_{p,50}(z)$ are the values of the basic wind velocity and of the peak velocity pressure for a 50 year return period.

Since the wind pressures w_e are linearly related to the peak velocity pressure by the pressure coefficients, then the wind pressure and the respective wind forces $F_{w,e}$ regarding a return period that is different from the 50 year return period considered, can also be obtained multiplying their 50 year return period values by c_{prob}^2 .

4.3. WIND TUNNEL TEST

An important point to be taken into account is whether the designer should use a local wind loading code or choose to determine the wind loadings through wind tunnel tests as represented in figure 4.13.

In many cases, wind actions can be adequately characterized by the different existing codes. However, for buildings and structures that have an unusual sensitivity to the action of wind or to which there is no previous experience, for buildings and structures of unusual aerodynamic shape or even in order to improve the structural performance and to achieve an optimum solution, wind tunnel tests become necessary. The latter reason is the primary one for the use of wind tunnel studies since the wind loads estimated through the use of wind tunnels often fall below the corresponding code values, thus leading to cost savings that can be very significant when compared to the cost of the structure's wind tunnel test.

In the particular case of tall buildings, and due to the importance of wind loads to the structure's cost and safety, the wind loads obtained through the codes often lack in precision and the use of wind tunnel testing becomes more appropriate.



Figure 4.13 – Wind tunnel test 1/350 scaled model [38]

Besides structural integrity related questions, wind tunnel tests can also give important information regarding serviceability issues such as wind-induced drift or horizontal accelerations which ultimately may affect occupant comfort.

The use of wind tunnels as a tool of civil engineering has been evolving for the last 40 years and has become a fundamental aid in the design of most major tall buildings since it allows the identification of the wind-induced structural loads and the response of the buildings superstructure.

As stated earlier, Davenport was responsible for the development of a chain comprised of five steps (Figure 1.4) which correspond to the different variables that are needed in order to determine wind loadings derived from wind tunnel tests. The first, wind climate, is related to the statistics of the wind speed and direction for the specific region where the structure is located. The surface roughness and topography is included in the Influence of Terrain while the aerodynamics of the building and the effects from nearby structures are inserted in the Aerodynamic Data step. The Dynamic Effects step represents the building wind-induced response. The last step corresponds to the Criteria used to assess the building and its response to wind.

4.3.1. WIND TUNNEL LAYOUTS

4.3.1.1. Open circuit type

This constitutes the simplest type of wind tunnel layout. Figure 4.14 shows the layout of an open circuit wind tunnel where it can be seen a flow straightener followed by a mesh screen located in a contraction zone. This has the function of smoothing out mean flow variations as well as reducing turbulence in the test section.

Given its function and since the atmospheric boundary layer flows are very turbulent, these contraction is not essential, but the simulation of atmospheric profiles and turbulence is easier when developed from an approximated uniform and smooth flow.

The axial fan placed downstream of the test section leads to a better flow but produces a pressure drop across the walls and floor of the test section that in case of an existing leak can constitute a problem. Another option is to place a centrifugal blower upstream of the test section. In this case and in order to eliminate the swirl downstream of the fan, it is essential the use of a contraction with screens. The latter configuration can be used in cases in which the wind tunnel testing is used to determine the point of failure of different elements such as in the case of the study made to determine the point of failure and the respective solutions to implement on the trees placed on the balconies of the Bosco Verticale building located near Tower A.

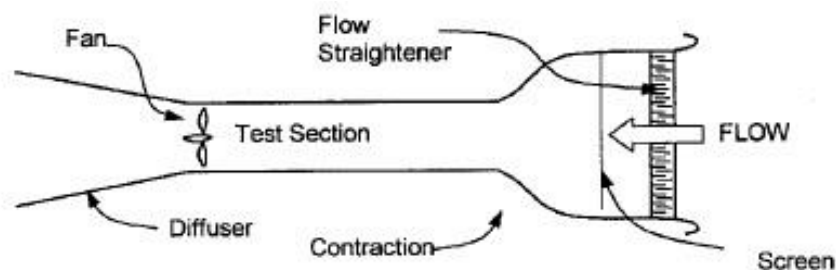


Figure 4.14 – Layout of an open circuit wind tunnel [14]

The diffuser placed downstream of the fan in figure 4.14 is not an essential component but reduces the amount of kinetic energy that is lost with the discharging air leading to cost savings during the wind tunnel tests.

4.3.1.2. Closed circuit type

Contrary to the open circuit type, in the closed circuit as the one shown in figure 4.15, the air is continuously recirculated leading to a less noisy and usually more efficient test. The closed circuit wind tunnels can also contain more than one test section which can have different characteristics and thus different and simultaneous tests can be made.

However the closed circuit wind tunnels have a higher capital cost and when temperature-sensitive instruments such as hot-wire anemometers which depend on the cooling of the air for their operation are used, the heat up of the air over a long period of operation constitutes a problem.

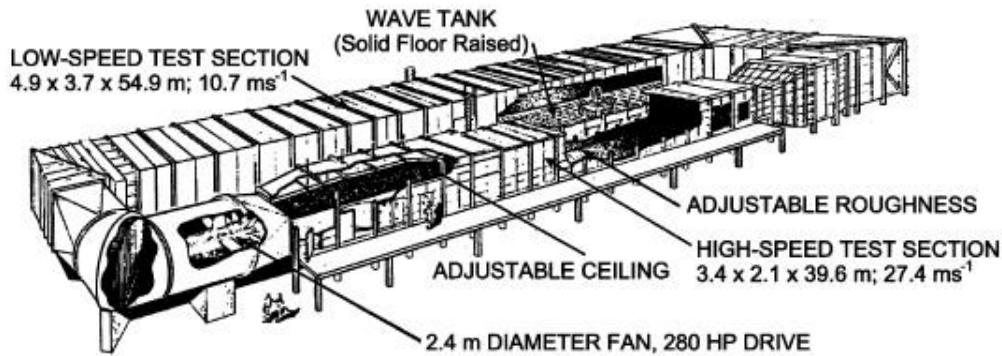


Figure 4.15 – The University of Western Ontario Boundary-Layer Wind Tunnel [33]

4.3.2. NATURAL WIND FLOW SIMULATION

Until the 1960's the wind tunnels used in aerodynamic tests of buildings would only reproduce uniform flows. In 1932, Flachsbart used the first boundary layer flow in order to study wind pressures on buildings after observing that wind pressures in shear flows would differ from the measurements made in uniform flow [34].

Flachsbart was followed by Jensen which gave the first steps in modern boundary layer wind tunnel testing techniques. It was Jensen who suggested, in 1958, the use of the roughness length z_0 as the important length scale in the atmospheric boundary layer flow. Later, in the 1970's, wind engineering studies of tall buildings, bridges and other large structures started to be made in larger boundary layer wind tunnels with either open or closed circuits.

The tests of tall structures are made in boundary layers that are still developing but have a sufficient height in order to envelop the whole model. Usually, in structural tests, a more rapidly boundary layer growth is promoted by a grid at the start of the test section.

As seen on chapter 2, the atmospheric boundary layer is affected by the rotation of the earth which is accounted for by the apparent Coriolis force. However, this effect cannot be achieved in the more usual wind tunnels. This does not constitute a problem since for the heights of most structures, the direction change is normally unimportant.

Even though the full height of the atmospheric boundary layer depends on the wind speed and latitude, its typical height is, as stated before, approximately 1 km. If e.g. a 1/500 geometric scaling ratio is used, then a minimum wind tunnel height of 2 m is needed to model the full atmosphere boundary layer. Normally lower boundary heights are accepted as long as the turbulent boundary layer flow envelops the model under test.

In order to achieve the similarity between the model and the prototype, the characteristics of the atmosphere flows which are expected to affect the structure, such as the variation of the mean wind speed with height, the variation of turbulence intensities and integral length scales with height as well as the spectra of turbulence, should be reproduced at the scale considered. The simulation of the atmospheric flows can be obtained in long tunnels, short tunnels and in tunnels which possess active devices.

In the first a boundary layer with a depth of 0.5 to 1 m develops naturally over a rough floor which may have a length up to 30 m. If necessary, the depth of the boundary layer can be increased by means of passive devices such as spires that are placed at the test section entrance. Older wind tunnels were usually equipped with roof that allowed a variation of its height in order to maintain a constant pressure gradient in the along wind direction. Furthermore the adjustable height should also lead to a reduced blockage error which if not accounted for could lead to significant increases on the flow velocity around the model and thus to an increase of the pressures measured. However, today it is known that for smaller models with lower blockage ratios it is unnecessary, in most situations, to continuously adjust the roof since the errors in the measurements for constant height roofs are small.

According to Simiu [6], long wind tunnels are the best ones to simulate atmospheric turbulence. Despite this fact, and even when passive devices are not used, the similitude between the turbulence in the wind tunnel and in the atmosphere is usually not achieved.

Short wind tunnels are a result of the conversion of tunnels used for aeronautical purposes, with lengths on the order of 5 m, into tunnels used for the study of civil engineering structures in the 1960's and 1970's in order to avoid the costs associated to the construction of new boundary layer wind tunnels. This conversion consisted on the application of passive devices such as the spires mentioned before but also of grids, barriers and fences.

The spires placed downstream produce a velocity gradient which develops into a mean wind profile within a short distance. The grids and barriers mentioned before are placed upstream together with the roughness arrays placed on the floor of the wind tunnel, in order to increase the turbulence intensity.

The flow produced on a short wind tunnel is usually still in a stage of rapid development at the end of the test section. This latter aspect together with the interaction of the vortex structures developed in the wakes of the different devices, may result in unwanted characteristics in the turbulence at the measurement point. Different studies showed that regardless of the different types of passive devices used, the similitude between the turbulence in the atmosphere and in the laboratory is generally not achieved [6]. However this does not constitute a problem since the wind pressures and forces on structures appear to be dependent mainly on single point statistics such as turbulence intensities and integral length scales in the along wind direction [14]

The wind tunnels with active devices consist of tunnels equipped with jets that enable an independent variation of the mean velocity profile and the flow turbulence. This type of tunnels are expensive and the flow simulation given by them is not necessarily superior.

4.3.3. MODELLING OF STRUCTURES FOR WIND EFFECTS

In order to analyze a particular problem that is expected to be studied experimentally, it is usual to identify a set of governing non-dimensional parameters. These parameters are obtained by first writing the partial differential equations that describe the respective physical system and then divide the key variables by a reference value having corresponding dimension. This process leads to non-dimensional groups that emerge as factors which govern the physical behavior of the system considered. If the values of this different groups are maintained unaltered from the prototype to the respective model, the similarity between the two is ensured.

According to Holmes [14], the response of a structure to wind loading is dependent on a number of basic variables such as \bar{U} the mean wind speed at some reference height, the roughness length z_0 , the standard deviations σ_u , σ_v and σ_w of longitudinal, lateral and vertical turbulence, the length scales L_u , L_v and L_w of longitudinal, lateral and vertical turbulence, the density of the air ρ , the viscosity of air ν , the acceleration due to gravity g , the density of the structure ρ_{st} , Young's modulus E and the Shear modulus for the structural material, the structural damping ratio η and the characteristic length of the structure L . This variables can then be transformed into independent non-dimensional groups that should be numerically equal in the model and in the prototype in order to obtain a correct scaling and similarity in behavior as seen above.

According to the Buckingham-Pi theorem, the variables can be reduced, among others, into the Jensen number $\frac{L}{z_0}$, the Reynolds number $\frac{\bar{U}}{L\nu}$, the Froude number $\frac{\bar{U}}{\sqrt{Lg}}$, a reduced frequency $\frac{f_{st}L}{\bar{U}}$, the length ratios $\frac{L_u}{L}$, $\frac{L_v}{L}$, $\frac{L_w}{L}$, the turbulence intensities $\frac{\sigma_u}{\bar{U}}$, $\frac{\sigma_v}{\bar{U}}$ and $\frac{\sigma_w}{\bar{U}}$, the density ratio $\frac{\rho_{st}}{\rho}$ and a Cauchy number $\frac{E}{\rho\bar{U}^2}$.

In the particular case of wind engineering, the large number of non-dimensional parameters involved on the description of the phenomenon makes it impossible to satisfy all the different conditions simultaneously [11].

In the non-dimensional numbers obtained above no distinction is made regarding the source or origin of a given parameter, i.e. it can be fluid, structural, or other. This implies that the ratios among quantities such as length, frequency, density or velocity must be maintained constant from the real structure to the model. This can be represented for example as

$$\left(\frac{\rho_{st}}{\rho}\right)_m = \left(\frac{\rho_{st}}{\rho}\right)_p \quad (4.46)$$

where m and p refer to the model and to the prototype respectively.

This implies that all model shapes must be geometrically similar to prototype shapes, frequencies from all sources must bear the same ratios to each other in the model and in the prototype, oscillating deflections must maintain proper proportionality and the non-dimensional damping ratios that affect the deflections must remain the same in both the model and the prototype.

Considering the definition of parameter scale λ_p of a parameter p as

$$\lambda_p = \frac{p_m}{p_p} \quad (4.47)$$

and since the models used in wind tunnel tests are geometrically similar to the prototype, usually the first parameter scale to be chosen is the length scale which can be expressed as

$$\lambda_L = \frac{L_m}{L_p} \quad (4.48)$$

The scaling of wind velocities used to scale wind turbulence follows the similarity requirement of a model scale Strouhal number equal to its full-scale value. This can be represented as

$$\left(\frac{fL}{U}\right)_m = \left(\frac{fL}{U}\right)_p \quad (4.49)$$

Since

$$\lambda_T = \frac{1}{\lambda_f} \quad (4.50)$$

it follows from equations 4.49 and 4.50 that

$$\lambda_T = \frac{\lambda_L}{\lambda_U} \quad (4.51)$$

where f is the frequency, L is a characteristic length and U the wind velocity, λ_T is the time scale, λ_f is the frequency scale and λ_U is the velocity scale.

The available wind tunnel speeds compared to the expected natural wind speed may lead to the choice of the velocity scale as the second parameter scale to be considered.

Considering the density has the third parameter scale, if the air on the wind tunnel has the same density as that surrounding the real structure then

$$\lambda_p = \frac{\rho_m}{\rho_p} = 1 \quad (4.52)$$

This three fixed choices will then condition all others due to the requirement that the non-dimensional groups maintain their consistency from prototype to model and conversely.

4.3.4. MEASUREMENTS OF LOCAL PRESSURES

Current models of buildings and other structures tested in wind tunnels are equipped with sensitive solid-state pressure sensors which can be individual transducers or part of a multichannel electronic scanning system. This pressure sensors allow near-simultaneous measurements of fluctuating wind pressures.

In the case of the wind tunnel test of Tower A, reasons of geometric constraint made it necessary to install the scanning unit away from the point where the pressure measurement is required. A tubing between the two points, as the one shown in figure 4.16, is then necessary in order to transmit the fluctuating pressure. Thus the correct measurement of the pressures, especially of peak pressures and suctions, becomes dependable of the dynamic frequency response of the complete pressure measurement system.

The transmission of the fluctuations through the pipes is affected by the mass inertia, compressibility and energy dissipation of air. This can lead to resonance peaks on the frequency response function of the system as well as to a nonlinear variation of the time lag with the frequency.

In order to determine the amplitude and the phase of the system so that a correction to the measured data can be applied after the sampling or to develop a system with specific characteristics that allow measurements to be done within a given frequency range without requiring the correction of the recorded data as it has been done in the wind tunnel test of Tower A, an evaluation of the response of the utilized pressure measurement system is required.

The most common systems which do not require corrections of the recorded data are the short tube systems, leaked tube systems and restricted tube systems. The latter tube system was the one used on the wind tunnel test of Tower A. These type of system allows a distance range of 150 to 500 mm between the pressure sensors and the measurement point and is very effective in removing resonant peaks and giving linear phase response characteristics. In the simplest systems of this type a section of narrower tube (known as damper) is inserted between the main tube section and the transducer.

In the wind tunnel test developed by CRIACIV, Teflon pipes with inner and outer diameters of 0.8 mm and 1.3 mm, respectively, were used. The dampers were materialized by 20 mm length Teflon pipes with a 0.3 mm inner diameter and an outer diameter equal to the inner diameter of the main pipes. The overall length of each pipe placed inside the model was equal to 500 mm in order to allow the settlement of the transducers under the model.



Figure 4.16 – Pressure measurement system [38]

The diameters mentioned above as well as the position of the damper in relation to the transducer were obtained through the calibration of the system so that an optimal solution could be obtained. This optimal solution is obtained for a specific distance of the damper in relation to the transducer that minimizes the difference between the signal transmitted by a transducer linked directly to the pressure tap and the signal transmitted by the 500 mm length pipes to the transducers placed under the model.

4.3.5. THE CRIACIV WIND ENGINEERING LABORATORY

Tower A as well as the spire placed on top of it were tested at the CRIACIV Wind Engineering Laboratory located in Prato near Florence. This laboratory contains apart from the wind tunnel itself, a series of instruments used for the measurement of the physic quantities of interest.

4.3.5.1. The CRIACIV Boundary Layer Wind Tunnel

The CRIACIV Boundary Layer Wind Tunnel shown in figure 4.17, is an open circuit wind tunnel with a target wind speed comprised in the range 0 to 35 m/s which is obtained through the regulation of the pitch of the 10 blades that constitute the fan and through the rotation speed of the latter. The fan and the motor that allows its rotation are placed downstream of the test section.



Figure 4.17 – CRIACIV Boundary Layer Wind Tunnel [33]

The cross section varies from sides with 2.2 by 1.6 m in the inlet to 2.4 by 1.6 m on the working section. The global length is about 27 m with an overall longitudinal dimension for the development of the boundary layer that is 8 m upstream and 3 m at the test section.

4.3.5.2. Boundary Layer Wind Tunnel Instruments

The instruments of the CRIACIV laboratory can be divided into wind speed and wind turbulence measurement instruments and pressure measurement instruments.

Each one of the three Pitot tubes present in the laboratory yields both the total and static pressure heads and is used to measure the mean wind speed.

The mean wind velocity as well as the turbulent flow are measured through a hot wire anemometer. This is a thermal transducer which can be used either in water or in air. The main advantages of this type of instrument is its high spatial resolution, little interference to flow and short response time.

As seen in 4.3.4, the pressure measurement system used in Tower A wind tunnel test, schematically represented in figure 4.18 was comprised of a series of pressure taps, Teflon pipes and pressure transducers. The damper, inserted along the pipe length, mentioned before is obtained through a reduction of the pipe cross-section as seen earlier and allows the pressures to be transmitted without undergoing distortions.

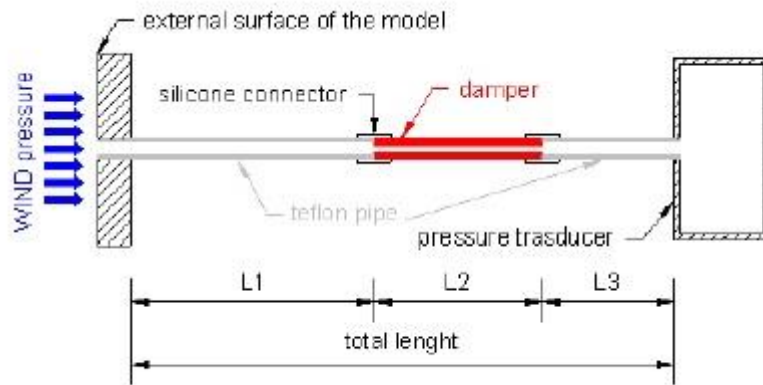


Figure 4.18 – Schematic representation of the connection between a pressure tap and a transducer [38]

The pressure measurement is made by the measurement of the resulting deformation of an elastic membrane due to the flow transmitted by the pipes into the transducer. This deformation is then transformed into an electrical signal which is later digitalized.

4.3.6. WIND TUNNEL TESTING OF TALL BUILDINGS

Depending on particular objectives and available resources, the procedures used in the study of wind tunnel models may vary widely, however, the more commonly used are, among others, the test of local pressures, the area and overall wind loads test, the high frequency force balance test, section model tests and aeroelastic studies.

In the current case study the test of local pressures and the high frequency force balance (HFFB) test (also known as high frequency base balance test) were used.

4.3.6.1. Local Pressures Test

The test of local pressures gives as result the values of the instantaneous pressure coefficients

$$C_{p,g}(t) = \frac{p(t) - p_0(z_{ref})}{P_{dyn}(z_{ref})} = \frac{p(t) - p_0(z_{ref})}{\frac{1}{2} \rho \bar{U}^2(z_{ref})} \quad (4.53)$$

where $p(t)$ is the instantaneous pressure acting on a certain point of the surface of the model, p_0 is the static pressure of the undisturbed flow, P_{dyn} is the dynamic pressure of the undisturbed flow, ρ is the air density, \bar{U} is the mean wind velocity and z_{ref} is the reference height above ground.

According to international codes, the instantaneous pressure coefficients should be divided by $1 + 7I_u(z_{ref})$, a correction that takes into account scaling problems of the frequencies. The pressure coefficient C_p is thus obtained by

$$C_p(t) = \frac{C_{p,g}(t)}{1 + 7I_u(z_{ref})} \quad (4.54)$$

where $1 + 7I_u(z_{ref}) = 6.5\%$ is the turbulence intensity at the reference height of the model $z_{ref} = 0.40$ corresponding to a full scale height $z = 140 \text{ m}$.

The pressure coefficients were then computed considering the dynamic and static pressures P_{dyn} and p_0 , respectively, at the top of the model. Since the variation with height of the static pressure is low, it was considered to be constant. However the same cannot be said about the variation with height of the dynamic pressure. Thus, according to the Italian Code in use at the time of the wind tunnel test, the respective local force F acting on an influence area A_p with its barycenter located at a point P could then be evaluated by

$$F(P) = q_{10} c_e c_d C_p(P) A_p \tag{4.55}$$

Where c_e is the exposure coefficient which is given by

$$c_e = k_r^2 c_t \ln\left(\frac{z_{ref}}{z_0}\right) \left[7 + c_t \ln\left(\frac{z_{ref}}{z_0}\right)\right] \tag{4.56}$$

The values of the different parameters were obtained through the Italian code (DM 16.01.1996)

The model of Tower A as well as its urban surroundings were 1/350 scaled. The first was instrumented with 140 pressure taps and logged at a sampling frequency of about 250 Hz during 30 seconds.

The map identifying the 140 pressure taps is presented on figure 4.19 while the corresponding areas of influence are shown in table 4.11.

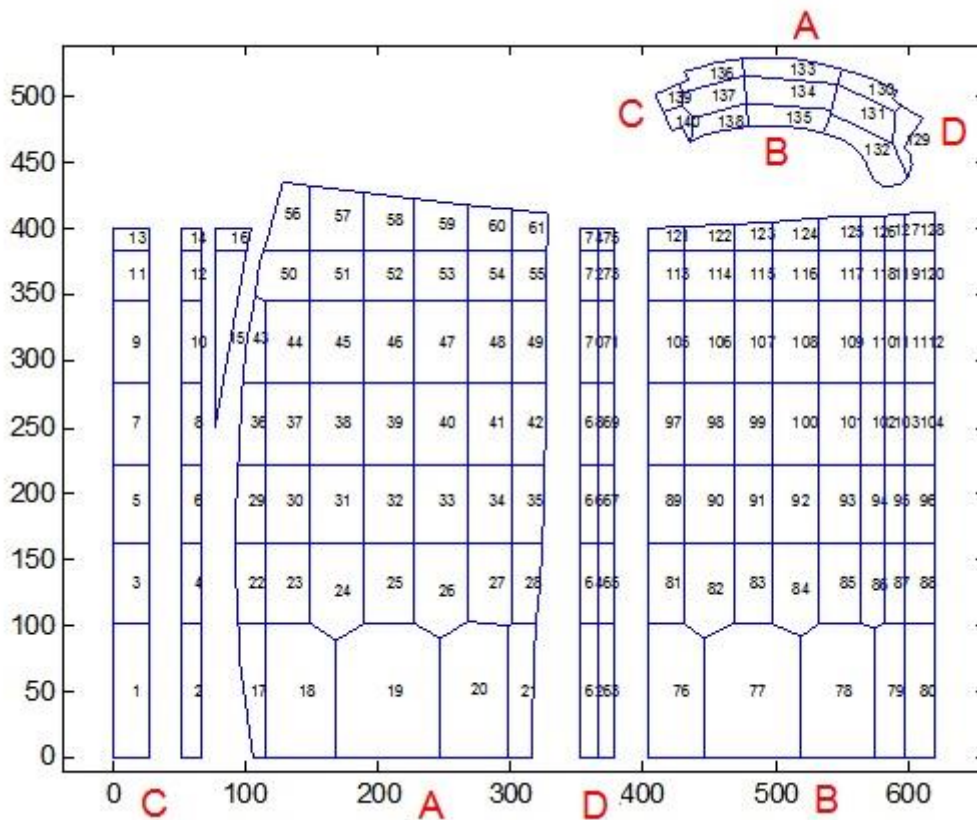


Figure 4.19 – Map of the pressure taps [38]

The pressure coefficients of each area of influence of the pressure taps installed on the surface of the model were evaluated for 16 different directions by rotating the test section table, as the one represented in figure 4.20 of an angle $0^\circ < \alpha < 337.5^\circ$ with a 22.5° step. For each one of this angles the results obtained were the mean value, the Gumbel maximum and minimum values and the absolute maximum

and minimum values of the pressure coefficients which maximize the base resultants F_x, F_y, M_x, M_y and M_z .

The 5 distribution of the pressure coefficients obtained for the 16 different directions lead to 80 different C_p sets for the wind loads.

The Gumbel extreme values obtained were computed through the Gumbel extreme value probability density function and correspond to a 50 year return period. The highest or lowest value of the resultant time history correspond to the absolute extreme values.

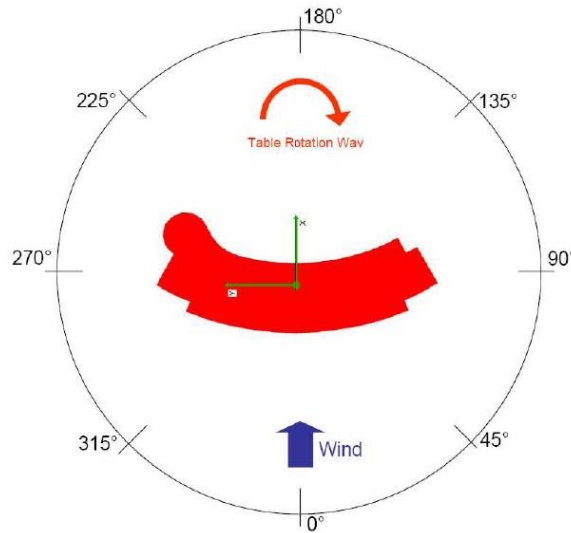


Figure 4.20 – Wind tunnel reference system [38]

Table 4.11 – Influence areas of the pressure taps

Tap	A(m ²)						
1	334.88	36	149.33	71	105.04	106	277.62
2	198.45	37	246.59	72	61.69	107	213.84
3	202.58	38	298.90	73	68.17	108	273.86
4	120.05	39	295.16	74	24.06	109	236.35
5	198.45	40	298.90	75	26.58	110	135.06
6	117.60	41	250.33	76	511.66	111	120.05
7	201.76	42	188.71	77	883.35	112	165.07
8	119.56	43	107.37	78	665.90	113	133.91
9	202.58	44	247.60	79	308.65	114	180.17
10	120.05	45	300.13	80	272.87	115	138.78
11	131.47	46	296.37	81	206.34	116	177.73
12	77.91	47	300.13	82	301.28	117	153.39

13	51.27	48	251.35	83	213.84	118	87.65
14	30.38	49	191.33	84	296.40	119	77.91
15	199.45	50	188.27	85	236.35	120	107.13
16	48.62	51	194.78	86	137.91	121	54.94
17	211.08	52	192.34	87	120.05	122	82.52
18	642.39	53	194.78	88	165.07	123	70.29
19	935.97	54	163.12	89	202.13	124	98.58
20	631.70	55	124.46	90	271.95	125	92.79
21	232.15	56	169.34	91	209.48	126	56.24
22	172.62	57	224.10	92	268.28	127	51.95
23	247.48	58	198.67	93	231.53	128	74.44
24	330.89	59	178.27	94	132.30	129	73.30
25	296.37	60	131.56	95	117.60	130	85.45
26	326.80	61	92.23	96	161.70	131	134.67
27	250.69	62	157.15	97	205.49	132	167.00
28	151.47	63	173.64	98	276.48	133	126.97
29	164.46	64	95.06	99	212.97	134	171.20
30	242.55	65	105.04	100	272.75	135	121.51
31	294.00	66	93.12	101	235.38	136	81.71
32	290.33	67	102.90	102	134.51	137	119.15
33	294.00	68	94.68	103	119.56	138	85.77
34	246.23	69	104.62	104	164.40	139	34.26
35	171.81	70	95.06	105	206.34	140	41.68

The integration (summation) along the entire model surface of the pressure coefficients multiplied by their respective influence area and decomposed along the absolute reference system allowed the determination of the time histories of five base resultant forces F_X , F_Y , M_X , M_Y and M_Z shown in figure 4.21.

In the same way as for the case of the pressure coefficients, different quantities of the base resultant forces were obtained from the respective time histories such as the mean value of the force, the standard deviation, the Gumbel maximum and minimum and the Absolute maximum and minimum values of the force.

Table 4.12 shows, for each considered angle, the maximum values, obtained through the Gumbel extreme value distribution, of the base resultant forces provided by the wind tunnel test by means of C_p

integration. These values are referred to the local axis. The procedure used to obtain the resultant base forces in the absolute reference system considered is shown ahead.

Table 4.12 – Maximum values of the base resultant forces obtained by means of C_p integration

Angle (°)	F_x (kN)	F_y (kN)	M_x (kN.m)	M_y (kN.m)	M_z (kN.m)
0.0	13789	936	49322	1082643	-47490
22.5	13132	-5161	375642	1020036	-98950
45.0	8444	-7620	574152	650502	-119717
67.5	2871	-2718	206145	224469	-88871
90.0	1542	3970	-342048	166443	-40618
112.5	4230	7956	-751284	422979	72380
135.0	10536	7360	-619962	878025	56957
157.5	14033	3375	-239739	1090278	50086
180.0	13056	-3253	265698	1013928	-52682
202.5	11178	-4230	332886	852066	-67952
225.0	10552	-7314	555828	794040	-64439
248.5	6780	-10200	792513	560409	-81847
270.0	3329	-4337	357318	216834	39397
292.5	4047	3726	-256536	311508	105516
315.0	7101	5100	-392439	575679	128268
337.5	11498	4428	-357318	903984	100019

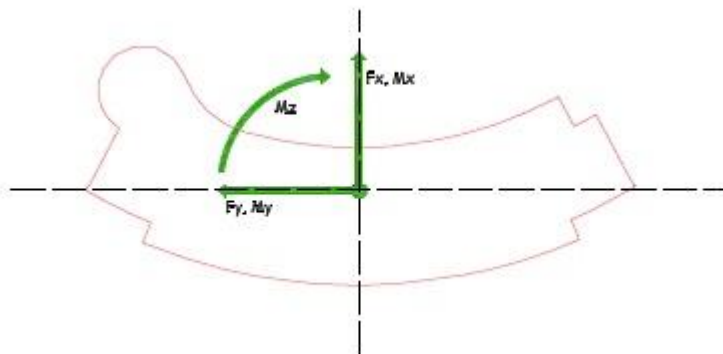


Figure 4.21 – Sign convention the base resultant forces [38]

4.3.6.2. High Frequency Force Balance (HFFB) Test

The HFFB test started to be developed on the 1970's but it was only in 1983 that this simplified dynamic analysis was formulated by Davenport. In the last 25 years, this test has become the standard wind tunnel method for the determination of wind loads and dynamic responses for most tall buildings mainly because it is a procedure that is relatively inexpensive when compared to the costly aeroelastic test, it is fast and is compatible with the installation of architectural details on the model's surface which could be incompatible with the use of pressure taps for the determination of local pressures. The wind tunnel models used on the HFFB test are simple and the basic dynamic properties can be easily incorporated and changed if needed, provided the exterior structural geometry is not altered. One of the drawbacks of this method is that it does not provide the vertical profile of the moments and shear force. Although the HFFB does not take into account aeroelastic effects, the fact that for most of the tall buildings this effects are usually considered to be negligible makes it the best method to be applied in the design of most of this type of buildings [33,36,39,40].

Contrary to the aeroelastic model test, in the HFFB test (figure 4.22) the aeroelastic properties of the building are not modeled, instead the model is rigid and is supported by a highly sensitive and stiff force balance allowing the model to be above the exciting forces of the wind thus avoiding distortions of the dynamic wind loads in the frequency range that affects the resonant response of the full scale structure.

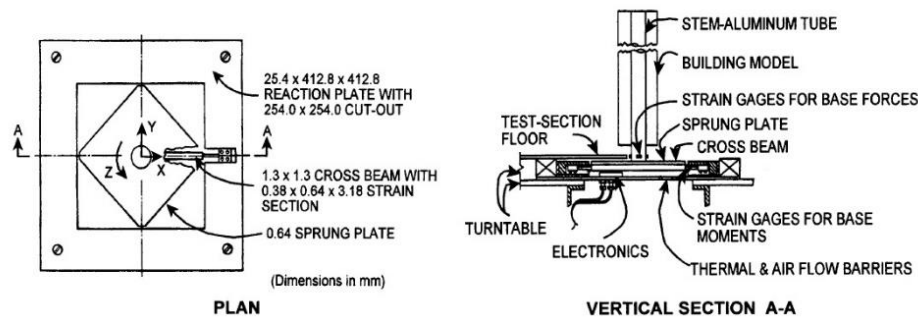


Figure 4.22 – High frequency base balance schematic representation [33]

The frequency of the dynamic loading in the wind tunnel which corresponds to the full-scale excitation at the natural frequency of the structure can be obtained through equation (4.51)

And is expressed by

$$f_m = f_p \frac{\bar{U}_m L_p}{\bar{U}_p L_m} \quad (4.57)$$

The high frequency force balance measures strains that are proportional to the base bending and torsional moments and to the base shears, corresponding to the mean and fluctuating components of the response, thus providing direct measurements for base moments and shears which result from the overall wind loads. The respective processed data can be used to obtain the mean, root mean square and peak overall wind loads, correlations for components of base moments and base shears, as well as spectra of base loads through which the resonant dynamic component is computed.

For the Unicredit high-rise building, the vertical distribution of wind loads, which included its mean and fluctuating components, was determined by the local pressure test which also allowed the determination of the base moments and shears time histories through C_p integration. However the base moments and base shears time histories obtained by this method can be inaccurate. Thus the correspondent direct measurements made by the HFFB were used to obtain the time histories of the different base resultant

moments and shears which were used to obtain their respective spectra which ultimately allowed the computation of the resonant dynamic component.

In the current case study, two different wind tunnel tests were made. The first was comprised of two distinct phases. The first phase enabled the characterization of the flow in the boundary layer where Tower A is inserted while the second, performed first on the 1/350 scaled model of the tower which included the spire, allowed the determination of the pressure coefficients for 16 different directions through the local pressure test using the 140 pressure taps logged at a sampling rate of about 250 Hz.

For each one of the critical angles (0° , 157.5° , 247.5° and 315°) to which corresponded the biggest values of the base forces obtained by means of the integration of the pressure coefficients determined through the local pressure test and for the 90° , 180° and 270° angles, the determination of the base resultant forces logged at a sampling frequency of 500 Hz during 180 s was done by means of the high frequency balance. In the latter test, where the balance was used, two configurations were considered, a B1 configuration without the spire and a B2 configuration with the spire.

This two methods were not used simultaneously since the model made it physically impossible to install the pipes needed for the local pressure test and the balance of the HFFB test at the same time.

Considering the sampling frequency f_s at which the base resultant forces were logged and the duration of the test d_s , the high frequency balance provided a number of samples n_s equal to

$$n_s = f_s d_s \quad (4.58)$$

$$n_s = 500 * 180 = 90000$$

In order to determine the wind velocity at full scale at a reference height $z = 140 \text{ m}$ which corresponded to the reference height considered on the model, it is necessary to obtain first the reference peak velocity pressure at the standard reference height $z_{ref} = 10 \text{ m}$.

$$q_{ref} = \frac{1}{2} \rho v_{ref}^2 = \frac{25^2}{1.6} = 390.63 \text{ Pa} \quad (4.59)$$

The pressure at the height $z = 140 \text{ m}$ can then be obtained through

$$q = q_{ref} c_e(z = 140) \quad (4.60)$$

where $c_e(z)$ is the exposure factor

$$c_e(z) = k_r^2 c_t \ln\left(\frac{z}{z_0}\right) \left[7 + c_t \ln\left(\frac{z}{z_0}\right)\right] \quad (4.61)$$

According to the Italian Code in use at the time of the design of the building, $k_r = 0.22$, $z_0 = 0.3 \text{ m}$, $z_{min} = 8 \text{ m}$ and $c_t = 1$ and thus $c_e(z = 140) = 3.91$ and $q(z = 140) = 1527 \text{ Pa}$

The corresponding wind velocity at $z = 140 \text{ m}$ was calculated through $q = \frac{1}{2} \rho v^2 = \frac{v^2}{1.6}$ and thus $v = 49.43 \frac{\text{m}}{\text{s}} = \bar{U}_p$.

Considering the geometric scale λ_L and the definition of the frequency scale $\lambda_f = \frac{\lambda_U}{\lambda_L} = \frac{\bar{U}_m}{\bar{U}_p} 350$

Since the wind velocity on the wind tunnel was equal to $\bar{U}_m = 21.07 \text{ m/s}$ then $\lambda_f = 149.205$ and $f_m = 149.205 f_p$

As seen before $\lambda_T = \frac{1}{\lambda_f}$ and thus $T_p = 149.205 T_m$.

Taking into account the standard averaging time of 10 minutes, the corresponding time series on the wind tunnel would have a duration of $T_m = \frac{10 \cdot 60}{149.205} = 4.02 \text{ s}$.

As the duration of the wind tunnel was in fact of 180 s, the amount of information obtained corresponded to $\frac{180}{4.02} = 44$ time series, each one comprised of $\frac{90000}{44} = 2045$ samples.

The second wind tunnel test was also comprised of two phases. The first was used, in the same way as for the first test, for the characterization of the boundary layer. The second was performed on a 1/100 scaled model of the spire, shown in figure 4.23 with a sampling frequency of 1000 Hz during 120 s. The upper part of the tower was also reproduced so that the aerodynamic effects of the surroundings at the base of the spire could also be taken into account. Since the spire is placed at the top of the tower, the effects of the boundary layer of the site are less marked along the spire. However, the flow may not be considered fully uniform at the height range where the spire is placed, so, in order to take into account both hypothesis, the laminar and small-scale turbulent flow were simulated. The first was simulated by removing all the obstacles such as roughness arrays, grids, fences and barriers while the latter was developed by means of a small mesh grid placed at 4.5 meters from the test section.

The analysis done for the 1/350 scaled model logged with a sampling frequency of 500 Hz can be developed in an analogous manner for the current values.

$$n_s = 1000 \cdot 120 = 120000 \quad (4.62)$$

The $z_{ref} = 60 \text{ m}$ in reference to the base of the spire corresponds to a $z_{ref} = 200 \text{ m}$ in reference to the ground and thus

$$c_e(z = 200) = 0.22^2 \cdot 1 \cdot \ln\left(\frac{200}{0.3}\right) \cdot \left[7 + 1 \cdot \ln\left(\frac{200}{0.3}\right)\right] = 4.25 \quad (4.63)$$

$$q = q_{ref} c_e(z = 200) = 390.63 \cdot 4.25 = 1259.91 \text{ Pa} \quad (4.64)$$

$$v = 51.53 \frac{\text{m}}{\text{s}} = \bar{U}_p \quad (4.65)$$

Since the wind velocity in the wind tunnel for the current case was 21.2 m/s and considering once again the geometric scale λ_L and the definition of the frequency scale, $\lambda_f = 41.14$ and thus $T_p = 41.14 T_m$ meaning that the real duration of the simulation of the phenomenon was 41.14 times the duration of the wind tunnel test.

For an averaging time of 10 minutes, $T_p = 10 \text{ m}$, and thus $T_m = 14.58 \text{ s}$.

Since the duration of the wind tunnel was 120 s, $\frac{120}{14.58} \cong 8$ time series were obtained each one comprised of $\frac{120000}{8} = 15000$ samples.

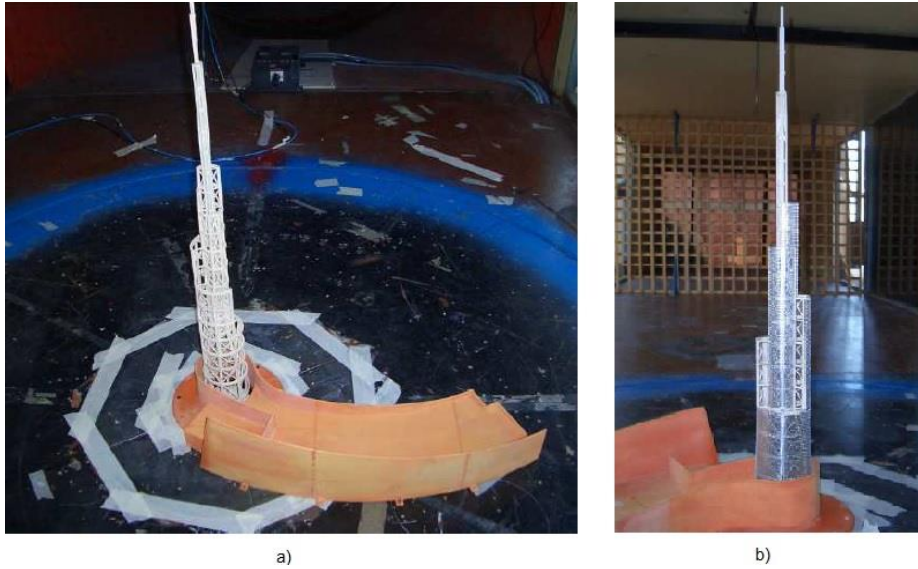


Figure 4.23 – Wind tunnel test 1/100 scaled spire model [37]

While in the small-scale turbulent flow test the spire was covered with a grid with 2 mm holes (configuration A3), in the laminar flow two different configurations were used, one with the same covering grid (configuration A2) and another without the covering grid (configuration A1).

For each one of the three mentioned configurations of the spire, the mean, standard deviation, Gumbel and absolute extreme values of the base resultant forces were obtained in 8 different directions $0 \leq \alpha \leq 315$ with a 45° step.

The forces obtained by the high frequency force balance F_b were divided according to national and international codes by $1 + 7I_u(z_{ref})$ and $P_{dyn}(z_{ref}) = \frac{1}{2}\rho v_m^2(z_{ref})$ where $z_{ref} = 60\text{ m}$, at full scale and measured from the base of the spire, was chosen by practical experimental convenience only.

In order to obtain the respective full-scale values of the base resultant forces F , the values of

$\frac{F_b}{[1+7I_u(z_{ref})]P_{dyn}(z_{ref})}$ were multiplied by $\left(\frac{1}{\lambda_L}\right)^2$ and thus

$$F = \frac{F_b}{[1 + 7I_u(z_{ref})] \frac{1}{2}\rho v_m^2(z_{ref})} \left(\frac{1}{\lambda_L}\right)^2 \quad (4.66)$$

The results of the base resultant forces on the base of the spire, for the different considered angles, obtained in the wind tunnel by means of the balance are shown in table 4.13 as design resultant base forces. These results correspond to the maximum values obtained through the Gumbel extreme value distribution.

For the base resultant forces F_x, F_y as well as for the moments M_x, M_y , the results were the ones obtained considering configuration A2 for all the angles.

For the base resultant moment M_z , the 0° angle corresponding value was obtained from configuration A1, the 45° angle value was obtained from configuration A3 while the remaining angles are related to the A3 configuration.

Table 4.13 – Design resultant base forces acting on the base of the spire

Angle (°)	F_x (kN)	F_y (kN)	M_x (kN.m)	M_y (kN.m)	M_z (kN.m)
0	578	46	-765	28778	4060
45	552	33	1102	28332	-4649
90	675	53	915	31749	-6303
135	693	.18	4312	30818	-5288
180	676	.23	1390	30064	-3733
225	658	24	-950	30547	6172
270	675	44	1472	31021	4453
315	712	103	-3857	31945	4535

In the same way as for the base resultant forces obtained by integration of the pressure coefficients and due to the fact that the high frequency balance rotates with the table, the base resultant forces were decomposed from the local reference system of the spire shown in figure 4.24 to the absolute reference system of the numerical model shown in figure 5.10.

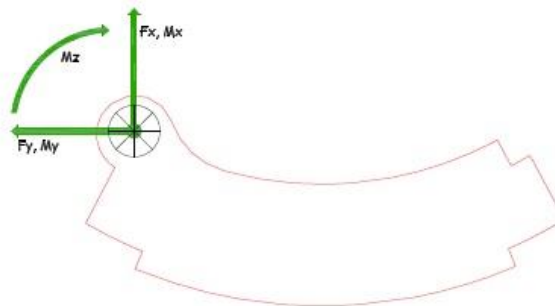


Figure 4.24 – Sign convention for the base resultant forces on the spire. [37]

Comparing the values of the base resultant forces shown in tables 4.9 and 4.10 obtained by the EN 1991-1-4 and the correspondent base resultant forces shown in table 4.12 obtained from the wind tunnel test by means of C_p integration, for a 0° , 180° angle and for 90° , 270° angle, corresponding, respectively, to the Y and X directions considered on the Eurocode analysis, one can verify if there was any advantage taken from the wind tunnel test.

Table 4.14 – Comparison between the base resultant forces obtained through the EN 1991-1-4 and through the wind tunnel test

Direction	$(F_{EN} - F_{WT})/F_{WT}$ (%)	$(M_{EN} - M_{WT})/M_{WT}$ (%)
$Y \equiv 0^\circ$	35.3	26.7
$Y \equiv 180^\circ$	42.9	35.3
$X \equiv 90^\circ$	166.3	90.8
$X \equiv 270^\circ$	23.3	46.5

The subscripts *EN* and *WT* are referred to the base resultant forces and moments obtained either by the EN 1991-1-4 or by the wind tunnel test respectively.

As it can be seen from the table, all the base resultant forces obtained by the EN 1991-1-4 are higher than the ones obtained through the wind tunnel test by values that are close to 25% / 35%, the usual value of gaining obtained through the wind tunnel test.

However, a particular discrepancy can be noticed on the $X=90^\circ$ direction.

Taking into account the figure 4.20, it can be seen that for the 90° angle direction, the wind acts on the smaller lateral side of the building. This discrepancy may be a result of two factors related to the simplifications considered during the EN 1991-1-4 wind loading analysis.

The first is related with the considered 18 m width of the side of the building and the second to the simplified wind pressure profile, obtained through the recommendation given by the Eurocode, comprised only of two different values.

In order to evaluate the adequacy of the 18 m considered width, this was compared to the largest and smallest widths that were reasonable to be considered, namely, the ones corresponding to the largest rectangle in which the plant of the building could be fully enveloped and to the projection of the smaller lateral side of the building in the direction perpendicular to the wind direction.

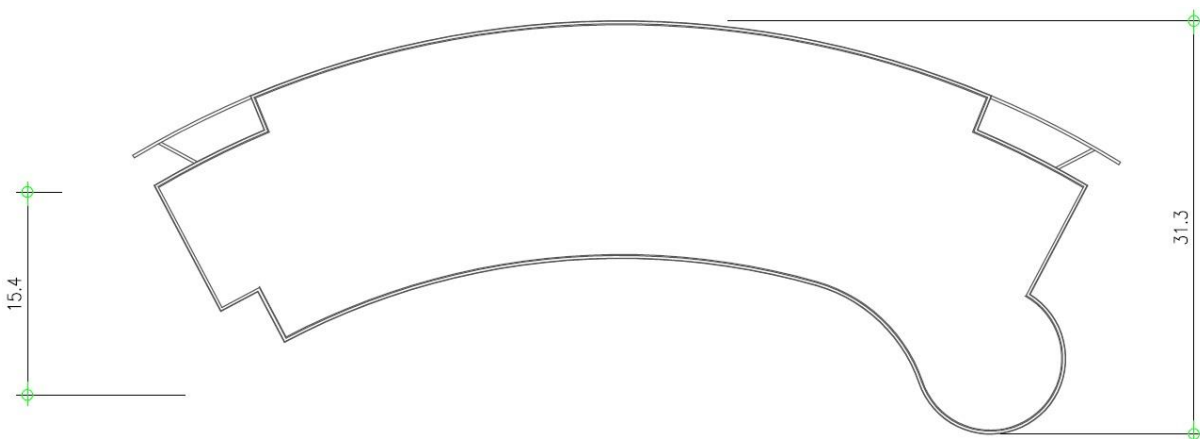


Figure 4.25 – Minimum and maximum side widths

As it can be concluded from figure 4.25, the adopted lateral dimension of the building is closer to its minimum value than to the correspondent larger one. If a larger width was considered, a larger area on which the wind pressures would act would be considered and thus a larger difference between the resultant base forces determined by the Eurocode and by the wind tunnel test would be obtained.

Considering the c_p maps shown in figures 4.27 and 4.26, obtained through the wind tunnel test, which lead to a base resultant value of $M_y=166443$ kN.m and $F_x=1542$ kN, their respective wind pressure profile can be obtained and compared with the wind profile obtained for the X direction.

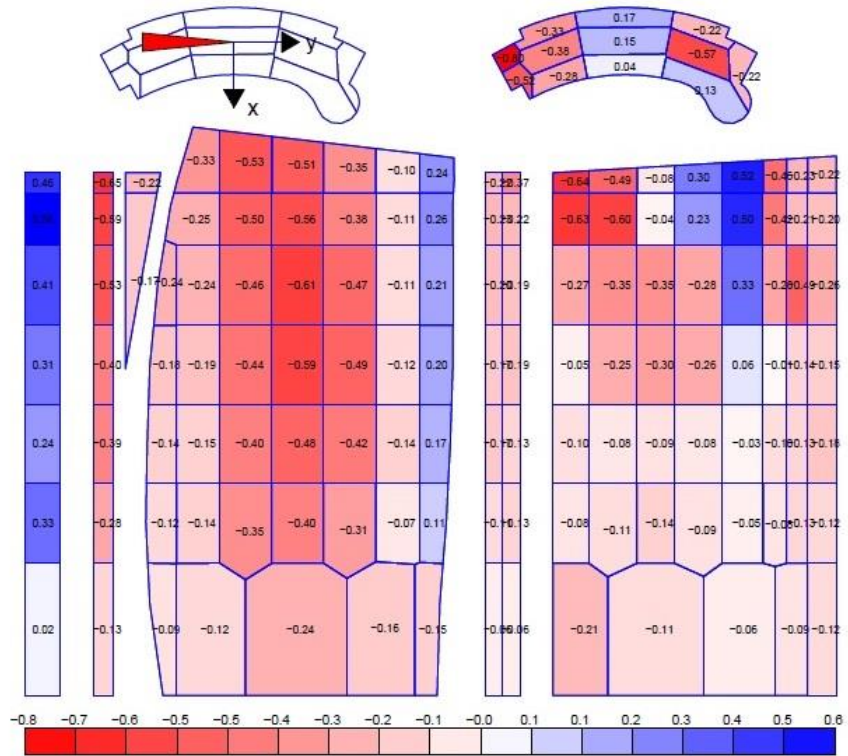


Figure 4.26 - c_p map for Gumbel extreme $F_x=1542$ kN for $\alpha=90^\circ$

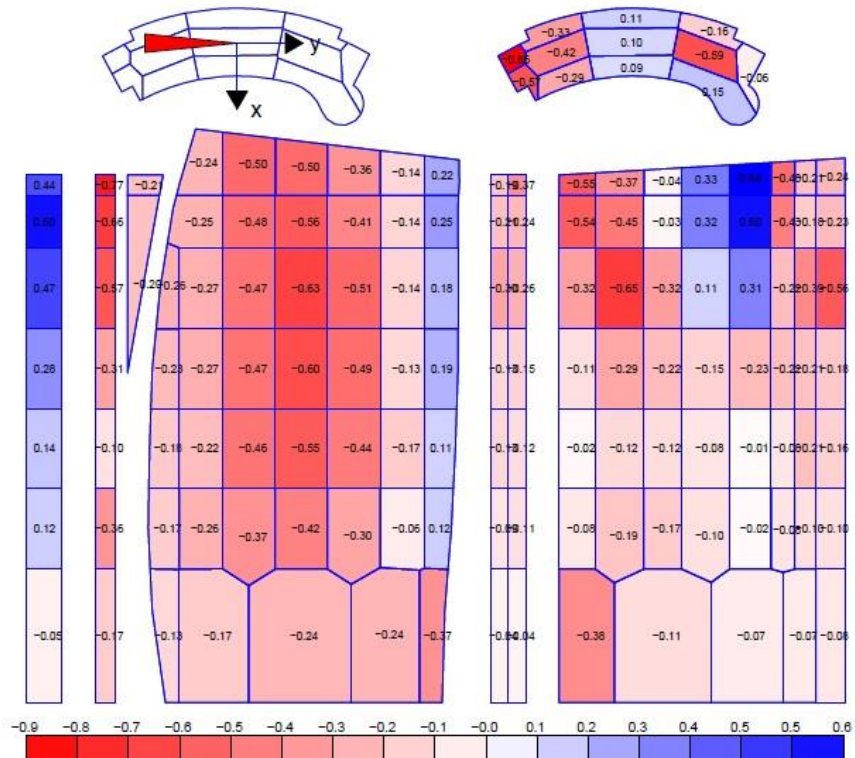


Figure 4.27 - c_p map for Gumbel extreme $M_y=166443$ kN.m for $\alpha=90^\circ$

For the development of the wind pressure profile obtained through the c_p values given in the maps, the height of each pressure tap of the wind ward and leeward sides was obtained, approximately, by the height of the model z_{im} shown in figure 4.19 and multiplied by 350 to obtain the respective full scale values z_{ip} .

$$\begin{aligned}
 z_{1m} &\cong 0.1 \text{ m} \equiv z_{1p} \cong 35 \text{ m} \\
 z_{2m} &\cong 0.16 \text{ m} \equiv z_{2p} \cong 56 \text{ m} \\
 z_{3m} &\cong 0.22 \text{ m} \equiv z_{1p} \cong 77 \text{ m} \\
 z_{4m} &\cong 0.28 \text{ m} \equiv z_{4p} \cong 98 \text{ m} \\
 z_{5m} &\cong 0.35 \text{ m} \equiv z_{1p} \cong 122.5 \text{ m} \\
 z_{6m} &\cong 0.38 \text{ m} \equiv z_{1p} \cong 133 \text{ m} \\
 z_{1m} &\cong 0.4 \text{ m} \equiv z_{1p} \cong 140 \text{ m}
 \end{aligned}$$

The peak velocity pressures $q_p(z)$, for the different heights, were calculated through equation (4.17) and the respective wind pressure, w_e , was determined by means of the equation (4.18).

For each side, windward and leeward (sides C and D on figure 4.19), 2 values of pressure at each height were obtained, corresponding to the two columns of pressure taps present in each side, Windward 1 and 2 (left and right columns) and Leeward 1 and 2 (left and right columns).

Table 4.15 and 4.16 show the values of the peak velocity pressure, pressure obtained for each reference height in each column of the windward and leeward sides for the configuration of the values of the pressure coefficients which maximize both the base resultant force and moment F_x and M_y .

Table 4.15 - F_x base resultant force wind profile values

		F_x base resultant force							
z (m)	$q_p(z)$ N/m^2	Windward 1		Windward 2		Leeward 1		Leeward 2	
		c_p	w_e (N/m^2)	c_p	w_e (N/m^2)	c_p	w_e (N/m^2)	c_p	w_e (N/m^2)
35	871.03	0.02	17.42	-0.13	-113.23	-0.06	-52.26	-0.06	-52.26
56	1017.70	0.33	335.84	-0.28	-284.96	-0.11	-111.95	-0.13	-132.30
77	1122.20	0.24	269.33	-0.39	-437.66	-0.17	-190.77	-0.13	-145.89
98	1204.09	0.31	373.27	-0.40	-481.64	-0.17	-204.70	-0.19	-228.78
122.5	1281.98	0.41	525.61	-0.53	-679.45	-0.20	-256.40	-0.19	-243.58
133	1311.20	0.58	760.50	-0.59	-773.61	-0.23	-301.58	-0.22	-288.46
140	1329.56	0.46	611.60	-0.65	-864.22	-0.22	-292.50	-0.37	-491.94

Table 4.16 - M_y base resultant moment wind profile values

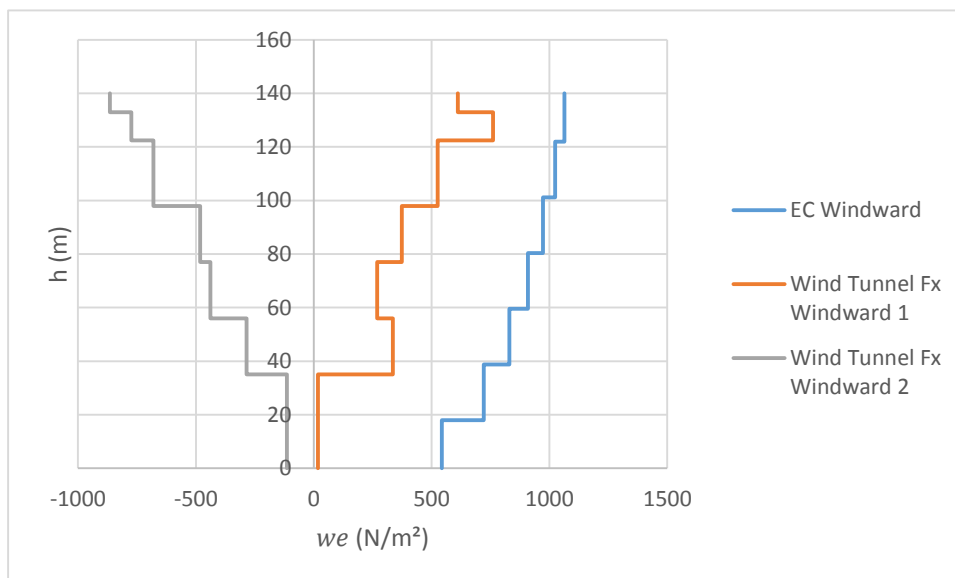
		M_y base resultant moment							
z (m)	$q_p(z)$ N/m^2	Windward 1		Windward 2		Leeward 1		Leeward 2	
		c_p	w_e (N/m^2)	c_p	w_e (N/m^2)	c_p	w_e (N/m^2)	c_p	w_e (N/m^2)
35	871.03	-0.05	-43.55	-0.17	-148.07	-0.04	-34.84	-0.04	-34.84
56	1017.70	0.12	122.12	-0.36	-366.37	-0.09	-91.59	-0.11	-111.95
77	1122.20	0.14	157.11	-0.10	-112.22	-0.13	-145.89	-0.12	-134.66
98	1204.09	0.28	337.15	-0.31	-373.27	-0.13	-156.53	-0.15	-180.61
122.5	1281.98	0.47	602.53	-0.57	-730.73	-0.30	-384.59	-0.26	-333.32
133	1311.20	0.60	786.72	-0.66	-865.39	-0.21	-275.35	-0.24	-314.69
140	1329.56	0.44	585.01	-0.77	-1023.76	-0.19	-252.62	-0.37	-491.94

Once calculated the values of the pressures along the different pressure taps, the respective profile can be represented, allowing an easier interpretation of the results.

Figures 4.28 and 4.29 show, respectively, the wind profile acting on the windward and leeward sides of the building for the configuration of pressure coefficients which maximize F_x .

Each of the figures 4.30 and 4.31 show the wind profile acting on the windward and leeward sides of the building for the configuration of pressure coefficients which maximize M_y .

For each one of the regarded wind pressure profiles the respective windward and leeward wind profile obtained from the Eurocode is represented in figure 4.10 a) by its absolute value.

Figure 4.28 – Windward 1 and 2 wind profile for F_x

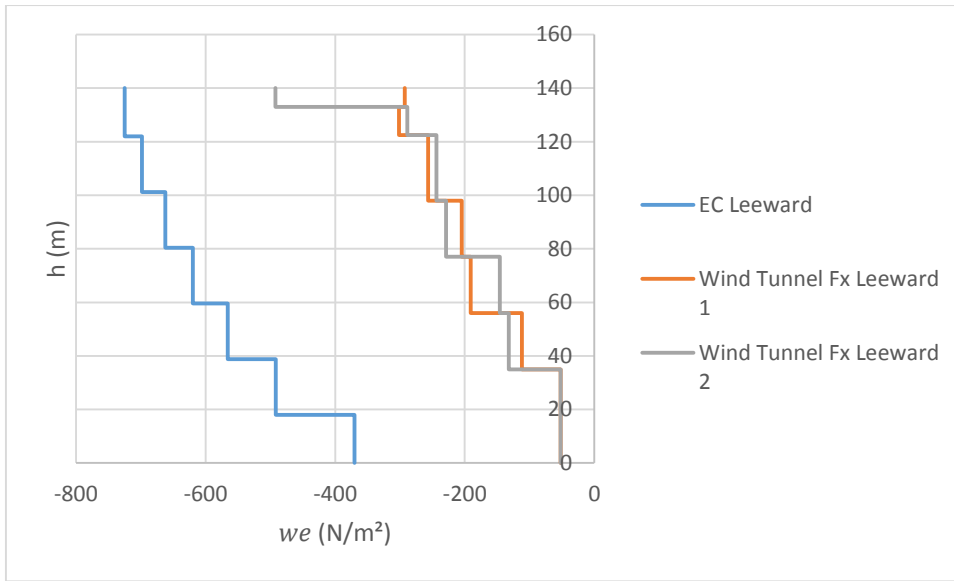


Figure 4.29 – Leeward 1 and 2 wind profile for F_x

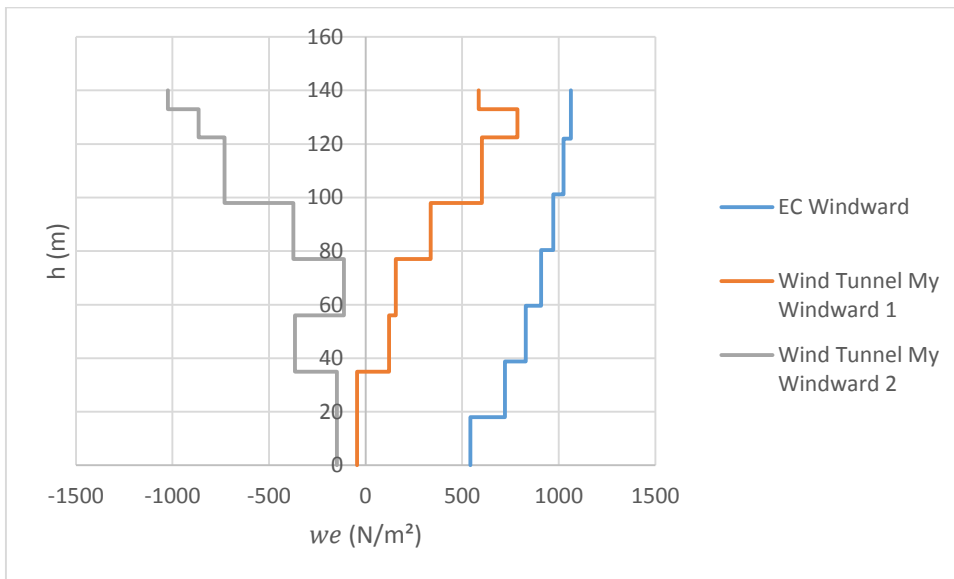


Figure 4.30 - Windward 1 and 2 wind profile for M_y

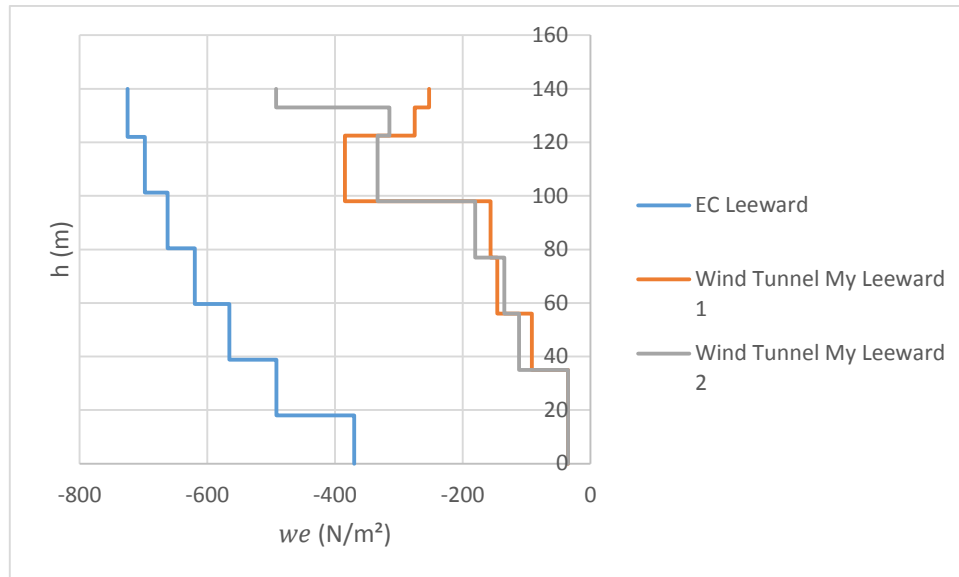


Figure 4.31 - Leeward 1 and 2 wind profile for M_y

Comparing the different wind profiles obtained from the pressure coefficients measured through the wind tunnel with the ones obtained by the Eurocode, it becomes clear that the latter constitutes a conservative envelope for both the windward and leeward wind profiles, hence contributing to the larger values of F_x and M_y obtained by the EN 1991-1-4. This conservative “behavior” is a result not only of the higher c_p values considered by the Eurocode, but also because the wind profile obtained by the latter is comprised, for this specific direction, of only two different values.

Furthermore, the windward 2 wind profiles for both F_x and M_y are negative, meaning that when the wind is acting along the direction in discussion, the areas corresponding to this wind profiles are suffering suctions, effect which is not considered on the Eurocode and that reduces the final value of F_x and M_y .

5

The Unicredit High-Rise Building

Numerical Model

5.1. INTRODUCTION

The overall geometrical shape of the structure as well as the shape of the elements that constitute it, the proprieties of the materials and the loads of the Unicredit high-rise building described in chapter 3 were represented in the respective numerical model developed with the Midas Gen structural analysis software.

During the design stage of the building various numerical models were created in order to develop different analysis.

The model used in the current study was obtained from the modification of one of these models in order to include the contribution of the construction stage so that a more realistic and correct evaluation of the stresses present on the elements of the structure could be obtained. Furthermore, during the design process of Tower A, different proprieties such as slab and wall thicknesses and concrete strength class of some slabs were altered and were not considered on the older model and had to be inserted on the updated numerical model. Different errors on the mesh such as the existence of free edges where a slab-wall connection was supposed to exist or a stair-wall connection were also fixed.

Below the plants of the foundation are shown, floor -2, ground floor, floor 1, floor 2, floor 3 and floor 16 as well as the spire created with the Midas Gen software.

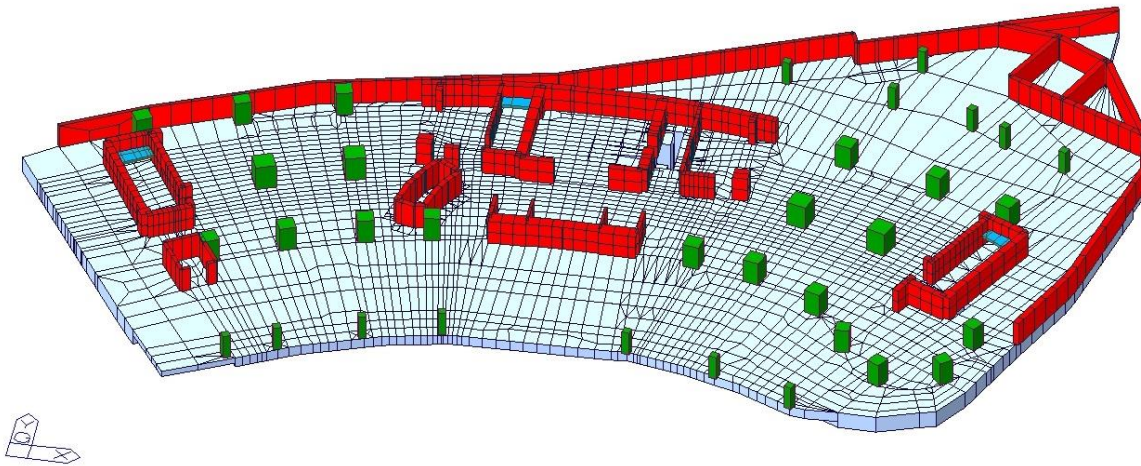


Figure 5.1 – Foundation of the numerical model

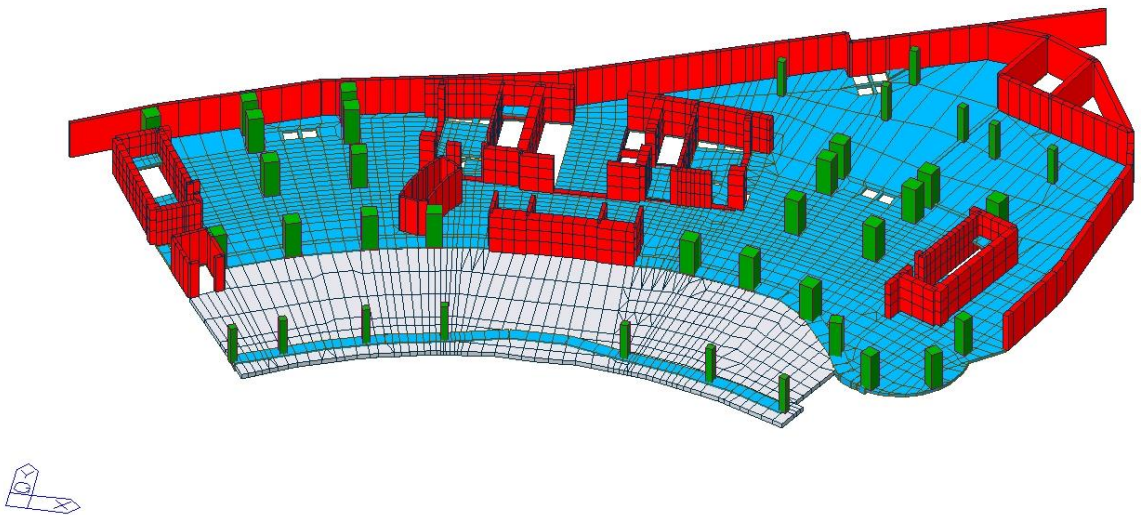


Figure 5.2 – Floor -2 of the numerical model

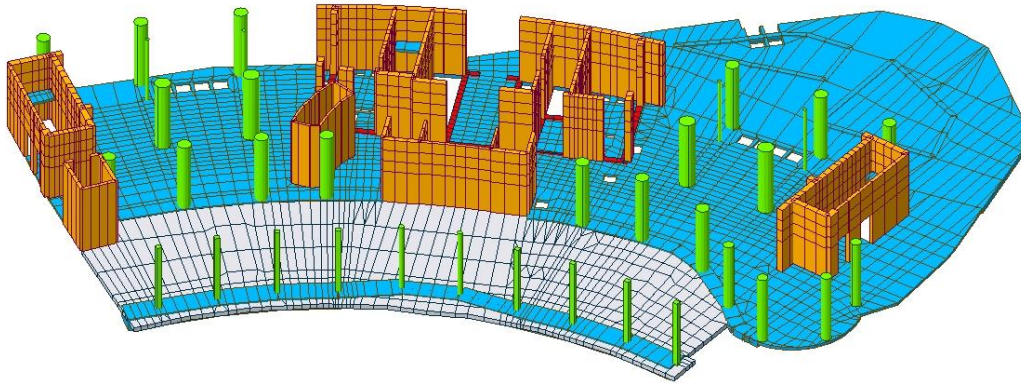


Figure 5.3 – Ground Floor of the numerical model

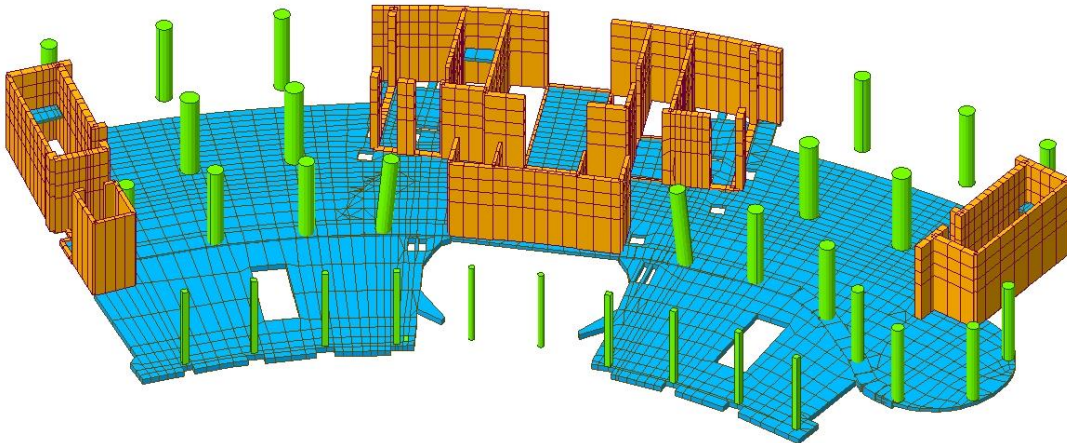


Figure 5.4 – Floor 1 of the numerical model

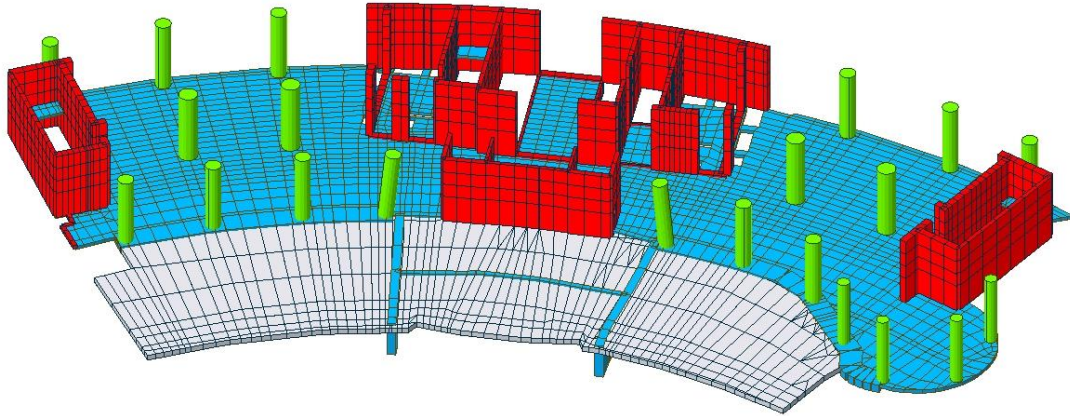


Figure 5.5 – Floor 2 of the numerical model

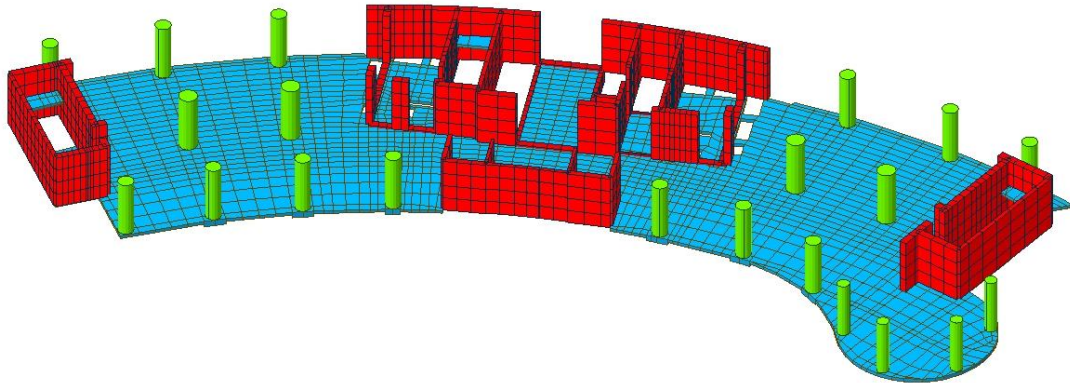


Figure 5.6 – Floor 3 of the numerical model

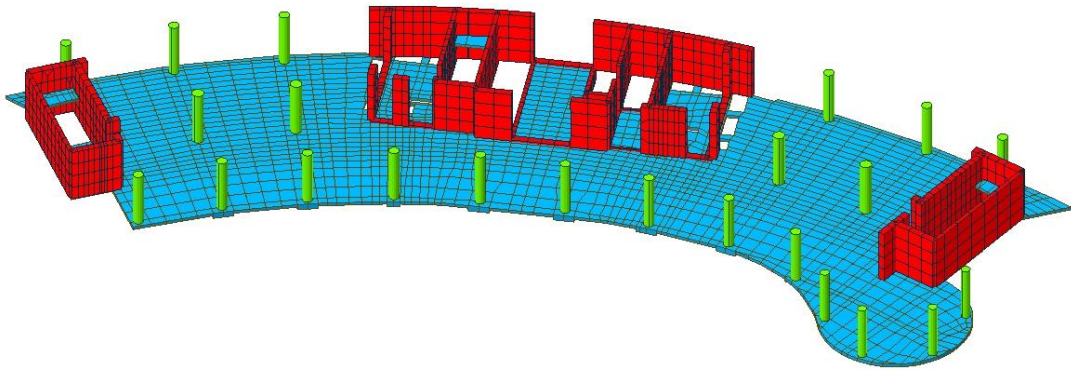


Figure 5.7 – Floor 16 of the numerical model

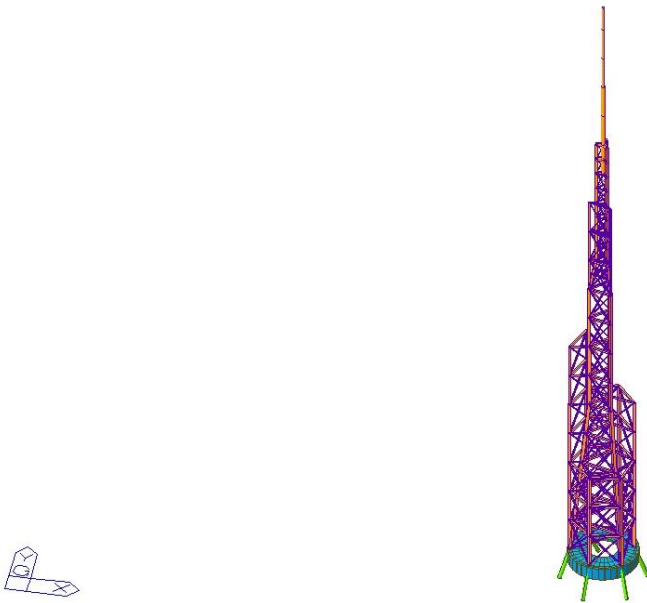


Figure 5.8 – Spire of the numerical model

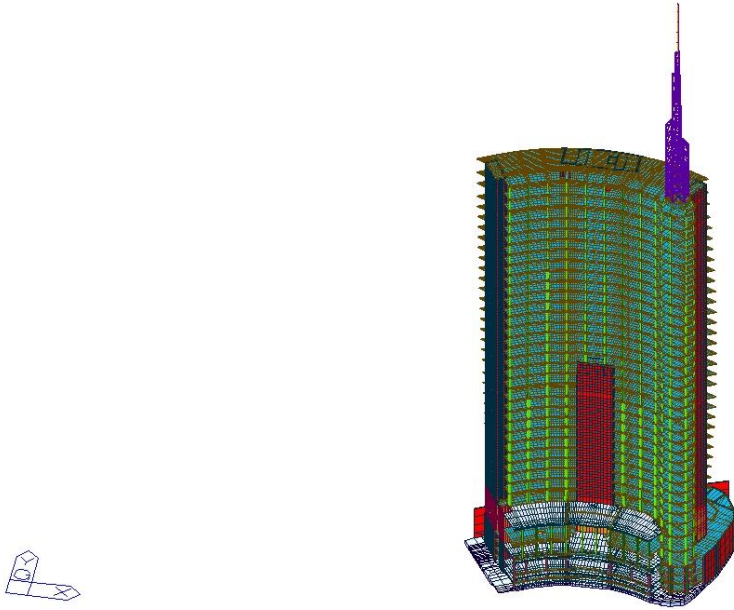


Figure 5.9 – Unicredit high-rise building numerical model

5.2. GENERAL

5.2.1. ABSOLUTE REFERENTIAL SYSTEM

As seen on chapter 4, the base resultant loads obtained through the wind tunnel tests were expressed on its respective relative reference system, shown in figure 4.19, which rotates for every wind direction thus maintaining the x axis as the axis of the wind direction.

Considering α the angle between the wind direction in the wind tunnel tests and the Y axis of the absolute reference system shown in figure 5.10 and 5.11, and that the loads in the local and in the numerical model reference system are positive if acting on the positive direction of the axis, the forces in the numerical model coordinate system can be obtained from the forces referred to the relative reference system through the following expressions.

$$F_X = F_x \sin \alpha + F_y \cos \alpha \quad (5.1)$$

$$F_Y = -F_x \cos \alpha + F_y \sin \alpha \quad (5.2)$$

Considering the orientation of the vector moment defined by the right hand rule, the bending moments are positive if acting in this same orientation.

$$M_X = -M_x \sin \alpha + M_y \cos \alpha \quad (5.3)$$

$$M_Y = -M_x \cos \alpha + M_y \sin \alpha \quad (5.4)$$

The torque moments in turn are positive in clockwise direction in the local reference system and positive in the counterclockwise direction in the global reference system and thus

$$M_Z = -M_z \quad (5.5)$$

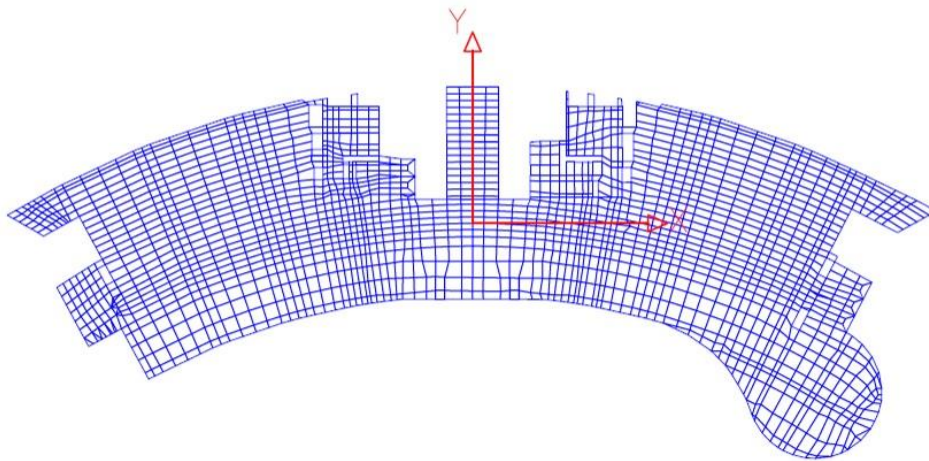


Figure 5.10 - Reference System of the numerical model

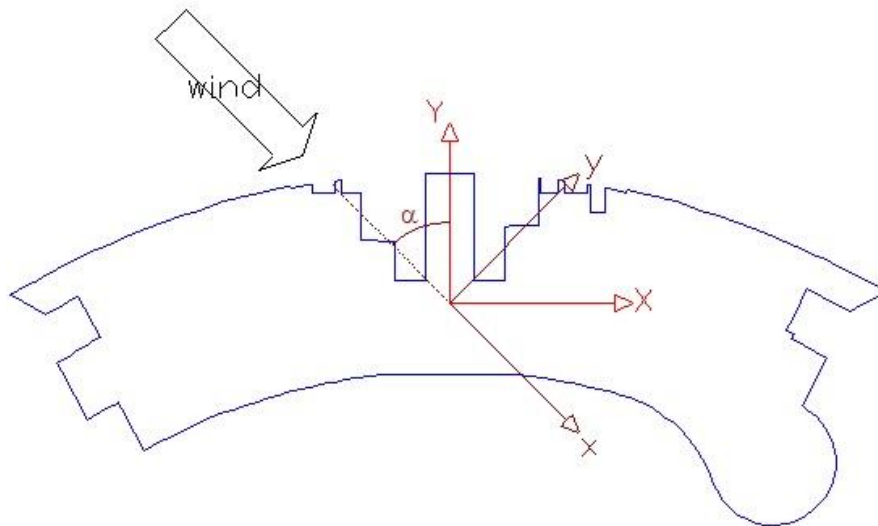


Figure 5.11 – Angle between the local and global referential systems

Once defined the relations that allow the change of the forces from the local reference system to the numerical model reference system, equations (5.1) to (5.5) can be applied to the loads presented in table 4.12 and 4.13 in order to obtain the base resultant forces referred to the latter reference system.

Table 5.1 – Base resultant forces (C_p Integration) on the global reference system

Angle ($^{\circ}$)	F_X (kN)	F_Y (kN)	M_X (kN.m)	M_Y (kN.m)	M_Z (kN.m)
0.0	936	-13789	1082643	-49322	47490
22.5	257	-14108	1086142	43303	98950
45.0	583	-11359	865961	53988	119717
67.5	1612	-3610	276354	128494	88871
90.0	1542	3970	-342048	166443	40618
112.5	863	8969	-855963	103278	-72380

135.0	2246	12655	-1059237	182478	-56957
157.5	2252	14256	-1099030	195741	-50086
180.0	3253	13056	-1013928	265698	52682
202.5	-370	11945	-914596	-18525	67952
225.0	-2289	12633	-954501	-168441	64439
248.5	-2360	12018	-946646	-214469	81847
270.0	-3329	4337	-357318	-216834	-39397
292.5	-2313	-4991	356217	-189624	-105516
315.0	-1414	-8627	684563	-129570	-128268
337.5	-309	-12318	971912	-15821	-100019

Table 5.2 – Base resultant forces of the spire in the global reference system

Angle (°)	F_x (kN)	F_y (kN)	M_x (kN.m)	M_y (kN.m)	M_z (kN.m)
0	46	-578	28778	765	-4060
45	413	-367	20813	19255	4649
90	675	53	915	31749	6303
135	503	477	-18742	24840	5288
180	23	676	-30064	1390	3733
225	-483	448	-20929	-22272	-6172
270	-675	-44	-1472	-31021	-4453
315	-431	-576	25316	-19861	-4535

5.2.2. CONSTRUCTION STAGE

In the more typical structural analysis, the loads considered to act on the structure are applied to the complete structure at once. For high-rise buildings, the contribution of the construction stage to the evaluation of the stresses is particularly important due to the fact that with an increasing scale of the building, and in particular with the increase of the number of stories, the discrepancy between the analysis with and without the consideration of the construction stage increases significantly.

This discrepancy is a result of the completely different columns shortening obtained between the analysis with the loads applied to the complete structure at once and the analysis with the correspondent construction stage which allows to consider the correct elastic deformation of the vertical resistant elements of the tower during its construction.

As reinforced concrete structures are typically constructed floor by floor, the construction dead loads do not affect the resistant elements of the upper floors until these are built and thus the largest deformations obtained due to the construction dead loads will be observed in the lower stories of the building.

In some cases in which the construction stage is not considered in the analysis, a less accurate distribution of the vertical loads can occur. The distribution of the loads will then be higher in the concrete walls when compared to the distribution to the surrounding frames.

In the specific case of the Unicredit high-rise building, the respective numerical model was subdivided into sub-models which correspond to the elements being constructed in the different erection stages.

Since in the current case the only boundaries were placed in the foundation mat, only one group of boundaries was created.

Also, different groups of loads were created in order to allow the non-simultaneous application of the loads during the construction stage.

The complete construction sequence could then be obtained by superimposing the different stages with the correspondent groups of elements, boundaries and loads.

The sub-models considered, corresponded to different stages of construction. The duration of the different stages is shown in table 5.3 along with the elements, boundaries and loads activated at each stage.

Table 5.3 – Construction stages

Stage	Elements activated	Boundaries activated	Loads activated	Stage duration (days)	Total time (days)
1	Foundation	Spring support	SW Foundation	18	18
2	Floor -3	-	SW F -3	18	36
3	Floor -2	-	SW F -2	18	54
4	Floor -1	-	SW F -1	18	72
5	Ground floor	-	SW GF	18	90
6	Floor 1	-	SW F1	18	108
7	Floor 2	-	SW F2	18	126
8	Floor 3	-	SW F3	10	136
9	Floor 4	-	SW F4 + DL Foundation	10	146
10	Floor 5	-	SW F5 + DL F -3	10	156
11	Floor 6	-	SW F6 + DL F -2	10	166
12	Floor 7	-	SW F7 + DL F -1	10	176
13	Floor 8	-	SW F8 + DL GF	10	186
14	Floor 9	-	SW F9 + DL F1	10	196
15	Floor 10	-	SW F10 + DL F2	10	206
16	Floor 11	-	SW F11 + DL F3	10	216
17	Floor 12	-	SW F12 + DL F4	10	226

18	Floor 13	-	SW F13 + DL F5	10	236
19	Floor 14	-	SW F14 + DL F6	10	246
20	Floor 15	-	SW F15 + DL F7	10	256
21	Floor 16	-	SW F16 + DL F8	10	266
22	Floor 17	-	SW F17 + DL F9	10	276
23	Floor 18	-	SW F18 + DL F10	10	286
24	Floor 19	-	SW F19 + DL F11	10	296
25	Floor 20	-	SW F20 + DL F12	10	306
26	Floor 21	-	SW F21 + DL F13	10	316
27	Floor 22	-	SW F22 + DL F14	10	326
28	Floor 23	-	SW F23 + DL F15	10	336
29	Floor 24	-	SW F24 + DL F16	10	346
30	Floor 25	-	SW F25 + DL F17	10	356
31	Floor 26	-	SW F26 + DL F18	10	366
32	Floor 27	-	SW F27 + DL F19	10	376
33	Floor 28	-	SW F28 + DL F20	10	386
34	Floor 29	-	SW F29 + DL F21	10	396
35	Floor 30	-	SW F30 + DL F22	10	406
36	Floor 31	-	SW F31 + DL F23	10	416
37	Roof	-	SW Roof + DL F24	10	426
38	Spire	-	Spire Loads + DL F25	10	436
39	-	-	DL F26	10	446
40	-	-	DL F27	10	456
41	-	-	DL F28	10	466
42	-	-	DL F29	10	476
43	-	-	DL F30	10	486
44	-	-	DL F31	10	496
45	-	-	DL Roof	10	506
46	-	-	Façade Weight	-	516

As one can see from the above table, the superimposed dead loads started to be applied on the 136th day of construction. The installation of the spire was considered to be made at once and the respective superimposed dead loads were simultaneously applied.

Finally, the facade was considered to be applied simultaneously along the full height of the building.

Figures 5.12, 5.13 and 5.14, presented below show the construction stages 6, 20 and 46, respectively, and the correspondent increase of the axial force in the different columns.

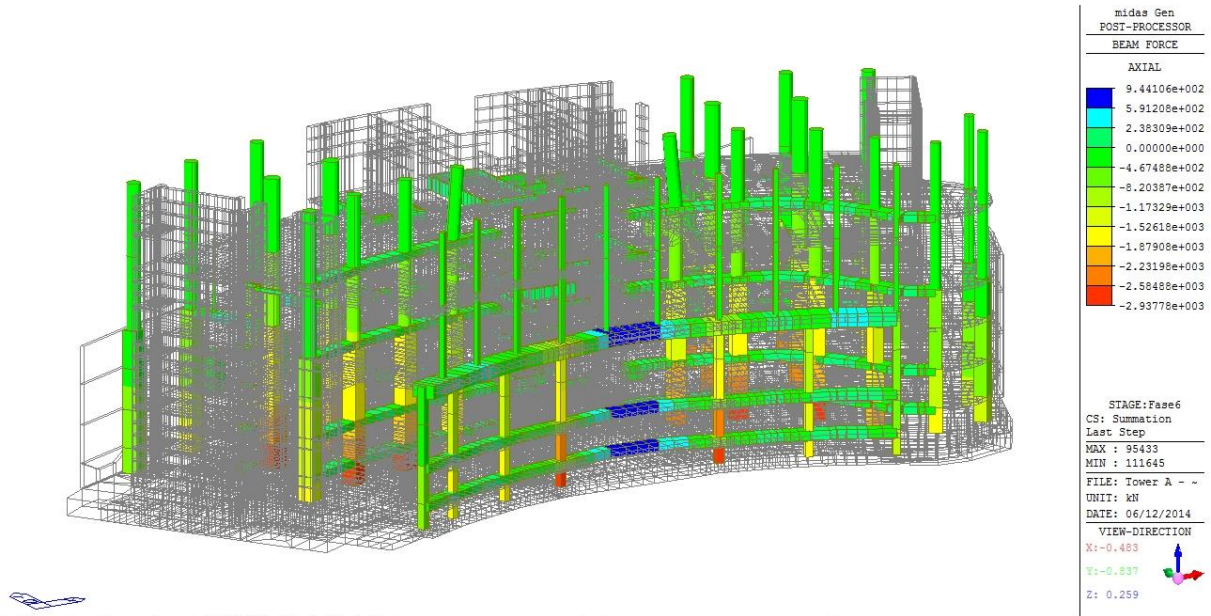


Figure 5.12 – Construction stage 6

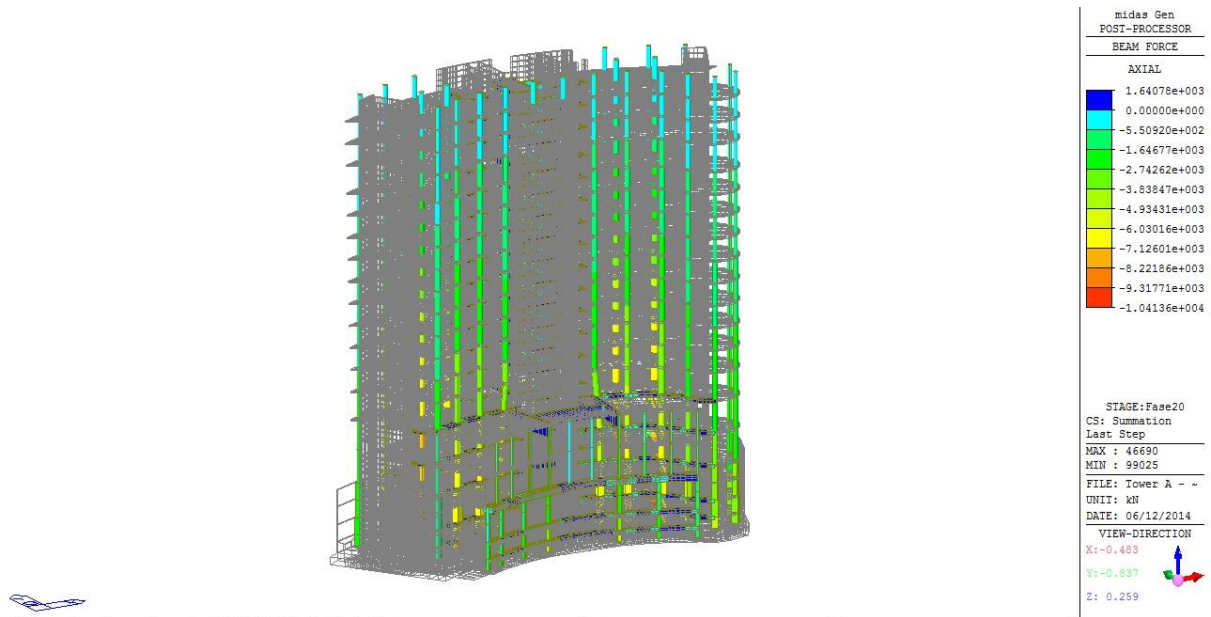


Figure 5.13 – Construction stage 20

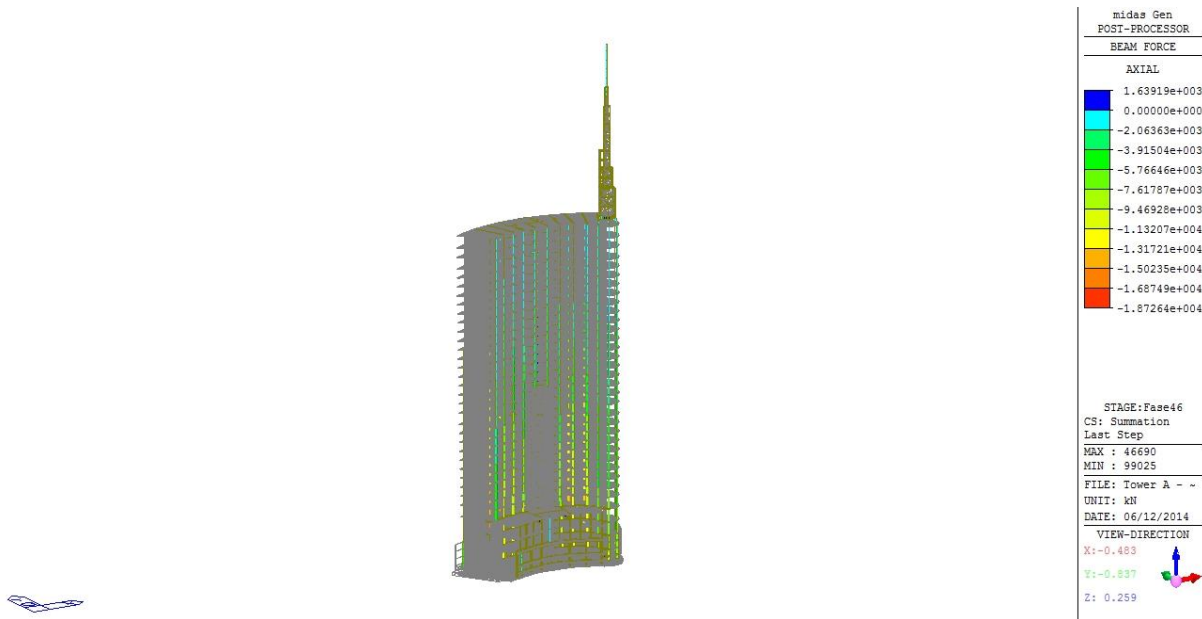


Figure 5.14 – Construction stage 46

5.2.3. LOAD COMBINATIONS

The combinations referred to the ultimate and serviceability limit states, represented as ULS and SLS respectively, were obtained through the DM05 Italian Code [42] in use at the time of the design of the building.

This code classifies the actions applied on the structure according to

- The manner in which they are applied (direct, indirect, entropy)
- The structural response (static, quasi-static, dynamic)
- The variation of their intensity with time (permanent, variable, accidental)

5.2.3.1. Ultimate Limit State (ULS)

The ULS is a limit state that concerns the safety of people and/or the safety of the structure itself. [43]

According to the DM05 Italian Code, the cases that may be treated as an ULS are as follows:

- Loss of equilibrium of the structure or part of it
- Deformation or excessive moment
- Exhaustion of the maximum capacity of resistant of parts of structures, connections or foundations
- Exhaustion of the maximum capacity of resistance of the structure as a whole
- Exhaustion of the maximum capacity of the soil
- Rupture of a member or connection due to fatigue
- Rupture of a member or connection due to other effects

The Ultimate Limit State combination is expressed by the equation

$$E_d = \sum_{j \geq 1} \gamma_{G,j} G_{k,j} (+) \gamma_P P_k (+) \gamma_{Q,1} \psi_{0,1} Q_{k,1} (+) \sum_{i > 1} \gamma_{Q,i} \psi_{0,i} Q_{k,i} \quad (5.6)$$

where E_d is the design action, (+) means “to combine to”, G_k is the effect of the dead loads, including the self-weight, γ_G is the combination factor for the dead loads, P_k is the effect for the prestress, γ_P is the combination factor for the prestress, Q_k is the effect of the live loads, γ_Q is the combination factor for the live loads and ψ_0 is the reduction factor for the secondary live loads.

Since that there are no prestressed elements on the building, the correspondent effect and combination factor are thus 0.

According to the DM05 Italian Code, the combination factors γ_G and γ_Q are limited to the maximum and minimum values presented in table 5.4.

Table 5.4 – Combination factors through the DM05 Italian Code

Code	γ_G		γ_Q	
	Maximum	Minimum	Maximum	Minimum
DM05	1.4	0.9	1.5	0

The reduction factors ψ_0 for the different type of loads were also obtained from the DM05 Code and are presented in table 5.5.

Table 5.5 – Reduction factors through the DM05 Italian Code

Code	ψ_0		
	Live Loads	Snow Loads	Wind Loads
DM05	0.7	0.6	0.6

Furthermore, in order to take into account the non-contemporaneity of the maximum values of the applied live loads on each floor, these type of loads were scaled to a factor $\alpha = 0.55$ on the floor and $\alpha = 0.2567$ on the stairs.

5.2.3.2. Serviceability Limit State (SLS)

The SLS is a limit state that concerns the functioning of the structure or structural members under normal use, the comfort of people and the appearance of the construction works.

According to the DM05 Italian Code, the cases that may be treated as a SLS are as followed

- Local damage (e.g. concrete cracking) that reduces the durability of the structure, its efficiency or appearance
- Excessive deformations and distortions that may limit the use of the building, its efficiency or appearance
- Excessive deformations or distortions that may compromise the efficiency and the appearance of non-structural elements and equipment.
- Excessive vibrations that can compromise the use of the building
- Fatigue damage that can compromise the durability
- Corrosion and/or deformation of materials as a function of environmental exposure

According to the DM05 code, the Serviceability Limit State design action E_d can be obtained through three different combinations, a rare combination, a frequent combination or a quasi-permanent combination.

For the current building, the rare combination was considered in order to verify its serviceability.

This combination can be expressed as

$$E_d = \sum_{j \geq 1} G_{k,j} (+) \gamma_P P_k (+) \sum_{j \geq 1} Q_{k,j} \tag{5.7}$$

Taking into account the aspects mentioned above, 8 different combinations were considered.

5 Ultimate Limit State combinations:

- Ultimate Limit State 1 (ULS1) corresponding to the maximum vertical loads without the wind action.
- Ultimate Limit State 2 (ULS2) corresponding to the maximum wind loads with a 50 year return period applied on the building, when it is comprised only of its structural elements
- Ultimate Limit State 3 (ULS3) corresponding to the maximum vertical loads with wind action as secondary load.
- Ultimate Limit State 4 (ULS4) corresponding to the maximum wind loads with vertical loads as secondary loads.
- Ultimate Limit State 5 (ULS5) corresponding to the maximum wind load for the “empty” building.

and 3 Serviceability Limit State combinations:

- Serviceability Limit State 1 (SLS1) corresponding to the rare combination with the wind as primary load.
- Serviceability Limit State 2 (SLS2) corresponding to the rare combination with the vertical loads as primary live loads.
- Serviceability Limit State 3 (SLS3) corresponding to the rare combination with the wind return period of 10 years.

The coefficients by which the different loads were multiplied for each Limit State combination are shown in table 5.6.

Table 5.6 – Limit State coefficients

Comb. / Loads	SLU1	SLU2	SLU3	SLU4	SLU5	SLS1	SLS2	SLS3
Self-weight	1.40	0.90	1.40	1.40	0.90	1.00	1.00	1.00
Dead Load	1.40	0.45	1.40	1.40	0.90	1.00	1.00	1.00
Floor Live Load	0.825	0.00	0.825	0.578	0.00	0.385	0.55	0.55
Stairs Live Load	1.125	0.00	0.385	0.270	0.00	0.180	0.2567	0.26

Roof Live Loads	0.825	0.00	0.825	0.578	0.00	0.385	0.55	0.55
Facade	1.40	0.90	1.40	1.40	0.90	1.00	1.00	1.00
Snow	0.90	0.00	0.90	0.90	0.00	0.60	0.60	0.60
Spire facade	1.40	0.90	1.40	1.40	0.90	1.00	1.00	1.00
Spire Dead Load	1.40	0.90	1.40	1.40	0.90	1.00	1.00	1.00
Spire Live Load	0.825	0.00	0.825	0.578	0.00	0.385	0.55	0.55
Spire Snow	0.90	0.00	0.90	0.90	0.00	0.60	0.60	0.60
Wind	0.00	1.50	1.1329	1.8883	1.8883	1.2588	0.7553	0.8136

Considering the 7 State Limit combinations which include wind action, the 5 different base resultant forces analyzed in the wind tunnel test, and the 140 pressure coefficients obtained for each one of the 16 directions, 78400 load cases would be needed in order to insert all this hypothesis into the numerical model. This would be impracticable.

In order to simplify the introduction of all these load cases, a procedure which makes use of different levels of “sub-combinations” was developed.

First, in the influence areas, A_i , of the different pressure tabs, the value $q_{ref}A_i$ was introduced. This made it possible to introduce the different values of the C_p coefficients obtained through the wind tunnel test, which maximize the base resultant forces for the different directions, simply by creating the “sub-combination” $\sum C_p q_{ref}A_i$ rather than introducing the $140 * 16 * 5 = 11200$ load cases one by one, making the whole process much more time efficient.

Since the wind action can be treated as a primary or secondary load on the different State Limit combinations, the 1st level “sub-combination” mentioned above was inserted into another combination in which the wind action was multiplied by the respective coefficients, which are a result of the different factors affecting the different load types, shown in table 5.6.

Finally, the latter 2nd level “sub-combination” was introduced in the different State Limit combinations, where all the different load types, affected by their respective coefficients, are considered.

5.3. QUASI-STATIC ANALYSIS

For the specific case of the Unicredit high-rise building, the wind action can be considered to be quasi-static, meaning that the wind action can be considered through a quasi-static load with its dynamic effect being taken into account by an increase of the intensity of these static loads. Thus, the correspondent quasi-static component is treated in the current Quasi-Static Analysis while the respective resonant effect will be considered in the Dynamic Analysis as an equivalent static load.

In the Quasi-Static Analysis here developed, two different scenarios will be considered. The first will comprise the effect of the vertical loads on the building while in the second, both vertical loads and the static component of the wind will be considered.

For each one of this scenarios different values of forces and displacements will be obtained in order to evaluate the behavior of the Unicredit high-rise building to horizontal actions, but also to allow a comparison of these values with the ones obtained for the Dynamic Analysis.

5.3.1. EFFECT OF THE VERTICAL LOADS

The first value to be extracted from the numerical model was the maximum axial force on the base of the columns for each one of the column groups shown in figure 5.15 and already mentioned in chapter 3.

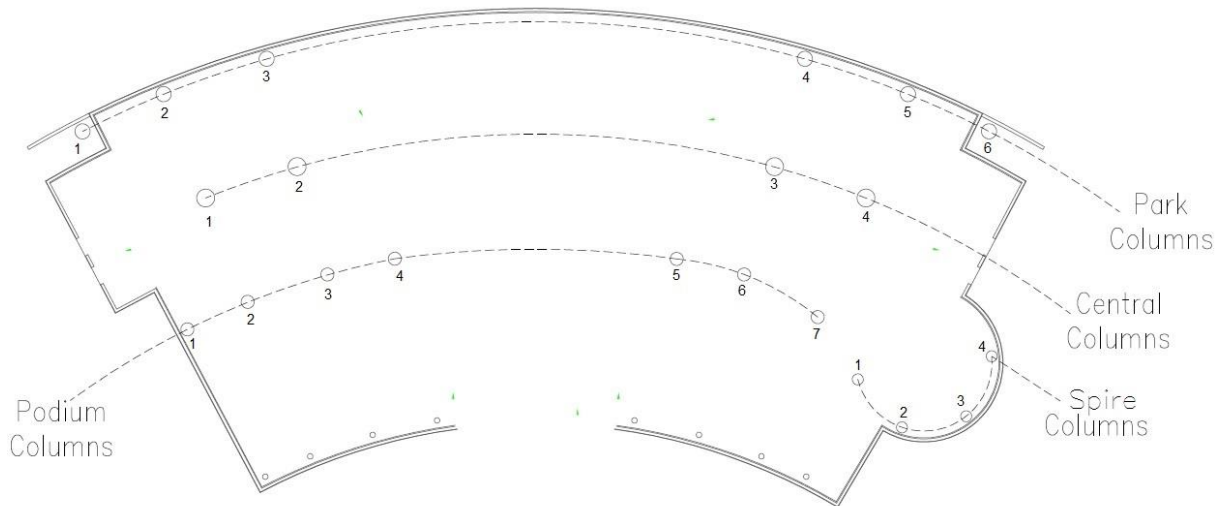


Figure 5.15 – Groups of columns considered

Since the only combination which did not consider the action of the wind is the Ultimate Limit State 1 combination, the values mentioned above are a result of this same combination. The obtained values are shown in table 5.7.

Table 5.7 – Axial force on the base of the columns due to the ULS 1 combination

Column	Column group	Combination	<i>N</i> (kN)
4	Park	ULS 1	-22247.1
1	Central	ULS 1	-31819.9
6	Podium	ULS 1	-22190.1
1	Spire	ULS 1	-15347.9

After obtaining the axial forces on the base of the columns, the value of the shear at the base of each core was obtained. Before this operation it was necessary to make sure that all the plate elements that constitute the cores had the same local axis in order to ensure that it was in fact the shear force that was being analyzed and to simplify the process of extracting the correspondent values.

In figures 5.16, 5.17, 5.18 and 5.19 the shear force diagrams developed on the low-rise core, right and left cores and in the central core for the ULS 1 combination are represented. Although the walls of the different cores present shear force, the overall resultant of this force without wind action is zero.

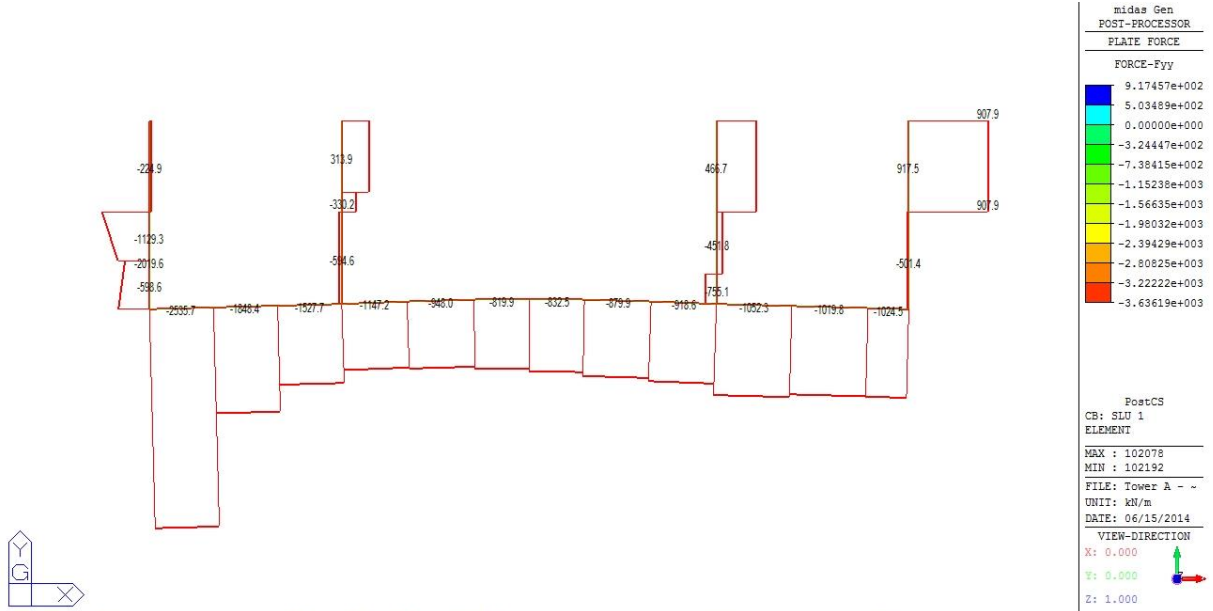


Figure 5.16 – Shear force diagram on the low-rise core due to the ULS 1 combination

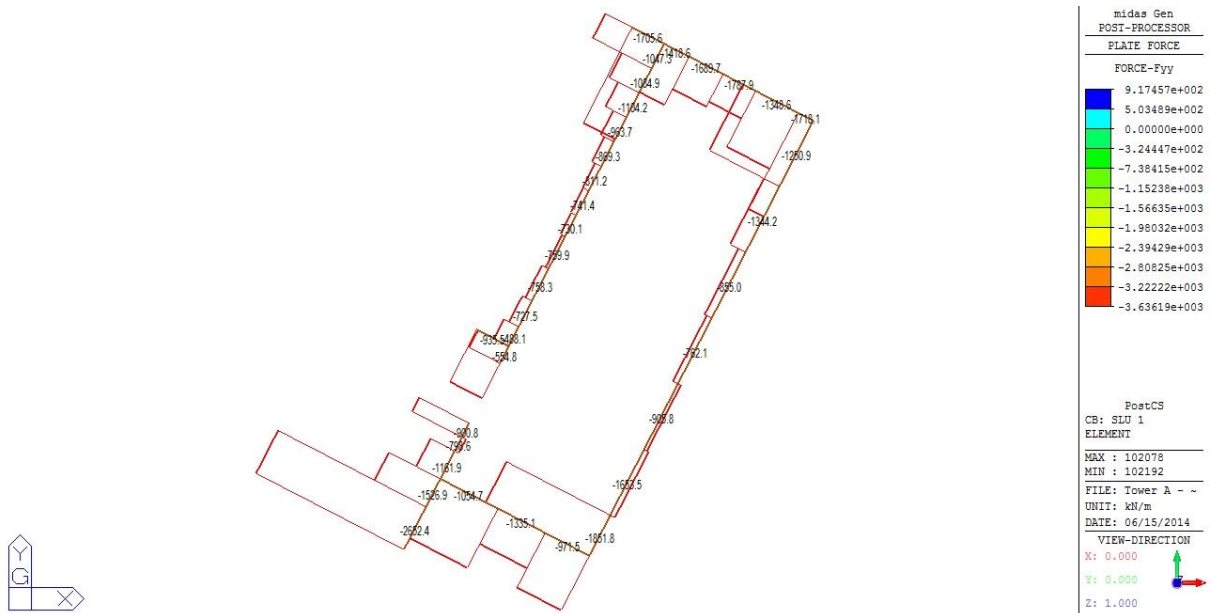


Figure 5.17 - Shear force diagram on the right core due to the ULS 1 combination

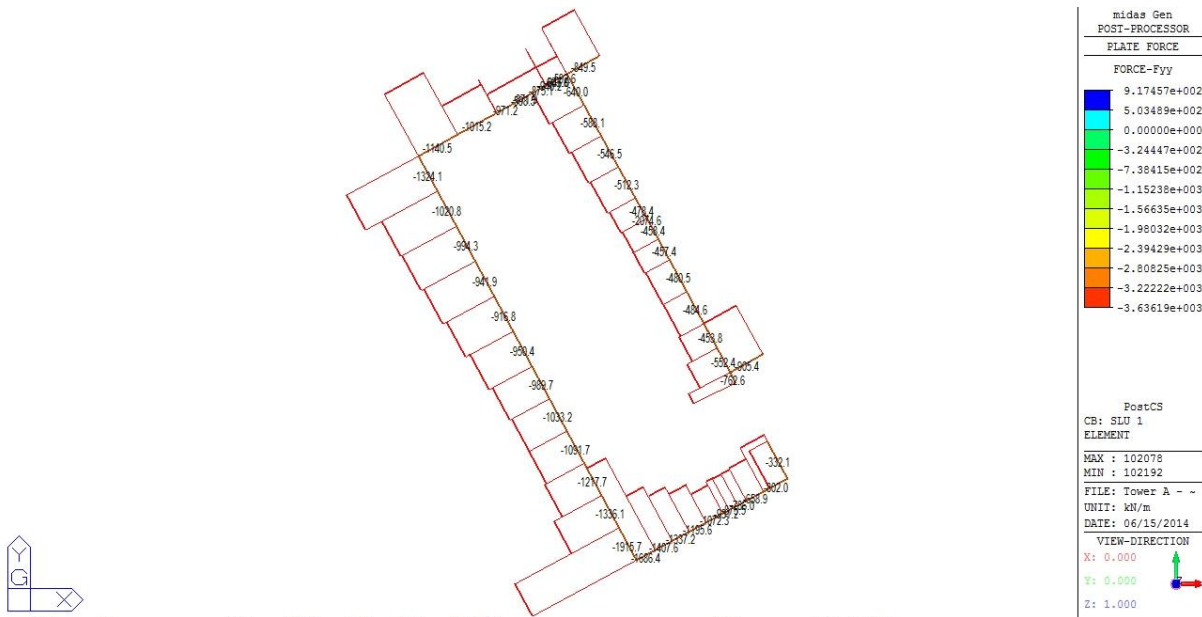


Figure 5.18 - Shear force diagram on the left core due to the ULS 1 combination

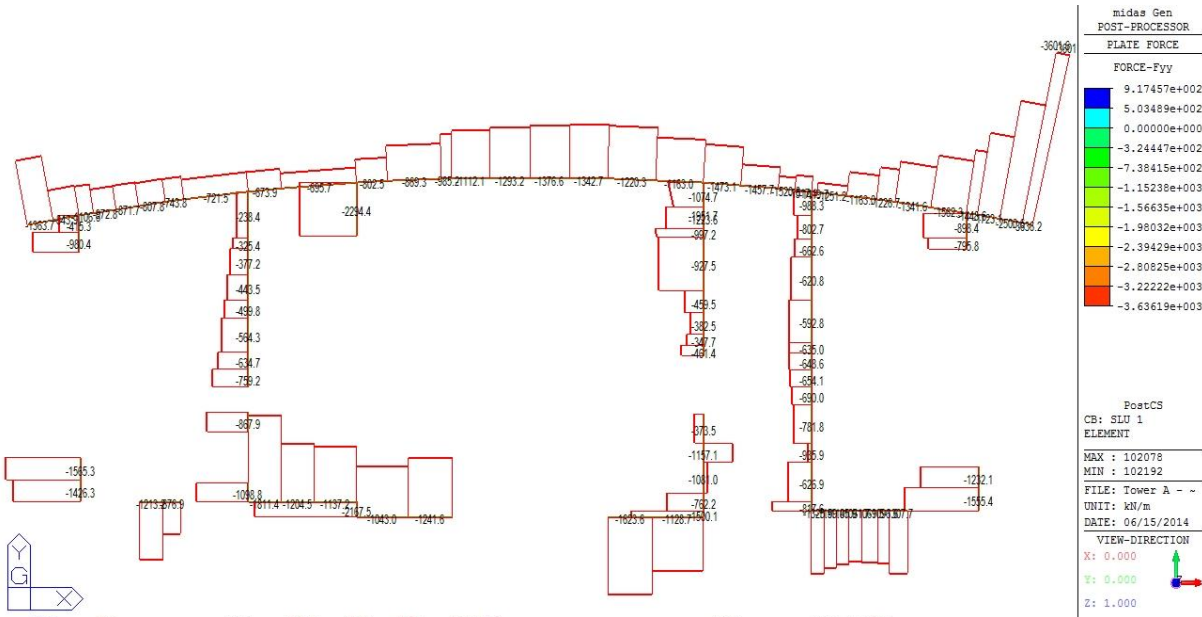


Figure 5.19 - Shear force diagram on the central core due to the ULS 1 combination

In figure 5.20 the displacement of the roof as well as its undeformed position is represented. As it can be seen, the maximum horizontal displacement d_{xy} obtained was 0.03 m and occurs in the area directly under the spire in the direction of the podium side of the building. The average displacement of the roof, characterized by the average displacement of each point that materializes the roof, is 0.016 m.

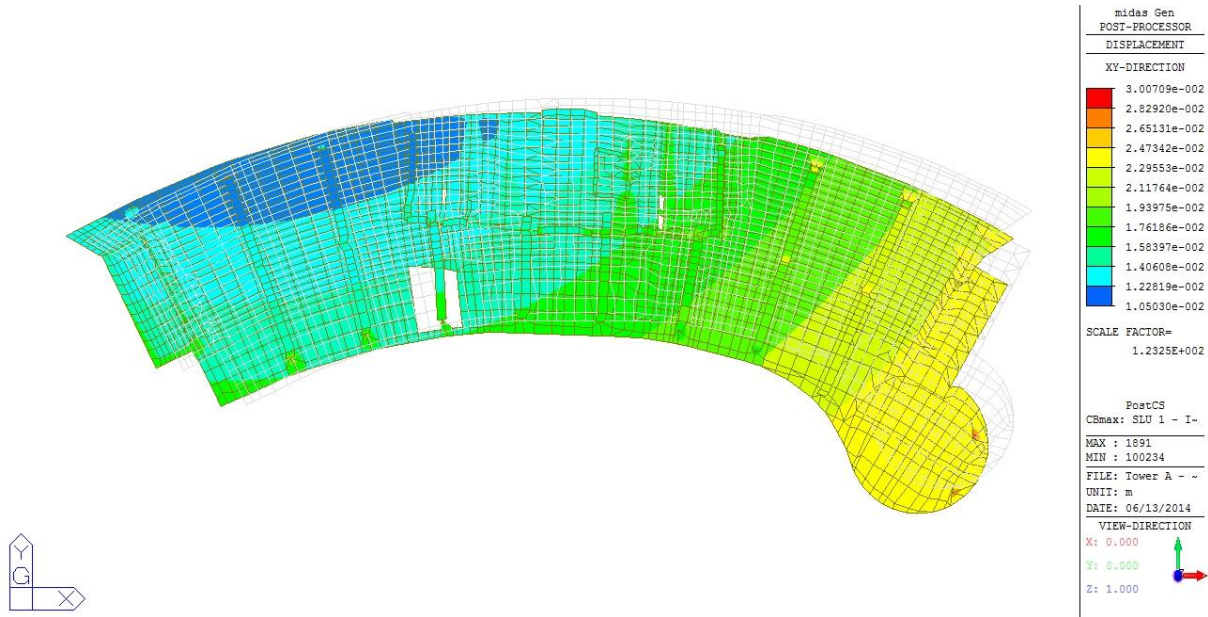


Figure 5.20 –Representation of the displacement of the roof due to the ULS 1 combination

5.3.2. WIND ACTION EFFECT

Once obtained the values of the axial force for the columns of each group with the respective highest value, the shear on each core as well as the displacement on the roof for the ULS 1 combination (without wind action), the respective values for the different combinations which included the action of wind were analyzed.

Table 5.8 shows the maximum axial force, obtained considering wind action, for the columns referred in table 5.7, the direction of wind that led to the respective axial force as well as the increment of axial force experienced by each considered column due to the correspondent State Limit combination that maximizes the axial force.

Table 5.8 – Increase of the axial force on the base of the columns due to the action of wind

Column	Column Group	Combination	Wind Direction	N_w (kN)	$(N_w - N)/N$ (%)
4	Park	ULS 4 - 39	157.5°	-24662.8	10.86
1	Central	ULS 3 - 33	135°	-31878.2	0.18
6	Podium	ULS 4 - 1	0°	-24102.4	8.62
1	Spire	ULS 4 - 76	337.5°	-18641.4	21.46

N_w is the axial force for a combination which includes the action of wind and where, ULS 4 -39 corresponds to the Ultimate Limit State Combination 4 for the wind direction 135° and for the particular set of pressure coefficients which maximize the base resultant moment M_y . In the same way ULS 4 - 1 corresponds to the Ultimate Limit State Combination 4 for the wind direction 0° and for the particular set of pressure coefficients which maximize the F_x base resultant while ULS 4 -76 is for the wind direction 337.5° and for the set of pressure coefficients which maximize the F_x base resultant force.

In order to evaluate the effect of the wind on the different cores, the maximum value present in a specific element of each core was then compared with the value of the shear force in the same element obtained for the Ultimate Limit State 1 combination represented in figures 5.16 to 5.19.

The following figures show the complete view of the diagrams in which is inserted the element with the maximum value of the shear force as well as an amplification of the region of the different cores where this element is located.

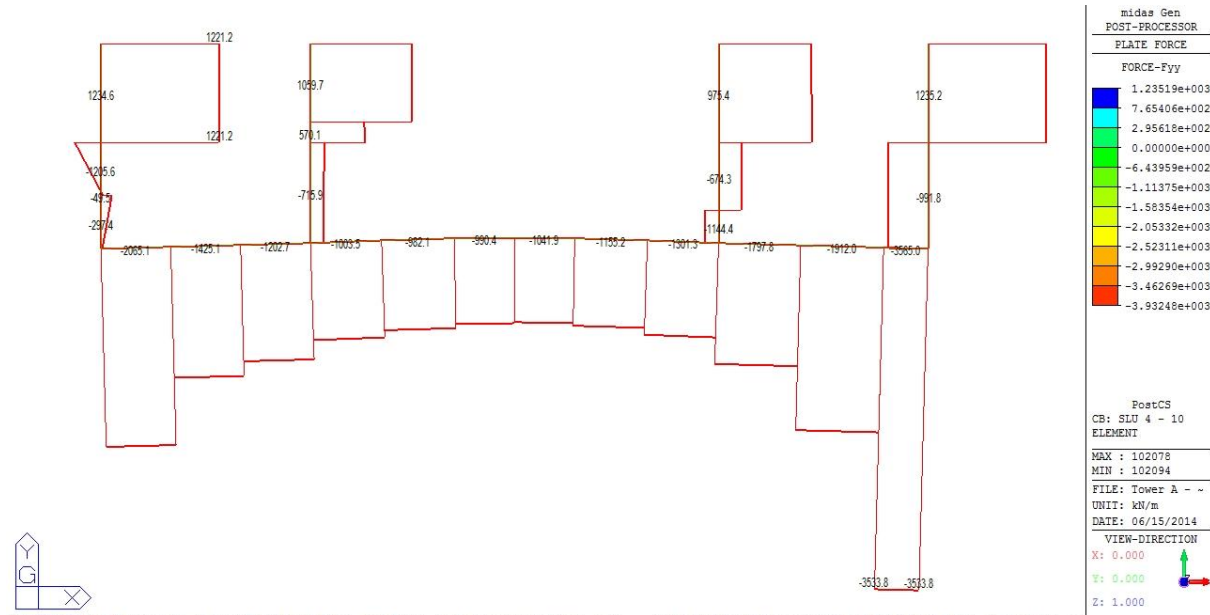


Figure 5.21 – Shear force diagram on the low-rise core due to the ULS 4 – 10 combination

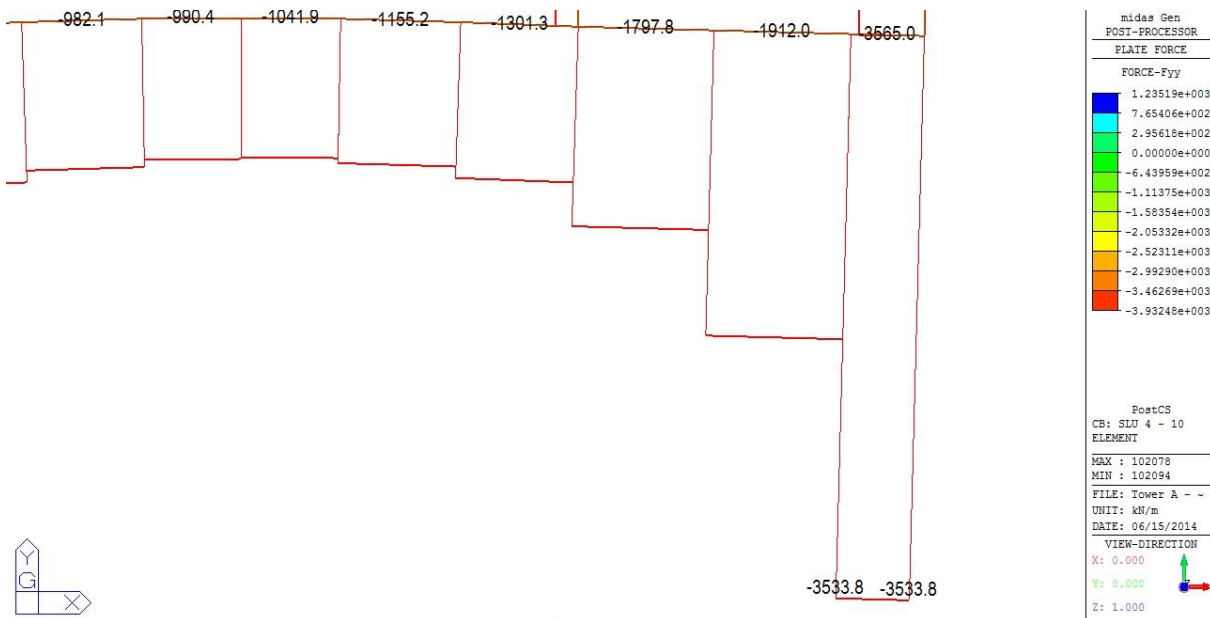


Figure 5.22 – Finite element with the maximum shear force on the base of the low-rise core

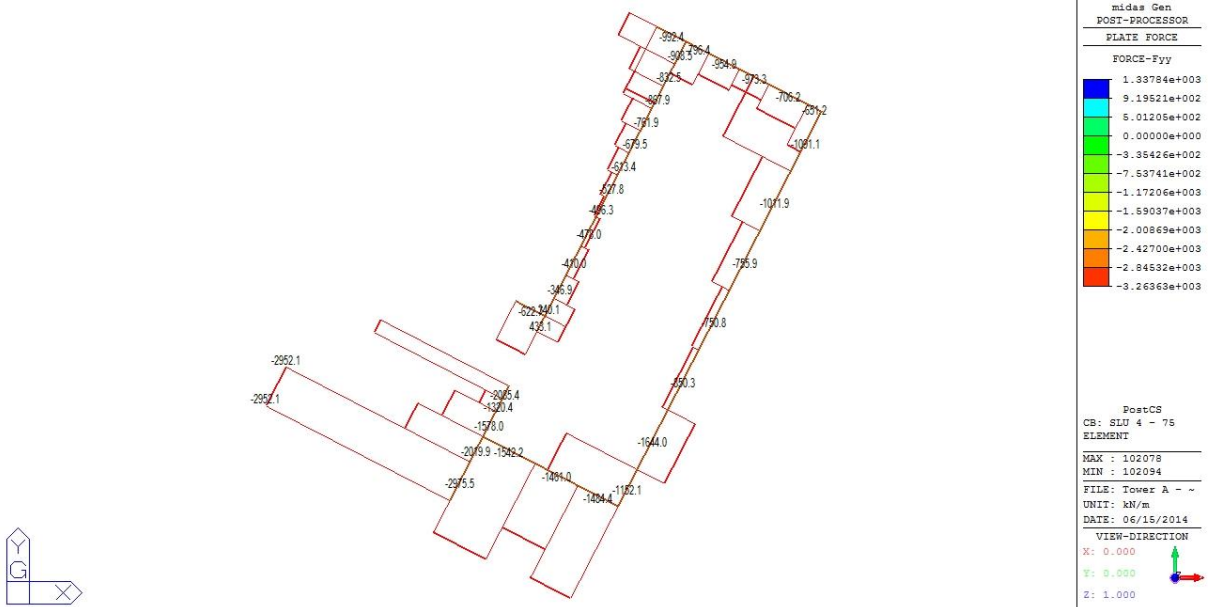


Figure 5.23 – Shear force diagram on the right core due to the ULS 4 – 75 combination

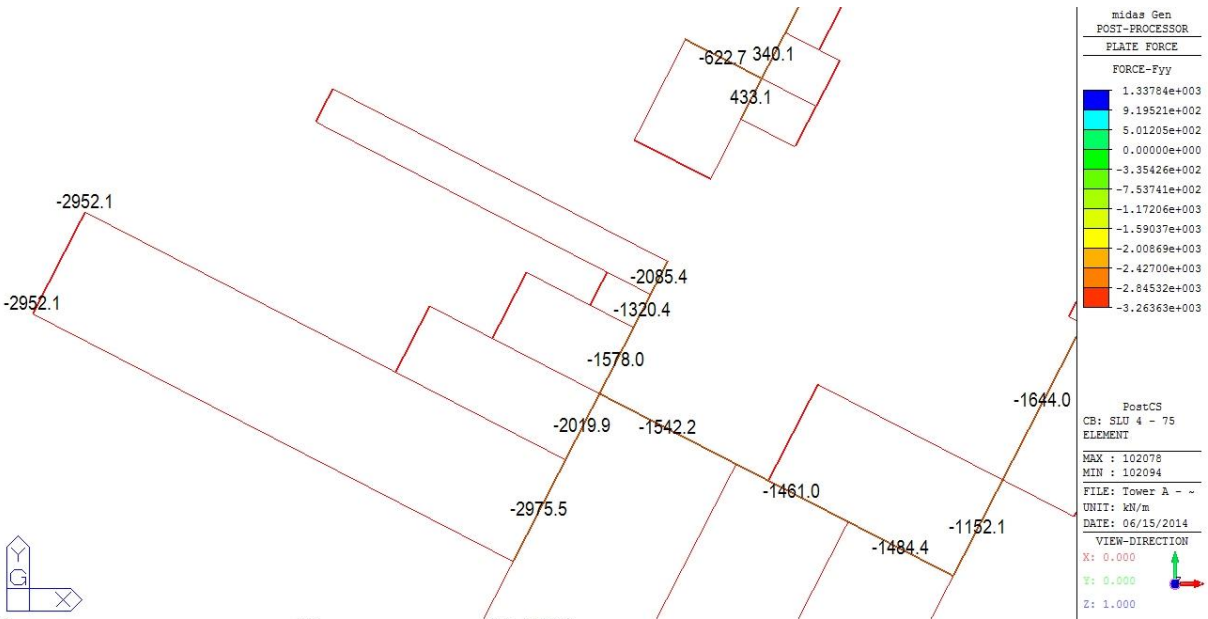


Figure 5.24 – Finite element with the maximum shear force on the base of the right core

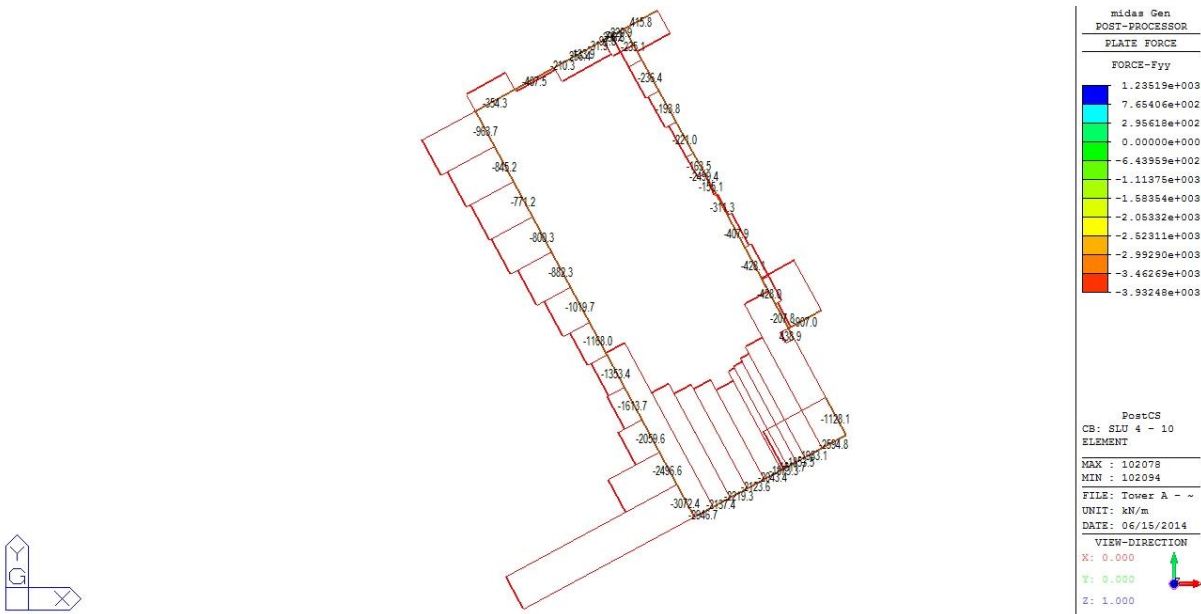


Figure 5.25 - Shear force diagram on the left core due to the ULS 4 – 10 combination

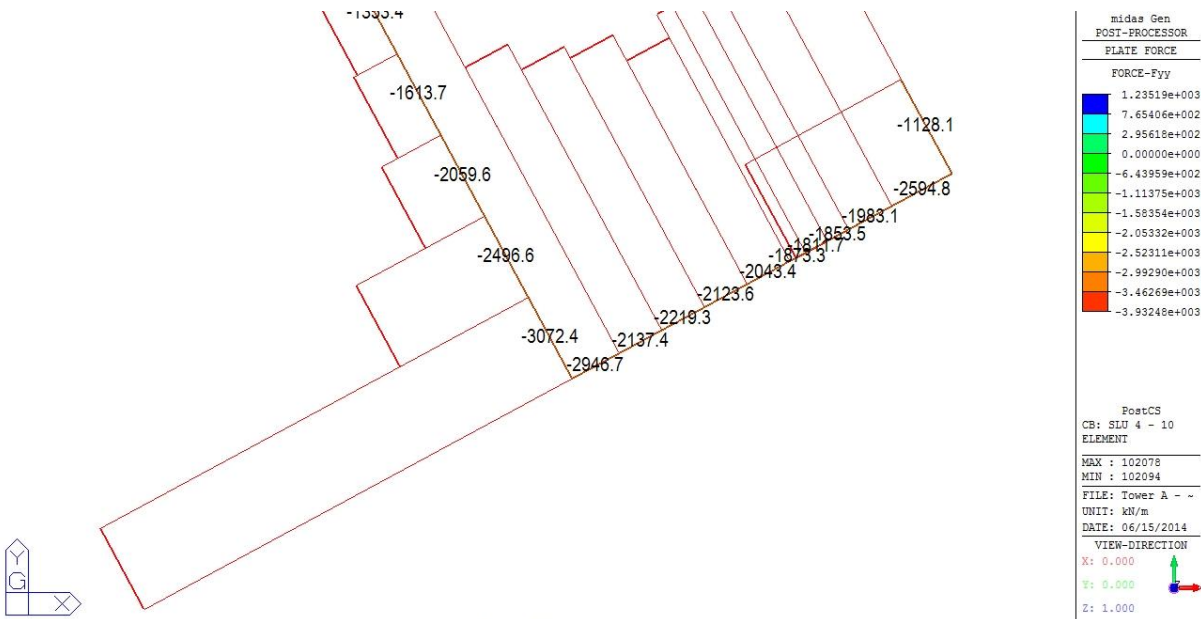


Figure 5.26 – Finite element with the maximum shear force on the base of the left core

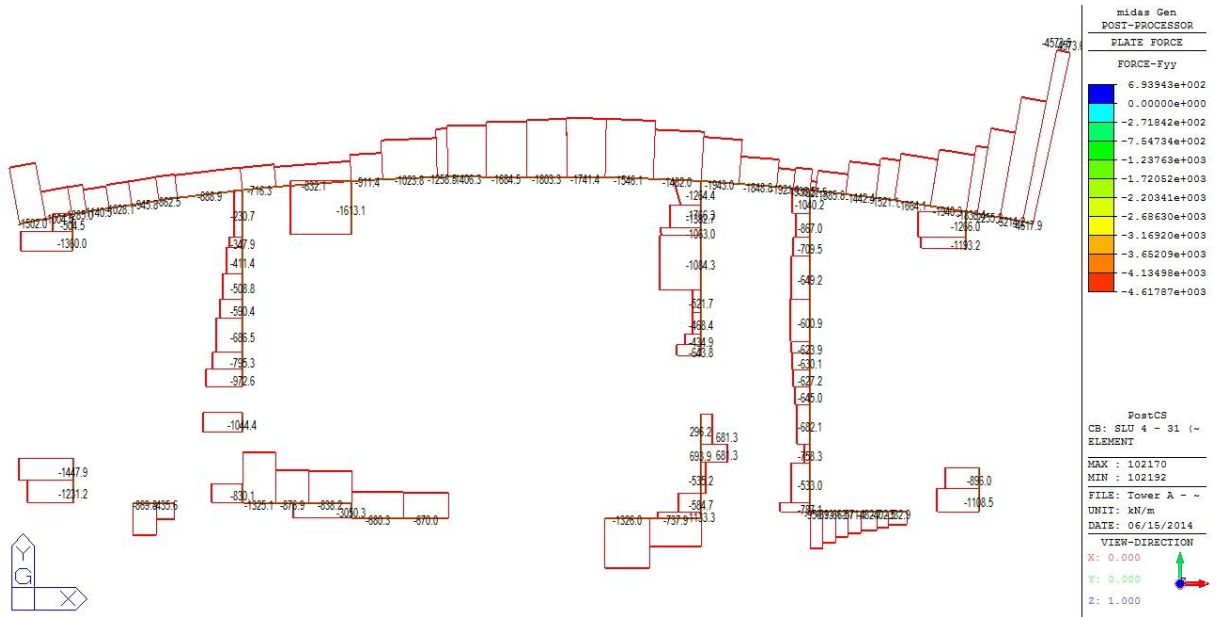


Figure 5.27 - Shear force diagram on the central core due to the ULS 4 – 31 combination

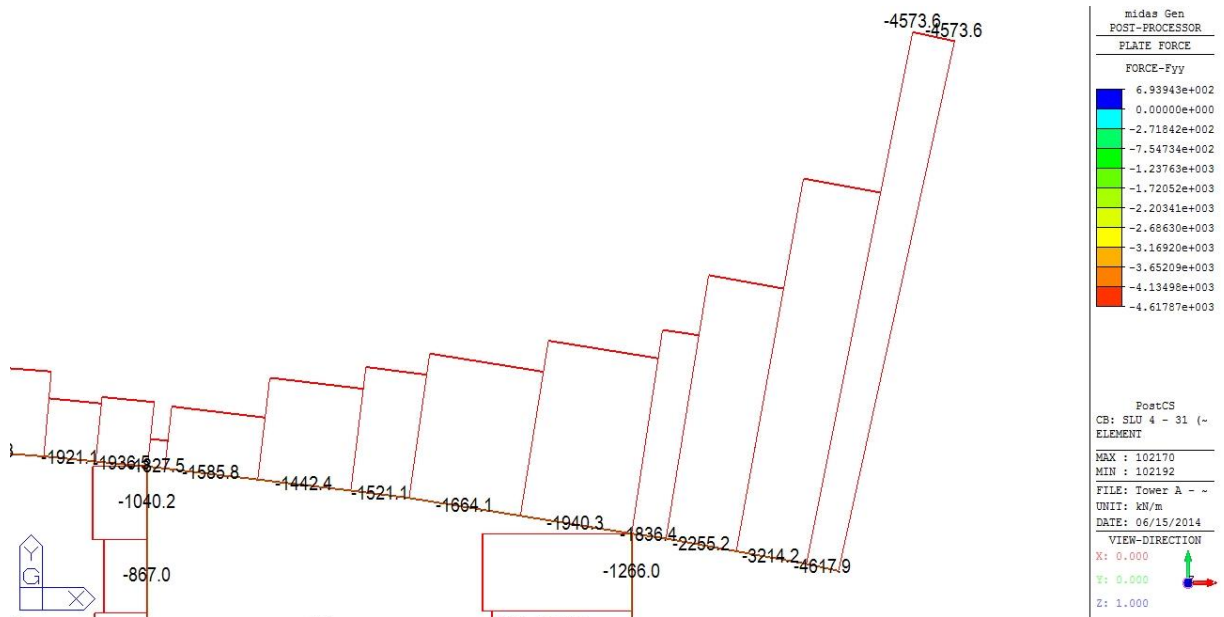


Figure 5.28 – Finite element with the maximum shear force on the base of the central core

Table 5.10 contains the values of the shear force obtained with the ULS 1 (F_{yy}) combination and with the combination that maximizes the shear force on each core as well as the respective increment of shear force obtained.

Table 5.9 – Increase of the shear force on a particular finite element due to wind action

Core	$F_{yy} \left(\frac{kN}{m} \right)$	Combination	$F_{yy,SLUi} \left(\frac{kN}{m} \right)$	$\frac{F_{yy,SLUi} - F_{yy}}{F_{yy}} (\%)$
Low-rise	-1024.5	ULS 4 -10	-3565.0	247.98
Right	-2652.4	ULS 4 - 75	-2975.5	12.18
Left	-1915.7	ULS 4 -10	-3072.4	60.38
Central	-3636.2	ULS 4 -31	-4617.9	27.0

As it can be seen from table 5.10, the different increments obtained in the elements with the maximum shear force when submitted to a particular combination that includes the wind action varies greatly. Furthermore, analyzing specifically the shear force on the element of the central core, and taking into account that the Ultimate Limit State combination 4 – 31 corresponds to the 135° angle direction of the wind action, and that for this wind direction the maximum base resultant force F_X obtained by the wind tunnel tests is 2246 kN, as shown in table 5.1, if one considers the simplified situation in which only the wall of the central core with the X direction (practically the same direction of the correspondent element with the maximum shear) is responsible for the resistance to the wind action, then the value of the shear per unit length on that 20.16 m wall (see figure 3.5) due to wind action would be 111.4 kN/m. Comparing the latter value with the shear force obtained with the ULS 1 combination, the influence of the wind in this element is 3.1% of the shear force obtained with the latter combination. However, this result is an outcome of the considered local analysis which is affected by the impossibility of expansion of the wall of the core which leads to the development of shear forces even without the contribution of horizontal loads. If the integration of the shear force of all the elements of the core for the ULS 1 combination was made, its value would be very low since that there is no external horizontal action considered on this combination.

On the contrary a more “generalized” analysis, representing the behavior of the entire core would lead to a result which would not be affected by the effect of the impossibility of the wall to expand. This can be obtained through the integration of the shear forces on all the elements, which in the case of the ULS 4 – 31 combination, the final value would correspond approximately to the base resultant force $F_X = 2246 \text{ kN}$ mentioned before. However, this is a complex procedure to be made due to the large number of elements that materialize each core and due to their different lengths and directions.

A more simple procedure was adopted to obtain the values of the shear force acting in each core. In this procedure, a single point located in the center of gravity of the cross-section of each core was created and then connected to the points that materialize the base of the respective core by means of rigid links. This way the value of the 3 reactions R_X , R_Y , R_Z and of the 3 moments M_X , M_Y and M_Z acting on the base of the core would act on this single point instead. Repeating this process for all the cores, the effect of the wind on each core can be evaluated.

For this purpose, another numerical model was developed from the original by deleting the foundation mat and creating the rigid links and the points mentioned above.

The results obtained with this procedure for the ULS 1 combination are shown in table 5.10.

Table 5.10 – Shear force at the base of each core due to the ULS 1 combination

Core	Combination	F_x (kN)	F_y (kN)
Central	ULS 1	1011.62	-4523.76
Low rise	ULS 1	-399.71	-199.375
Right	ULS 1	-2724.8	-906.26
Left	ULS 1	2388.42	1329.06

Considering only the wind action in the 135° direction without the influence of any combination or reduction factor, the total horizontal reaction obtained on the base of the tower along the X axis was 2979.65 kN. The difference between the latter and the one obtained in the wind tunnel can be explained by the influence of the position of the floors that are located near the boundary between two pressure taps. The force to be applied on the edge of the slabs in the numerical model corresponds to the pressure given by the pressure tap, acting on an area which is defined by the width of the pressure tap at full-scale and by a height which corresponds to the sum of half the interstory height over the slab and half the interstory height below the slab. For slabs that are located near the edges of two pressure taps, half the height considered above or below the slab can be influenced by two different pressures, making it more difficult and time consuming to determine the correspondent force to be applied on the numerical model, thus for the slabs in which this situation was verified, the pressure tap with the larger pressure was considered to be acting on the influence area of the slab, leading to a more simplified, yet conservative approach to this difficulty.

The results for each core, of the latter procedure are shown on the tables below. Table 5.11 contains the absolute maximum values of the shear due to the mean and fluctuating components of wind action $F_{W,X}$ and $F_{W,Y}$ while the values shown in table 5.12 were obtained only for the critical directions and within each one of these directions for the configurations that maximize the M_x , M_y and M_z base resultant forces. This latter approach was considered so that the comparison between the values of the shear considering only the quasi-static component and the same values considering both the quasi-static and resonant components of the response may be possible to develop in Chapter 6.

Table 5.11 – Increase of the shear force at the base of each core due to wind action

Core	Direction X		Direction Y		$\frac{F_{W,X} - F_x}{F_x}$	$\frac{F_{W,Y} - F_y}{F_y}$
	$F_{W,X}$ (kN)	Combination	$F_{W,Y}$ (kN)	Combination	(%)	(%)
Central	6437.13	ULS 4 – 39	-9051.15	ULS 4 – 51	536.32	100.08
Low rise	-3992.29	ULS 4 – 10	-734.10	ULS 4 – 51	898.80	268.20
Right	-5987.27	ULS 4 – 1	-6576.38	ULS 4 – 76	119.73	625.66
Left	4271.14	ULS 4 - 37	6302.93	ULS 4 – 10	78.83	374.24

Table 5.12 – Shear force at the base of each core for the critical directions

Core	Direction X		Direction Y	
	$F_{W,X}$ (kN)	Combination	$F_{W,Y}$ (kN)	Combination
Central	6437.13	ULS 4 – 39	-8689.67	ULS 4 – 59
Low rise	-3093.73	ULS 4 – 4	-711.46	ULS 4 – 59
Right	-5918.76	ULS 4 – 4	-6150.19	ULS 4 – 75
Left	4238.83	ULS 4 – 39	4849.406	ULS 4 – 4

As it can be seen from table 5.11, and as it was expected, the shear on the different cores has a great increase due to the lateral force developed by the wind action.

In order to classify the structure according to its resistant system to horizontal actions, the cores or the frames materialized by the columns and horizontal diaphragms (slabs), a comparison between the shear force on the base of the cores and on the base of the columns was made. For this purpose, the horizontal supports of the wall facing the park were released so that its influence wouldn't distort the results.

Table 5.13 shows the summation of the shear on the base of the different cores and columns as well as the percentage of shear force on the cores normalized to the sum of this latter value with the shear on the columns. These values were obtained for the combinations that maximized the shear on a certain column for the X and Y directions and also for the combinations that maximized the shear on some core for both the X and Y directions.

Table 5.13 – Influence of the action of wind on the cores and on the columns

Element	Direction	Combination	$\sum F_{cores}$ (kN)	$\sum F_{columns}$ (kN)	$\frac{\sum F_{cores}}{\sum F_{cores} + \sum F_{columns}}$ (%)
Column 2 Park	X	ULS 4 – 10	3968.63	1338.84	74.77
Column 6 Park	Y	ULS 4 – 76	14220.63	6923.05	67.26
Right Core	X	ULS 4 – 41	-3306.42	-2392.10	58.02
Central Core	Y	ULS 4 – 36	-23380.50	-4076.57	85.15

Analyzing the values of the column on the right side of table 5.13 it is clear that for every considered combination, the horizontal load developed by the action of wind leads to a larger shear on the cores than on the columns and thus the resistant system is materialized by the cores.

Figure 5.29 shows the displacement of the roof and its undeformed position for the SLS 3 – 10 combination (22.5° wind direction) with which the larger displacement at roof level is achieved. The Serviceability Limit State combination 3 is referred, as stated before, to a 10 year return period due to the fact that this is usually one of the return periods considered to evaluate the behavior of a structure for comfort related issues such as excessive displacements and accelerations of the structure.

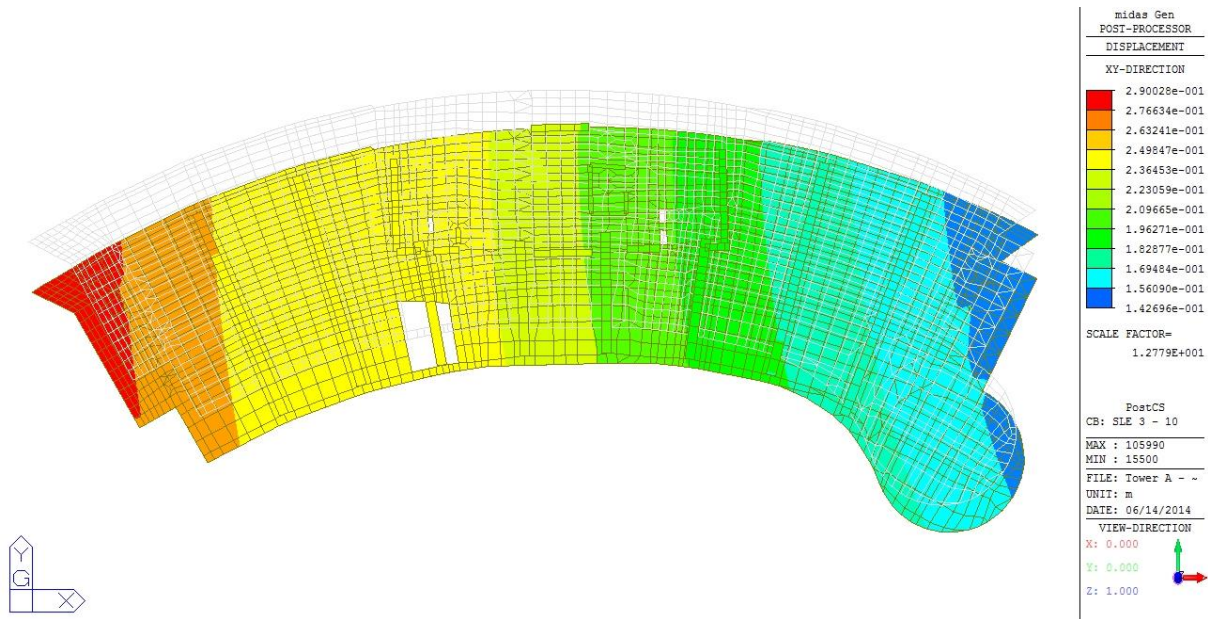


Figure 5.29 - Representation of the displacement of the roof due to the SLS 3 - 10 combination

The functional performance and behavior of a structure is controlled as seen earlier by the Serviceability Limit States which include the control of deformations and vibrations. The first is influenced by both the quasi-static and dynamic components of the response of the structure to wind action while the latter depends only on the dynamic behavior.

If the deformations are controlled, the damage to the cladding on the building facade, to partitions and to interior finishes will also be under control. Furthermore, a limited deformation will contribute not only to reduce the effects of motion perceptibility but will also limit the P-Delta effects [44, 45].

These deformations are usually controlled by drift limits which can be specified in terms of an average for the whole building, known as total building drift index, expressed as

$$\frac{\Delta}{H} \tag{5.8}$$

where Δ is the deflection of the last occupied floor and H is the height of the building.

The drift limits can also be specified as interstory drifts or as the interstory drift index which can be defined by the following expression

$$\frac{\delta_n - \delta_{n-1}}{h} \tag{5.9}$$

where δ_n is the displacement of the n^{th} floor, δ_{n-1} is the displacement of the $(n - 1)^{th}$ floor and h is the distance between consecutive floors [44].

Usually, the serviceability of a structure is considered to be ensured if the total building drift obtained is inferior to $H/100$ to $H/600$ and if the interstory drift is smaller than $h/200$ to $h/600$ [44]. Although the value to be considered depends on the type of building being analyzed and on the materials used in the construction, the most widely used values are the ones contained in the interval $1/400$ to $1/500$.

Table 5.14 shows the values of the Floor 1 and Roof interstory drift index for the critical directions already mentioned.

Table 5.14 – Interstory drift at roof and floor 1 level

Combination	Floor 1 drift	Roof drift
ULS 3 – 1 (0°)	1/1634	1/655
ULS 3 – 23 (90°)	1/2981	1/1780
ULS 3 – 39 (157.5°)	1/1228	1/641
ULS 3 – 44 (180°)	1/1339	1/717
ULS 3 – 58 (247.5°)	1/1250	1/810
ULS 3 – 63 (270°)	1/2030	1/2179
ULS 3 – 75 (315°)	1/2334	1/1308

Considering a limit of $h/600$ for the interstory drift design value s_{di} , the respective limit of the interstory drift index is $1/600$.

In order to allow an easier and faster analysis of this limit, the distribution of both the floor 1 and roof drift index for each direction is represented in figure 5.30.

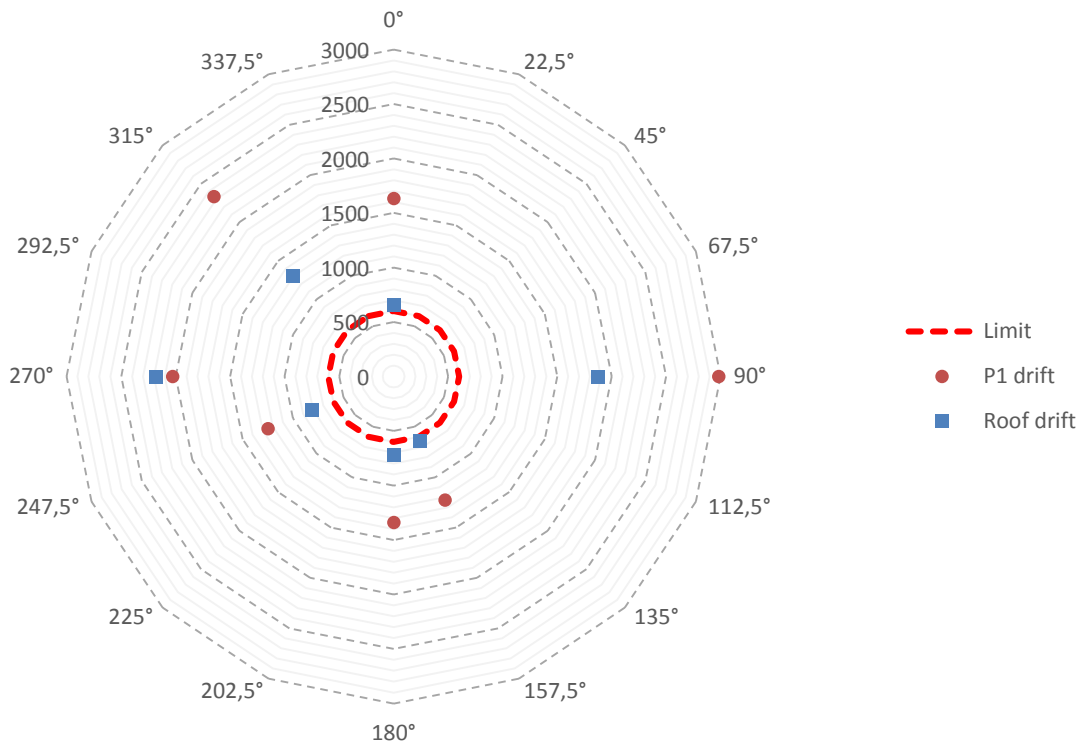


Figure 5.30 – Map of the Roof and Floor 1 drift according to the different wind directions

It is clear, from the observation of figure 5.30, that the drift of both the levels for every considered direction respects the established limit of $1/600$. Furthermore it can be seen that for every direction

with the exception of the 270° angle direction, the drift developed on the roof exceeds the one developed between the ground and the first floor.

The horizontal displacement between the floors is governed not only by the shear acting on each one but also by the stiffness of the vertical elements that connect them.

The drift on floor 1 is a result of a larger shear value acting on the different vertical elements than the one acting on the same elements located between the roof and floor 31. However, as shown in chapter 3, the low-rise core is only present at the height of the 14th floor, leading to a reduction of the overall stiffness of the floors placed above this level. Furthermore, the cross section of the different groups of columns is reduced along the height of the building as shown in table 3.2, increasing even more the difference in stiffness between the roof and the floor 1 levels. Thus, for the current case, the stiffness is the responsible for the larger drift at roof level.

Once evaluated the interstory drift on the upper level of the building and on its lower aboveground part, the considered limit of the overall displacement design values at roof level s_d was also verified.

The values of the total building drift are shown in table 5.15 and represented, along with the respective limit, in figure 5.31.

Table 5.15 – Total building drift

Combination	Total building drift
ULS 3 – 1 (0°)	1/696
ULS 3 – 23 (90°)	1/3148
ULS 3 – 39 (157.5°)	1/779
ULS 3 – 44 (180°)	1/863
ULS 3 – 58 (247.5°)	1/923
ULS 3 – 63 (270°)	1/2244
ULS 3 – 75 (315°)	1/1216

For the case of the total building drift, a $H/500$ limit for the overall displacement design value at roof level was considered. In the same way as for the interstory drift at roof and floor 1 level, a representation of the limit and of the values of the drift index was obtained.

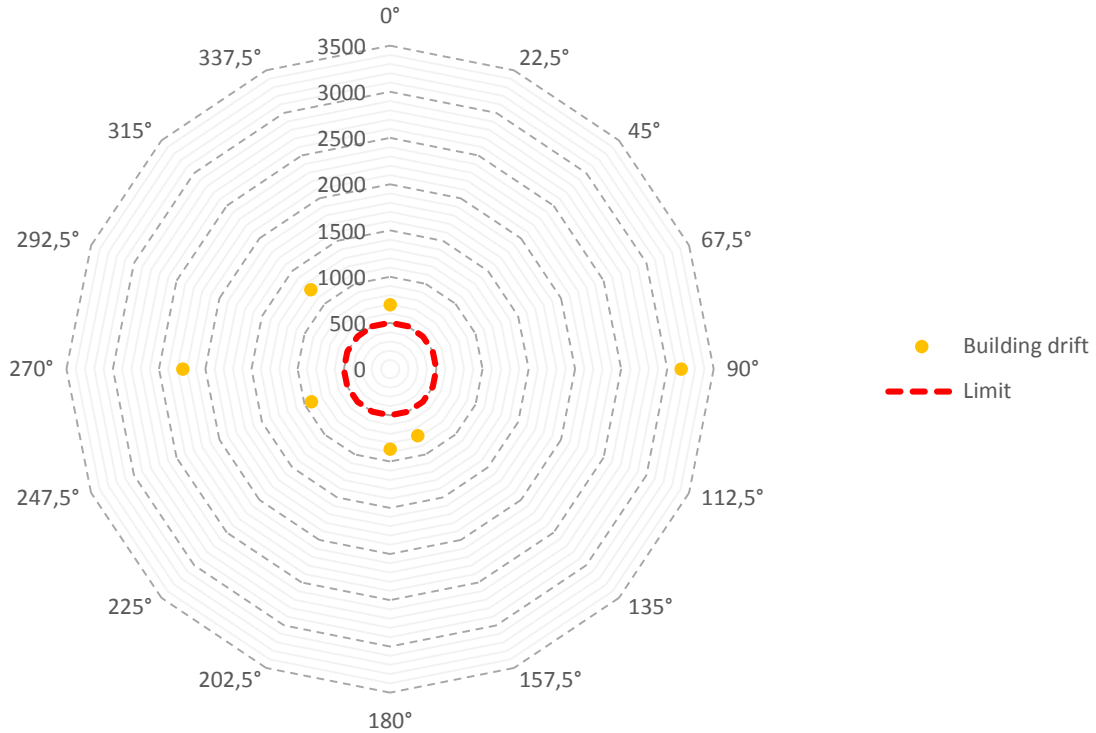


Figure 5.31 - Map of the total building drift according to the different wind directions

As it can be seen from the figure above, the total building drift for every critical direction respects the $1/500$ limit imposed.

As the interstory drifts and the total building drift are comprised within the current limits, it can be stated that the Unicredit high-rise building shows a good functional performance.

6

Dynamic Effects of Wind The Unicredit High-Rise Building

6.1. INTRODUCTION

After evaluating the effect of the static component of the wind action on the structure, namely through the evaluation of different forces at the base of the columns and at the base of the cores but also by evaluating the induced displacements, it becomes crucial to evaluate the effect of the resonant component of the wind action on the response of the building.

In the following chapter, a sensitivity analysis of the resonant moments to changes on the frequency and damping of the structure is developed. The method used to obtain the equivalent static forces of the resonant component of the action of wind is also shown.

The obtained equivalent static forces inputted on the numerical model were then used to extract different results which ultimately allowed a comparison between the wind action with and without its resonant component.

Furthermore, the determination of the displacements and accelerations developed on the structure due to the total wind action allowed an evaluation of the functional performance of the Unicredit high-rise building.

6.2. RESONANT WIND LOADS

Once determined the mean and fluctuating components of the responses, the resonant dynamic component has to be added. The latter component is represented by its respective resonant wind loads which are equivalent static loads that are applied to the building so that the dynamic effects of the wind action can be taken into account.

As mentioned before, the base balance was used on the wind tunnel for the two different configurations B1 and B2, for the tower without and with the spire, respectively. However, for the evaluation of the resonant loads, only the latter was considered as it corresponds to the configuration that maximizes the stresses on the structure.

For the 4 principal directions 0° , 90° , 180° and 270° plus the 3 directions which maximize the base forces 157.5° , 247.5° and 315° stated earlier, the mean value, the maximum and minimum absolute value and

the maximum and minimum Gumbel value, with a 50 year return period, have been estimated for each moment M_x , M_y and M_z in the local reference.

As seen on chapter 4, the real duration of the simulated phenomenon is 149.205 times the duration of the wind tunnel test thus corresponding to 26856.9 s in the real time scale. Furthermore, for the 10 minute average, the wind tunnel test led to 44 time history series each one with 2045 samples. Such a high amount of data is very important because it enables the averaging of a large number of time histories, thus leading to a smooth shape of the Power Spectral Density (PSD) function.

In order to determine the resonant wind forces to be applied to the tower, the frequencies of the structure had to be obtained. For that purpose, a copy of the used model was created and the construction stage deleted, since it does not influence the results of the frequencies and reduces the computational effort required. Furthermore the different existing loads were turned into masses.

The participation coefficients of the masses to be applied on the tower are shown in table 6.1.

Table 6.1 – Participation coefficients of the masses

Load	Participation Coefficient
Self-weight	1.0
Dead Load	1.0
Facade weight	1.0
Live Load	0.3
Live Load on stairs	0.3
Snow	0.2
Spire facade	1.0
Spire grill	1.0
Spire Live Load	0.3
Spire Snow	0.2

Table 6.2 contains, for the first 20 modes, the respective frequencies as well as the respective periods.

Table 6.2 – Natural frequencies and respective periods

Mode Number	Frequency		Period
	ω (rad/s)	f (Hz)	T (s)
1	1.3174	0.2097	4.7695
2	1.4794	0.2354	4.2472
3	1.8429	0.2933	3.4093
4	4.3839	0.6977	1.4333

5	4.7567	0.7571	1.3209
6	6.0844	0.9684	1.0327
7	6.6312	1.0554	0.9475
8	7.0130	1.1162	0.8959
9	7.5315	1.1987	0.8343
10	8.3505	1.3290	0.7524
11	9.8512	1.5679	0.6378
12	13.1380	2.0910	0.4782
13	14.6902	2.3380	0.4277
14	15.8445	2.5217	0.3966
15	16.7599	2.6674	0.3749
16	17.2693	2.7485	0.3638
17	17.9523	2.8572	0.3500
18	19.1652	3.0502	0.3278
19	19.7825	3.1485	0.3176
20	20.5791	3.2753	0.3053

Table 6.3 contains, for the first 20 modes, the modal participation masses for the translations along the X, Y and Z axis as well as the modal participation mass for the rotation along the Z axis.

Table 6.3 – Modal participation masses

Mode Number	Translational-X		Translational-Y		Translational-Z		Rotational-Z	
	Mass(%)	Sum(%)	Mass(%)	Sum(%)	Mass(%)	Sum(%)	Mass(%)	Sum(%)
1	3,9972	3,9972	43,953	43,953	0,0001	0,0001	2,53	2,53
2	42,9543	46,9515	3,0352	46,9882	0,0011	0,0012	0,7747	3,3047
3	0,2979	47,2494	1,8816	48,8698	0,0051	0,0063	42,1672	45,4718
4	0,1503	47,3997	0,0059	48,8757	0	0,0063	0,0018	45,4736
5	0,0179	47,4176	0,0081	48,8839	0,0003	0,0066	0,012	45,4857
6	12,3476	59,7652	0,001	48,8849	0,0081	0,0146	0,0828	45,5684
7	0,004	59,7692	13,5387	62,4236	0,0337	0,0484	0,6357	46,2041
8	0,1647	59,9339	0,0838	62,5074	0,0016	0,05	0,0001	46,2042
9	0,0017	59,9357	0,0042	62,5116	0,0011	0,0511	0,0012	46,2054
10	0,2521	60,1877	0,3493	62,8609	0,0065	0,0576	11,6139	57,8193
11	0,0823	60,27	0,047	62,908	0,0023	0,06	0,5641	58,3834

12	0,9655	61,2355	0,0813	62,9893	0,0476	0,1076	0,007	58,3904
13	4,5725	65,808	0,1306	63,1199	0,4546	0,5621	0,0909	58,4813
14	0,073	65,881	4,8753	67,9952	0,2333	0,7954	0,0474	58,5287
15	0,0049	65,8859	0,1646	68,1598	0,8376	1,633	0,3882	58,9169
16	0,0003	65,8862	0,0161	68,1759	0,8811	2,5141	0,0701	58,9869
17	0,015	65,9012	0,1192	68,295	66,5418	69,0559	0,0294	59,0163
18	0,0881	65,9894	0,0181	68,3131	4,1654	73,2213	0,3903	59,4067
19	0,2095	66,1989	0,0869	68,4	3,4645	76,6859	2,7958	62,2025
20	0,0056	66,2045	0,0143	68,4143	0,0076	76,6935	0,0518	62,2543

Figures 6.1 to 6.6 show the deformed shapes of the first 3 natural modes of the structure.

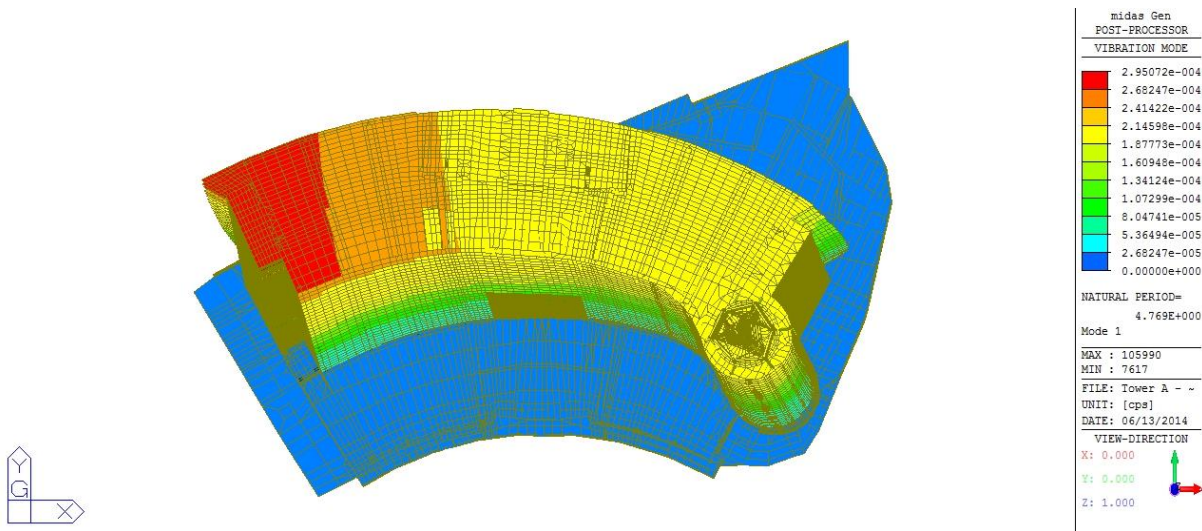


Figure 6.1 – Top view of mode shape 1

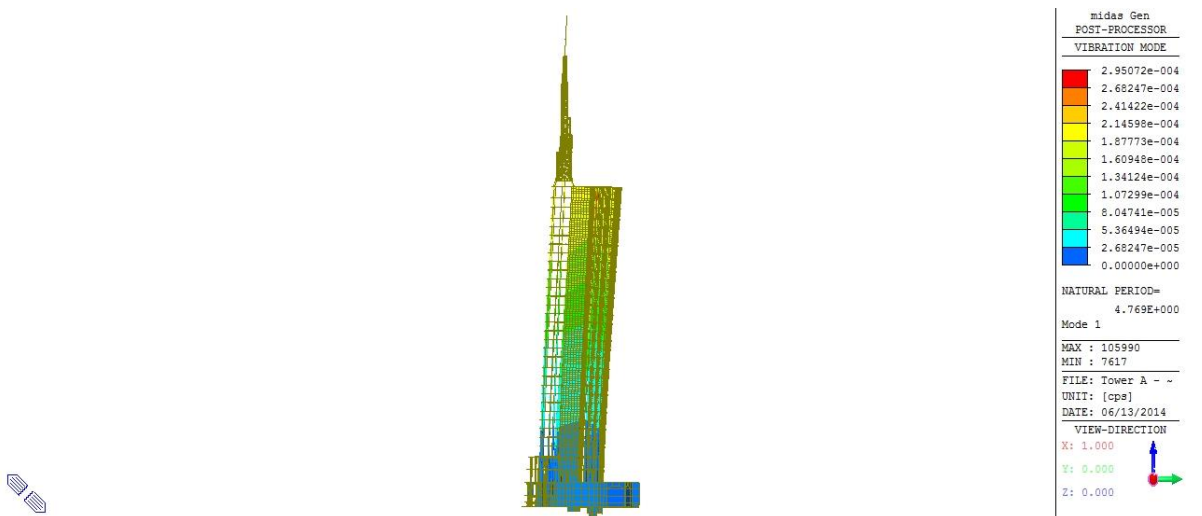


Figure 6.2 – Side view of mode shape 1

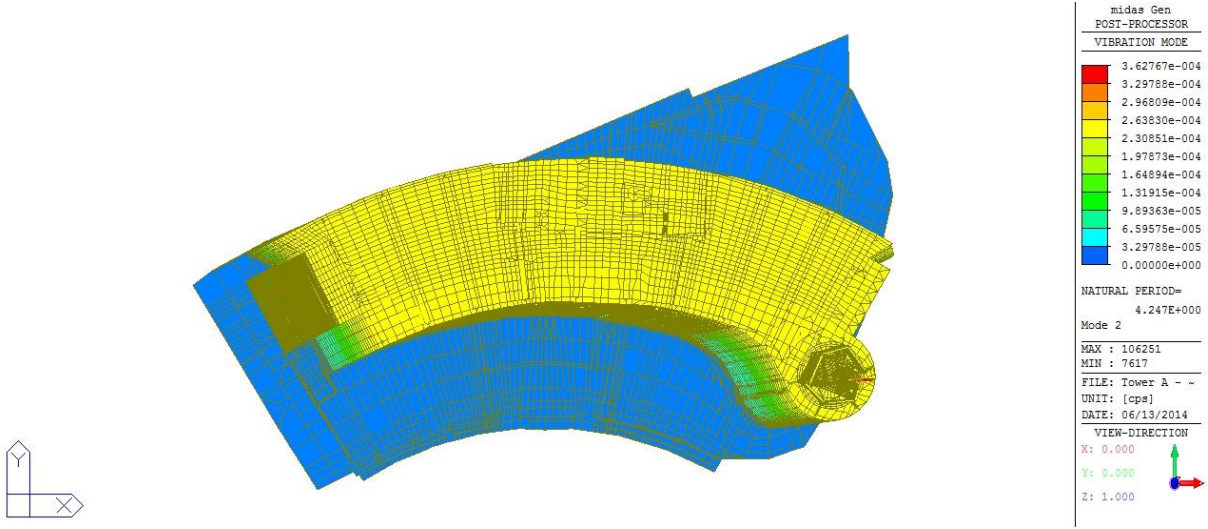


Figure 6.3 – Top view of mode shape 2

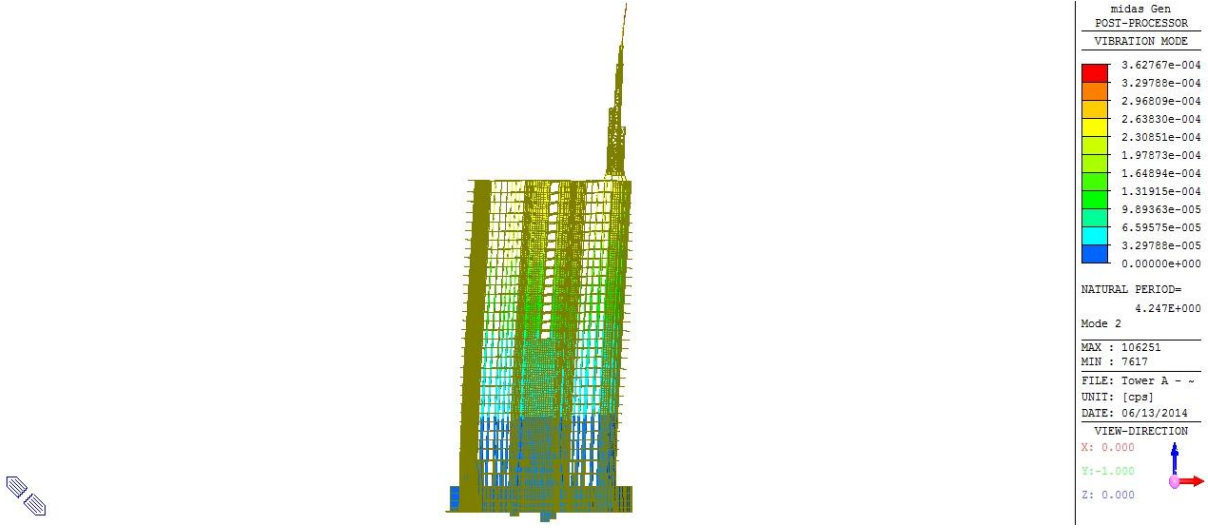


Figure 6.4 – Front view of mode shape 2

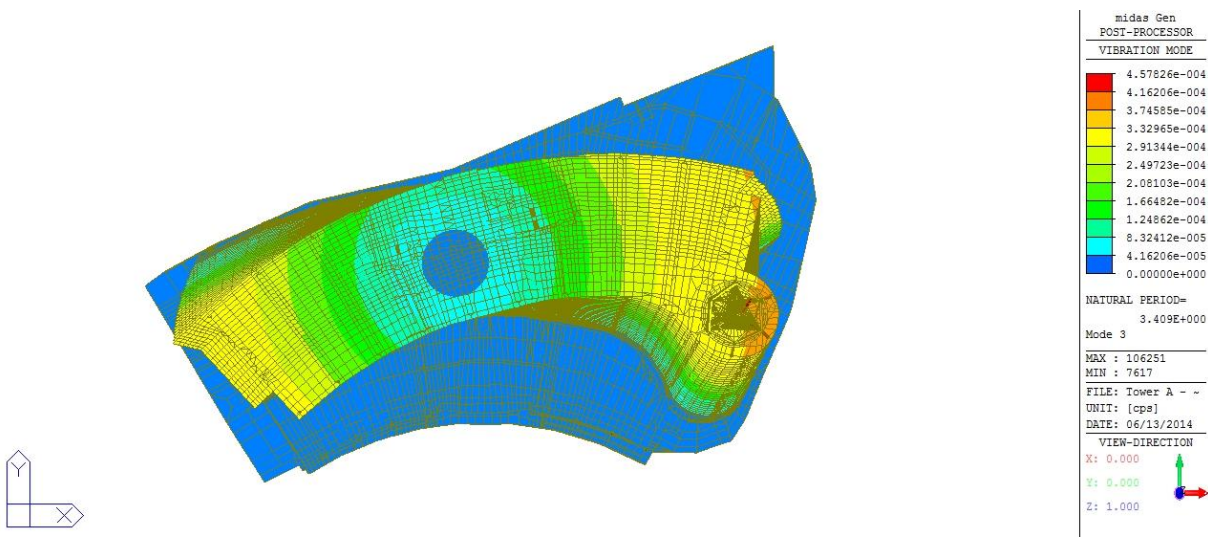


Figure 6.5 – Top view of mode shape 3

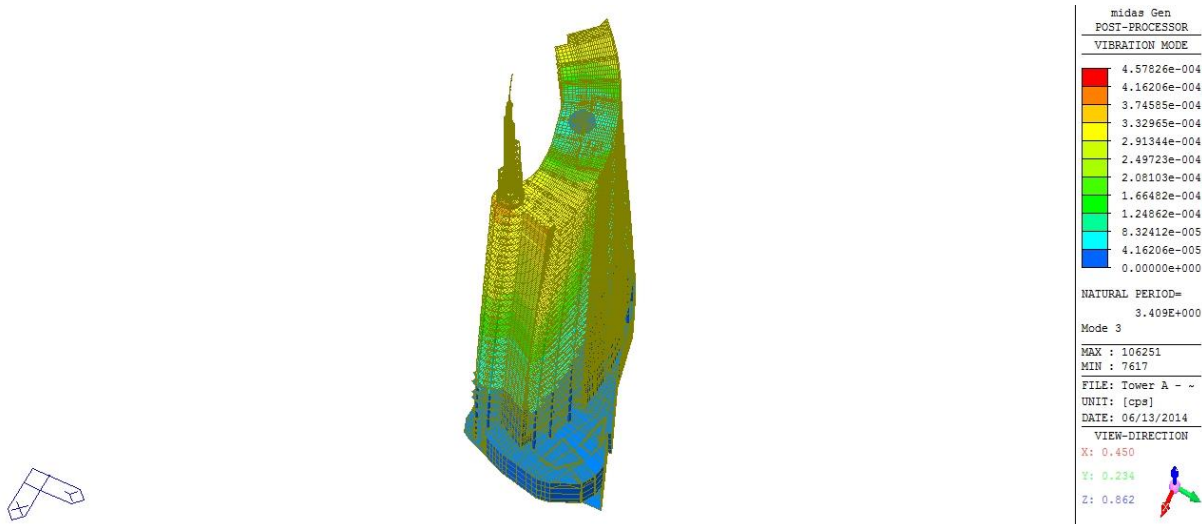


Figure 6.6 – Perspective view of mode shape 3

Analyzing the figures shown above it can be seen that the first three natural mode shapes correspond, respectively to a bending along the X axis, a bending along the Y axis and a torsion along the Z axis.

As mentioned before the time history of each base resultant moment, recorded for each direction can be used to obtain the respective Power Spectral Density $S_M(f)$, needed to determine the resonant dynamic component of the response, by means of a Fourier transform.

The figures below represent the obtained PSD of the M_X , M_Y and M_Z base resultant moments for the 0° direction.

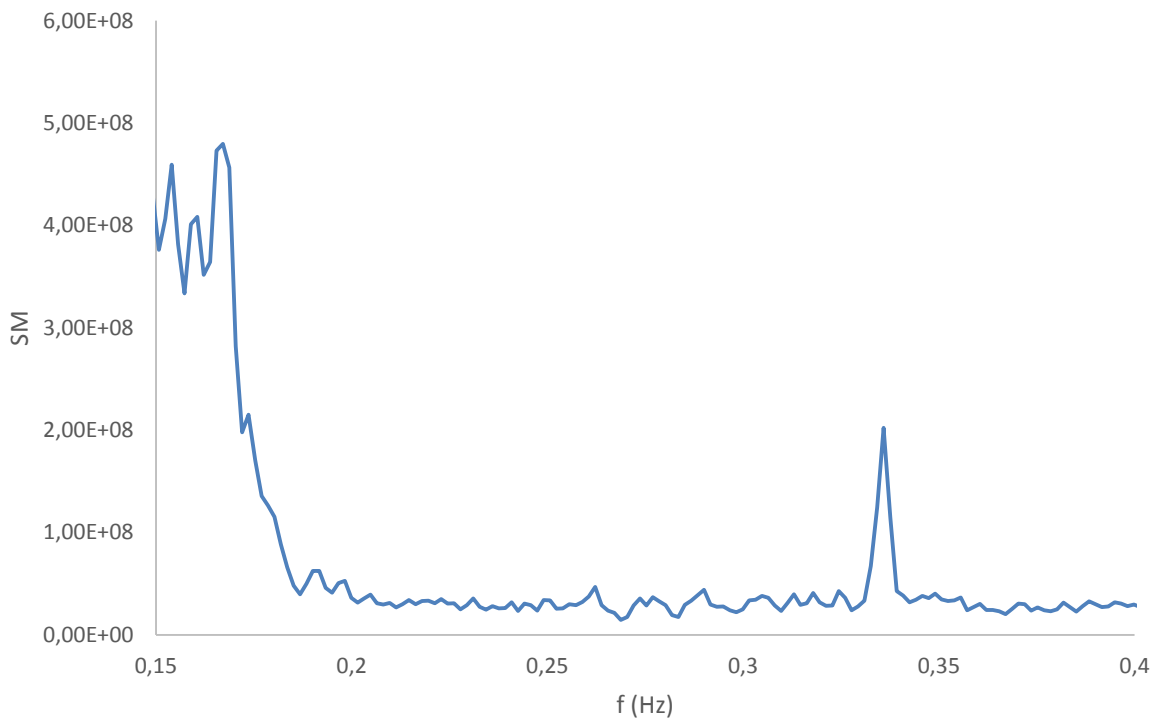
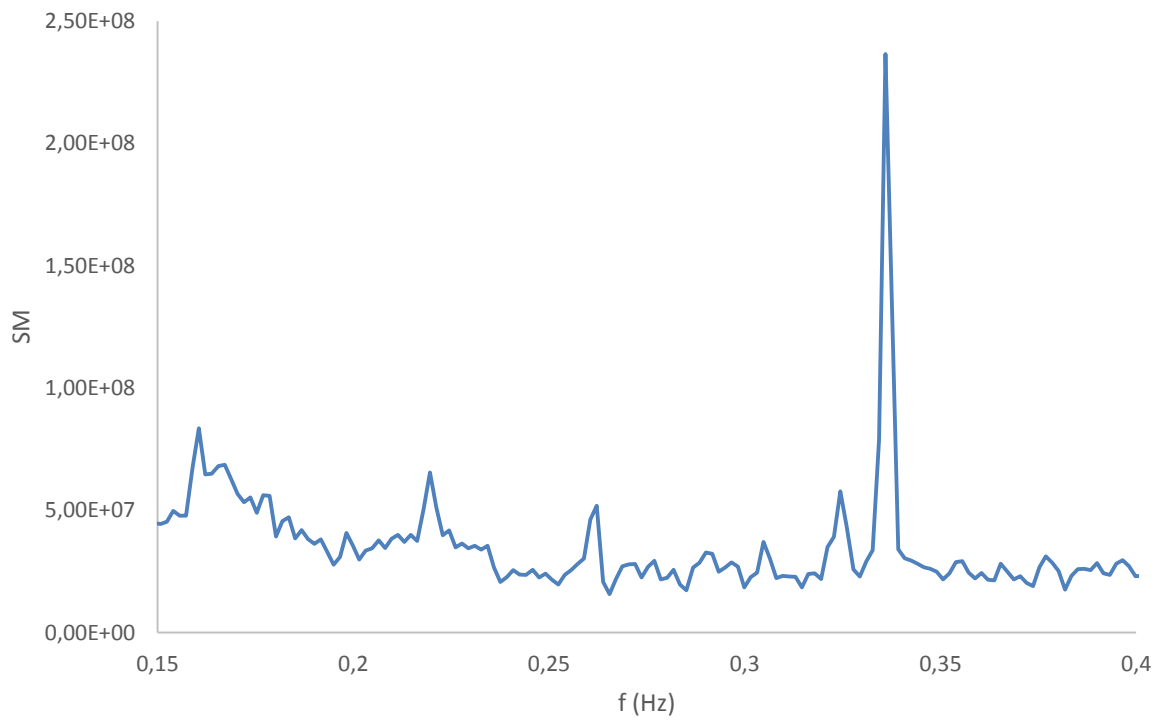
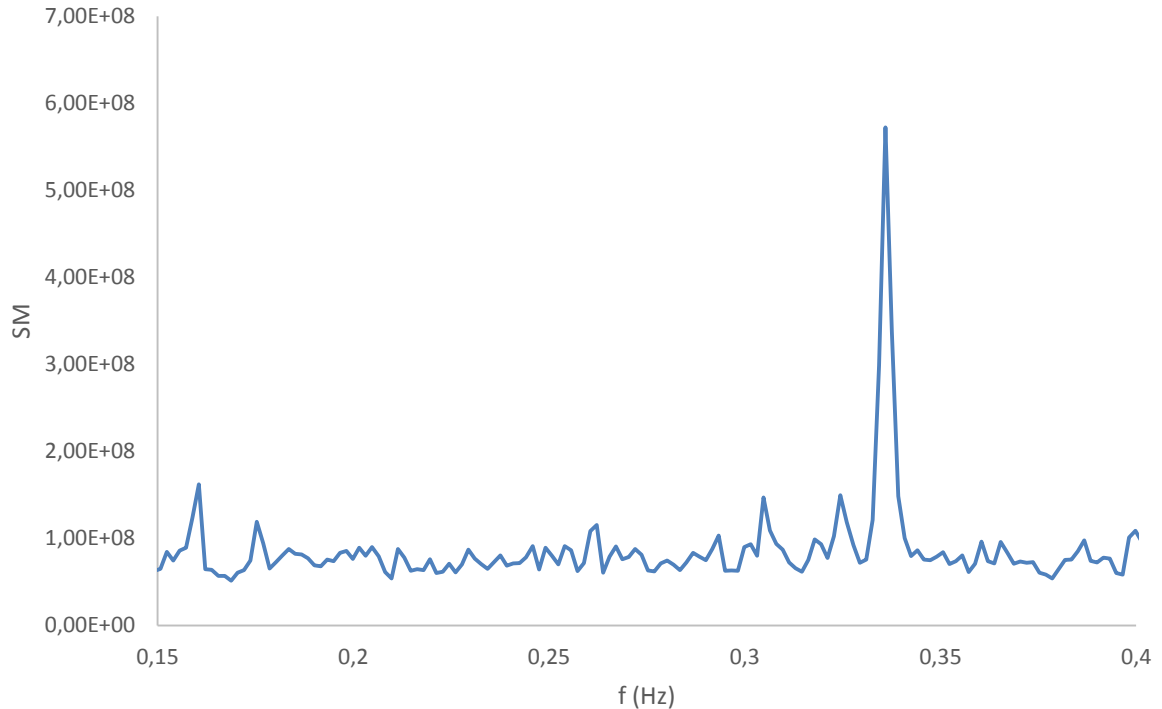


Figure 6.7 – Power Spectral Density function of the base moment M_X for 0° direction

Figure 6.8 - Power Spectral Density function of the base moment M_y for 0° directionFigure 6.9 - Power Spectral Density function of the base moment M_z for 0° direction

As it can be seen, the different PSDs are comprised of a series of peaks, one of them with a considerably higher value than the rest, this was not the result of a resonance between the rigid model

and the wind action to which it was subjected but rather the result of constrain of the test layout and data processing.

Considering the hypothesis that the dynamic response depends only upon the first three vibration modes, the fundamental idea is that the base moment can be expressed as the sum of the three contributions already stated, the mean and fluctuating components of the wind force, respectively \bar{M} and $g_B M_B$ represented by the correspondent Gumbel extreme value and the resonant term $g_R M_R$. This can be expressed as

$$M = \bar{M} + g_B M_B + g_R M_R \quad (6.1)$$

where M is the total base moment, \bar{M} is the mean value of the acquired time history, M_B is the quasi-static fluctuation and M_R is the resonant moment. g_B is the peak factor of the quasi-static component of wind velocity, commonly taken to be 3.5 and g_R is the resonant peak factor. Thus the dynamic or resonant effects can be obtained through

$$M_R = g_R \sqrt{\frac{\pi}{4\xi_j} f_j S_M(f_j)} \quad (6.2)$$

with g_R , the resonant peak factor given by

$$g_R = \sqrt{2 \ln(f_j T) + \frac{0.5772}{\sqrt{2 \ln(f_j T)}}} \quad (6.3)$$

where f_j is the j^{th} vibration frequency of the tower, $S_M(f_j)$ is the power spectral density of the base moment evaluated for the j^{th} frequency, ξ_j is the damping coefficient and T is the duration of the phenomenon, in the current case 600 s.

Once obtained the resonant base moments for each one of the X , Y and Z axis, the respective total moment at the base of the tower expressed by equation (6.4), (6.5) and (6.6) can be determined.

$$M_X = \bar{M}_X + g_{B,X} M_{B,X} + g_{R,X} M_{R,X} \quad (6.4)$$

$$M_Y = \bar{M}_Y + g_{B,Y} M_{B,Y} + g_{R,Y} M_{R,Y} \quad (6.5)$$

$$M_Z = \bar{M}_Z + g_{B,Z} M_{B,Z} + g_{R,Z} M_{R,Z} \quad (6.6)$$

In order to reproduce the known resonant base moments M_Y and M_X and the resonant base torque M_Z , a set of equivalent static wind loads $F_{R,X}$, $F_{R,Y}$ and equivalent moments $\Gamma_{R,Z}$, acting at the different heights of each floor i can be obtained through equations (6.7), (6.8) and (6.9) [41, 46].

$$F_{R,X}(z_i) = M_{R,Y} \frac{m(z_i) \varphi_2(z_i)}{\sum_{i=1}^n m(z_i) \varphi_2(z_i) z_i} \quad (6.7)$$

$$F_{R,Y}(z_i) = -M_{R,X} \frac{m(z_i) \varphi_1(z_i)}{\sum_{i=1}^n m(z_i) \varphi_1(z_i) z_i} \quad (6.8)$$

$$\Gamma_{R,Z}(z_i) = M_{R,Z} \frac{I(z_i) \varphi_3(z_i)}{\sum_{i=1}^n I(z_i) \varphi_3(z_i) z_i} \quad (6.9)$$

where $F_{R,X}(z_i)$, $F_{R,Y}(z_i)$ are the resonant components of the equivalent static wind loading at the i^{th} floor, $\Gamma_{R,Z}(z_i)$ is the resonant component of the equivalent static wind moment around the Z axis at the i^{th} floor. $m(z_i)$ and $I(z_i)$ are, respectively, the mass and the mass moment of inertia of the i^{th} floor and $\varphi_m(z_i)$ is the fundamental mode shape in the relevant directions, with $m= 1$ to 3.

As the eigenmodes are uncoupled, meaning that they just show deformation along a certain direction (X, Y or Z), the definition of the equivalent static wind loads only applies to the relevant moments and torque which yields deformation along the eigenmode direction [44].

6.3. STATISTICAL COMBINATION OF DESIGN WIND LOADS

Since the different components of the wind loads do not act on the structure simultaneously with their maximum values in the different considered directions, a statistic combination must be estimated. Furthermore, as the resonant peak loads and their respective responses are determined independently for each principal direction X, Y and Z, it is unlikely that these peak loads will occur simultaneously in all directions.

In order to take into account the contribution of the resonant loads in the three axes of the global reference system, influence coefficients can be applied in the following manner

$$M_R(\alpha) = \gamma_X(\alpha)M_{R,X} + \gamma_Y(\alpha)M_{R,Y} + \gamma_Z(\alpha)M_{R,Z} \quad (6.10)$$

where α is the wind direction, $\gamma(\alpha)$ is the combination coefficient and “+” mean “to be combined with”.

The first step to obtain the combination coefficients $\gamma(\alpha)$ for the different base moments M_X , M_Y and M_Z was to select the time history of each base moment, which are defined in the local reference system. Considering that the time history of the base moment M_X was the first to be selected, the instants t^* for which the values of M_X exceeded their respective 50 year return period Gumbel value were selected. The values of the three base moments at the instants t^* were then averaged, leading to the mean values $\overline{M_{XX}^*}$, $\overline{M_{XY}^*}$ and $\overline{M_{XZ}^*}$. This process is then repeated for both the M_Y and M_Z leading to the two groups of mean values $\overline{M_{YX}^*}$, $\overline{M_{YY}^*}$ and $\overline{M_{YZ}^*}$ and $\overline{M_{ZX}^*}$, $\overline{M_{ZY}^*}$ and $\overline{M_{ZZ}^*}$.

Since the eigenvectors of the structure have their deformed shape in the planes of the global reference system, the resonant wind forces expressed by equations (6.7) to (6.9) are also defined in this same reference system. However, the static wind loads obtained by means of the C_p maps correspond to the configurations which maximize the 5 components of the base resultant forces F_X , F_Y , M_X , M_Y and M_Z which are defined in the local reference system mentioned earlier. So, in order to superimpose the resonant wind contribution to the static one, the three base moments M_X , M_Y and M_Z were converted to the global reference system through equations (5.3) to (5.5).

Selecting these latter values, the load combination factors were computed for each selected base moment.

$$\gamma_X = \frac{\overline{M_X^*}}{M_X^{50}} \quad (6.11)$$

$$\gamma_Y = \frac{\overline{M_Y^*}}{M_Y^{50}} \quad (6.12)$$

$$\gamma_Z = \frac{\overline{M_Z^*}}{M_Z^{50}} \quad (6.13)$$

where M^{50} is the 50 year return period Gumbel value.

As it can be seen from equations 6.11 to 6.13, and from the respective exposed procedure, the combination factors were defined considering the static component of the wind action. The hypothesis

that these same combination factors could be applied to the resonant component was made since that to compute this combination factors considering the resonant loads as well the effect of the motion of the structure and thus an aeroelastic model would have been needed.

Thus, the total wind loads to be applied to the structure were given by

$$F_X(\alpha) = \gamma_{XY}(\alpha)[F_{S,X} + F_{R,X}] + \gamma_{XX}(\alpha)[F_{S,Y} + F_{R,Y}] + \gamma_{XZ}(\alpha)[F_{S,Z} + F_{R,Z}] \quad (6.14)$$

$$F_Y(\alpha) = \gamma_{YY}(\alpha)[F_{S,X} + F_{R,X}] + \gamma_{YX}(\alpha)[F_{S,Y} + F_{R,Y}] + \gamma_{YZ}(\alpha)[F_{S,Z} + F_{R,Z}] \quad (6.15)$$

$$F_Z(\alpha) = \gamma_{ZY}(\alpha)[F_{S,X} + F_{R,X}] + \gamma_{ZX}(\alpha)[F_{S,Y} + F_{R,Y}] + \gamma_{ZZ}(\alpha)[F_{S,Z} + F_{R,Z}] \quad (6.16)$$

which correspond to a weighted sum of the static and resonant components F_S, F_R respectively.

As it can be seen, the $\gamma_Y(\alpha)$ and $\gamma_X(\alpha)$ combination factors are multiplied by the F_X and F_Y forces. This is due to the relation between the resonant and the corresponding moment as it can be noticed with equations (6.7) to (6.9).

Since the Gumbel values of each base moment have been computed independently, the procedure exposed above refers to the mono-variate extreme theory, which might be too conservative. Thus it might be better to apply the multivariate extreme theory in order to have the most likely combination coefficients. However the determination of the combination coefficients and especially the ones related to the resonant component are still under examination and will continue to be one of the subjects to be studied by future researchers [44].

6.4. ACCELERATIONS FROM RESONANT WIND LOADS

As stated before, the serviceability of a structure is guaranteed if its deformations and vibrations are limited to a certain value. The latter is related only to the resonant component and is controlled by limiting the accelerations suffered by the structure.

According to Kareem et Zhou [46], the peak acceleration for the three mode shapes considered in the current analysis can be obtained through the following equations

$$\ddot{X}(z_i) = \frac{\sum_{i=1}^n F_{R,X}(z_i) \varphi_2(z_i)}{\sum_{i=u}^n m(z_i) \varphi_2^2(z_i)} \varphi_2(z_i) \quad (6.17)$$

$$\ddot{Y}(z_i) = \frac{\sum_{i=1}^n F_{R,Y}(z_i) \varphi_1(z_i)}{\sum_{i=u}^n m(z_i) \varphi_1^2(z_i)} \varphi_1(z_i) \quad (6.18)$$

$$\ddot{\theta}(z_i) = \frac{\sum_{i=1}^n \Gamma_{R,X}(z_i) \varphi_3(z_i)}{\sum_{i=u}^n m(z_i) \varphi_3^2(z_i)} \varphi_3(z_i) \quad (6.19)$$

where $\ddot{X}(z_i)$ and $\ddot{Y}(z_i)$ are the linear accelerations, respectively in the X and Y directions at the i^{th} floor and $\ddot{\theta}(z_i)$ is the angular acceleration around the Z axis at the i^{th} floor.

The angular acceleration can be transformed in translational ones around the center of rotation by multiplying the angular acceleration by the distance between the furthest point in the plan of the floor and the center of rotation. This decomposition of torsional accelerations into translational ones is represented below.

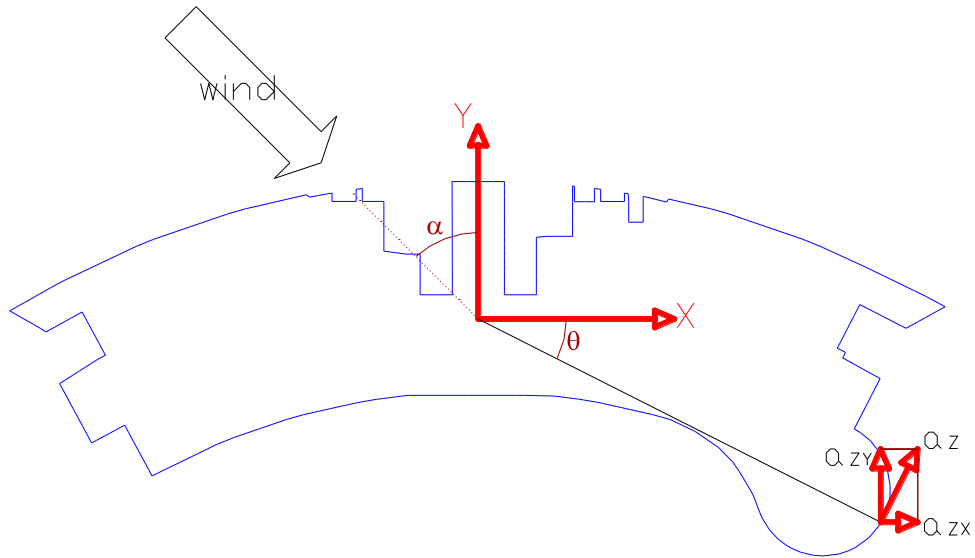


Figure 6.10 – Decomposition of torsional accelerations into translational accelerations

The translational components of the torsional acceleration can then be combined with the linear accelerations to obtain the combined effects by means of the SRSS (square root of sum of squares) method.

6.5. DYNAMIC ANALYSIS

The dynamic analysis here developed starts with a sensitivity analysis of the resonant moments to changes both in frequency and in damping.

Table 6.4 shows the first three natural frequencies of the older model, the one without the updated materials and thicknesses, and those of the new one which includes the modifications mentioned on chapter 5.

Table 6.4 – Natural frequencies of the new and old numerical models

Mode	f (Hz) of the old model	f (Hz) of the new model
1	0.2386	0.2097
2	0.2543	0.2354
3	0.3213	0.2933

As it can be seen from the table above, the natural frequencies of both models are quite similar.

Considering the values above, the respective resonant base moment $M_{R,X}$, $M_{R,Y}$ and $M_{R,Z}$ associated respectively to the 1st, 2nd and 3rd mode shapes for the critical directions and considering a 0.05 damping coefficient ξ are shown on table 6.5.

Table 6.5 – Resonant base moments for the old and new numerical models

Model	Direction	$M_{R,X}$ (kN.m)	$M_{R,Y}$ (kN.m)	$M_{R,Z}$ (kN.m)
Old	0	48276.2	45006.0	103357.7
	90	43613.8	58919.2	88319.6
	157.5	43847.0	48696.7	96540.0
	180	43316.0	83857.74	81439.9
	247.5	38332.5	76978.4	77932.9
	270	45569.4	75561.0	115776.9
	315	59755.2	53339.7	115097.0
	New	0	44435.6	50706.2
90		58238.6	47849.1	75301.4
157.5		53570.9	64675.3	86936.8
180		45133.0	60065.0	91909.1
247.5		42314.8	47730.0	77895.8
270		47871.5	55455.9	94353.2
315		43811.0	49628.4	113191.6

Analyzing the table above, it becomes clear that within each resonant base moment, for the different directions, there are some resonant base moments which are higher on the older model and others that are bigger for the new one.

Considering the average, for each resonant base moment, of the different values associated with the different directions, it can be seen that the difference between the resonant base moment obtained with the frequencies of the old model and the ones obtained with the frequencies of the new one do not diverge much.

If different frequencies are considered, the values of their respective resonant base moments do not appear to follow a specific trend, increasing or decreasing with the frequency. This is a result of the shape of the PSD, which varies considerably along the range of frequencies displayed in figures 6.7 to 6.9.

Table 6.6 – Resonant base moments for a 0.15 Hz and 0.30 Hz frequency

Frequency (Hz)	Direction	$M_{R,X}$ (kN.m)	$M_{R,Y}$ (kN.m)	$M_{R,Z}$ (kN.m)
0.15	0	135359.8	43820.7	59885.1
	90	132981.8	48992.4	68212.7
	157.5	129290.2	131657.9	79170.7
	180	111563.9	50449.5	77155.0
	247.5	131502.5	39181.7	44834.2
	270	127931.1	42883.2	59968.4
	315	38126.7	128959.6	68402.7
	0.30	0	56888.4	51032.0
90		48167.0	48775.6	76306.3
157.5		54956.9	53910.9	98039.4
180		41972.8	54515.7	86672.6
247.5		39853.2	41246.8	75750.6
270		49369.9	67230.7	91157.8
315		54932.0	50250.0	92439.5

Another parameter that influences the resonant base moments is the damping coefficient.

Focusing on the case of the updated model and considering its natural frequencies, the effect of a smaller or larger damping coefficient can be evaluated for each resonant base moment and for the different directions.

Table 6.7 – Resonant base moment $M_{R,X}$ for different damping coefficients ξ

Direction	$M_{R,X}$ (kN.m)		
	$\xi = 0.01$	$\xi = 0.03$	$\xi = 0.07$
0	99361.1	57366.1	37555.0
90	130225.5	75185.7	49220.6
157.5	119788.2	69159.8	45275.7
180	100920.6	58266.5	38144.4
247.5	94618.7	54628.1	35762.5
270	107043.9	61801.9	40458.8
315	97964.5	56559.8	37027.1

Table 6.8 - Resonant base moment $M_{R,Y}$ for different damping coefficients ξ

Direction	$M_{R,Y} (kN.m)$		
	$\xi = 0.01$	$\xi = 0.03$	$\xi = 0.07$
0	113382.4	65461.3	42584.5
90	106993.9	61722.9	40439.9
157.5	144618.5	83495.5	54660.7
180	134309.3	77543.5	50764.2
247.5	106727.4	61619.1	40339.2
270	124003.1	71593.2	46868.8
315	110972.6	64070.0	41943.7

Table 6.9 - Resonant base moment $M_{R,Z}$ for different damping coefficients ξ

Direction	$M_{R,Z} (kN.m)$		
	$\xi = 0.01$	$\xi = 0.03$	$\xi = 0.07$
0	220170.7	127115.6	83216.7
90	168379.0	97213.7	63641.3
157.5	194396.8	112235.0	73475.1
180	205514.9	118654.1	77677.3
247.5	1741802.2	100563.0	65833.9
270	210980.3	121809.5	79743.1
315	253104.3	146129.8	95664.4

Through the analysis of tables 6.7 to 6.9 it is clear the influence of the damping on the resonant base moments developed on the structure. As it can be seen, for increasing damping coefficients the three resonant base moments $M_{R,X}$, $M_{R,Y}$ and $M_{R,Z}$ suffer a considerable decrease.

As seen in 6.2, the static forces equivalent to the resonant component depend on the eigenvectors at the different levels for the different mode shapes. In order to obtain the eigenvectors, the center of mass of each floor of the tower and the center of mass of each floor of the spire has to be determined. Once determined the different centers of mass, the displacement of each one of these points in the different directions of interest U_X , U_Y and U_Z as well as its rotations R_X , R_Y and R_Z have to be evaluated. Furthermore, the mass and mass moment of inertia of the various floors need to be determined.

As it can be understood from the description above, this is a difficult and time consuming process. So, in order to simplify the process of obtaining the equivalent forces, and since the mode shapes of the two models as well as their respective frequencies are very similar, the inputted loads on the updated model, correspond to those obtained for the older model.

Furthermore, since, as it was seen before, the difference between the resonant moments of the two models are small and both correspond only to a small fraction of the base moment of the quasi-static component, the error introduced by this hypothesis will be negligible.

In the table below the resonant moments ($\xi = 0.05$) with their correspondent Gumbel extreme value obtained from the wind tunnel test are compared.

Table 6.10 – Resonant and Gumbel base moments

Base Moment	0	90	157.5	180	247.5	270	315
$M_{R,x}$ (kN.m)	44435.6	58238.6	53570.9	45133.0	42314.8	47871.5	43811.0
$M_{Gumbel,x}$ (kN.m)	1082643	-342048	-1099030	-1013928	-946646	-357318	684563
$M_{R,y}$ (kN.m)	50706.2	47849.1	64675.3	60065.0	47730.0	55455.9	49628.4
$M_{Gumbel,y}$ (kN.m)	-49322	166443	195741	265698	-214469	-216834	-129570
$M_{R,z}$ (kN.m)	98463.4	75301.4	86936.8	91909.1	77895.8	94353.2	113191.6
$M_{Gumbel,z}$ (kN.m)	47490	40618	-50086	52682	81847	-39397	-128268

After introducing the equivalent static forces of the resonant component of the wind load affected by the respective combination factors into the numerical model, the values of the axial force at the base of the columns considered in chapter 5, as well as the shear force at the base of the columns and of the cores and the displacements at ground level and at the level of the 1st, 31st and roof floor referred to the full wind action were obtained.

A comparison between the latter values and the ones obtained considering only the static component of the action of wind is presented below.

Table 6.11 shows the axial force at the base of the columns for the total action of the wind and its respective increase to the values obtained considering only the static component.

Table 6.11 – Axial force at the base of the columns due to wind action with the resonant component

Column	Column Group	Combination	Wind Direction	N_W (kN)	N_R (kN)	$\frac{(N_R - N_W)}{N_W}$ (%)
4	Park	ULS 4 - 39	157.5°	-24662.8	-24689.5	0.1083
1	Central	ULS 3 - 39	157.5°	-30381.8	-30383.8	0.0066
6	Podium	ULS 4 - 4	0°	-24002	-24016.3	0.0596
1	Spire	ULS 4 - 75	337.5°	-18676.9	-18703.1	0.1403

Analyzing the table above, and especially its last column, it is clear that the increase of axial force at the base of the columns due to the resonant component of the wind action is neglectable.

Furthermore, from table 6.12 it can be concluded that as well as for the axial force, the effect of the resonant component on the shear force of the different cores is also neglectable.

Table 6.12 – Shear force at the base of the cores due to wind action with the resonant component

Core	Direction X		Direction Y		$\frac{F_{R,X} - F_{W,X}}{F_{W,X}}$	$\frac{F_{R,Y} - F_{W,Y}}{F_{W,Y}}$
	$F_{R,X}$ (kN)	Combination	$F_{R,Y}$ (kN)	Combination	(%)	(%)
Central	6463.92	ULS 4 – 39	-8717.58	ULS 4 – 59	0.416	0.321
Low rise	-3101.32	ULS 4 – 4	-714.99	ULS 4 – 59	0.245	0.496
Right	-5927.99	ULS 4 – 4	-6188.96	ULS 4 – 75	0.156	0.630
Left	4242.66	ULS 4 – 39	4870.40	ULS 4 – 4	0.090	0.433

After extracting all the values of the shear and axial forces on the different elements mentioned above, the numerical model allowed once again for the determination of the displacements on the floors considered earlier on the Static Analysis which were then used to evaluate the interstory and total building drifts for the wind action comprised of all its components.

Table 6.13 – Interstory drift due to wind action with the resonant component

Combination	Floor 1 drift	Roof drift
ULS 3 – 10 (22.5°)	1/1393	1/624
ULS 3 – 1 (0°)	1/1515	1/655
ULS 3 – 23 (90°)	1/2980	1/1757
ULS 3 – 39 (157.5°)	1/1226	1/637
ULS 3 – 44 (180°)	1/1338	1/714
ULS 3 – 58 (247.5°)	1/1245	1/806
ULS 3 – 63 (270°)	1/2015	1/2139
ULS 3 – 75 (315°)	1/2321	1/1301

Table 6.13 contains the interstory drift index values for the different critical directions as well as the maximum drift obtained with the ULS 3 – 10 combination for both the roof and the floor 1 levels.

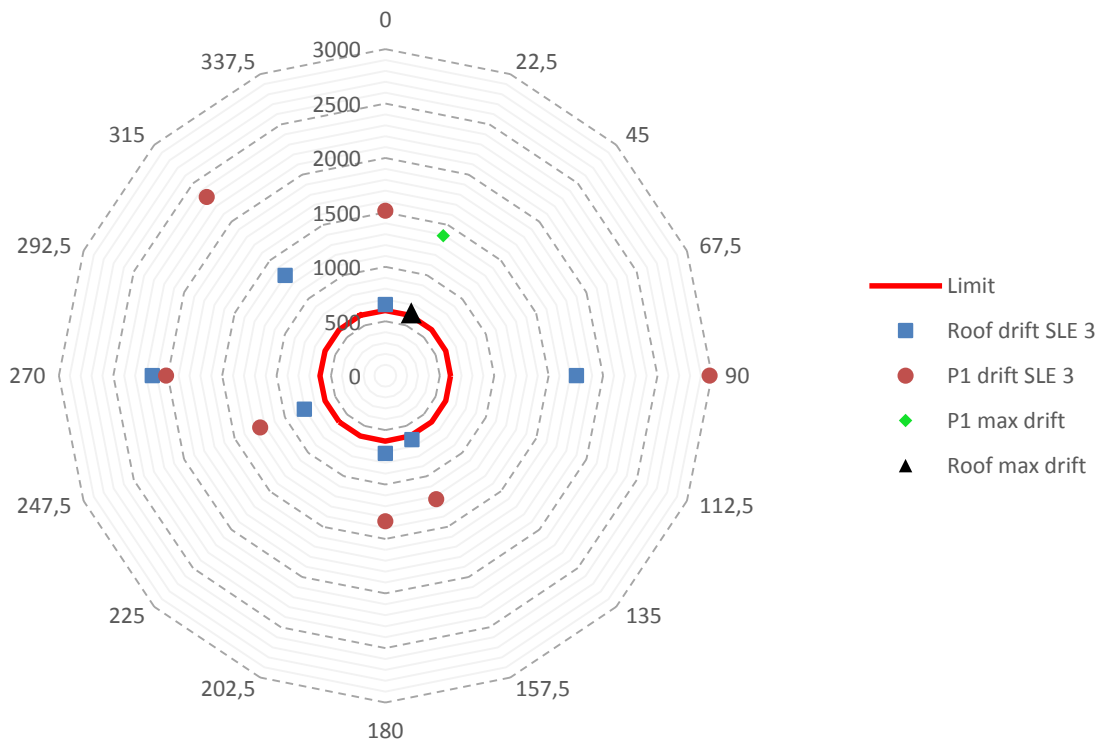


Figure 6.11 – Representation of the interstory drift for different wind directions

As it can be seen from figure 6.11, the values of the interstory drift of both levels, although higher than for the previous case analyzed in chapter 5 as it was expected, respect the imposed limit.

Taking into account the values of the total building drift shown on table 6.14 and represented on figure 6.12 along with its respective limit it is clear that the total building drift limit is also respected.

Table 6.14 – Total building drift due to wind action with the resonant component

Combination	Total building drift
ULS 3 – 10 (22.5°)	666
ULS 3 – 1 (0°)	696
ULS 3 – 23 (90°)	3089
ULS 3 – 39 (157.5°)	775
ULS 3 – 44 (180°)	859
ULS 3 – 58 (247.5°)	918
ULS 3 – 63 (270°)	2207
ULS 3 – 75 (315°)	1209

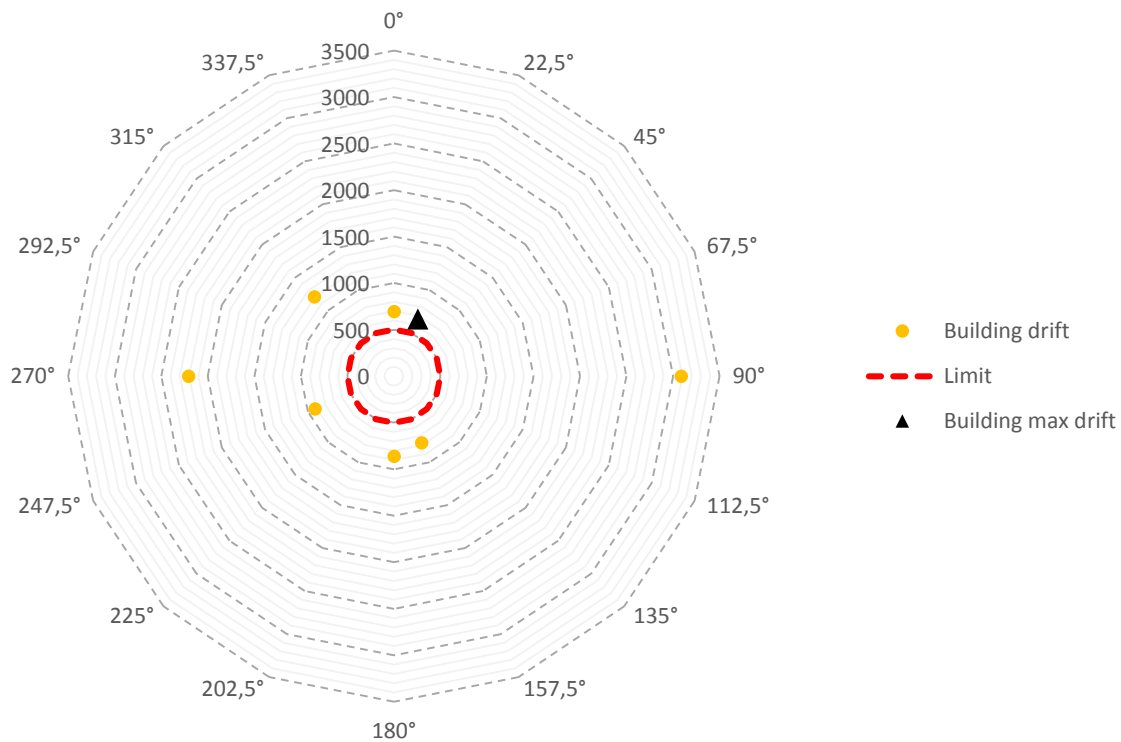


Figure 6.12 – Representation of the total building drift for different wind directions

Once guaranteed that the deformations of the Unicredit high-rise building respect their serviceability limits, the evaluation of the maximum accelerations developed on the tower have to be evaluated and compared to current limits in order to be possible to evaluate its overall functional performance and behavior.

Although it is known that the wind-induced motion can affect the building occupants' activities, there is no generally accepted international standards for comfort criteria, in part because human perception of motion and tolerance to wind-induced vibration are essentially subjective assessments.

A considerable amount of data related to the physiological and psychological parameters that affect human perception of motion and vibration is available in different published literatures. However, this data concerns mainly the vibration related to ship, vehicular and other types of transportation as well as industrial and manufacturing related vibrations which are mostly large amplitude vibrations and are included in a frequency range that is outside the range of frequency that concerns building motion.

The specific studies related to human perception of motion in buildings excited by the wind action can be divided, according to Kareem et al [12], in three different categories: field experiments and survey-based studies of building occupants in wind-excited tall buildings, motion simulators and shake table experiments and field experiments conducted in artificially excited buildings.

The different available tests allowed researchers to determine the different factors that affect human response to building motion. Field tests have shown that perception and tolerance to acceleration tends to increase as the building frequency decreases within the range of frequency that is of interest to tall buildings. The age, body posture and body orientation are also factors that influence the motion perception. While the sensitivity of humans to motion is an inverse function of age and thus children

are more sensitive than adults, it is proportional to the distance of the person's head from the floor, and thus, the higher the person's head the greater the sensitivity. The expectancy of motion as well as the body movement are also important factors, it is known that the threshold acceleration for the case of no knowledge is approximately twice that for the case of prior knowledge. In the same way, for the latter, the perception threshold is more than twice as much between walking subjects and standing subjects.

Visual and acoustic cues also play an important part in a person's perception of motion since the eyes can perceive the motion of objects in a building and the rotation of the building relatively to fixed landmarks. In the same way, the sounds originated by the sway of the building and from the wind whistling are known to lower the perception threshold.

As seen before, a certain point belonging to the plan of some floor can be subjected to translational and torsional accelerations. In the case of human perception, the angular motion appears to be more noticeable to occupants.

Although the motion perception may be measured by both the peak acceleration and the root-mean-square (RMS) accelerations, currently, the peak acceleration is the standard for the evaluation of motion perception in buildings because it is the best compromise of the various parameters mentioned above.

Table 6.15 shows some proposed limits of the peak acceleration.

Table 6.15 – Peak acceleration limits

Peak acceleration		Comfort limit
<0.5% g	<5 mg	Not perceptible
0.5% g to 1.5% g	5 mg to 15 mg	Threshold of perceptibility
1.5% g to 5.0% g	15 mg to 50 mg	Annoying
5% g to 15% g	50 mg to 150 mg	Very annoying
>15% g	>150 mg	Intolerable

Considering the method described in 6.4 to determine the components of the acceleration it was possible to obtain the correspondent values for the different directions at roof level.

Table 6.16 – Roof \ddot{X} translational acceleration

$\ddot{X} (m/s^2)$						
0°	90°	157.5°	180°	247.5°	270°	315°
0.01595	0.01505	0.02034	0.01889	0.01501	0.01744	0.01561
$\ddot{X} (mg)$						
0°	90°	157.5°	180°	247.5°	270°	315°
1.62635	1.53471	2.0744	1.92653	1.53089	1.77869	1.59178

Table 6.17 - Roof \ddot{Y} translational acceleration

$\ddot{Y} (m/s^2)$						
0°	90°	157.5°	180°	247.5°	270°	315°
-0.014	-0.0184	-0.0169	-0.0143	-0.0134	-0.0151	-0.0138
$\ddot{Y} (mg)$						
0°	90°	157.5°	180°	247.5°	270°	315°
-1.4317	-1.8764	-1.726	-1.4542	-1.3634	-1.5424	-1.4116

Table 6.18 - Roof $\ddot{\vartheta}$ angular acceleration

$\ddot{\vartheta} (rad/s^2)$						
0°	90°	157.5°	180°	247.5°	270°	315°
0.00842	0.00631	0.00771	0.00814	0.00689	0.00834	0.00997

Multiplying the angular acceleration by the distance between the furthest point in the plan of the floor and the center of rotation (36.5 m) the angular acceleration can be converted into a translational one.

Table 6.19 – Translational component of the angular acceleration

$\vartheta_{XY}'' (m/s^2)$						
0°	90°	157.5°	180°	247.5°	270°	315°
0.30742	0.23036	0.28151	0.29704	0.25154	0.30452	0.36404

Taking into account the angle between the line defined by the center of rotation and the furthest point, and the X axis, represented by θ on figure 6.10, the latter translational acceleration can be decomposed along the X and Y axis by the following equations

$$\ddot{\vartheta}_X = \vartheta_{XY}'' \sin \theta \quad (6.20)$$

$$\ddot{\vartheta}_Y = \vartheta_{XY}'' \cos \theta \quad (6.21)$$

For the furthest point of the roof slab, the angle described above is equal to $\theta=26^\circ$.

Taking into account the tables above, the maximum acceleration will be developed for a wind action acting along the 315° direction.

$$\ddot{X} = 1.59178 mg$$

$$\ddot{Y} = -1.4116 mg$$

$$\ddot{\vartheta}_X = 16.274 \text{ mg}$$

$$\ddot{\vartheta}_Y = 33.3667 \text{ mg}$$

Applying the SRSS method to combine the translational components of the torsional acceleration with the linear ones

$$\ddot{a}_X = \sqrt{\ddot{X}^2 + \ddot{\vartheta}_X^2} \quad (6.22)$$

$$\ddot{a}_X = \sqrt{1.59178^2 + 16.274^2} = 16.3517 \text{ mg}$$

$$\ddot{a}_Y = \sqrt{\ddot{Y}^2 + \ddot{\vartheta}_Y^2} \quad (6.23)$$

$$\ddot{a}_Y = \sqrt{-1.4116^2 + 33.3667^2} = 33.3965 \text{ mg}$$

Comparing the acceleration values obtained with their respective limits, it becomes clear that for both the directions the threshold of perceptibility is surpassed. However some considerations must be made regarding the obtained results.

In the current analysis the two linear accelerations were combined with the torsional one. However the usual limits presented on table 6.15 and other limits present in different literatures only consider the contribute of the linear accelerations which, for the current case, are considerably below their limit values.

Furthermore the analysis is made for the point of the roof slab which is furthest from its rotation center, making it the worst possible point of the building to the evaluation of the acceleration both in the horizontal plan and in elevation. Thus, the acceleration felt by the buildings' occupants will be certainly lower than the ones obtained in this analysis.

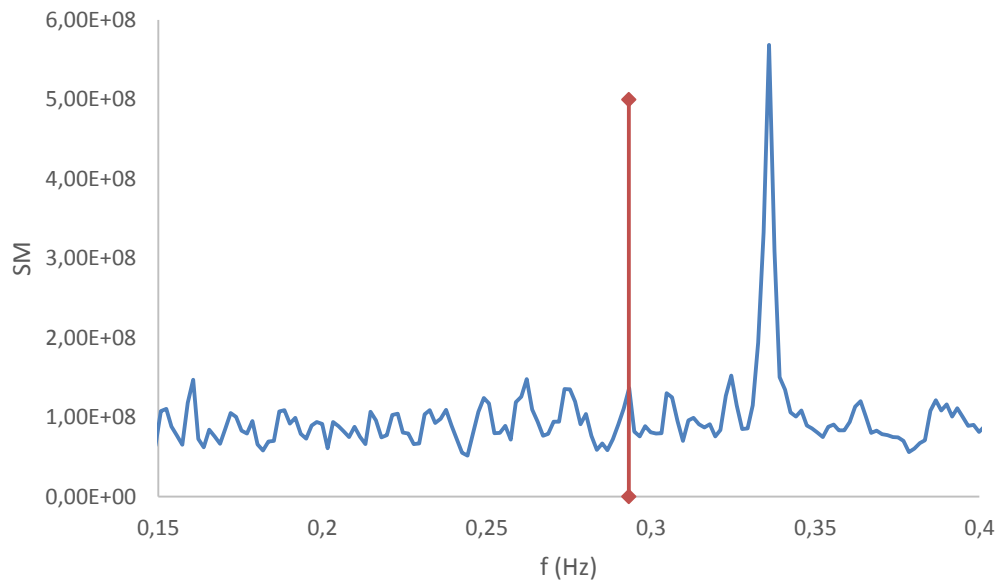


Figure 6.13 - Power Spectral Density function of the base moment M_z for 315° direction

7

Conclusions

7.1. FINAL CONSIDERATIONS

The work developed in this thesis unveiled a small part of the large diversity of subjects that constitute the field of Wind Engineering. Through this dissertation it was possible to understand some of the key concepts and procedures which allow the determination of wind loads and enable the evaluation of the response of a structure, in the current case the response of the Unicredit high-rise building.

The main results and conclusions obtained in each one of the chapters that constitute this work are exposed below.

This work began with a chapter dedicated exclusively to the definition of the wind, from the description and characterization of the main mechanisms that generate the different types of wind as well as the main global atmospheric circulation movements and other local phenomenon. Afterwards, the characterization of the atmospheric boundary layer was made through the description of the different mean velocity profiles and the different factors that influence it such as terrain roughness and topography. Once the different wind profiles were defined, the extreme wind speeds and respective extreme value distributions were then described. After the description of the mean velocity component, the fluctuating part was introduced and characterized through the different descriptors normally associated to it.

Chapter three consisted on a description of the overall redevelopment project of the three districts, Garibaldi, Varesima and Isola as well as of the “Città della Moda” where the Unicredit high-rise building is inserted. Afterwards, the plants of the different floors as well as the interstory height between them were exposed. Furthermore, the different geometric characteristics of the different columns and the thicknesses of both the walls that materialize the cores and those of the slabs were presented. Once defined the materials used on the construction of the building and on the spire the various vertical loads to be considered on the analysis were described.

Chapter four begins with the procedure used to obtain the wind loads through the EN 1991-1-4. First both the fundamental base wind velocity and the base wind velocity were obtained for the particular case of Milan through the Italian National Annex. This National Annex also allowed for the determination of the terrain category in which the city of Milan is inserted as well as the minimum height z_{min} and the roughness length z_0 . Once obtained the wind profile through the Eurocode, the characterization of the fluctuating component associated to the turbulence was made through its intensity which ultimately allowed for the determination of the peak velocity pressure at the reference height.

Next, the procedure to obtain the wind action which acted in the form of pressures or forces was described.

Once obtained the wind pressures at different reference heights it was possible to develop the respective diagrams along the height of the structure which then allowed the evaluation of the base resultant forces and moments.

The second part of chapter four focused on the specific case of the wind tunnel-testing and in particular to the measurements obtained by local pressures and by the HFFB method.

The different kind of wind tunnels currently in use were described. Also, the different aspects of the simulation of the natural wind flow as well as the modelling aspects of the structure were mentioned. Furthermore, the procedure and the different instruments used to measure the local pressures as well as the procedure to measure the base resultant forces and moments through the high-frequency balance were exposed. Also, a description of the CRIACIV wind engineering laboratory along with its wind tunnel and respective instruments was done.

After exposing the base resultant forces and moments obtained both through the Eurocode and through the wind tunnel test, by integration of the C_p coefficients, it was possible to compare them. From this comparison it was possible to conclude that the wind tunnel test developed on this particular structure brought advantages mainly related to cost savings.

From this comparison it was also possible to notice that for a specific wind direction the gain obtained with the wind tunnel test was particularly high. A specific analysis of the wind pressure profiles developed for the wind direction allowed for the understanding of the reasons to why this particular direction showed such behavior. As shown, the Eurocode wind profiles constitute a conservative envelope of the real wind pressures, leading to higher base resultant forces and moments. Furthermore, for the specific case of the Unicredit high-rise building, suctions are developed along the wind ward side for the 90° wind direction. These suctions are not taken into account on the Eurocode therefore leading to an even greater difference between the base resultant forces obtained through the Eurocode and through the wind tunnel.

The numerical model used to obtain the response of the structure to the wind loads was described in chapter five. Since the reference system of the wind tunnel and that of the numerical model were different a procedure to convert the base resultant forces and moments from the first to the latter had to be developed and was exposed in this same chapter. Next, the description of the construction stages, introduced on the model and the different combinations and their respective combination factors were also exposed.

This chapter ends with a quasi-static analysis of the wind action. For that purpose, the values of the axial force at the base of the columns as well as the shear at the base of the cores was compared to the combination in which only the vertical loads were applied. In both cases the respective values were higher when the wind loads were applied, being the increase of the shear considerably higher since the wind action, although with a vertical component at roof level, is mainly a horizontal action.

Furthermore the comparison between the distribution of the shear between the base of the columns and the base of the cores allowed for the understanding of how the structure responds to horizontal actions. From the results obtained it is clear that the cores are the main system which withstands the horizontal actions developed, in the current work by the wind action.

Afterwards, an evaluation of the serviceability conditions of the tower was developed taking into account the displacements induced on the structure at the roof and 31st floor levels and at 1st and ground level. This allowed the analysis of the interstory drift at roof level and at the level of the first floor. The

total building drift was also obtained taking into account the displacement at the roof level and at ground level. These values were then compared to the limits which are usually considered to be appropriate for the functional behavior and performance of tall buildings.

Chapter six contains the first twenty natural frequencies of the structure obtained through the numerical model as well as the modal participation masses and a representation of the mode shapes of interest to the analysis. The Power Spectral Density functions obtained from the time histories which in turn were obtained from the wind tunnel test are represented for the three base moments obtained for the 0° direction.

Afterwards the method used to obtain the resonant loads represented by equivalent static loads was described as well as the procedure to acquire the combination coefficients that take into account the non-simultaneity of the maximum resonant loads in each direction. Once determined the equivalent static loads, the method used to obtain the respective induced accelerations was described.

This chapter ends with a dynamic analysis which includes the resonant component of the wind action. The same values obtained in the quasi-static analysis were also extracted for the case of the total wind action allowing for the comparison between both situations and thus enabling the evaluation of the effect of the resonant component on the response of the structure.

As seen through the difference of the values of the forces mentioned before, the effect of the resonant component on the response of the structure is negligible when compared to the quasi-static component.

As in the previous case, the serviceability conditions of the structure were also verified. The interstory drifts and the total building drift evaluated led to the conclusion that the deformations of the building respect the limits usually imposed. Since the resonant component is related to the vibration of the structure, the latter had to be verified through the accelerations induced on the building.

These accelerations were evaluated considering the two linear components along the X and Y axis as well as the torsional component associated to the Z axis. The values referred to the linear accelerations respected, with a considerable margin, the limits usually imposed. In order to consider the contribution of both the linear and torsional accelerations, the latter had to be decomposed into its correspondent translational components along the X and Y axis which were then combined with the linear components by means of the SRSS (square root of sum of squares) method. The final accelerations surpassed the threshold of perceptibility. However it has to be taken into account that the worst possible point was considered, that these limits are usually related only to the linear components of the acceleration.

7.2. FUTURE DEVELOPMENTS

The analysis developed in the current work was based on the experimental data obtained from the wind tunnel test which allowed for the determination of the equivalent static loads to be inputted on the numerical model.

The rapid evolution of computer technology has allowed the development of numerical simulations which enable the study of the fluid-structure interaction (FSI). This method could be applied to the current case since fluid-structure interaction problems deal with solid structures that interact with a surrounding fluid flow, in the current case the wind flow. This analysis, applied to the Unicredit high-rise building could lead to a more economical solution.

Another future development related to this work consists on the study of different methods which would allow for the determination of more accurate combination coefficients which could also lead to more economical solutions.

Finally, in order to describe the complete behavior of the Unicredit high-rise building, different analysis such as a seismic and a non-linear one may be developed.

REFERENCES

- [1] Baker, C. J. "Wind engineering—Past, present and future". *Journal of Wind Engineering and Industrial Aerodynamics*. Vol. 95. n.º 9–11 (2007). p. 843-870.
- [2] Davenport, Alan G. "Past, present and future of wind engineering". *Journal of Wind Engineering and Industrial Aerodynamics*. Vol. 90. n.º 12–15 (2002). p. 1371-1380.
- [3] Isyumov, Nicholas. "Alan G. Davenport's mark on wind engineering". *Journal of Wind Engineering and Industrial Aerodynamics*. Vol. 104–106. n.º 0 (2012). p. 12-24.
- [4] Wikipedia - "Wind". 2014. <http://en.wikipedia.org/wiki/Wind>. Consulted on 16/03/2014
- [5] Wikipedia - "Anemoi". 2014. <http://en.wikipedia.org/wiki/Anemoi>. Consulted on 16/03/2014
- [6] Simu, Emil; Scanlan, Robert H. "Wind effects on structures fundamentals and applications to design". John Wiley & Sons, Inc: New York, 1996. 0-471-12157-6
- [7] Urbano, Diana. "Termodinâmica". FEUP. Porto. 2011
- [8] Cengel, Yunus A; Boles, Michael A; Kanoglu, Mehmet. "Thermodynamics: an engineering approach". McGraw-Hill New York, 2011.
- [9] Bastos, Fernando Jorge Dias da Costa. "Comportamento aerodinâmico de estruturas esbeltas análise de efeitos de rajada". Porto:: [s. n.], 2009.
- [10] Katoh, Shigeo; Yoshida, Fumitake. "Biochemical engineering: a textbook for engineers, chemists and biologists". John Wiley & Sons, 2009. 3527627650
- [11] Dyrbye, Claës; Hansen, Svend Ole. "Wind loads on structures". John Wiley & Sons, 1996.
- [12] Kareem, Ahsan; 幸雄; 田村. "Advanced Structural Wind Engineering". Springer, 2013. 4431543368
- [13] Palutikof, JP; Brabson, BB; Lister, DH; Adcock, ST . "A review of methods to calculate extreme wind speeds". *Meteorological applications*. Vol. 6. n.º 2 (1999). p. 119-132. 1469-8080
- [14] Holmes, John D. "Wind loading of structures". CRC Press, 2001.
- [15] Klemen, M. "Wind speed data and its application to wind generated power". Homepower, 1997.
- [16] Brock, Fred V; Richardson, Scott J. "Meteorological measurement systems". Oxford University Press New York, 2001.
- [17] Harper, BA; Kepert, JD; Ginger, JD. "Guidelines for converting between various wind averaging periods in tropical cyclone conditions". *World Meteorological Organization, WMO/TD*. n.º 1555 (2010).
- [18] Li, CW. "Wind directionality effects on design wind pressures of Hong Kong Buildings".
- [19] Kaimal, Jagadish Chandran; Finnigan, John J. "Atmospheric boundary layer flows: their structure and measurement". (1994).
- [20] "Porta Nuova Business District". 2014. <http://businessdistrict.porta-nuova.com/en/index.php>.
- [21] von Hoffman, Nicholas. "Cesar Pelli. Creating na architecture that is responsive to function and place". 2005. http://www.architecturaldigest.com/architecture/archive/pelli_article_032005
- [22] "People. Cesar Pelli". 2014. <http://pcparch.com/firm/people/cesar-pelli-faia>

- [23] Luigi Zoia, Ivo. "Analisi Strutturale della torre di Garibaldi Repubblica soggetta a Carico di vento" Corso si Laurea in Ingegneria Civile. Politecnico di Milano. 2006
- [24] Crespi, Giuseppe Pietro. Personal notes.
- [25] "Eurocode 2: Design of Concrete Structures: Part 1-1: General rules and rules for buildings" (EN 1992-1-1, 2010). Comite Europeen de Normalisation. Bruxles. Belgium. 2010
- [26] "Eurocode 1: Actions on Structures: Part 1-4: General actions. Wind actions" (EN 1991-1-4, 2010). Comite Europeen de Normalisation. Brussels. Belgium. 2010
- [27] "ASCE 07-05 - Minimum Design Loads for Buildings and Other Structures", American Society of Civil Engineers, 2005.
- [28] "AIJ Recommendations for Loads on Buildings", Architectural Institute of Japan, 2004.
- [29] "Australian/New Zealand Standard 1170.2 - Structural Design Actions - Wind Actions", Standards Australia / Standards New Zealand International Ltd, 2002.
- [30] "BS 6399-2: Loading for buildings - Code of practice for wind loads", British Standard Institution, 1997
- [31] Cook, Nicholas; Expert, Eurocodes - Designers' Guide to EN 1991-1-4: Eurocode 1: Actions on Structures, General Actions: Part 1-4: Wind Actions. Thomas Telford, 2007. 0727731521
- [32] "Appendice Nazionale Italiana alla UNI EN 1991-1-4". Ministero delle Infrastrutture e dei Transporti. Rome. Italy. 2013
- [33] Cermak, Jack E. "Wind-tunnel development and trends in applications to civil engineering". *Journal of Wind Engineering and Industrial Aerodynamics*. Vol. 91. n.º 3 (2003). p. 355-370.
- [34] Duthinh, Dat; Simiu, Emil. "The Use of Wind Tunnel Measurements in Building Design".
- [35] Irwin, Peter; Denoon, Roy; Scott, David. "Wind Tunnel Testing of High-Rise Buildings". Routledge, 2013. 1317999959
- [36] Cermak, Jack E; Isyumov, Nicholas. "Wind tunnel studies of buildings and structures". American Society of Civil Engineers, 1999.
- [37] Spinelli, P; Bartoli, G; Pasto, S; Procino, L. "Garibaldi-Repubblica Complex in Milan (Italy): Wind Tunnel-Test Assessment of Pressures and Forces in Dynamic Field". CRIACIV. 2006
- [38] Spinelli, P; Bartoli, G; Pasto, S; Procino, L; Borri, C. " Garibaldi-Repubblica Complex in Milan (Italy): Wind Tunnel-Test Assessment of Pressures and Forces in Dynamic Field on the Antenna of the Tower Building". CRIACIV. 2006
- [39] Holmes, JD; Rofail, Antonios; Aurelius, Leighton. "High frequency base balance methodologies for tall buildings with torsional and coupled resonant modes". Texas Tech Univ., 2003.
- [40] Simiu, E. "Design of Buildings for Wind: A Guide for ASCE 7-10 Standard Users and Designers of Special Structures". Wiley, 2011.
- [41] warsido, Workamaw. "Dynamic optimization for the wind-induced response of a tall building".
- [42] "Norme tecniche per le costruzioni". Ministero delle Infrastrutture e dei Transporti. Rome. Italy. 2005
- [43] "Eurocode: Basis of Structural Design" (EN 1990), Comite Europeen de Normalisation. Brussels. Belgium. 2009

- [44] Pasto, Stefano; Facchini, Luca; Procino, Lorenzo; Spinelli, Paolo. "Equivalent static wind loads on tall buildings". 2008.
- [45] Griffis, Lawrence G. "Serviceability limit states under wind load". *Engineering Journal-American Institute of Steel Construction Inc.* Vol. 30. n.º 1 (1993). p. 1-16. 0013-8029
- [46] Mendis, P; Ngo, T; Haritos, N; Hira, A; Samali, B; Cheung, J. "Wind loading on tall buildings". *EJSE Special Issue: Loading on Structures*. Vol. 3. (2007). p. 41-54.
- [47] Zhou, Yin; Kijewski, Tracy; Kareem, Ahsan. "Aerodynamic loads on tall buildings: interactive database". *Journal of structural engineering*. Vol. 129. n.º 3 (2003). p. 394-404. 0733-9445
- [48] Ferreira, Nuno André Costa. "Efeito do vento em edifícios altos aplicação a um caso concreto". Porto:: FEUP, 2008.
- [49] Henriques, Jorge Fernando Martins. "Projecto de torres eólicas reticuladas de grande altura (150M)". Porto:: FEUP, 2012.
- [50] Lopes, Adelino Vasconcelos. "A acção do vento e a resposta dinâmica de edifícios altos". Porto:: FEUP, 1992.